Microslots: Scalable Electromagnetic Instrumentation

by

Yael Gregory Eli Maguire

Submitted to the Program in Media Arts and Sciences, School of Architecture and
Planning in partial fulfillment of the requirements for the degree of

Doctor of Philosophy

at the

MASSACHUSETTS INSTITUTE OF TECHNOLOGY

September 2004

© MIT, MMIV. All rights reserved.

Author ....
Program in Media Arts and Sciences
August 20, 2004

Certified by ....
Neil A. Gershenfeld
Associate Professor of Media Arts and Sciences
Thesis Supervisor

Accepted by ....
Andrew Lippman
Chairman, Department Committee on Graduate Students

MASSACHUSETTS INSTITUTE
OF TECHNOLOGY
SEP 28 2005
LIBRARIES

ROTCH

Microslots: Scalable Electromagnetic Instrumentation

by

Yael Gregory Eli Maguire

Submitted to the Program in Media Arts and Sciences, School of Architecture and Planning on August 20,
2004, in partial fulfillment of the
requirements for the degree of
Doctor of Philosophy

Abstract

This thesis explores spin manipulation, fabrication techniques and boundary conditions of electromagnetism to bridge the macroscopic and microscopic worlds of biology, chemistry and electronics. This work is centered around the design of a novel electromagnetic device scalable from centimeters to micrometers called a microslot. By creating a small slot in a planarized waveguide called a microstrip, the boundary conditions of the system force an electromagnetic wave to create a concentrated magnetic field around the slot that can be used to detect or produce magnetic fields. By constructing suitable boundary conditions, a detector of electric fields can be produced as well. One of the most important applications of this technology is for Nuclear Magnetic Resonance (NMR). As demonstrated experimentally in this thesis, microslots improves the mass-limited detectability of NMR by orders of magnitude over conventional technology and may move us closer to the dream of NMR on a chip. Improving sensitivity in NMR may lead to a dramatic increase in the rate and accessibility of protein structural information accumulation and a host of other applications for fundamental understanding of biology and biomedical applications, and micro/macroscopic engineering.

This microslot structure was constructed at both 6.9mm and 297μm in order to understand the properties as a function of scale. The 297μm structure has the best signal to noise ratio of any published planar detector and promises to have higher sensitivity with decreasing size. The detector has been used to analyze water and a relatively simple organic molecule with nanomole sensitivity. 940 picomoles of a small peptide was analyzed and a 2D correlation spectra was obtained which allowed identification of the amino acids in the peptide and could be further used to determine structure.

This 297μm microslot probe was constructed using conventional printed circuit board fabrication and a laser micromachining center. A homebuilt probe was made to house the circuit board. Since this geometry is simpler than previously demonstrated techniques, fabrication can be automated for arrays and is inherently scalable to small sizes (less than 10 μm). The planar nature of the device makes it ideal for integration with microfluidics, transceivers and applications such as cell/neuron chemistry, protein arrays, and HPLC-NMR on pico to nanomoles of sample.

Furthermore, this work suggests that a physically scalable, near-field device may have a variety of further uses in integrated circuit chip diagnosis, spintronic devices, nanomanipulation, and magnetic/electric field imaging of surfaces.

Thesis Supervisor: Neil A. Gershenfeld
Title: Associate Professor of Media Arts and Sciences

Microslots: Scalable Electromagnetic Instrumentation

Yael Gregory Eli Maguire

Submitted to the Program in Media Arts and Sciences, School of Architecture and Planning in partial fulfillment of the requirements for the Degree of Doctor of Philosophy

at the Massachusetts Institute of Technology, September 2004

8/24/04

Neil A. Gershenfeld Thesis Advisor
Associate Professor of Media Arts and Sciences
MIT

07 Sep 04

Isaac L. Chuang Thesis Reader
Associate Professor of Physics; Associate Professor of Media Arts and Sciences
MIT

8/15 2004

Shuguang Zhang Thesis Reader
Associate Director, Center for Biomedical Engineering
MIT

Acknowledgments

'*...I have not yet lost that sense of wonder, and of delight, that this delicate motion should reside in all ordinary things around us, revealing itself only to him who looks for it*'. E.M. Purcell, NMR Nobel Lecture, 1952

This thesis is the product of tremendous support from some amazing people. Utmost thanks to Neil Gershenfeld for giving me the opportunity to participate in the most wonderful experience I could have imagined. Further thanks to Neil for providing enough cool toys to make something different. The Media Lab is the best playground in the world for pushing the boundaries, and I thank all who are there for creating such a stimulating environment. Thanks to my committee member Isaac Chuang for reading this thesis, allowing me to use his spectrometer, and for his insights and comments on this work. Thanks to Shuguang Zhang for also reading this thesis, introducing me to the wonderful world of biology and an interesting set of challenges. Special thanks to Peter Carr for being so helpful with the technical NMR and biology details. Thanks to the Physics and Media Group and alumni: Ben Vigoda, Ravi Pappu, Matt Reynolds, Rehmi Post, Bernd Schoner, Rich Fletcher, Jason Taylor, Ben Recht, Raffi Krikorian, Manu Prakash, Xu Sun, Amy Sun. Thanks to Ken Brown, Rob Clark and Steve Yang for being so understanding and helpful with spectrometer time and class E work. Thanks to Saul Griffith, Dave Mosely, Vikas Anant, Brian Chow and Eric Wilhelm in the Molecular Machines Group for equipment/software access and helpful suggestions. To John DiFrancesco for great advice in all things machining. Thanks to David Cory for first introducing me to NMR and for helpful suggestions about probe design. Thanks to Arnold Schwartz, Knut Meier, Tom Barbara, Wes Anderson and Tom de Sweit at Varian for their extremely helpful suggestions and input. Thanks to the administrators Susan Bottari and Mike Houlihan that were so key to getting this work done. Special thanks to Linda Peterson for being incredibly supportive and helpful throughout my tenure at MIT.

Special thanks to Ben Vigoda and Saul Griffith, the partners in crime, for riding the thesis out with me and for being true friends. Thanks to friends Aggelos Bletsas, John Maloney, Nitin Sawhney, Sam Dias and all the people here in Cambridge and around the world for all that friends do. Thanks to my family Louisa, Jack, Pinta, Devin, Dace, π and Zehn for just being, with special thanks to my mom for pushing me all those years. And special thanks to Diana Young for being my best friend and love.

Financial resources for this thesis were provided through the Center for Bits and Atoms NSF research grant number CCR-0122419.

It is my utmost hope that the technology described in this thesis, if used by others, will be used with a conscious respect for all humankind and the fragile world we live in.

Contents

Contents 11

Figures 20

Tables 21

1 Introduction 23

1.1 The Challenge 24

1.2 The Approach 25

1.3 Background and Prior Art 27

1.4 Outline of Thesis 31

2 Scaling NMR 33

2.1 Methods to Increase SNR 33

2.2 Polarization Enhancement 33

2.2.1 Optical Pumping 33

2.2.2 DNP 34

2.2.3 Photo-CIDNP 34

2.2.4 MIONP 35

2.3 Detection Enhancement 35

2.3.1 Mechanical Detection 35

2.3.2 Optical Detection 36

2.3.3 Inductive Detector Miniaturization 36

2.3.4 3D Fabrication Techniques 41

2.4 Observations 42

2.5 Microslots and Striplines 42

2.6 Comparison of Inductive and Mechanical Detection 47

3 Numerical Modeling **49**

3.1 1.5mm Simulation 49

3.2 Models for Actual Device Fabrication 55

3.2.1 6.9mm Simulation 55

3.2.2 297μm Simulation 58

3.3 RF Inhomogeneity 61

3.4 Modeling Observations 67

3.5 Geometry Scaling 67

4 Physical Construction and Network Analysis **71**

4.1 Board fabrication 71

4.2 Micromachining 72

4.3 Polishing 73

4.4 Probe Construction 74

4.5 Probe Assembly 76

4.6 Sample Preparation 79

4.7 Network Analysis 80

5 NMR Results **87**

5.1 Experimental Setup 87

5.1.1 Probe Centering 87

5.2 Water Analysis 89

5.2.1 Parametric Analysis 90

5.2.2 Nutation Plots For Model Verification 94

5.2.3 T_1 Measurement 97

5.2.4 T_2 Measurement 99

5.2.5 RF Imaging 99

5.3 Sucrose Analysis 101

5.4 Susceptibility Matching of the Slot 104

6 Biology Experiments **107**

6.1 DAR Peptide 107

6.2 1D Experiments 108

6.3 2D Experiments 108

6.4 Analysis 119

7 Results and Discussion **121**
7.1 Contributions 121
7.2 Microslot Improvements 122
7.3 Ultimate Microslot Scaling 123
7.4 Future NMR Applications 124
7.5 Other Applications 125

A Introduction to NMR **129**
A.1 Nuclear Paramagnetism for an Ensemble of Spin s Nuclei 129
A.2 Nuclear Spin Dynamics of a Spin in a Static Field 131
A.3 Spin Dynamics with a Rotating Magnetic Field 132
A.4 The NMR Hamiltonian 133
A.5 Spin Echos and CPMG 134
A.6 2D Fourier Spectroscopy (COSY) 135

B Introduction to Proteins and Structure Determination **139**
B.1 Alpha- and Beta-Helices 139
B.2 Beta Sheets 141
B.3 Water 141
B.4 Structure Determination 144
  B.4.1 X-ray Crystallography 144
  B.4.2 NMR 144

C Relevant Instrumentation and Electromagnetics **147**
C.1 Class E Amplifiers 147
  C.1.1 System of Equations for Class E Amplifiers 148
  C.1.2 Class E Experiment 149
C.2 Susceptibility Mismatch and Magnetic Boundary Conditions 152

D Simulation Code **155**
D.1 6.9mm simulation 155
D.2 297μm simulation 159
D.3 Scaling simulation 162

E CAD drawings **165**

List of Figures

1-1 Scanning Electron Microscope (SEM) image of a 297 μm wide microslot designed and built for this thesis work. This is the first microstrip technology to have been used for nuclear magnetic resonance. The microslot holds an NMR sample (not shown), suspended vertically above its surface, oriented in the axial direction of the microstrip. 25

1-2 (a) Isoshells for the magnitude of the magnetic flux density $|B|$ around the microslot from figure 1-1, showing increased flux density around the microslot in the middle. (b) Top view of the microslot modeled in (a). 26

1-3 NMR spectrum from a 15.6 nmol sample of sucrose in 100% D_20, measured using the 297 μm microslot probe. The peaks correspond to different chemical species within the sucrose molecule. They are separated by frequency in units of part per million of 500 MHz from the water peak shown. 27

1-4 Canonical NMR spectrometer schematic. 28

2-1 Model of a solenoid, showing parameterization for analysis. 37

2-2 Plot of equation 2.20 for a planar coil along the z-axis, indicating inhomogeneity. 40

2-3 Field profile along the axis of a solenoid, showing homogeneity. The parameters used are referenced in figure 2-1. 40

2-4 Solenoidal microcoils made by two different methods. (a) coil winding (with conventional wire) around a 360μm capillary [96]. (b) microcontact printing on a 324 μm wide capillary (length 1.6 mm) [68]. 41

2-5 Three types of 3D microcoil microfabrication research. (a) coil make using an electrodeposition technique, taken from [53]. (b) sampling of stress-engineered microfabricated coils, taken from [20]. (c) post-release process creating an out-of-plane coil, taken from [31]. . . . 42

2-6 Microslot geometry, used for analysis. 42

2-7 Parallel plate model of a microslot and symmetrization used to analyze the structure. 43

2-8 $Z_0(W)$ for a microstrip. 4 orders of magnitude width change corresponds to 1 order of magnitude impedance change. 45

2-9 $\epsilon_0(W)$ for a microstrip. 4 orders of magnitude width change corresponds to less than a factor of 2 dielectric constant change. 45

2-10 Symmetry is very important for susceptibility-matching and hence more useful for NMR. (a) shows the original microslot concept. (b),(c) Show the symmetrized versions of the microslot introduced in this thesis. From the cartoons of the parallel plate representation, one can see the inductance for the symmetric case is half that of the asymmetric case. For (c), one can make a transformation (by symmetry) on each half of the parallel plate model to yield (b). Hence (c) has the same inductance as (b). 46

2-11 Ratio of signal to noise ratio of force detection (given by Leskowitz et al. [50]) to inductive detection. 48

3-1 Geometry for the microslot inductor. A=1mm, A'=100μm, b=1mm (see figures 2-6 and 2-7), and the copper thickness is 60μm. Microstrip feed points are on either side of the microslot. 50

3-2 Geometry for the square inductor. 51

3-3 Isoshells for B_x (in Tesla) showing increased flux density around the microslot. This represents the preferred direction for the microslot and demonstrates flux concentration around the microslot. 52

3-4 Isoshells for B_y, (in Tesla) showing strong flux density on either side of the microslot, away from the top where a cylindrical/ellipsoidal sample would be placed. 52

3-5 Isoshells for B_z (in Tesla) for the microslot, showing very minimal contribution. 53

3-6 Isoshells for B_x (in Tesla) for the square inductor, showing strong density above the inductor. In this figure and the following two, It is difficult to see where and what geometry of sample could be placed to achieve high RF homoegeneity and a preferred orientation. 53

3-7 Isoshells for B_y (in Tesla) for the square inductor, showing strong density above the inductor. 54

3-8 Isoshells for B_z (in Tesla) for the square inductor, showing strong density above the inductor. 54

3-9 Microslot geometry used for the 6.9mm simulation. 55

3-10 Isoshells for B_x (in Tesla) for the 6.9mm microslot, showing flux density concentration around the microslot. 56

3-11 Isoshells for B_y (in Tesla) for the 6.9mm microslot, showing flux density concentration on either side of the microslot. 56

3-12 Isoshells for B_z (in Tesla) for the 6.9mm microslot, showing lower flux density concentration. 57

3-13 Geometry for actual fabrication of the 297 μm microslot. 58

3-14 Isoshells of $|\vec{B}|$ (in Tesla), showing flux density concentration around the microslot. 59

3-15 Isoshells of B_x (in Tesla), showing flux density concentration around the microslot. 59

3-16 Isoshells of B_y (in Tesla), showing flux density concentration on either side of the microslot. Due to the current distribution, this field is mainly confined to the sides of the microstrip. . . 60

3-17 isoshells of B_z (in Tesla), showing very little flux density concentration in the direction of the static field (z). 60

3-18 Simulation of RF homogeneity on the simple function $\vec{B}_1(\vec{x}) = B_1 - \alpha|x|$, for $-x_0 \leq x \leq x_0$. $B_1 = 4mT$, $\alpha = 0.8mT$, $x_0 = 1$ and $\pi/2 = 10.2\mu s$. A_{270}/A_{90} is 0.955. 62

3-19 1st view of the parameterization of the nutation plot as a function of cylinder height above the surface of the 297μm microslot. In contrast to a simple wire, the RF homogeneity and field strength both improve for the microslot as the cylinder approaches the surface. 63

3-20 2nd view of the parameterization of the nutation plot as a function of cylinder height above the surface of the 297 μm microslot. Raising the sample decreases the B/i ratio quite significantly. 64

3-21 Nutation plots for the two extremes of height of the cylinder above the surface. Note that RF homogeneity and sensitivity both improve with the capillary tube closer to the surface. . . . 64

3-22 1st view of the parameterization of the nutation plot as a function of length of a cylindrical sample above the 297 μm microslot. Sensitivity is compromised for RF homogeneity. 65

3-23 2nd view of the parameterization of the nutation plot as a function of length of a cylindrical sample above the 297 μm microslot. 65

3-24 Nutation plots for the two extremes of the length of the cylinder. Note the large tradeoff in RF homogeneity for sensitivity for the type (b) slot (from figure 2-10). 66

3-25 Power (dBm) versus tpwr setting for H^1 channel, slope=0.9913, offset=-19.15. 66

3-26 Comparison of the field produced as a function of frequency. With the skin effect aside, there are no wavelength-dependent effects for the microslot. However, there are frequency-dependent effects. (a) is a simulation of a microstrip at 60 Hz, while (b) is the same simulation at 500 MHz. 67

3-27 Plot showing 1/r dependence of $\langle|B|\rangle/i$ versus microslot width. Data is computed between 60μm and 1.2mm. 68

4-1 Final chemical etch of the probe circuit board showing the 300 μm wide macroscopic microslot (the microscopic microslot not yet fabricated). The back side of the board is full copper. 72

4-2 This is an example of microslot immediately after micromachining. One can see debris produced by the excimer laser and surface features from the original electroplating/rolling and chemical etching. 73

4-3 Example progression from an original unpolished microslot (1) to the final finished state (9). 74

4-4 Photograph of the base of the probe. A CAD drawing of these pieces can be found in figure E-1. The width is 2.5" and the height is 1.74". The thickness of the base plate is 0.25". . . . 75

4-5 Photograph of the nonmagnetic bulkhead BNC jack soldered to nonmagnetic semirigid coaxial cable. This cable carries the signal from the spectrometer console to the probe in the center of the magnet and also carries the NMR signal from the sample back to the console. The end of the jack is 0.437" in diameter. 76

4-6 CAD drawing of the probe base assembly with the first PCB cutout and semi-rigid coaxial cables. 77

4-7 Photograph showing the assembled stacked cutout structure soldered to the semi-rigid coaxial cable and attached to the base. Each copper cutout is 1.435" in diameter. 78

4-8 Two views of the unpopulated probe circuit board mounted in the 297 μm probe. The copper cutout is 1.435" in diameter. 78

4-9 The final probe. The total length, not including acrylic rods is 22.5". 79

4-10 Microcapillary viewed under a microscope with a contrasting reflector. The outer diameter is 165 μm and in the inner diameter is 100μm. Note the meniscus of the deionized water. The end is sealed with a wax plug. 80

4-11 Models of inductor (a) and capacitor (b) at RF frequencies. 80

4-12 Reduced network model of the probe. 81

4-13 Log magnitude of S_{11} for the 6.9mm probe at 448 MHz, with a fixed capacitance for C_1 to find the inductance and resistance of the structure. 82

4-14 Smithchart for the 6.9mm probe at 448 MHz, showing the the network is matched to 50 Ω. . 82

4-15 Log magnitude of S_{11} for the 297μm probe at 431 MHz, with a fixed capacitance for C_1 to find the inductance and resistance of the structure. 83

4-16 Smith chart for the 297μm probe at 431 MHz, showing that the network is matched to 50 Ω. 83

4-17 Simulation of the 297μm probe network using measured and derived values at 500 MHz. . . 84

4-18 Log magnitude of S_{11} for the 6.9mm probe at 500 MHz (using the calculated impedances), showing strong absorption. 84

4-19 Smith chart for the 6.9mm probe at 500 MHz, showing the network is matched to 50 Ω. . . . 85

4-20 Log magnitudeof S_{11} for the 297μm probe at 500 MHz (using the calculated impedances), showing strong absorption. 85

4-21 Smith chart for the 297μm probe at 500 MHz, showing the network is matched to 50 Ω. . . . 86

5-1 Photograph of the capillary tube showing the total length to be 4.22 mm. In the background, a vertical strip of polyimide tape can be seen. 88

5-2 Varying z_1 4.0mm below the centerline of the probe. Various z_1 settings are marked. 88

5-3 Varying z_1 2.7mm above the centerline of the probe. Various z_1 settings are marked. Notice the positions of the z_1=9377 and -11103 are swapped relative to figure 5-2. 89

5-4 Varying $z_1 \approx 0.0$mm from the centerline of the probe. Various z_1 settings are marked. Each spectrum is now overlapping with the z_1 shim, changing the frequency variance of the spin distribution rather than the position. 89

5-5 Water signal from 6.9mm probe for 10% H_2O in D_2O. The linewidths at various heights of the Lorentzian peak are given. 90

5-6 Water signal from the 297μm probe for 32 nL of 100% deionized H_2O. The linewidth is 1.1Hz 50%, 54Hz 0.55%. 91

5-7 A closer inspection of the previous plot shows broad tails that could either be from the slot itself or a non-vertical alignment of the probe circuit board. 91

5-8 Water signal from the 297 μm probe with a 248 μm wide capillary tube. The linewidth was measured to be 3.4Hz wide, with an SNR of 5810. 92

5-9 Nutation plot with y_0=140μm. The ratio of A_{270} to A_{90} is 0.91. (Dashed lines represent error limits from calculation.) 93

5-10 Nutation plot with y_0=0μm. The ratio of A_{270} to A_{90} is 0.84. (Dashed lines represent error limits from calculation.) 93

5-11 Concatenation of the spectra as a function of pulse width for tpwr=45 (29.55 dBm) for over 5π cycles. The ratio of A_{270} to A_{90} is 0.95. (Dashed lines represent error limits from calculation.) 94

5-12 Nutation plot of experimental data from the 297μm probe, exponential line fit, and FEM prediction with error curves using tpwr=45 (29.55 dBm) data and experimentally measured current gain. The ratio of A_{270} to A_{90} is 0.97. (Dashed lines represent error limits from calculation.) 95

5-13 Nutation plot of experimental data from the 297μm probe, exponential line fit, and FEM prediction using tpwr=51 (35.27 dBm) data and experimentally measured current gain. The ratio of A_{270} to A_{90} is 0.97. (Dashed lines represent error limits from calculation.) 95

5-14 Nutation plot of experimental data from the 6.9mm probe, exponential line fit, and FEM prediction using tpwr=58 (38.25 dBm) data and experimentally measured current gain. The ratio of A_{270} to A_{90} is 0.71. (Dashed lines represent error limits from calculation.) 96

5-15 Pulse sequence for the T_1 measurement experiment. 97

5-16 Stacked FID plot for the data collected for various settings for τ to recover T_1. Exponential fit of equation 5.2 for the data collected. T_1=3.7 ± 0.1 s. 98

5-17 CPMG sequence used for determining T_2. 99

5-18 Exponential fit of the data collected for the T_2 experiment. T_2=1.8 ± 0.2 s. 100

5-19 The homospoil spin echo experiment for mapping the RF field. The rectangles on the z-axis indicate the applications of the homospoil gradient. 100

5-20 Subset of the gmapz experimental results for varying lengths of the pulse width pw. Note the peak heights are changing due to their relative B/i, but the largest signal is coming from the center. Note also a large peak at the part of the sample furthest downfield. 101
5-21 Plot of the spectrum at 9μs used to measure the effective sample volume. 102
5-22 Photograph of the probe board showing imperfections in the larger microslot stripline on the downfield side. Arrows indicate imperfections. 102
5-23 Sucrose molecule, with the anomeric proton highlighted. 103
5-24 361 μmol of sucrose dissolved in 600 μL of 100% D_2O. The observe volume is 220 μL. The anomeric proton is represented by the peak furthest to the left. 103
5-25 Photograph of the capillary tube containing sucrose solution, showing the total length to be 3.38 mm. 104
5-26 15.6 nmol of sucrose in 100% D_20. The signal to noise ratio of the anomeric proton is 50.1. 1.3 Hz of line broadening was applied. The plot shows the sum of 16 scans (each with an acquisition time of 1.25s). Note the peak positions for the microslot probe, possible caused by temperature differences and/or absence of lock signal, are about 0.13 ppm from the Nalorac probe. 104
5-27 Image of 4 glass microspheres, 20-30μm in diameter to fill the slot for susceptibility matching. The spheres were electrostatically bound. 105

6-1 Tranverse view the DAR molecule. Arginine is at the bottom. 108
6-2 Axial view of the DAR molecule. 109
6-3 Photograph of the capillary tube showing the total length of the sample to be 3.94 mm. . . . 109
6-4 In (a), 1.1 μmols DAR 1D spectrum from Nalorac 5mm probe. The total acquisition time is approximately 3.7 minutes. In (b), 940 pmols of DAR 1D spectrum from microslot probe with a least squares baseline subtraction. The total acquisition time is approximately 25 minutes. The numbers represent the peaks of interest. The circled peaks are expanded in figures 6-5 and 6-6. The line broadening for (b) was 1.0 Hz, while 0.0 Hz was applied to (a). 110
6-5 Closeups of the 1.5ppm peak given by the Nalorac probe (on top) and the microslot probe (on bottom). The numbers on the graph give more detailed information on peak locations. The microslot probe structure produced peaks 0.112 ppm from the Nalorac data. 111
6-6 Closeups of the 1.9ppm peak given by the Nalorac probe (on top) and the microslot probe (on bottom). The numbers of the graph give more detailed information on peak locations. 112
6-7 The canonical COSY sequence showing the two dimensions that are used to produce a two-dimensional spectrum. 112
6-8 COSY spectrum from the Nalorac probe. lb=0.0, sb=0.116, lb1=0.32, sb1=0.058. 113
6-9 COSY spectrum from the microslot probe before drift correction was applied. There is no evidence of correlations. lb=0.6, gf=0.08, lb1=0.61, sb1=0.078, gf1=0.4. 114

6-10 Plot of the residual H_2O peak showing the drift of approximately 30Hz over 25 minutes. . . 115

6-11 Top plot shows the drift from the Nalorac probe when the lock is on but the lock signal is marginal. Bottom is the drift for the same lock signal, but with the lock simply turned off. . . 116

6-12 Plot of the drift of the water peak during a nearly 6-hour COSY experiment for the microslot probe. The linear part of the curve shows no data was gathered between 6 and 9 hours. At the 9th hour (3 hours after data collection stopped), a single acquisition was made, showing that the heating is not from the probe itself. 117

6-13 COSY spectrum from the microslot probe. lb=0.6, gf=0.08, lb1=0.61, sb1=0.078, gf1=0.4. . 118

6-14 Final assignment of the DAR molecule to the 1D spectrum based on the spectrogram obtained from the microslot probe and the COSY plot. Note peak 6 represents an impurity present (also present in the Nalorac probe data). 120

7-1 Sensitivity scaling of the microslot as a function of the microstrip width at room temperature (300 K) and at 100 mK. At room temperature, the limit of detection of nuclear spins is about 100 fmol-10 pmol and about 10×10^4 at 100 mK. 124

7-2 Sketch of a microslot could be used to control biomolecules attached to nanoparticles. 126

7-3 Sketch of pads on an integrated circuit with one pad being scanned by a microslot. 126

7-4 Slotline with a microdisturbance. This geometry creates a concentrated E-field, while the inductance in unaffected. 127

A-1 Plots of the polarization versus temperature for an ensemble of spin particles and the Boltzmann approximation. 131

A-2 Basic spin echo sequence that demonstrates the difference between reversible and irreversible coherence times. 134

A-3 Two different graphical ways to understand the spin echo. On the left is the angle versus time of isochromats in the transverse plane. On the right is the motion of the spin vectors on the Bloch sphere. 135

A-4 Basic COrrelation SpectroscopY (COSY) experiment. 136

A-5 COSY plot for two coupled heteronuclear spins showing chemical shift evolution separated from J-coupling. 138

B-1 The 20 L-amino acids. Only the side chains are shown except for alanine, which is shown with its backbone. The boxed amino acids are the components of the peptide analyzed in Chapter 6. 140

B-2 Formation of a peptide bond. 141

B-3 Peptide bond with bond lengths shown in Å. 141

B-4 Picture of a 16 residue α-helix, showing the stick-model amino acids. Rendered using PyMOL [25]. 142
B-5 Picture of a 16 residue β-sheet, showing the stick-model amino acids. Rendered using PyMOL [25]. 142
B-6 The schematic and orbital versions of water. 143

C-1 General schematic for a class E amplifier 148
C-2 Schematic for the class E amplifier to operate at 34 MHz. 150
C-3 Fabricated class E amplifier operating at 34 MHz for ^{35}Cl. This amplifier was capable of about 4W of output power. The dimensions are 3cm × 5.5cm. 150
C-4 FID from the PQR apparatus showing good signal to noise ratio. 150
C-5 Class E amplifier with an integrated probe. 151
C-6 A proposed design for an integrated class E amplifier and probe. 151

D-1 Microslot geometry used for the 6.9mm simulation. 155
D-2 Geometry for the 297 μm microslot simulation. 159

E-1 Probe base. Scale is 1:1. 166
E-2 Probe tube. Scale is 1:7.41. 167
E-3 Tube assembly. Scale is 1:1 and 1:6.67. 168
E-4 FEP/Teflon base. Scale is 1:1. 169
E-5 FEP/Teflon base top. Scale is 1:1. 169

List of Tables

2.1 Limits of detection for various Analytical methods used for capillary separations. Taken from [48]. 33

4.1 Measured properties of the circuit in figure 4-12 for the 297μm and 6.9mm probe needed to calculate the capacitors required at 500 MHz. 84

5.1 Properties of various capillary tubes used. 92
5.2 Performance of various probes for sucrose. Nalorac and microcoil data taken from [48] and planar microfluidic data taken from [55]. 103

6.1 Amino acids in the DAR molecule. 119

Chapter 1

Introduction

One of the most important scientific results over the past century is that the fundamental building blocks of nature are macromolecules, such as DNA and proteins, and the form of a molecule equals its function [23]. Detecting and manipulating biological macromolecules will have profound consequences on our fundamental understanding of biology, biomedical technologies, and nano-micro/macroscopic engineering. Researchers have recently determined the identity and sequence of the human genome (i.e. the information storage medium, the "bits"), which contains about 30,000 genes [3], but this is only the first step towards a blueprint for our species. Proteins, aptly named by chemists in the early 1800s after the Greek word "proteios", meaning "holding first place", embody the physical make-up (the atoms), and hence the next task (and a much more important one) is decoding the human proteome. It is estimated that humans alone have about 300,000 proteins [49] made by the genome, and this figure is complicated by the fact that proteins interact with each other in diverse ways. Furthermore, this is only the proverbial 'tip of the iceberg', since it does not reflect the proteins that humans modify or create from scratch nor those of the other species on the planet [98]. The total number of proteins decoded at the time of writing is 26811 [8]. This number is the result of over 50 years of hard work, as each one has taken several months to years to complete.

A grand challenge question one may ask is 'are there tools to generalize the proteome so that one does not have to find the structure of each protein individually'? Unfortunately, the answer is currently 'no'. Modeling is not a solution, as there are no generalizable theoretical tools and the fastest supercomputers on the planet are unable to simulate the entire folding process of proteins from a primary amino acid chain to a final, folded and linked tertiary structure [28]. Classification is not feasible. A story of a 'periodic table' for proteins is beginning to emerge, but there is no simple way to discover with analytical tools the 'elements', without acquiring an entire structure [86]. In practice the field of structural genomics is left with native proteins alone, using tools such as x-ray diffraction, Nuclear Magnetic Resonance (NMR), and to a lesser extent cryo-electric spectroscopy [19].

A tremendous body of work has been generated over the past 30 years to begin to collate structural information of proteins and nucleic acids. While these databases are growing, the process for gathering individual structures is unpredictable, error prone, and most importantly extremely time-consuming [13]. The techniques used are phenomenal from a scientific point of view, but pose enormous preparation costs. In the specific case of Nuclear Magnetic Resonance, the technique gives indirect structural results of macromolecules in solution, but in conventional spectrometers requires milligrams of each sample and samples of high concentration. For many applications, the preparation of these quantities of molecules is what separates pipe dreams from practical reality, since the starting material from a gel (or other means) may be on the scale of pico- to nano-grams.

Beyond a collection of structures for a world database is a host of future applications for which getting access to structural information is enormously important. In medicine, there exist no analytical tools to examine the proteins of our bodies to give advanced warnings of disease. In many disease cases [100] in which protein disfunction is the cause, such as Alzheimer's, early detection could save lives by allowing doctors to start drug or other therapies earlier rather than later, when physiological or mental deficiencies appear. It would be tremendously useful to have a benchtop or lab-size tool for this task to add to the analytical arsenal in hospitals around the world.

Beyond rational drug design will be rational life design [44]. Entire organisms, from individual molecules up to macroscopic lifeforms, could be made in laboratories. But, without a tool to image structures of biomolecules, how will we understand what we have made beyond gross, macroscopic information?

As we learn to engineer biomolecules, we will need tools that allow us to characterize molecules, not only for structure, but also for kinetics and dynamics. Eventually we will need analytical models for these systems. If we can not solely use computational models, it may be possible to use the molecules themselves as a protein 'co-processor' to validate or build models by enabling the molecules to do their own dynamics and kinetics.

1.1 The Challenge

One of the great advantages of Nuclear Magnetic Resonance is that it can measure kinetics, dynamics and molecular structure, but its poor sensitivity (described later in this chapter) makes the applications described earlier currently infeasible. In this thesis, a new type of detector is detailed that was designed and fabricated to enable a conventional NMR spectrometer to exploit the geometric scaling of electromagnetic structures to increase sensitivity per unit volume on several orders of magnitude less sample than conventionally used. This result can decrease the time to obtain structural information by several orders of magnitude, increasing the rate in which research groups can acquire structures and perhaps allowing some of the applications described above.

Such a sensor may have very far-reaching extensions. This sensor may not only be useful for detection of tiny magnetic fields produced by small volumes of biomolecules, but also for the detection of any localized electric or magnetic RF/microwave field. Such a technology could be very useful for the semiconductor and printed circuit board communities for contactless imaging of semiconductor chips. As we continue to shrink down integrated circuits [4] or make integrated circuits three-dimensional [31], using probe stations to probe points in a circuit may be difficult. Contactless measurements may make chip diagnosis easier in the future. In MRAM devices, a wire is used to flip a spin state in a magnetic tunnel junction [74]. A microslot device may allow these memory elements to switch faster or use less power.

1.2 The Approach

In this thesis a novel electromagnetic geometry is demonstrated that overcomes problems exhibited by previous attempts at microfabricated magnetic sensors. The design will be motivated both theoretically and experimentally to demonstrate that this technique has high sensitivity in the context of obtaining spectroscopic information from less than a nanomole of biological sample, 3-4 orders of magnitude less than conventionally required. This is a novel approach that is very different from the existing prior art of microstructures for mass-limited detection.

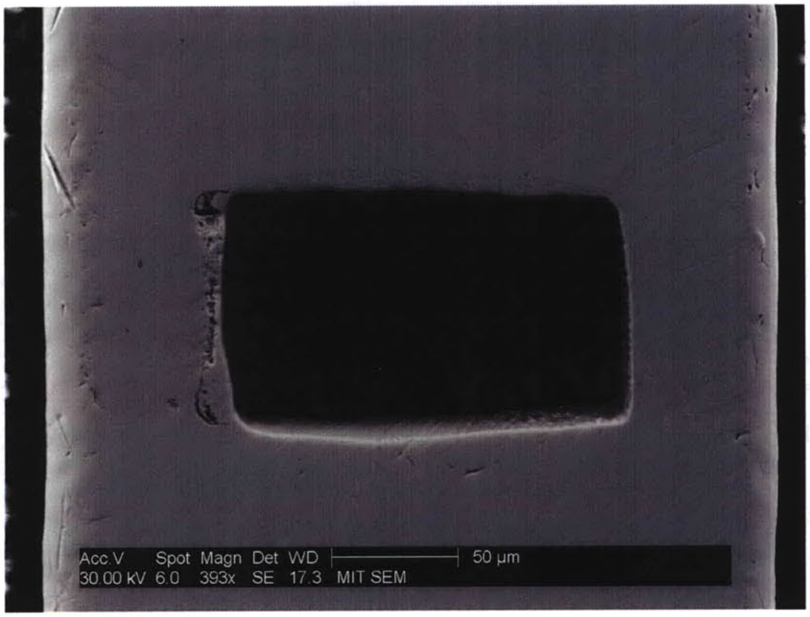

Figure 1-1: Scanning Electron Microscope (SEM) image of a 297 μm wide microslot designed and built for this thesis work. This is the first microstrip technology to have been used for nuclear magnetic resonance. The microslot holds an NMR sample (not shown), suspended vertically above its surface, oriented in the axial direction of the microstrip.

The concept is based on modifications to a staple of the microwave industry, a planar waveguide called the microstrip. A microstrip is a dual layer, metallic, planar waveguide used for transporting radio frequency signals in printed circuit boards, microcircuits and antennas. A low-loss dielectric material separates this structure from the ground plane below. The microstrip can be fabricated using a conventional printed circuit board process (chemical etching).

Microslot Probe

Figure 1-1 shows a high impedance radio frequency microstrip circuit with a small slot cut out of the microstrip. Once the slot is cut in the microstrip, the slot produces a pure series inductance that creates a strong, near-field magnetic radiation pattern around the slot. These field lines are more homogeneous than can be produced from a planar spiral inductor. The magnetic flux isoshells for this strip are shown in figure 1-2. By placing a fused-silica tube or drop of sample just above the slot, a strong signal will be received by the nuclear spins of this sample, and the signal produced by the nuclear spins can also be detected with this probe. This structure can be made in sizes of 1cm to less than 1μm.

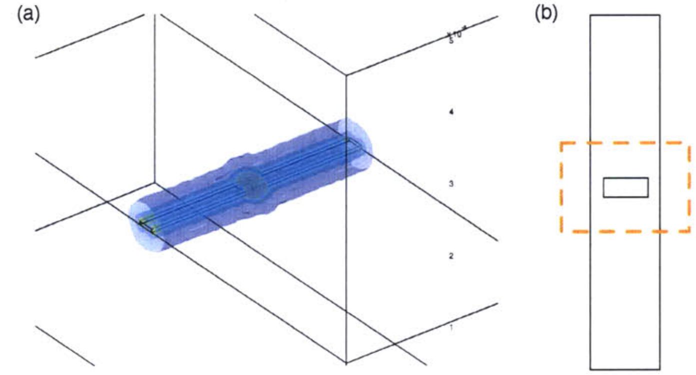

Figure 1-2: (a) Isoshells for the magnitude of the magnetic flux density $|B|$ around the microslot from figure 1-1, showing increased flux density around the microslot in the middle. (b) Top view of the microslot modeled in (a).

The microslot probe can be combined easily into the rest of a conventional probe circuit with no lead impedances. Since the microslot probe is simply a printed circuit board, it can be integrated into a chemical and biological apparatus so that the RF characteristics of the sample itself can be characterized for optimal signal reception. The data shown in figure 1-3 (obtained from the probe in figure 1-1) shows this behavior for a sample of sucrose in a 500 MHz commercial spectrometer.

One objective of this thesis is to contextualize this detector for other applications. An application of this device in the immediate future is a non-contact detector of electromagnetic fields produced by integrated circuits while they are powered. There is a burgeoning field of scanning microwave spectroscopy using the tip of a coaxial cable [91], a small hole in a waveguide, a microstrip resonator [84] or conventional Scanning Force Microscope (SFM) [89] to scan surfaces. It has been shown both for microwaves and optical wavelengths that by geometric boundary conditions, evanescent waves can obtain resolution much smaller than the diffraction limit [5] ($\lambda/10^6$ in demonstrated cases [46]). These techniques have been used to monitor individual digital lines using an Electric Force Microscope (EFM) [38] and image passive structures as small as 8μm using a dipole patterned on a Scanning Tunneling Microscope (STM) [2]. This microstrip structure

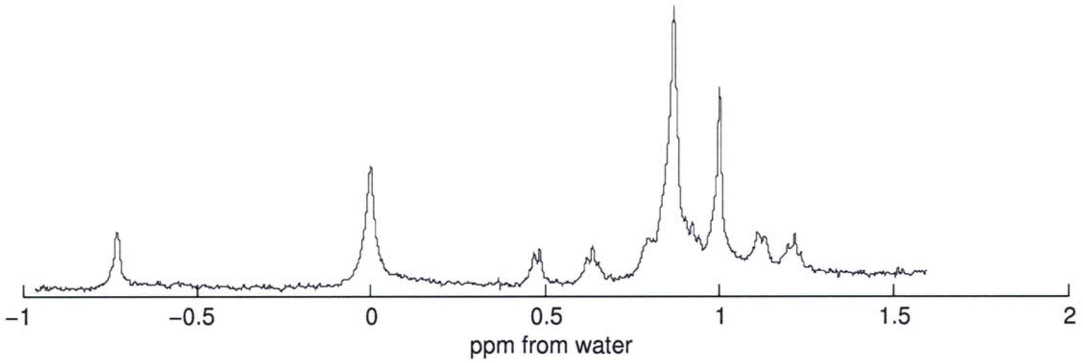

Figure 1-3: NMR spectrum from a 15.6 nmol sample of sucrose in 100% D_20, measured using the 297 μm microslot probe. The peaks correspond to different chemical species within the sucrose molecule. They are separated by frequency in units of part per million of 500 MHz from the water peak shown.

may have the potential to scan the electromagnetic signature of a powered integrated circuit to learn about good and bad design, characterize faulty chips, and potentially replace expensive probe scanners.

1.3 Background and Prior Art

In its 50 year history, Nuclear Magnetic Resonance (NMR) has emerged from observations of the fundamental dynamics of nature to an amazing analytical tool for monitoring molecular dynamics, in vivo tissue and whole body imaging and spectroscopy, and structure determination of complex biomolecules. NMR is unmatched in two important areas: In terms of spectral resolution, a typical commercial NMR spectrometer can resolve lines as narrow as fractions of one part per billion, while other types of spectroscopy are typically orders of magnitude more coarse [37]; NMR also has a computational aspect, as long before the advent of quantum computing using NMR [32], compiled programs of radio frequency pulses have stimulated a wide range of inter- and intra-molecular dynamics, and these have led to amazing applications such as structure determination and reaction kinetics. Despite NMR's versatility, "bread and butter" techniques such as Fourier Transform InfraRed (FTIR) Spectroscopy, fluorescence spectroscopy, and mass spectroscopy offer orders of magnitude higher sensitivity than NMR. In fact, NMR is one of the least sensitive tools for analytical research (as discussed in detail in Chapter 2).

Because of its lack of sensitivity, NMR has been relegated to analysis of samples that can be obtained in large volumes, or, in the case of important structure determination, to those samples produced by painstaking bacteria amplification by genetic substitution in weeks or even months. Increasing the sensitivity of NMR for small samples would be a significant contribution to analytical research.

The schematic for a typical NMR spectrometer is shown in figure 1-4. A superconducting magnet is required to cause an energy level-splitting in the nuclear spins in a sample. This energy level-splitting causes these nuclear spins to 'resonate' at a characteristic frequency called the Larmor frequency. An inductive coil is placed around the sample to couple magnetic energy in and out of the system. A transmitter translates an intermediate frequency (IF) to the Larmor frequency. In the simplest case, pulses are applied by gating a stable source oscillator, generating so-called 'hard pulses'. More complex instruments are able to generate arbitrary waveforms for more articulate types of spin control. Usually the same inductive coil is used to detect the small NMR signal. Analog superheterodyne receivers are generally chosen based on the assumption that noise at different frequencies is uncorrelated. A high isolation switch is needed to protect the low noise receiver from the high power transmit signals. Finally, a computer acquisition system samples the data, and basic signal processing techniques such as Fast Fourier Transforms (FFT) and digital filtering are applied to simplify analysis.

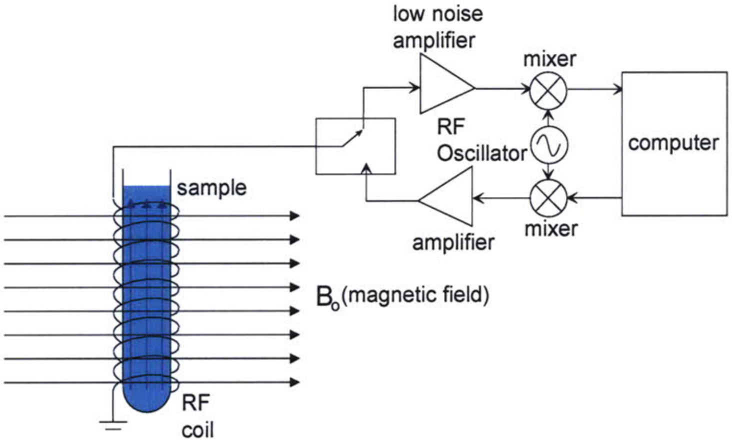

Figure 1-4: Canonical NMR spectrometer schematic.

Researchers have tried several innovative approaches to improve the sensitivity of NMR. A very novel approach is to transfer polarization from an optically pumped species, for example ^{129}Xe [29]. For some specific molecules, enhancement factors of 50-70 have been realized in liquid xenon. A second approach is to reduce the receiver noise to improve sensitivity using either high temperature superconductor [12] or cryogenically cooled coils [54]. These methods have improved the sensitivity over a conventional probe by a factor of 4-5. By far the largest (by 2 orders of magnitude) and most general improvement has come from miniaturizing the inductive detectors [96].

One important question to ask is "what is the benefit of miniaturization of near-field probes?" One of the few but extremely important near-field probe miniaturization examples is the read/write head used in magnetic storage. New technologies were developed, including the MR (magnetoresistance) effect and the GMR (giant magnetoresistance) effect, to increase the bit sensitivity as the size of the bits decreases. In the field of magnetic resonance, recent work has shown that miniaturization of probes in nuclear magnetic resonance can also improve sensitivity [61]. Researchers have used microfabrication techniques to miniaturize the radio frequency coils and samples. This work started with the fabrication of planar coils on gallium arsenide (GaAs) substrates [63]. While this work demonstrated microliter sensitivity, far better than done with conventional NMR spectrometers, this system was not able to reach its full potential due to limited RF homogeneity, poor linewidth, and poor sensitivity and shimming ability. A different approach was followed by Olsen et al, in which they hand-wound a solenoidal microcoil around a 357 μm glass capillary using 50 μm wire. To overcome homogeneity problems, they bathed the whole coil and sample in a susceptibility matching fluid. This produced higher sensitivity (nanoliter range) and high homogeneity (2 parts per billion) [61]. This technique has been very successful and has even been applied to two-dimensional spectroscopy experiments [83] [99] [82]. (Two-dimensional spectroscopy is one of the standard tools for biomolecule structure determination [18]). The main deficiency of this technique is that there are no general tools for three-dimensional fabrication that lend to further miniaturization and integration. There are some examples of three-dimensional microfabrication [45] [97] [53], but none have produced scalable results with good radio frequency performance. To understand why smaller magnetic detectors have increased sensitivity, the fundamental sensitivity for a inductive detector was analyzed by Hoult and Richards [39] [62]:

$$\mathrm{SNR} = \frac{\text{peak signal}}{\text{RMS noise}} = \frac{k_0 (B_1/i) \nu_S N \gamma \hbar^2 I(I+1) \omega_0^2 / 3 / \sqrt{2} k_B T}{V_{\text{noise}}} \propto \frac{\omega_0^2 (B_1/i) \nu_S}{V_{\text{noise}}}. \tag{1.1}$$

Here, k_0 is a scaling constant to deal with inhomogeneity of the RF field, (B_1/i) is the transverse magnetic field induced in the detector by a unit current, v_s is the volume of the sample, N is the spin density, γ is the gyromagnetic ratio of the spin, $\hbar$ is Planck's constant, I is the spin quantum number, ω is the nuclear precession frequency, k_B is Boltzmann's constant and T is temperature of the spins. For a fixed temperature, the sensitivity is only dependent on the static magnetic field (proportional to ω_0, i.e. $B_0 = \gamma/2\pi\omega_0$), the ratio B_1/i, the sample volume, and the noise voltage produced from the detector. The static magnetic field, produced from a low temperature superconducting coil, has reached engineering limits and cannot be scaled much further without exponential resources [41]. For the term B_1/i, consider the field produced from a continuous piece of current carrying wire in 3-dimensions via the Biot-Savart Law [43]:

$$\vec{B} = \frac{\mu_0}{4\pi} \int \frac{i dl \times \vec{x}}{|\vec{x}|^3} \Rightarrow \vec{B}/i = f(\vec{x}), \tag{1.2}$$

where $f(\vec{x})$ is a function of the geometry. This suggests that it is possible to construct a structure with a scale dependent on the size of the geometry. To take a specific example, consider the on-axis sensitivity in the center of an ideal, single-layer solenoid of many turns ($N \gg 1$) from the Biot-Savart Law above:

$$\begin{aligned} \vec{B}/i &= \frac{\mu_0}{4\pi}\int_{h/2}^{h/2} \frac{dl \times \vec{x}}{|\vec{x}|^3}\hat{z} \\ &= \frac{\mu_0 n}{4\pi}\int_{h/2}^{h/2} \frac{r^2 d\theta dz}{(r^2+z^2)^{\frac{3}{2}}}\hat{z} \\ &= \frac{\mu_0 ni}{2}\frac{z}{(r^2+z^2)^{\frac{1}{2}}}\Big|_{-h/2}^{h/2}\hat{z} \\ &= \frac{\mu_0}{2}\frac{nh}{d/2(1+(\frac{h}{d})^2)^{\frac{1}{2}}}\hat{z} = \frac{\mu_0 N}{d\sqrt{1+(\frac{h}{d})^2}}\hat{z}. \end{aligned} \tag{1.3}$$

If the ratio h/d is kept constant, (B/i) scales inversely with the diameter of the coil. Now, looking at the V_{noise} term, we use the Nyquist formula:

$$V_{\text{noise}} = \sqrt{4k_B T R_{\text{noise}} \Delta f}. \tag{1.4}$$

R_{noise} is the resistance of the magnetic structure. Δf is the bandwidth of the coil, defined as the full width at half maximum for a resonant circuit. For the same coil structure,

$$\begin{aligned} R_{\text{noise}} &= \frac{\rho l}{A} \approx (\frac{\rho l}{\pi d\delta})\xi \\ &\approx \frac{3\rho N^2 d\xi}{2h\delta} \quad N \gg 1. \end{aligned} \tag{1.5}$$

ξ is a scaling factor to account for the proximity effect (typically between 1 and 3) [62] [17], where the field produced between turns of the solenoid produces a reduced pathway for the current. $\delta = (\mu_0 \pi \sigma \omega_0 / 2\pi)^{-1/2}$ is the familiar skin effect for metals, where σ is the conductivity of the metal. An interesting observation concerning this approximation is that the resistance of the coil is constant with geometric scaling, assuming the ratio of height to diameter of the coil is constant. Putting this all together, the sensitivity can be expressed as:

$$\text{SNR}/\nu_S \propto \frac{w_0^{5/4} Q^{1/2}}{d}. \tag{1.6}$$

Here Q is defined as the quality factor of the detector circuit, where $Q = w_0/(2\pi\Delta f)$. This shows a geometric dependence on the sensitivity, i.e. the smaller the structure is made, the greater the sensitivity increases per unit volume. A corollary to this statement is that a stronger magnetic field can be generated per unit current by decreasing the size of the structure. This is very important in the case of write heads in hard drives, in which decreasing the size of the microfabricated inductors generates stronger fields with less inductance, thereby producing faster write times [85].

It should be noted that this result (found for solenoidal coils) is true for a planar coil as well [81]. The problem with both planar or solenoidal microcoil approaches can be understood with the previous two equations. With multiple turn coils, the proximity effect can be large, dramatically reducing the quality factor of the coil. There is a limit in the sensitivity of the solenoidal coils because d can only be made as small as the size of winding wire [62], or in the case of microcontact printing [68], the limit is about 250 μm [58].

Even with this limitation and the fact that microfabrication has yielded much smaller structures [81], the solenoidal coils have had much better success. There are three reasons: 1) winding wire by hand is much easier than microfabrication, and so designs can be modified and iterated very easily; 2) the substrates used for fabricating these coils (GaAs) are quite lossy leading to low Q values [63] [64]; 3) there is a strong static and RF inhomogeneity of the field near the surface of a surface coil, and so the sample must be lifted off the surface, decreasing its sensitivity. Despite these issues, the impact of geometric scaling is still significant. Both types of detectors have produced limits of detection of one nanoliter or less [81] [58].

1.4 Outline of Thesis

Presented in the following chapters is a significant contribution to the field of analytical tools for chemistry and biology, an inductive geometry that overcomes all three of these problems: scalability to small sizes to further improve the detection limit, high quality factor, and high RF homogeneity. The sequence of chapters that spans theoretical and experimental results is as follows:

- **Chapter 2** covers a review of the sensitivity of theoretically scalable inductive detectors. It discusses complications associated with three-dimensional fabrication and introduces the concept and theory of the microslot as a means to create scalable inductors in two dimensions.

- **Chapter 3** shows numerical models for the microslot, since analytical models cannot be solved. It shows the flux concentration property of microslots through an example and then covers simulations of designs actually fabricated. Finally, this chapter covers background theory for calculating RF inhomogeneity from these models.

- **Chapter 4** details fabrication of a microslot probe and the electromagnetic properties measured.

- **Chapter 5** contains the major non-biological experimental results on water and sucrose for the microslot probe. Here, sensitivity and linewidth, design optimization and NMR parameter measurements are presented for water. A more complex molecule, sucrose, was analyzed to compare the microslot probe to other probe technologies.

- **Chapter 6** contains a biological experiment on a small peptide. One- and two-dimensional spectroscopy was done to fully label the peptide.

- **Chapter 7** summarizes the contributions of the past chapters. It further discusses microslot improvements, ultimate scaling, future NMR application and microslot applications to other fields.

- **Appendix A** contains a basic introduction to Nuclear Magnetic Resonance theory applicable to this document.
- **Appendix B** contains a basic introduction to proteins and structure applicable to this document.
- **Appendix C** discusses theory and demonstrated experimental data from a Class E digital amplifier. One future application of this thesis work is table-top NMR and the ability to create small high-performance amplifiers is a necessary part of the solution (in addition to microslots).
- **Appendix D** contains the source code to generate the simulations of microslot probes built. Also included is a scaling study.

Chapter 2

Scaling NMR

2.1 Methods to Increase SNR

Nuclear magnetic resonance is a very insensitive method compared to other analytical techniques due to the low polarization at room temperature (see table 2.1). This chapter considers the various methods used to increase signal to noise ratio in NMR. It ignores all signal processing that can be done after acquisition and digitization and focuses on physical measurement, unitary and nonunitary control. See Appendix A for a derivation of thermal polarization in NMR.

There are two main categories of methods used to increase sensitivity in NMR, polarization enhancement and detection enhancement. The former includes techniques such as optical pumping, DNP, photo-CIDNP and MIONP. The latter includes mechanical, optical and inductive detection techniques. These are discussed below.

2.2 Polarization Enhancement

2.2.1 Optical Pumping

Optical pumping is a technique used to polarize nuclear spins while keeping the bulk material at room temperature. Each quantum of circularly polarized laser light carries one unit of angular momentum. A specific

method	LOD (mol)
fluorescence	10^{-18}-10^{-23}
mass spectrometry	10^{-13}-10^{-21}
electrochemical	10^{-15}-10^{-19}
radiochemical	10^{-14}-10^{-19}
UV-vis absorbance	10^{-13}-10^{-16}
NMR	10^{-9}-10^{-11}

Table 2.1: Limits of detection for various Analytical methods used for capillary separations. Taken from [48].

absorption line of atoms in the gas phase is pumped with a continuous wave laser, creating a highly polarized electronic state. With simple noble gases that do not interact and have simple electronic orbital structure, it is possible to perform a coherence transfer to the nuclear spins in these atoms. High polarizations, over 70%, have been reached using optical pumping [29]. Happer et al started this pioneering work on optical pumping of rubidium gases, which transfers polarization via Van der Walls molecule of formation to ^{129}Xe (or ^{3}He directly from the laser) to obtain $\mathcal{O}(1)$ polarization. The polarized ^{3}He or ^{129}Xe then cross-relaxes with the NMR species and depends on the relaxation rates of the species in a technique known as Spin Polarization Induced Nuclear Overhauser Enhancement (SPINOE) [29]. Only isolated progress has been made in polarizing liquids, since there is a complex energy level diagram and relaxation structure in generic molecules that makes it both difficult to find lines to pump as well as maintain populations. Nevertheless, enhancements of about 50 fold for ^{1}H and 70 fold for ^{13}C have been realized for compounds soluble in liquid Xenon [52].

2.2.2 DNP

Dynamic Nuclear Polarization, or DNP, is a technique in which paramagnetic centers in a solid sample at low temperature are used to transfer large electron spin polarization to the nuclear spin system using microwave radiation via cross-relaxation. The electron and nucleus are coupled via the hyperfine interaction. Unusually high enhancements of polarization at room temperature using DNP, specifically a factor of 5500 for proton spins in a single crystal of napthalene doped with a small concentration of pentacene molecules, have been obtained [88]. The DNP enhancement can apply in liquids via cross-relaxation between a free radical in a diamagnetic solvent solution via the Overhauser effect [47]. For solid state NMR, DNP enhancements can improve solid state biomolecule detection, but this technique is limited to molecules with paramagnetic centers and is therefore not generally applicable.

2.2.3 Photo-CIDNP

PhotoChemically Induced Dynamic Nuclear Polarization, or Photo-DNP, is a technique by which electron radical pairs interact with aromatic side chains of a protein-solvent interface, causing increased absorptive or emissive spin polarization [95]. The crucial feature of photo-CIDNP is that the evolution of the radical pair is governed by the spins of its two unpaired electrons. Usually part of the solution is composed of a flavin sensitizer in which a laser breaks a singlet bond, creating an excited triplet state (adding one unit of angular momentum). This process extracts hydrogen from an amino acid (e.g. tyrosine) to form a radical pair in a spin-correlated triplet state. Recombination is not possible without interconversion back to a singlet state. As the flavin molecule drifts from the amino acid, the energy difference between the singlet and triplet state decreases such that interconversion can be sensitive to local energy perturbations such as the hyperfine interaction with the nucleus. This effect has been observed in tyrosine, histidine and tryptophan, shown in Appendix B-1. (Flavins occur in nature as the coenzymes flavin mononucleotide and flavin adenine dinucleotide [87].)

2.2.4 MIONP

Another approach for polarization enhancement is a technique called Microwave-Induced Optical Nuclear Polarization, or MIONP, which occurs in organic materials such as phenanthrene or pentacene [42]. These materials are diamagnetic in their electronic ground states, but when photo-excited they become paramagnetic in their triplet states. For example, electrons in pentacene can be excited to higher singlet states with a laser beam, and then will transition to the lowest triplet state (via the spin-orbit interaction). These triplet states are long-lived, so with microwave radiation at the triplet nuclear spin-splitting one can transfer polarization from the electron spin to the nuclear spin. Because the ground state is diamagnetic, there are no further interactions between the electrons and protons. At liquid nitrogen temperatures, protons have been polarized to 32% [42], and at room temperature to 0.5%, [35] in a crystal of napthalene doped with pentacene. These results are very promising, but the specific energy level diagram and magnetic moment properties at the ground singlet state and excited triplet state are not found in amino acids, and hence MIONP is not generally applicable.

2.3 Detection Enhancement

2.3.1 Mechanical Detection

Though NMR uses magnetic induction to detect nuclear spins, it is not the only means available. In fact, the first experimental detection of NMR by Rabi et al. used force detection via the Stern-Gerlach force for state-dependent separation [67]. Sidles first proposed coupling motion of a mechanical oscillator to the harmonic magnetization of a single nuclear spin [75]. This proposal described a mechanical oscillator mounted on a scanning head to image a single biomolecule. The image is not based on high resolution spectroscopy, but on gradient localization. The mechanical oscillator has a magnet that creates a field gradient ($\vec{B}$) that interacts with the magnetic moments of the nuclear spins ($\vec{m}$). This interaction results in a force

$$\vec{F} = \nabla(\vec{m} \cdot \vec{B}). \tag{2.1}$$

Sidles' technique was first tested experimentally by Rugar et al. for a single electron spin [70]. Using an ultra-thin cantilever, small numbers of both protons [71] as well as fluorine atoms [92] were detected, both at low temperature. This mechanical detection technique is now known as Magnetic Resonance Force Microscopy (MRFM). It has been shown that at small length scales, the noise model of Brownian motion of the cantilever is superior to inductive detection [76], as discussed at the end of this chapter.

2.3.2 Optical Detection

Optically detected NMR, in which spins can be polarized, detected and manipulated at low temperatures, is another approach to measuring nuclear spin states [72]. One approach using a femtosecond laser has been successful in GaAs quantum wells, but is not generally applicable.

Another optical detection technique has been used on a single molecule, for which the relaxation dynamics of the electron spin are controlled by hyperfine or quadrupolar interaction with the nucleus and observed via fluorescence. This Fluorescence Detected Magnetic Resonance (FDMR) has been accomplished with single pentacene molecules containing ^{13}C or ^{1}H in a para-terphenyl crystal matrix [72] [14]. In the case of ^{13}C, a single nucleus was detected through its interaction with the triplet electron spin [14]. It is possible to obtain high resolution spectra from this technique [15], but only for a very specific molecule (pentacene) to date.

2.3.3 Inductive Detector Miniaturization

To understand the signal produced by a liquid sample via inductive detection, we invoke the reciprocity theorem, which allows us to understand the voltage produced by a magnetization $\vec{m}$. Proper application of this function could potentially increase sensitivity to nuclear spin magnetization, while retaining high resolution spectroscopy. The signal to noise ratio of an inductive detector is

$$\mathrm{SNR} = \frac{\text{peak signal}}{\text{RMS noise}} = \frac{\mathcal{E}}{V_{\text{noise}}}, \tag{2.2}$$

where $\mathcal{E}$ is the voltage produced by a time varying spin magnetization and V_{noise} is the thermal noise voltage. To calculate $\mathcal{E}$ and prove the reciprocity theorem, from Lenz's Law:

$$\begin{aligned} \mathcal{E} &= -\frac{\partial}{\partial t}\int \vec{B}\cdot\hat{n}dS \\ &= -\frac{\partial}{\partial t}\int \nabla\times\vec{A}\cdot\hat{n}dS \\ &= -\frac{\partial}{\partial t}\oint \vec{A}\cdot dl. \end{aligned} \tag{2.3}$$

This last line comes from Stokes' Theorem, where $\vec{A}$ is the magnetic vector potential. Now we can use an approximation for the magnetic vector potential in the near field via Taylor expansion:

$$A = \frac{\mu_0}{4\pi}\frac{\vec{m}\times r}{|r|^3}, \tag{2.4}$$

therefore,

$$\mathcal{E} = -\frac{\mu_0}{4\pi}\frac{\partial}{\partial t}\oint \frac{\vec{m}\times\vec{r}}{|r|^3}\cdot dl. \tag{2.5}$$

Now from standard vector equalities, $\vec{a}\cdot(\vec{b}\times\vec{c}) = \vec{b}\cdot(\vec{c}\times\vec{a})$. Assuming also that the magnetization is constant over the integration path,

$$\mathcal{E} = \frac{\mu_0}{4\pi}\frac{\partial}{\partial t}\vec{m}\cdot\oint\frac{dl\times\vec{r}}{|r|^3}, \tag{2.6}$$

but we note that the Biot-Savart Law is

$$\vec{B} = \frac{\mu_0}{4\pi}\oint\frac{dl\times\vec{r}}{|r|^3}, \tag{2.7}$$

Therefore,

$$\mathcal{E} = \frac{\partial}{\partial t}(\vec{m}\cdot\vec{B}/i). \tag{2.8}$$

From Appendix A, at room temperature, the magnetization $\vec{m}$ is

$$\langle\vec{m}\rangle = \frac{\nu_S N\gamma^2\hbar^2 I(I+1)B_0}{3k_B T}\hat{z}. \tag{2.9}$$

Combining this with equations 2.2 and 2.8, the signal to noise ratio is [39]

$$\mathrm{SNR} = \frac{k_0(B_1/i)\nu_S N\gamma\hbar^2 I(I+1)\omega_o^2/3\sqrt{2}k_B T}{V_{\text{noise}}} \propto \frac{\omega_0^2(B_1/i)\nu_S}{V_{\text{noise}}}. \tag{2.10}$$

We see the NMR signal is proportional to ω^2. B_1 is the flux density in the RF coil produced by a unit current i in a sample volume v_S. The signal is also proportional to a spin density N, gyromagnetic ratio γ, and spin quantum number of the sample I. The factor k_0 is the RF inhomogeneity of the probe. The noise is thermal noise described as

$$V_{\text{noise}} = \sqrt{4k_B T R_{\text{noise}}\delta f}. \tag{2.11}$$

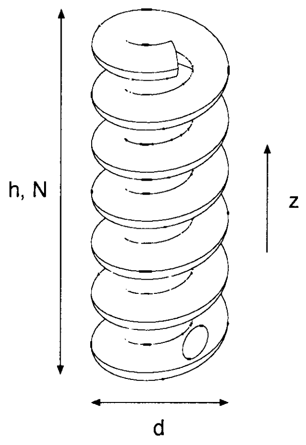

Figure 2-1: Model of a solenoid, showing parameterization for analysis.

R_{noise} is used to represent the conductive losses of the coil as well as magnetic (eddy current) and dielectric losses in the sample and surrounding structures, and is based on the constant spectral density $S_i = \sqrt{4k_BTR}$ over the small bandwidth of the tank circuit.

Let us first consider, as an example, the scaling of a solenoid. The ideal on-axis sensitivity in the center of an ideal single-layer solenoid of many turns ($N \gg 1$) is

$$B_1/i = \frac{\mu_0 N}{d\sqrt{1+(\frac{h}{d})^2}}. \tag{2.12}$$

B/i is derived from the Biot-Savart Law as

$$\begin{aligned}
\vec{B} &= \frac{\mu_0}{4\pi}\int_{h/2}^{h/2}\frac{\mathrm{dl}\times\vec{x}}{|\vec{x}|^3}\hat{z} \\
&= \frac{\mu_0\,\mathrm{ni}}{4\pi}\int_{h/2}^{h/2}\frac{r^2 d\theta\,\mathrm{dz}}{(r^2+z^2)^{\frac{3}{2}}}\hat{z} = \frac{\mu_0\,\mathrm{ni}}{2}\frac{z}{(r^2+z^2)^{\frac{1}{2}}}\Big|_{-h/2}^{h/2}\hat{z} \\
&= \frac{\mu_0}{2}\frac{\mathrm{nhi}}{d/2(1+(\frac{h}{d})^2)^{\frac{1}{2}}}\hat{z} = \frac{\mu_0\,\mathrm{Ni}}{d\sqrt{1+(\frac{h}{d})^2}}\hat{z},
\end{aligned} \tag{2.13}$$

where n is the turns density ($N = nh$). We see the field strength is inversely proportional to the diameter of the coil. This means that the sensitivity per unit volume of a solenoidal detector is inversely proportional to its diameter. This is an amazing result, because it shows that with prior knowledge of the number of spins and concentration, the size of the optimal inductive detector should be as small as the sample itself. In other words, to detect small samples, one needs a small detector.

However, the analysis is incomplete without consideration of the resistance of the coil. At AC frequencies, the current density in any metal decays exponentially within the conductor. The $1/e$ point is termed the skin depth and is described by $\delta = (\mu_0\pi\sigma f)^{-1/2}$. Another factor that increases resistance in coils is called the proximity effect: wires in close proximity induce fields that force the current distribution within the conductor to be confined to minimize loss. Combining all these effects together:

$$\begin{aligned}
R_{\text{coil}} &= R_{\text{dc}} + R_{\text{skin}} + R_{\text{prox}} \\
&= R_{\text{dc}}\left[1 + F + u_{\text{eff}}G\left(\frac{d}{s}\right)^2\right].
\end{aligned} \tag{2.14}$$

u_{eff} is a factor to account for inter-turn magnetic coupling of a particular geometry. The skin effect and proximity effect terms (F and G) are functions of d and δ, respectively through the dimensionless parameter $z = d/\delta$. s is the inter-turn spacing. These functions have been analyzed in previous work [62][16][17]. When the diameter of the coil is much larger than the skin depth, both F and G are linear functions of z and can be combined. Therefore, the system can be analyzed as a straight wire with a linear prefactor and we can rewrite equation 2.14 as

$$R_{\text{coil}} = \xi \frac{\rho l}{A}, \tag{2.15}$$

where ξ is the proximity effect factor, and typically $1 \leq \xi \leq 3$. If the inter-turn spacing is $1.5d$, a factor chosen to maximize inductance and minimize loss, then

$$R \approx \frac{\rho \pi d N}{\pi d_{\text{wire}} \delta} \xi \approx \frac{\rho 3 d N^2}{2 \delta h} \xi. \tag{2.16}$$

Thus the overall signal to noise ratio per unit sample is

$$\text{SNR}_{\text{puv}} \propto \frac{\omega_0^{7/4} [N/d \sqrt{1 + (h/d)^2}]}{\sqrt{(N^2)(d/h)}}. \tag{2.17}$$

We assume that d/h will be a fixed factor in scaling, giving a final SNR in the skin depth regime:

$$\text{SNR}_{\text{puv}} \propto \frac{\omega^{7/4}}{d}. \tag{2.18}$$

Compare this to the uniform current regime ($d \leq \delta$), in which we assume that $s = h/N$:

$$R \approx \frac{\rho \pi d N}{\pi d_{\text{wire}}^2} \xi \approx \frac{9 \rho N^2 N/h}{4h/d} \xi. \tag{2.19}$$

Since $N/h \propto N/d$, $\text{SNR}_{\text{puv}} \propto \omega_0^2 / \sqrt{Nd}$. For a planar coil of radius r,

$$\begin{aligned}
\vec{B} &= \frac{\mu_0}{4\pi} \int \frac{\mathrm{dl} \times \vec{x}}{|\vec{x}|^3} \hat{z} \\
&= \frac{\mu_0 \,\mathrm{ni}}{4\pi} \int_0^r \frac{r^2 d\theta \,\mathrm{dr}}{(r^2 + z^2)^{\frac{3}{2}}} \hat{z} \\
&= \frac{\mu_0 \,\mathrm{ni}}{2} \left[\frac{-r}{\sqrt{r^2 + z^2}} + \ln\left(\frac{r}{|z|} + \sqrt{1 + \frac{r^2}{z^2}}\right) \right] \\
&= \frac{\mu_0 \,\mathrm{Ni}}{2} \left[\frac{-1}{r\sqrt{1 + (\frac{z}{r})^2}} + \frac{1}{r} \ln\left(\frac{r}{|z|} + \sqrt{1 + \frac{r^2}{z^2}}\right) \right].
\end{aligned} \tag{2.20}$$

Notice equation 2.20 has a similar form to 2.13, except for a sign change and the extra logarithmic term, which vanishes when $z \gg r$. A plot of B_z is shown in figure 2-2 with a very inhomogeneous response. This inhomogeneity is one reason why a planar solenoid is not a good magnetic resonance detector. Compare this to the interior of a solenoid in figure 2-3, which shows a homogeneous profile. Both planar and solenoidal coils have been fabricated and used for magnetic resonance. The initial work with planar coils started with microfabrication techniques on glass [62] and gallium arsenide [81], but the results exhibited much lower signal to noise ratio than those of solenoidal microcoils [62] [61]. Planar microcoils with microfabricated sample cells have also been made by Massin [55] and Walton [93]. The work of Massin et al. has yet to

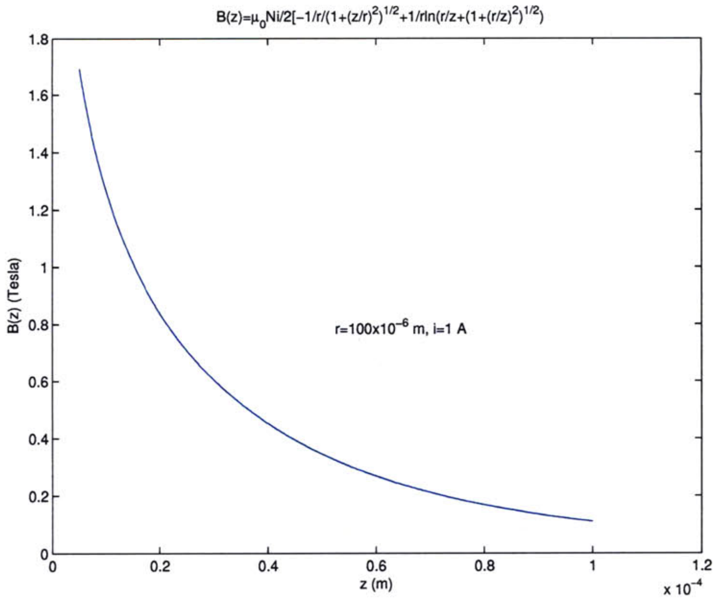

Figure 2-2: Plot of equation 2.20 for a planar coil along the z-axis, indicating inhomogeneity.

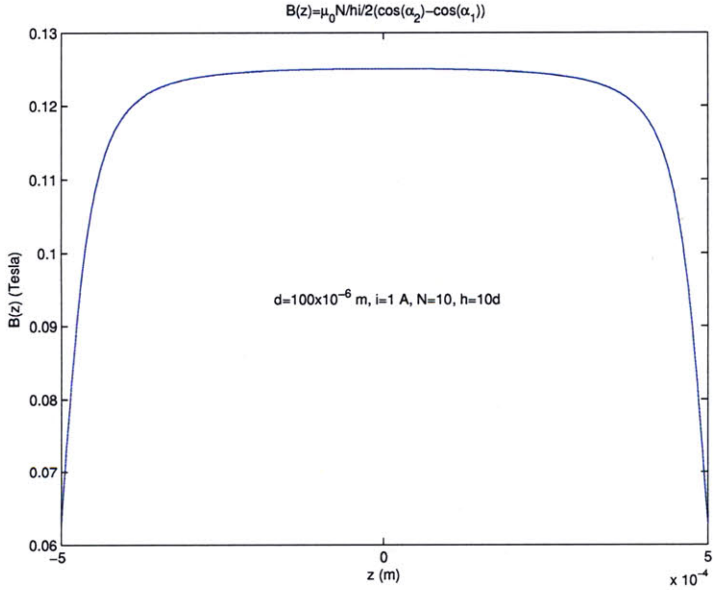

Figure 2-3: Field profile along the axis of a solenoid, showing homogeneity. The parameters used are referenced in figure 2-1.

achieve the same resolution or sensitivity of commercial probes for proton detection but demonstrates very nice electromagnetic and microfluidic results. The work of Walton et al. demonstrates successful detection of ^{31}P and ^{13}C and achieves similar performance to commercial probes using a Helmholtz pair.

Solenoidal coils, which have largely been the work of the Webb and Sweedler groups [96], exhibit the highest SNR for microscale NMR, but are very difficult to scale to smaller sizes. Some work has been done to investigate the potential of using microfabrication techniques to make coils [68], but those produced demonstrated poor sensitivity compared to those made of conventional wire. A summary of the relevant microcoil results can be found in Chapter 5.

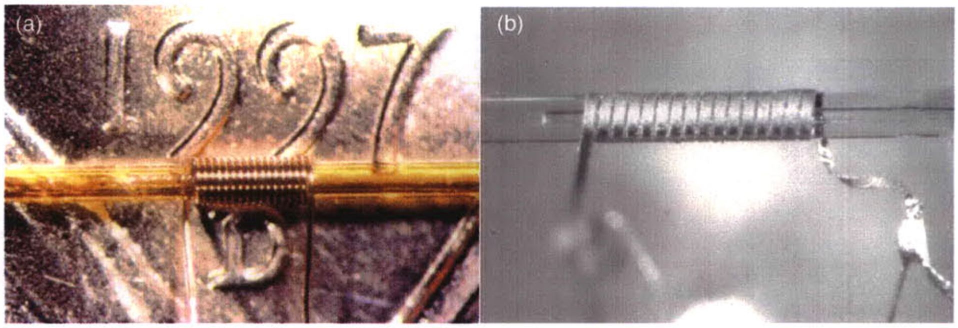

Figure 2-4: Solenoidal microcoils made by two different methods. (a) coil winding (with conventional wire) around a 360μm capillary [96]. (b) microcontact printing on a 324 μm wide capillary (length 1.6 mm) [68].

2.3.4 3D Fabrication Techniques

Three-dimensional microfabrication is at an inchoate stage, serving niche needs. As a result, it is very difficult to microfabricate very high performance coils whose circuit models are primarily inductive at UHF frequencies. Three techniques illustrate this problem.

The first, one of the most general techniques for 3D microfabrication of metals, is electrodeposition using a very fine platinum wire [53]. Metal coils with diameters in the hundreds of micrometers, one of which is shown in figure 2-5, have been made using this technique. The problem is that these coils have granular structures, resulting in lower than bulk conductivity. Coils have also been fabricated using nickel, which is less conductive and much more magnetic than copper, both disadvantages for NMR.

A second technique relies on creating residual stress between bilayers of material to cause structures to "self-assemble" in three dimensions [20]. This impressive method relies on fabrication with standard semiconductor batch processing techniques on unaltered low-resistance silicon, and has produced record-high quality factor inductors of over 70 at 1 GHz to make all-integrated oscillators. However, because the stress of the materials used sets a specific radius of curvature, this approach does not promise to scale to any size.

The final technique features a two-dimensional fabrication process with a post-release folding process [31]. The resulting structure must be perforated along the copper wire to allow the release process to occur. Here, perforation likely causes poor RF properties. These structures are also rather large, typically on the order of 1mm on a side.

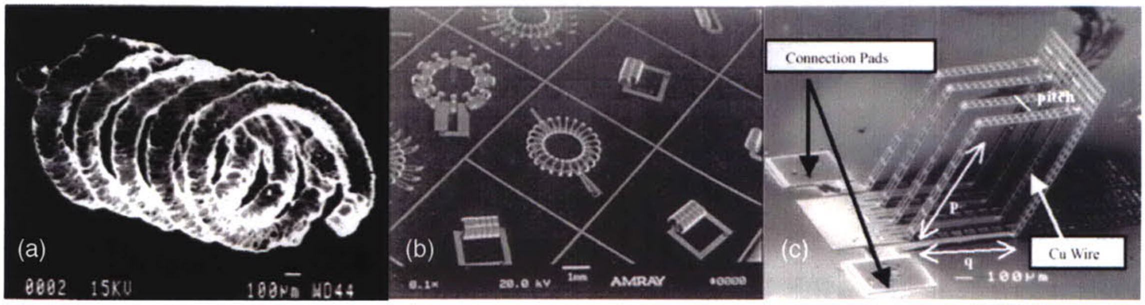

Figure 2-5: Three types of 3D microcoil microfabrication research. (a) coil make using an electrodeposition technique, taken from [53]. (b) sampling of stress-engineered microfabricated coils, taken from [20]. (c) post-release process creating an out-of-plane coil, taken from [31].

2.4 Observations

With the complications of three-dimensional fabrication and the non-ideality of solenoids as scalable detectors, the survey of current techniques used for inductive detection was disappointing. Therefore, when beginning this thesis work, an altogether new approach was desired – one that would have the sensitivity of microcoils, but also the simplicity of a planar, manufacturable structure with no parasitics at any scale. Micropatch antennas have all of these properties except that their behaviour is fixed to a specific wavelength for a far-field radiation pattern. Though a non-obvious path, near-field planar structures were explored.

2.5 Microslots and Striplines

The novel idea introduced in this thesis is to use discontinuity in a stripline as a radiative element to probe nuclear spins. Boundary conditions on planar substrates have not previously been considered for flux concentration. From [36], a narrow slot cut into a microstrip line can be modeled as a pure, small series inductor. The parameters describing this inductor are extremely interesting. A diagram of the slot is shown in figure 2-6:

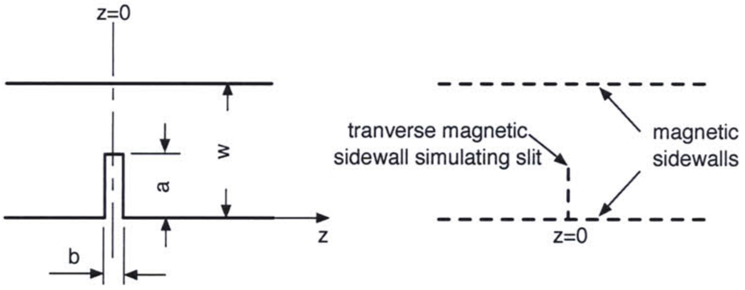

Figure 2-6: Microslot geometry, used for analysis.

In order to achieve flux concentration, a perturbation in the microstrip structure is created that causes the magnetic field component of the quasi-TEM (Transverse ElectroMagnetic) wave to re-orient, while the electric field component of the wave remains largely unaffected. To perform an analysis of a microslot, one assumption is made, that is, the perturbation of the field can be modeled as a dipole. This assumption is true in the near field, due to the moment expansion of the magnetic vector potential. To overcome the difficult analysis of the slot in a highly non-uniform field, an equivalent volume concept allows one to transform the asymmetric microstrip model to a symmetric parallel plate model that has magnetic side walls. In this symmetric parallel plate model [36], the spacing between parallel plates is the same as the microstrip height, h, but the width of the parallel plate is not the same (see figure 2-7):

$$A = \frac{h}{Z_0}\sqrt{\frac{\mu_0}{\epsilon_{\text{eff}}\epsilon_0}}, \tag{2.21}$$

where Z_0 is the original microstrip impedance and ϵ_{eff} is the effective dielectric constant for the strip [66]. If the length l of the line section is much greater than the width $2a$ of the obstacle, but small compared to the wavelength, the relative increase in inductance can be expressed as the volume ratio

$$\frac{\Delta L_s}{L_s} = \frac{V_{ob}}{V_l}, \tag{2.22}$$

where V_{ob} is the effective volume of the obstacle, and V_l is the volume of the model section. The volumes V_{ob} and V_l are:

$$\begin{aligned} V_{ob} &= \pi a^2 h \\ V_l &= 2Alh. \end{aligned} \tag{2.23}$$

To calculate the inductance of the parallel strip, we use Maxwell's equation to calculate the field:

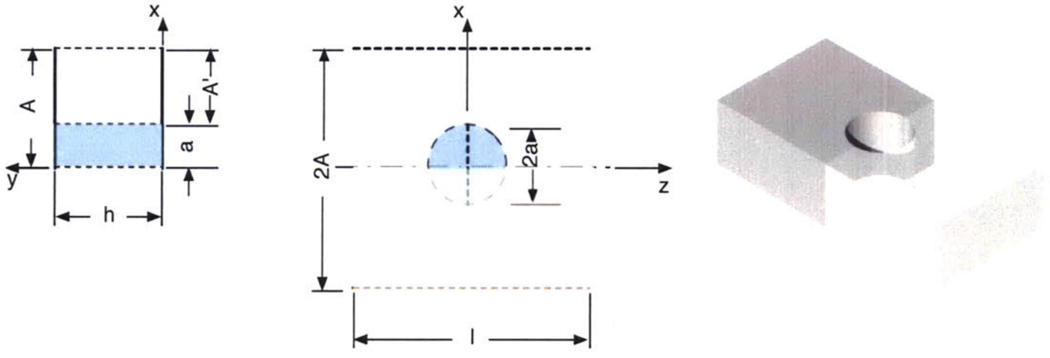

Figure 2-7: Parallel plate model of a microslot and symmetrization used to analyze the structure.

$$\begin{aligned}\nabla \vec{H} &= \vec{J} \\ \oint_C \vec{H} \cdot d\vec{l} &= \int \vec{J} \cdot d\vec{A} \\ H2A &= i \\ \Longrightarrow H &= \frac{i}{2A},\end{aligned} \tag{2.24}$$

since

$$\begin{aligned}L &= \mu_0 \int_S \vec{H} \cdot d\vec{A}/i \\ &= \frac{\mu_0}{2A} lh.\end{aligned} \tag{2.25}$$

Combining equations 2.25, 2.23 and 2.22 together and dividing ΔL by a factor of 2 due to the symmetry we introduced, we obtain

$$\Delta L = \frac{\mu_0 h\pi}{2}(\frac{a}{A})^2. \tag{2.26}$$

Pausing for a moment, notice that the inductance is a ratio of the two widths. If one can keep the ratios constant, the inductance will stay constant as a function of scale. This characteristic reflects the dipole assumption, which is not strictly true in a real system. Using equation 2.21, since $a = A - A'$,

$$L = \frac{\mu_0 \pi}{2} h[1 - \frac{Z_0}{Z_0'}\sqrt{\frac{\epsilon_{\text{eff}}}{\epsilon_{\text{eff}}'}}]^2 \tag{2.27}$$

is the formula for the inductance in Henrys. Z_0' and ϵ_{eff} represent the impedance and effective dielectric constant of a microstrip of width A'. This is true for $a/w < 0.9$, $b \ll h$ and $b \ll \lambda$. See the plots of the functions $Z_0(W)$ and $\epsilon_0(W)$ in figures 2-8 and 2-9. Considering other symmetric boundaries, if one were to place a slot directly in the center of the conductor, it is easy to see from the above analysis that the inductance will be half that of the asymmetric case. If we invert the structure so the conductor is in the center, in effect creating two microslots back to back, the inductance will be half the original case. Figure 2-10 shows these relationships.

Now that we have an equation for the inductance, how can we relate this to the magnetic field around the slot? Equation 2.27 indicates only qualitative information about the magnetic flux density. Since

$$\Delta L = \phi/i = \frac{\int_S B \cdot dA}{i}, \tag{2.28}$$

with a current i and closed surface boundary S, constant with or without the slot, the sum of the flux density over that surface must increase. Because the conformal map integral for a microstrip does not have enough symmetries to be solved analytically, we must perform a numerical analysis [66]. This work is found in the next chapter.

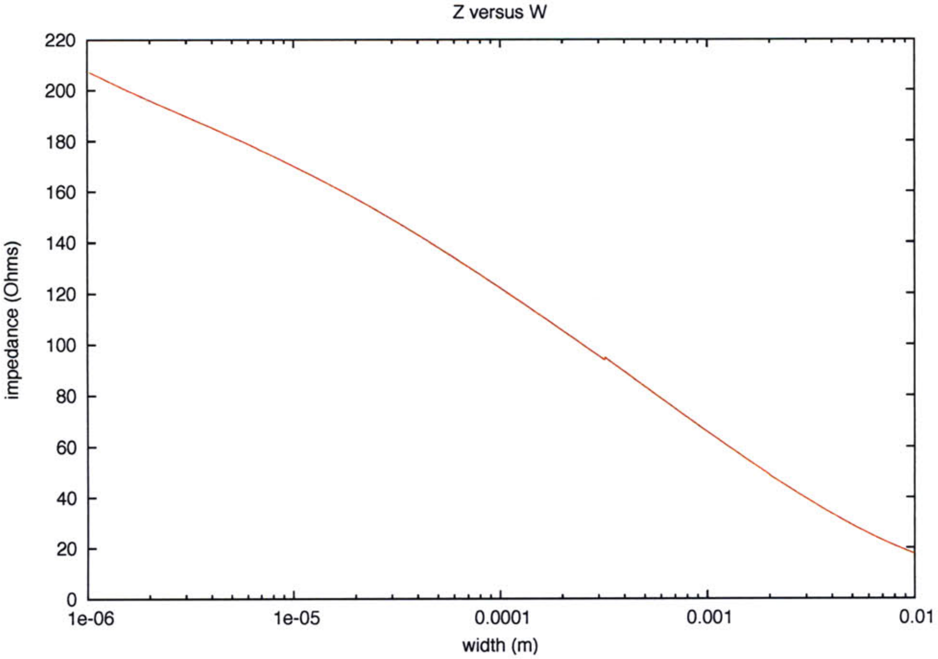

Figure 2-8: $Z_0(W)$ for a microstrip. 4 orders of magnitude width change corresponds to 1 order of magnitude impedance change.

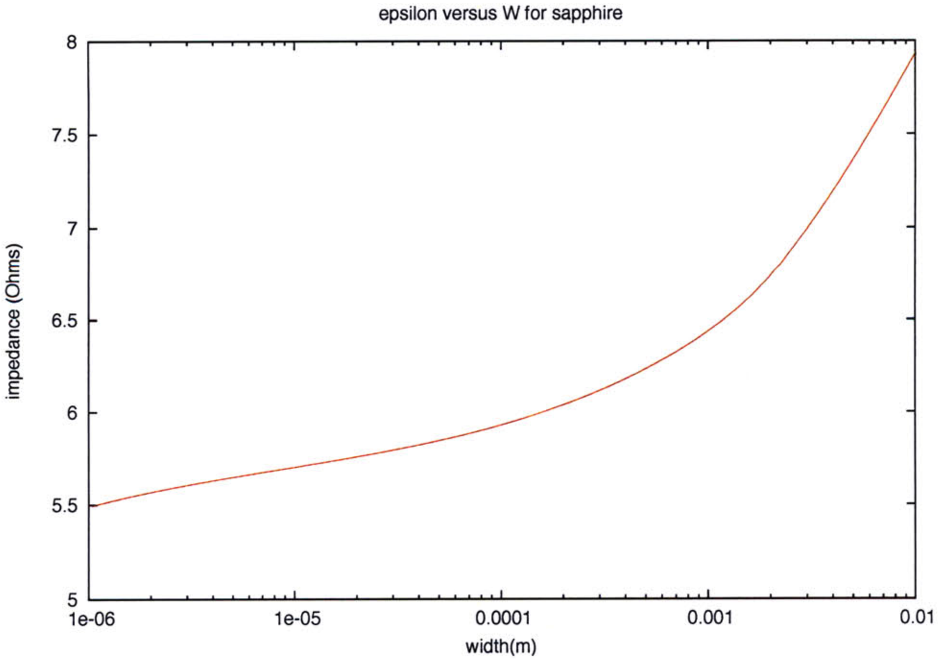

Figure 2-9: $\epsilon_0(W)$ for a microstrip. 4 orders of magnitude width change corresponds to less than a factor of 2 dielectric constant change.

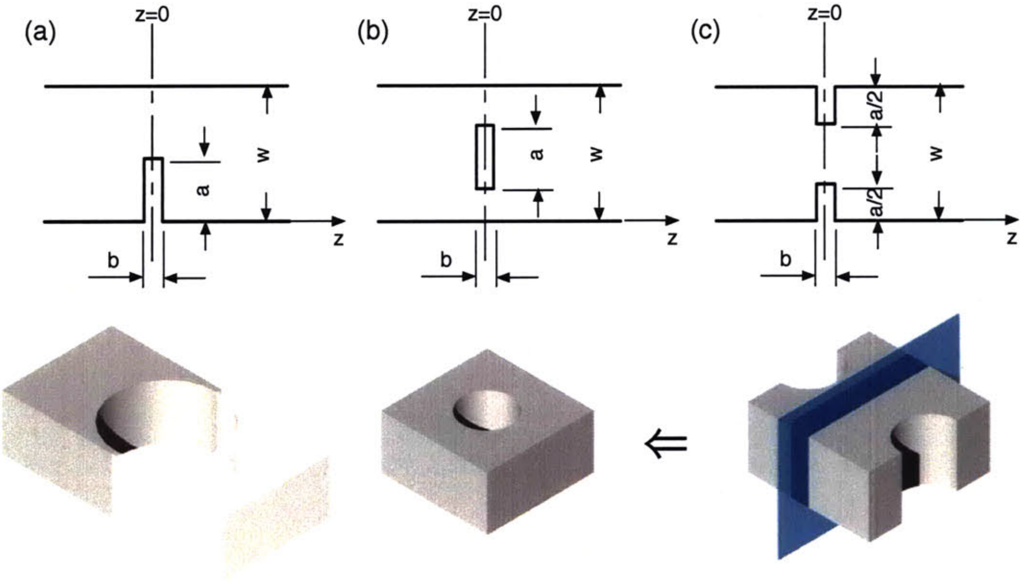

Figure 2-10: Symmetry is very important for susceptibility-matching and hence more useful for NMR. (a) shows the original microslot concept. (b),(c) Show the symmetrized versions of the microslot introduced in this thesis. From the cartoons of the parallel plate representation, one can see the inductance for the symmetric case is half that of the asymmetric case. For (c), one can make a transformation (by symmetry) on each half of the parallel plate model to yield (b). Hence (c) has the same inductance as (b).

2.6 Comparison of Inductive and Mechanical Detection

The signal to noise scaling comparison of mechanical and inductive detection has been studied in depth [50]. For both techniques, the limiting condition for sensitivity is thermal noise on the detector. For mechanical detection, the limitation is Brownian motion of the oscillator, and for inductive detection it is Johnson noise in the resonant circuit. The noise spectral density of force detection in Newtons per root Hertz is

$$S_F = \sqrt{4k_B T\alpha}\ \ (N\sqrt{\text{Hz}}), \tag{2.29}$$

where $\alpha = m\omega_F/Q_F$ is the damping constant of the oscillator of mass m and temperature T. It is assumed, as in the case of inductive detection, that the thermal energy is much larger than the oscillation energy of the system, that is, $k_B T \gg \hbar\omega_F$. A force is produced by the dipole (μ_s) and the detector (μ_d), which have the differential moments $M_s dV_s \hat{z}$ and $M_d dV_d \hat{z}$, respectively, where M_S and M_d are the magnetizations of the sample and detector. If the sample is uniformly magnetized, the peak force magnitude is

$$|F| = \frac{\kappa_F \mu_0 V_s M_s M_d}{R_{max}}, \tag{2.30}$$

where V_s is the sample volume, R_{max} is the distance between the center of the sample and the detector, and κ_F is a dimensionless constant that represents integration over a particular geometry. Combining equations 2.30 and 2.29 and considering the rms force rather than the peak force, yields an overall SNR of

$$SNR_F = \frac{\kappa_F \mu_0 V_s M_s M_d}{R_{max}\sqrt{8k_B T\alpha\Delta f}}. \tag{2.31}$$

This function has a linear dependence on ω_0 in M_s, rather than a quadratic dependence in the inductive case:

$$SNR_F/SNR_I = \frac{\kappa_F}{\kappa_I}\frac{M_d}{\omega_0}\sqrt{\frac{\alpha\omega_F}{R\omega_I}}. \tag{2.32}$$

A comparison is made in [50] between mechanical and inductive detection for a hypothetical 60 μm spherical sample with 4 μm clearance from the detector at 2T. This calculation provides an example set of constants required in equation 2.32 to solve for the ratio of sensitivities as a function of magnetic field, as shown in figure 2-11. The quality factor in the paper was estimated to be 1.1 for a solenoidal microcoil, but this is lower than has been recently determined [96]. Even adjusting for a quality factor of 40, force detection should be more sensitive for small samples ($<$ 100 μm), but to date this has not demonstrated at room temperature. Another problem with mechanical detection is that it does not give high resolution spectra, but only the magnitude of the Free Induction Decay (FID).

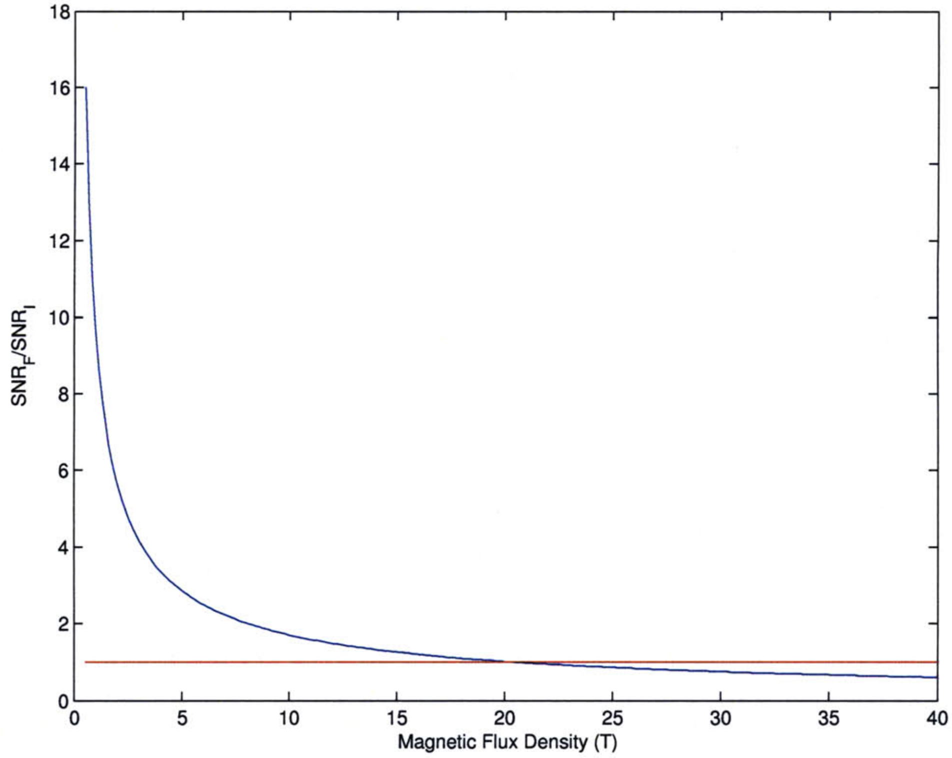

Figure 2-11: Ratio of signal to noise ratio of force detection (given by Leskowitz et al. [50]) to inductive detection.

Chapter 3

Numerical Modeling

It is very difficult, if not impossible, to determine the field distribution around a microstrip using analytical integration. The traditional method for solving these problems is to map the solution through conformal mapping, but due to the boundary conditions of this problem, the solution can only be found numerically [66]. The numerical modeling technique used here was Finite Element Analysis (FEA), chosen because of the flexibility of this technique for creating a variety of geometries.

Consider the following set of quasi-static finite element models. The first is a 1.5mm, symmetric microslot, which we will compare to a 3-turn square inductor. The second example is an asymmetric microslot at 6.9 mm (that was actually fabricated). The final example is a 297μm microslot (that was also fabricated) and was used for the majority of NMR experiments detailed in this thesis. Issues relating to the three models are discussed in the following sections.

3.1 1.5mm Simulation

The geometry for the microslot is shown below in figure 3-1. The conductor thickness is 100μm, the width of the microstrip is 1.5mm, the length is 4mm, a is 1.2mm, b is 1mm (see figure 2-10), and the dielectric thickness is 3mm. The dielectric width is 10mm and the air height is 5mm. The geometry for the square inductor is shown in figure 3-2. The square inductor has a thickness of 20μm, a track width of 22μm, and longest length of 232μm, and has no dielectric.

The script for creating the FEM is found in Appendix D. All numerical modeling was done with Femlab 2.3 from Comsol. To do convergence tests, the script allows different mesh densities to be automatically created. Results at a few different mesh densities were initially performed to verify results were consistent.

In NMR the static field is oriented in a single direction. Thus it is important for the strongest component of the field generated by the probe to be homogeneous and orthogonal to the static field or else there will be high RF inhomogeneity and the RF field will not be effective at rotating spins [27]. Therefore, in a

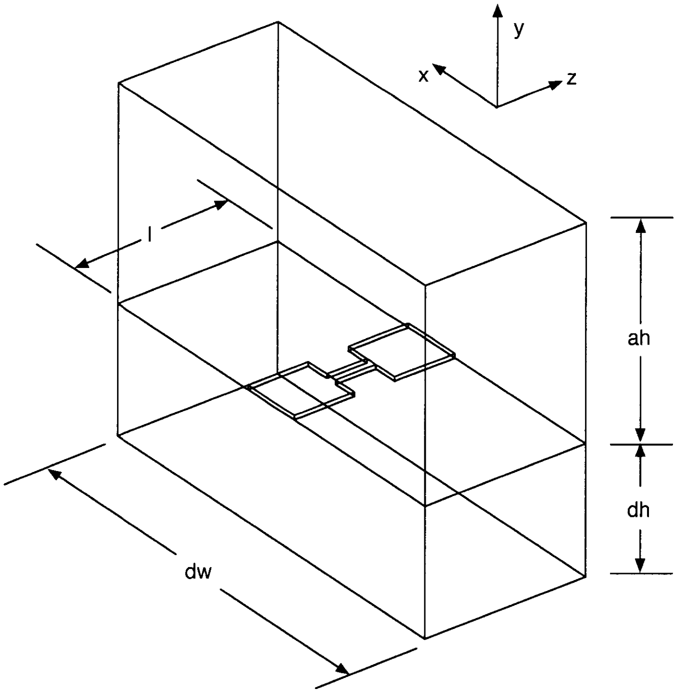

Figure 3-1: Geometry for the microslot inductor. A=1mm, A'=100μm, b=1mm (see figures 2-6 and 2-7), and the copper thickness is 60μm. Microstrip feed points are on either side of the microslot.

simulation of a candidate probe geometry, it is important to observe a preferred direction of the magnetic field. The final modeling simulation results are shown as isoshells of each component of the flux density in figures 3-3 through 3-8 for both the microslot and the square inductor. Isoshells are an important means of viewing 3D simulations of magnetic fields because they indicate field lines and the optimal sample shape for a particular probe geometry. From the simulations shown, a preferred direction in the near field distinguishes the microslot from the square inductor. Also of note is that flux concentration has been achieved by boundary conditions (a symmetric slot in the microstrip line) and not by increasing the number of turns of a current carrying loop structure. Suspended above the microslot is a strong B_x field (in figure 3-3), absent in the microstrip feed. This shows the flux concentration of the microslot coming from the increased inductance of the structure. There is a strong B_y field (in figure 3-4), but it is confined to the top plane of the dielectric on either side of the slot. The B_z field exists only at the junction of the microstrip lines (in figure 3-5). In contrast, the isoshells for the square inductor have no preferred orientation and are equally strong in every direction. The isoshell shape suggests an hourglass sample shape that can not be made orthogonal to a static magnetic field oriented in a single direction. Even further away from the structure, all three components of $\vec{B}$ are strong, and their spatial distribution results in an inhomogeneous field.

In comparing the two geometries, these figures show that a microslot should be a higher performance device for spin detection based on field orientation and geometry. This analysis shows that if one were to use a cylindrical or ellipsoidal sample, it should be placed either (1) above the slot where the RF field will

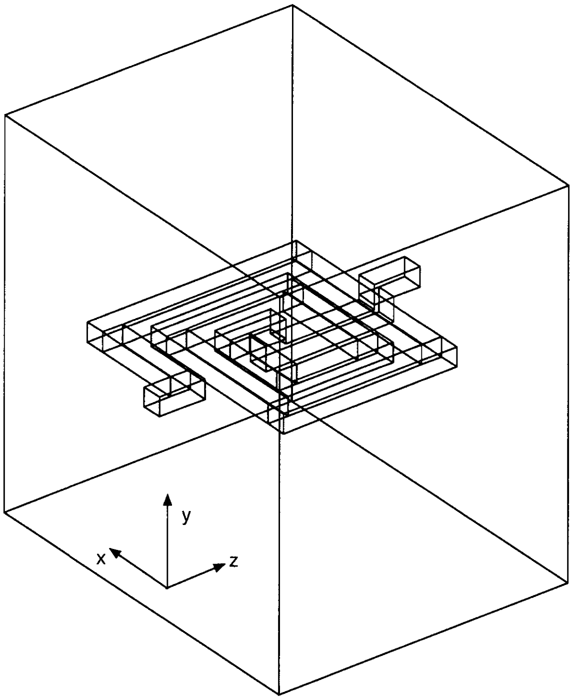

Figure 3-2: Geometry for the square inductor.

be B_x with the sample oriented in the direction of current flow, or (2) underneath the microslot. The latter is more difficult, but may be useful for future microfluidic integration. Even in this configuration, the field B_x will vary over the sample if the sample is in a capillary or in drop form, but if the sample is in the form of a cylindrical shell (e.g. shaped *around* a tube), the field will be very homogeneous.

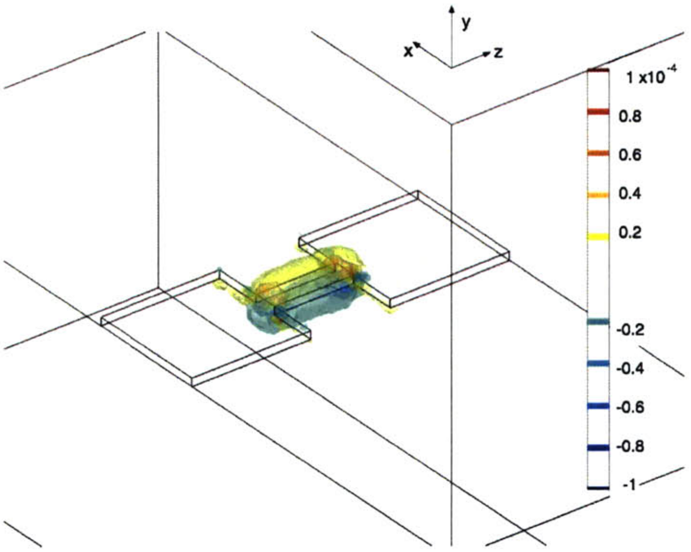
y
x
z
1 x10^-4
0.8
0.6
0.4
0.2
-0.2
-0.4
-0.6
-0.8
-1

Figure 3-3: Isoshells for B_x (in Tesla) showing increased flux density around the microslot. This represents the preferred direction for the microslot and demonstrates flux concentration around the microslot.

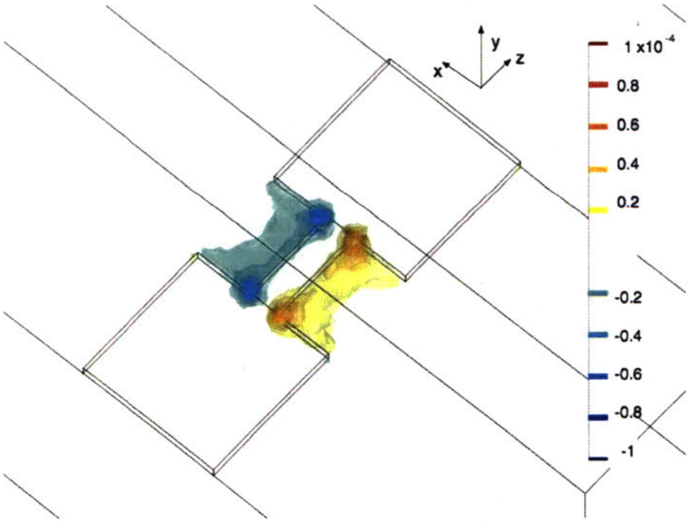
y
x
z
1 x10^-4
0.8
0.6
0.4
0.2
-0.2
-0.4
-0.6
-0.8
-1

Figure 3-4: Isoshells for B_y, (in Tesla) showing strong flux density on either side of the microslot, away from the top where a cylindrical/ellipsoidal sample would be placed.

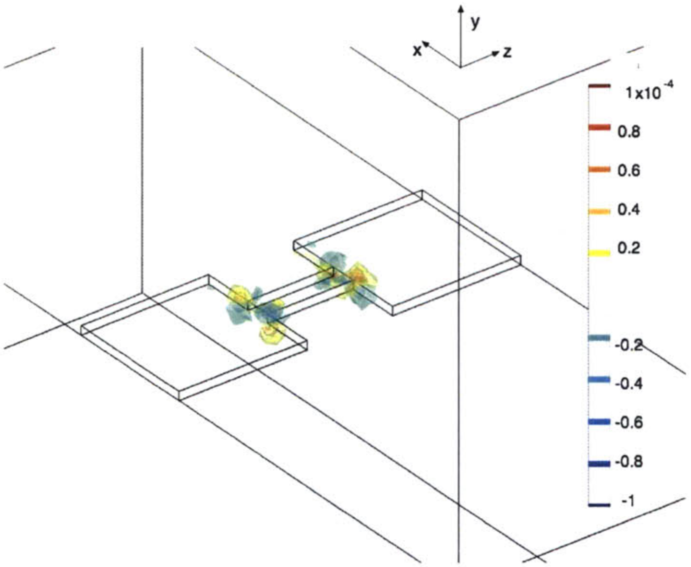

Figure 3-5: Isoshells for B_z (in Tesla) for the microslot, showing very minimal contribution.

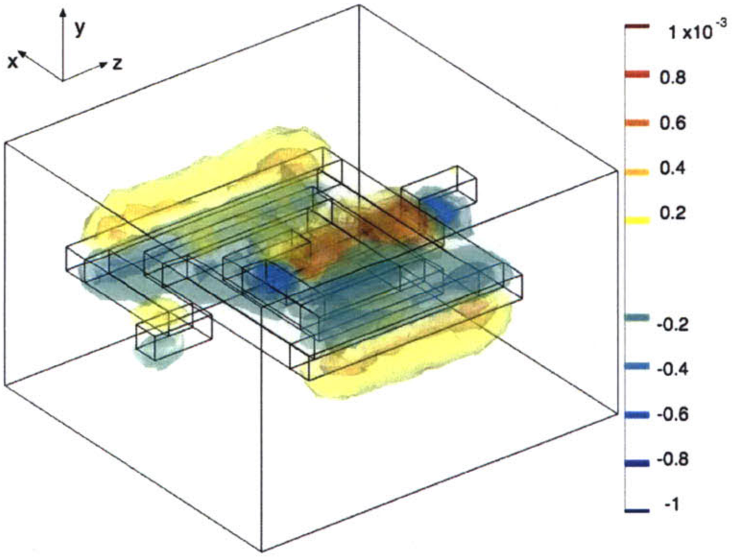

Figure 3-6: Isoshells for B_x (in Tesla) for the square inductor, showing strong density above the inductor. In this figure and the following two, It is difficult to see where and what geometry of sample could be placed to achieve high RF homoegeneity and a preferred orientation.

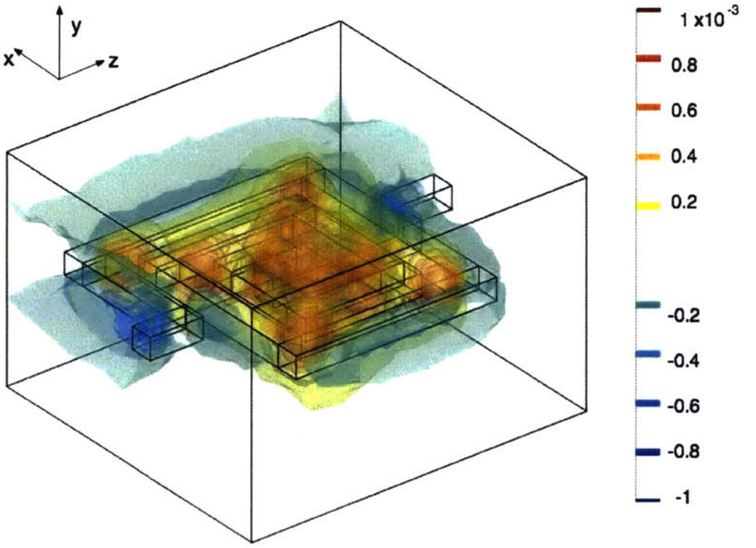
y
x
z
1 x10^{-3}
0.8
0.6
0.4
0.2
-0.2
-0.4
-0.6
-0.8
-1

Figure 3-7: Isoshells for B_y (in Tesla) for the square inductor, showing strong density above the inductor.

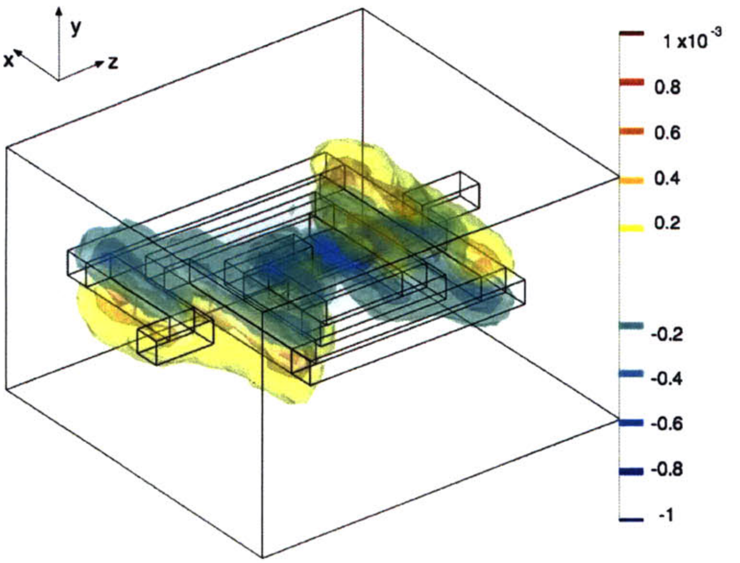
y
x
z
1 x10^{-3}
0.8
0.6
0.4
0.2
-0.2
-0.4
-0.6
-0.8
-1

Figure 3-8: Isoshells for B_z (in Tesla) for the square inductor, showing strong density above the inductor.

3.2 Models for Actual Device Fabrication

3.2.1 6.9mm Simulation

The geometry for the 6.9mm microslot is shown below in figure 3-9. The conductor thickness is 60μm, the width of the microstrip is 6.9mm, the length is 30.4mm, a is 0.9mm, b is 3.1mm (see figure 2-10), and the dielectric thickness is 3mm. The dielectric width is 29.2mm and the air height is 15mm. The script for creating the FEM is found in Appendix D. The results are shown as isoshells in figures 3-10 through 3-12 and qualitatively show the same behavior as those of the 1.5 mm simulation.

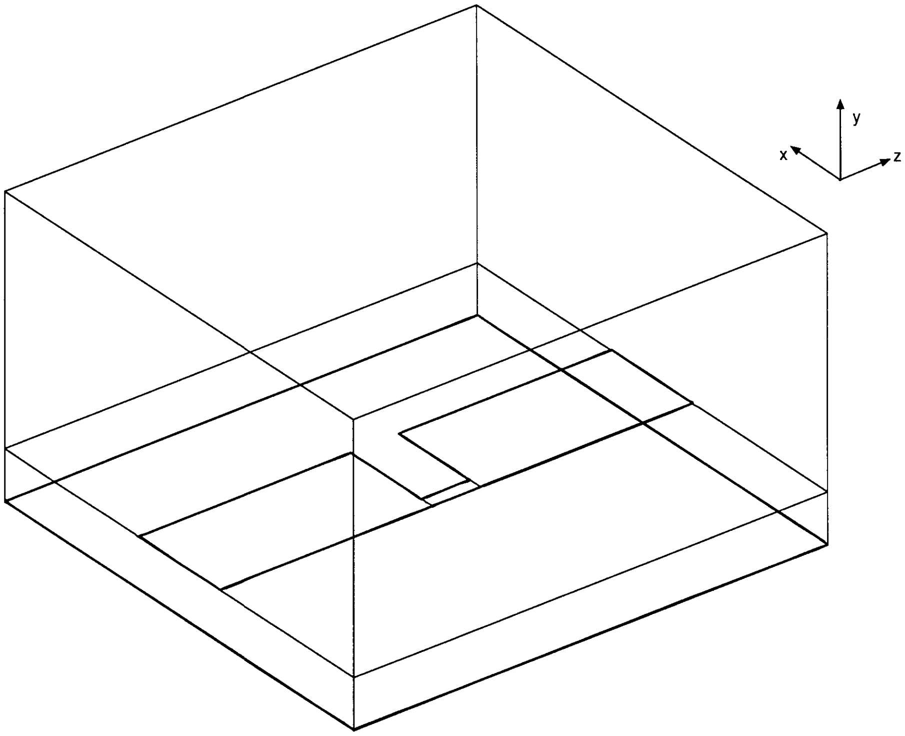

Figure 3-9: Microslot geometry used for the 6.9mm simulation.

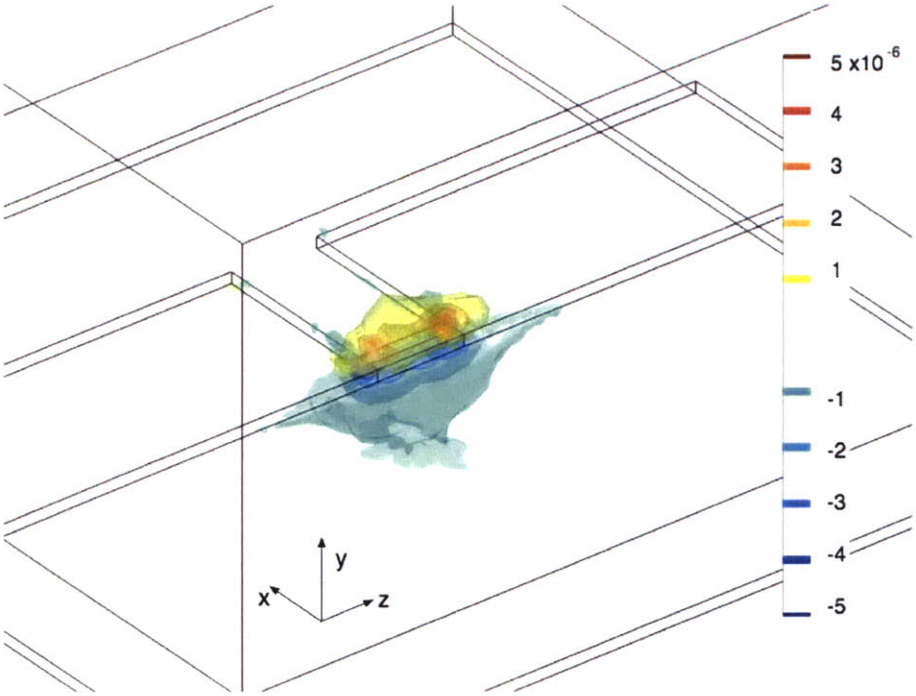

5 x10^{-6}
4
3
2
1
-1
-2
-3
-4
-5
y
x
z

Figure 3-10: Isoshells for B_x (in Tesla) for the 6.9mm microslot, showing flux density concentration around the microslot.

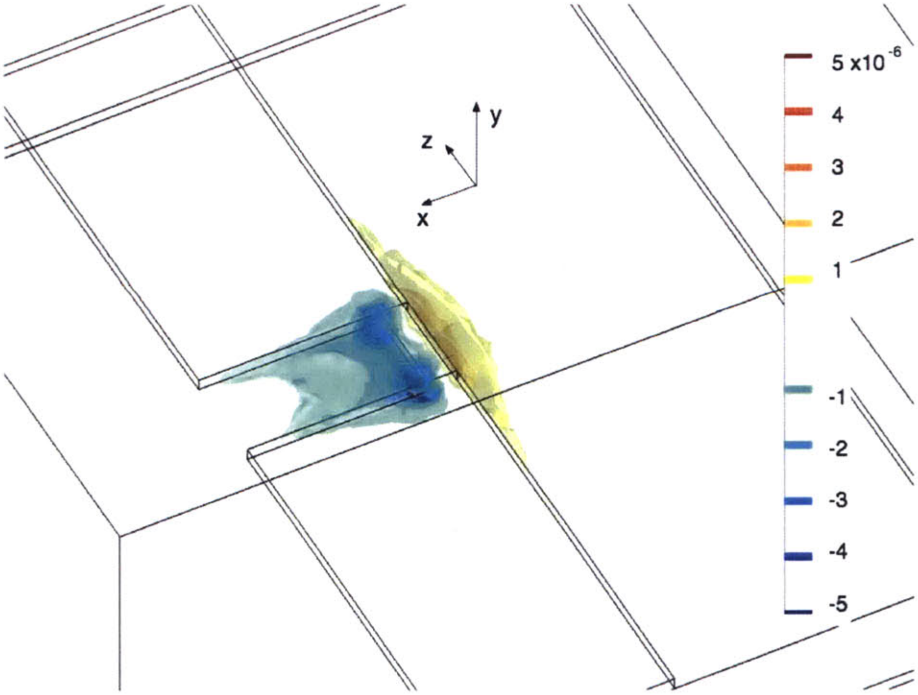

5 x10^{-6}
4
3
2
1
-1
-2
-3
-4
-5
y
z
x

Figure 3-11: Isoshells for B_y (in Tesla) for the 6.9mm microslot, showing flux density concentration on either side of the microslot.

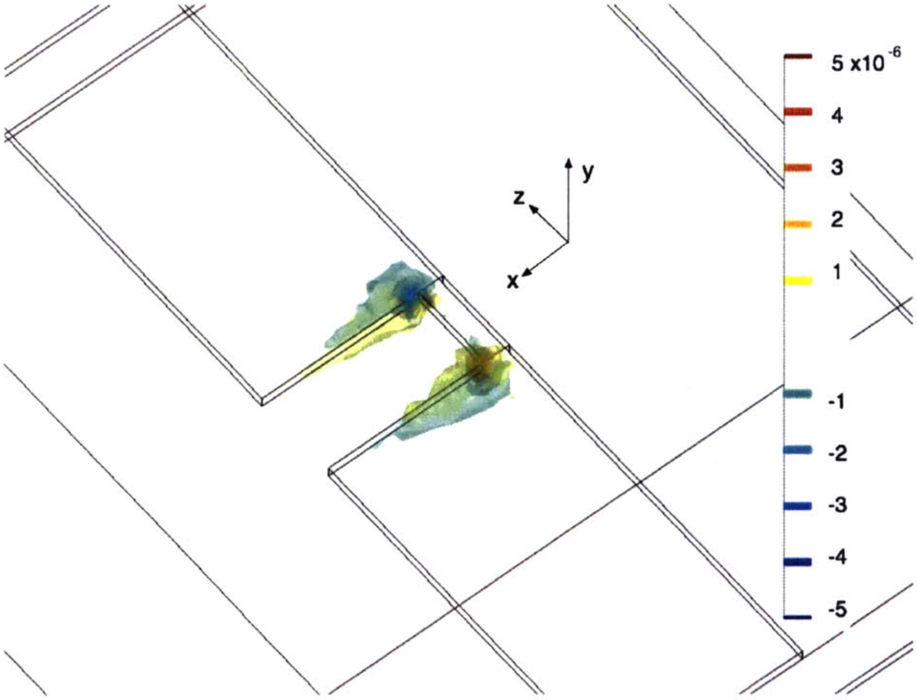

Figure 3-12: Isoshells for B_z (in Tesla) for the 6.9mm microslot, showing lower flux density concentration.

3.2.2 297μm Simulation

The geometry for the 297μm microslot is shown below in figure 3-13. The conductor thickness is 60μm, the width of the microstrip is 297μm, the length is 4mm, a is 197μm, b is 100μm (see figure 2-10), and the dielectric thickness is 3mm. The dielectric width is 10mm and the air height is 5mm. The script for creating the FEM is found in Appendix D. The results are shown as isoshells in figures 3-14 through 3-17 and qualitatively show the same behavior as those of the 1.5 mm simulation.

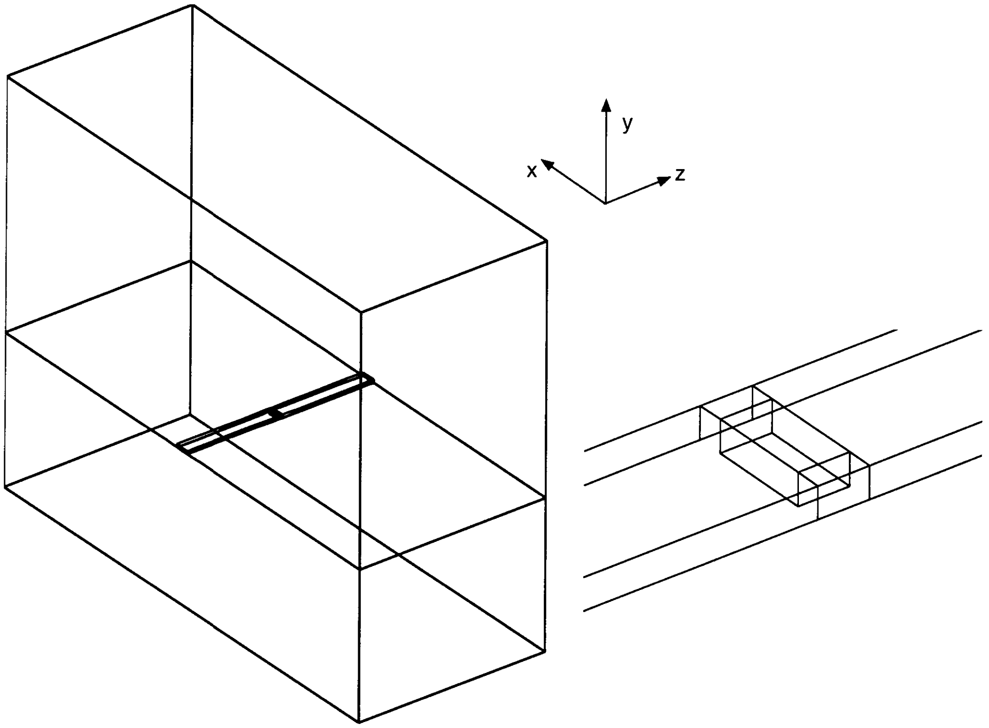

Figure 3-13: Geometry for actual fabrication of the 297 μm microslot.

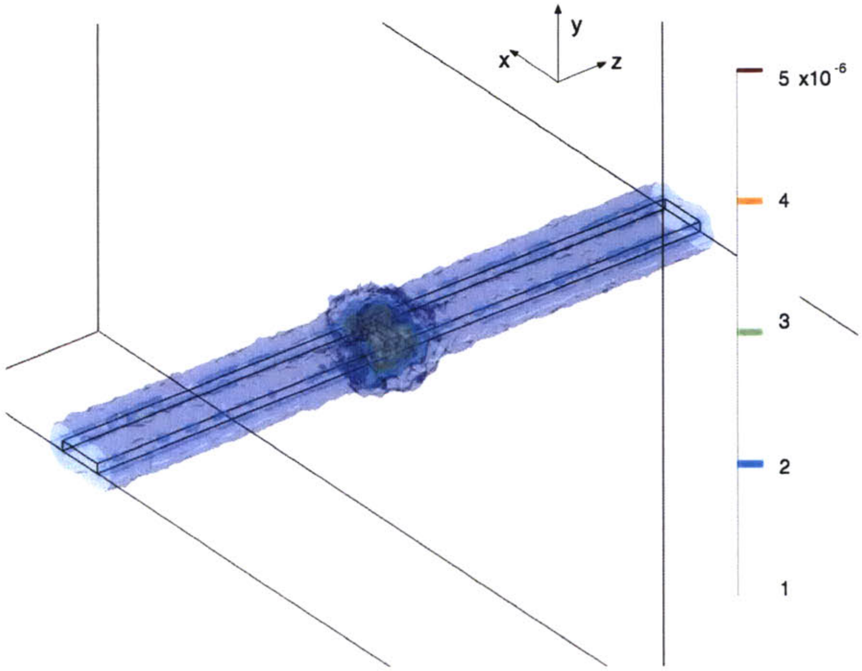
y
x
z
5 x10^{-6}
4
3
2
1

Figure 3-14: Isoshells of $|\vec{B}|$ (in Tesla), showing flux density concentration around the microslot.

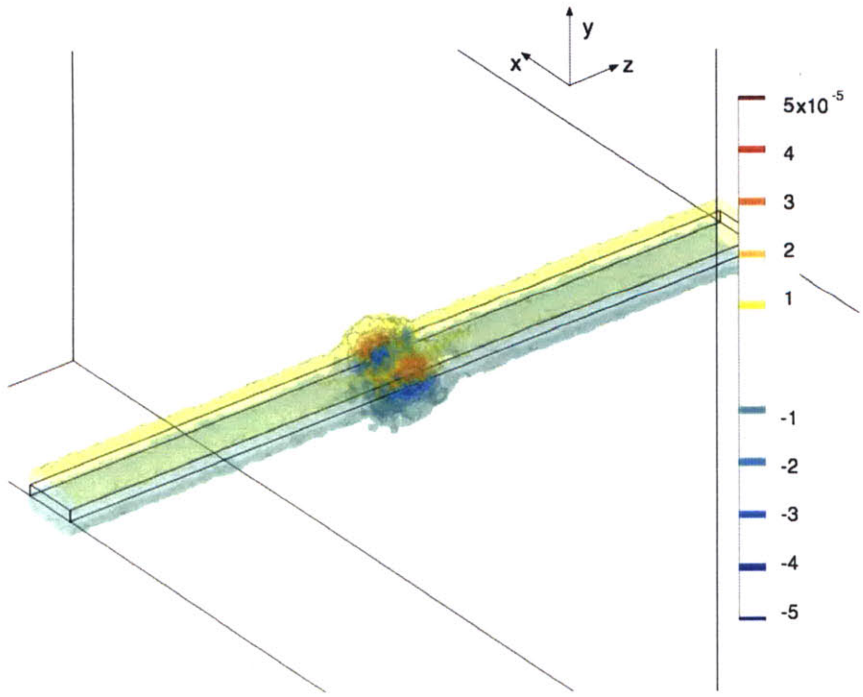
y
x
z
5x10^{-5}
4
3
2
1
-1
-2
-3
-4
-5

Figure 3-15: Isoshells of B_x (in Tesla), showing flux density concentration around the microslot.

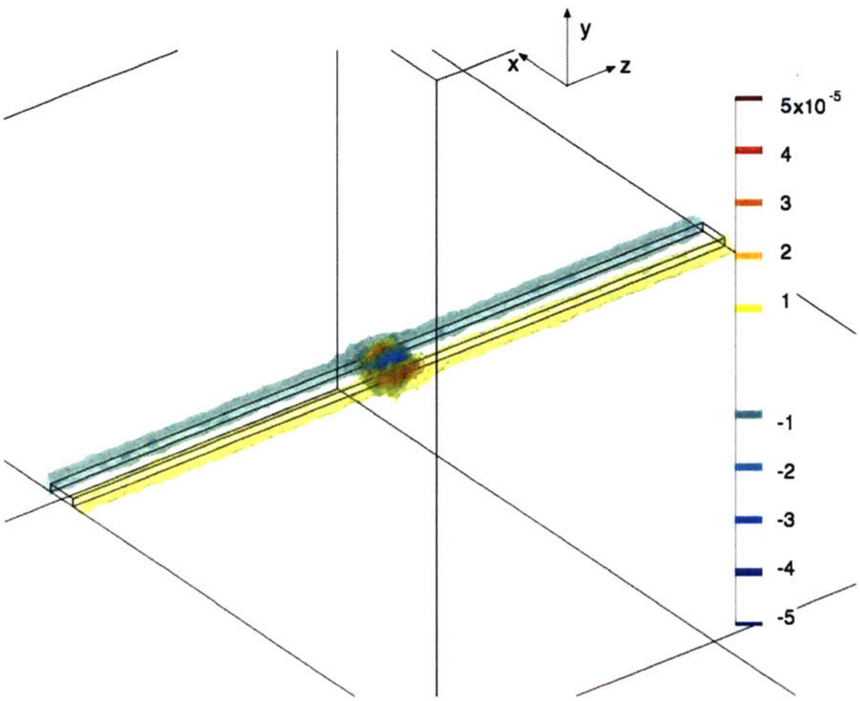
y
x
z
5x10^{-5}
4
3
2
1
-1
-2
-3
-4
-5

Figure 3-16: Isoshells of B_y (in Tesla), showing flux density concentration on either side of the microslot. Due to the current distribution, this field is mainly confined to the sides of the microstrip.

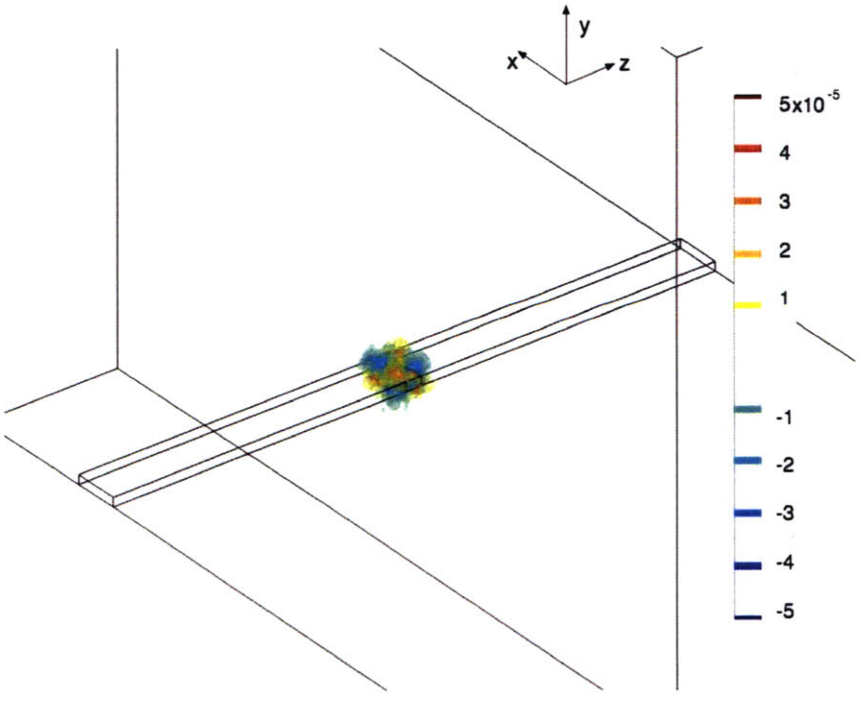
y
x
z
5x10^{-5}
4
3
2
1
-1
-2
-3
-4
-5

Figure 3-17: isoshells of B_z (in Tesla), showing very little flux density concentration in the direction of the static field (z).

3.3 RF Inhomogeneity

An important piece of model validation for a new probe is to calculate the RF inhomogeneity as seen by the spin sample. To keep the analysis of RF inhomogeneity straightforward, we will assume an ideal, isotropic sample within a volume V that is perfectly contained in free space. It is assumed there is no sample holder that could contribute permeability mismatch and further RF inhomogeneity. Let us further assume all active spins in a sample are pointing in the z-direction (i.e. we have I_z from a perfectly homogeneous B_0 field). After a pulse of time T, we will have the state:

$$I_z \rightarrow I_z \cos(\gamma|\vec{B}_{1xy}(\vec{x})|T) - \cos(\phi) I_y \sin(\gamma|\vec{B}_{1xy}(\vec{x})|T) + \sin(\phi) I_x \sin(\gamma|\vec{B}_{1xy}|(\vec{x})|T). \tag{3.1}$$

$\vec{B}_{1xy}(\vec{x})$ is the vector field of the RF field in the $x - y$ plane. ϕ is the angle defined by the ratio of B_{1x} and B_{1y} ($\phi = \arctan B_{1x}/B_{1y}$). We assume the impact on the z component of the RF field has no effect. We also assume that the phase of the RF field over distance is negligible in this size scale in which any dimension $\ll \lambda$.

Assuming a uniform density, the signal that is observed over the sample is

$$f(t) = \exp(-i\omega(\vec{x})t) \int_V \frac{1}{V} \exp(-i\phi) \sin(\gamma|\vec{B}_1(\vec{x})|T) d\vec{x}. \tag{3.2}$$

As a simple example, assume $\vec{B}_1(\vec{x}) = B_1 - \alpha|x|, -x_o \leq x \leq x_o$. If we also assume the static field is uniform over the sample, $f(t)$ is as follows:

$$\begin{aligned} f(t) &= \exp(-i\omega(\vec{x})t) \int_x \frac{1}{2x_o} \sin(\gamma|\vec{B}_1(\vec{x})|T) dx \\ &= \exp(-i\omega(\vec{x})t) \frac{c\beta c\alpha + s\alpha s\beta - c\beta}{\alpha}. \end{aligned} \tag{3.3}$$

In figure 3-18, this response is plotted. The ratio of the peak $3\pi/2$ peak to the $\pi/2$ peak is 0.9551 (the figure of merit). An alternate method for calculating the figure of merit is to fit an exponential function to this plot and set the amplitude to 1.0 at $t = \pi/2$. This is equivalent to taking the square root of the previous figure of merit (0.9773).

To parameterize the field strength and RF homogeneity, equation 3.2 was solved for two scenarios. The first is that in which a 4mm long cylinder that is 100μm in diameter is placed above the 297μm microslot and simulated at various heights above the surface, spanning from 0 to 210μm. The second scenario is that in which the length of the cylinder is changed from 100μm to 4mm at a fixed height from the surface to show the tradeoff between sensitivity and RF homogeneity. The data for each of these two cases was computed in about 6 hours on a 3 GHz P4 machine using Femlab 2.3. A nutation plot for each position was normalized to 1 to allow comparison of the B/i ratio.

See figure 3-19, which corresponds to the first case. Note that both the RF field strength and homogeneity

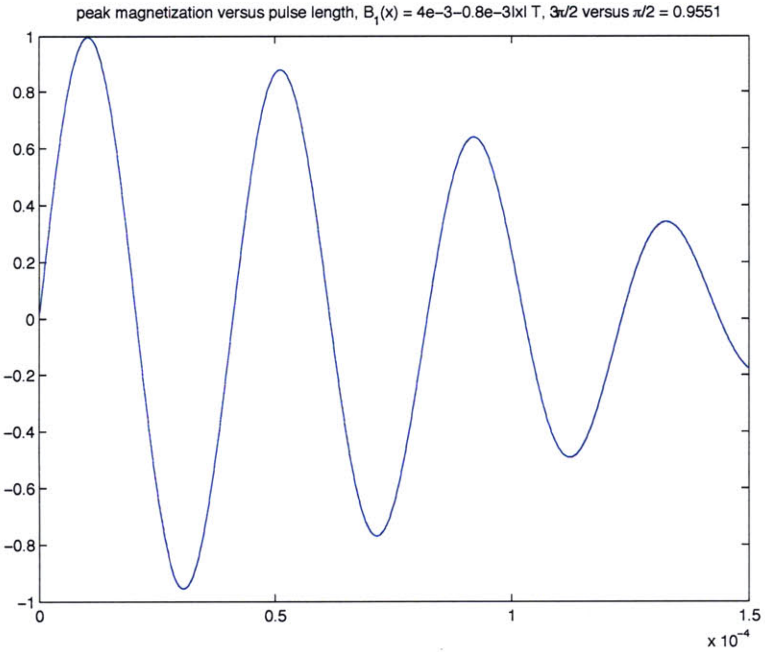
peak magnetization versus pulse length, $B_1(x) = 4e{-}3{-}0.8e{-}3|x|$ T, $3\pi/2$ versus $\pi/2 = 0.9551$

Figure 3-18: Simulation of RF homogeneity on the simple function $\vec{B}_1(\vec{x}) = B_1 - \alpha|x|$, for $-x_0 \leq x \leq x_0$. $B_1 = 4mT$, $\alpha = 0.8mT$, $x_0 = 1$ and $\pi/2 = 10.2\mu s$. A_{270}/A_{90} is 0.955.

improve as we move closer to the surface of the probe. This is because the nonuniform current distribution within the conductor makes the field lines more flat, resulting in higher homogeneity. As we move further away from the surface, the field lines approach a more ellipsoidal shape. It should be noted that the RF homogeneity may be quite different for different sample shapes.

Considering the second case in figures 3-22 to 3-23, it is apparent one can make a large sacrifice in RF homogeneity for sensitivity. This assumes no permeability mismatch in the slot itself. Figure 2-10 shows that the slot (b) type is not optimal for spin detection, but is better suited than (c) for the manufacturing technique developed in Chapter 4.

Let us look at the extremes of figure 3-22, shown in figure 3-24. We can see the RF homogeneity goes from $A_{270}/A_{90} = 0.91$ for the 4mm long sample to $A_{270}/A_{90} = 0.17$ for the 100μm sample, but the time to reach A_{90} is 6.25× faster than for the longer sample.

To calculate the RF homogeneity used in the analysis above, we used equation 3.2. In order to normalize the field generated by the current and take into account other effects, such as series resonance and polarization, some experimental constants were required. To calculate the series resonance gain, we first must factor the experimental current transmitted into the probe to be able to match the data. To do this, a calibration was made for the proton channel on an Inova 500 spectrometer and an HP 437B power meter (shown in figure 3-25). For tpwr set to 58, the power was measured to be 38.15 dBm. Converting from dBm to voltage, this power represents a peak voltage of 25.6 V and gives a peak-to-peak current across the whole structure of 0.511 A. For a parallel resonance, the gain in current across the inductor (i_L) for the circuit is:

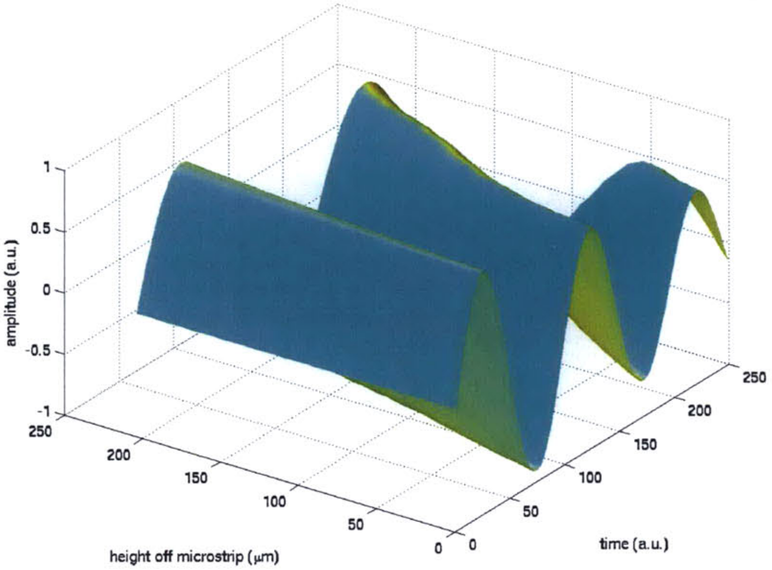

Figure 3-19: 1st view of the parameterization of the nutation plot as a function of cylinder height above the surface of the 297μm microslot. In contrast to a simple wire, the RF homogeneity and field strength both improve for the microslot as the cylinder approaches the surface.

$$\begin{aligned} i_{in} &= i_L + i_{C1} \\ i_L Z_L &= i_{C1} Z_{C1} \\ \Rightarrow i_L &= i_{in} \frac{Z_{C1}}{Z_L + Z_{C1}}. \end{aligned} \tag{3.4}$$

To calculate the impedances, we consult the network impedance measurements from Chapter 4. L = 11.45 nH, C_1 = 8.39 pF. The magnitude of the current gain is 18.61.The last effect to consider is polarization. The polarization generated by the inductor is linearly polarized, that is, its direction is fixed as

$$\mathbf{P} = (B_x \vec{x} + B_y \vec{y}) \cos \omega t. \tag{3.5}$$

Nuclear spins respond to circular polarization, so we must convert bases. The linear polarization can be represented as the sum of left and right circular polarizations:

$$\mathbf{P} = \frac{1}{2}|B|\{\cos{(\omega t + \phi_B)}\vec{x} + \sin{(\omega t + \phi_B)}\vec{y}\} + \frac{1}{2}|B|\{\cos{(\omega t + \phi_B)}\vec{x} - \sin{(\omega t + \phi_B)}\vec{y}\}. \tag{3.6}$$

Depending on the sign of γ, the spin Hamiltonian is either the first or second term of equation 3.6, but not both. Therefore, the field strength for the Hamiltonian is $\frac{1}{2}|B|$.

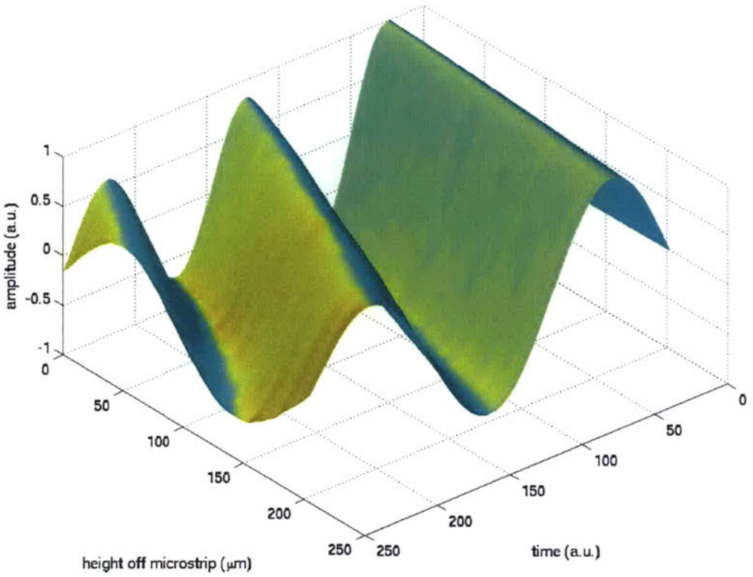

Figure 3-20: 2nd view of the parameterization of the nutation plot as a function of cylinder height above the surface of the 297 μm microslot. Raising the sample decreases the B/i ratio quite significantly.

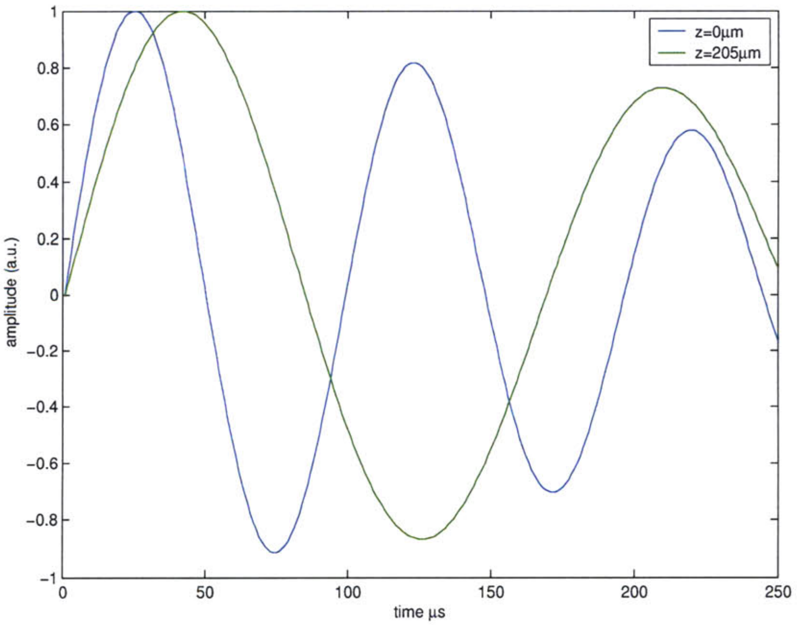

Figure 3-21: Nutation plots for the two extremes of height of the cylinder above the surface. Note that RF homogeneity and sensitivity both improve with the capillary tube closer to the surface.

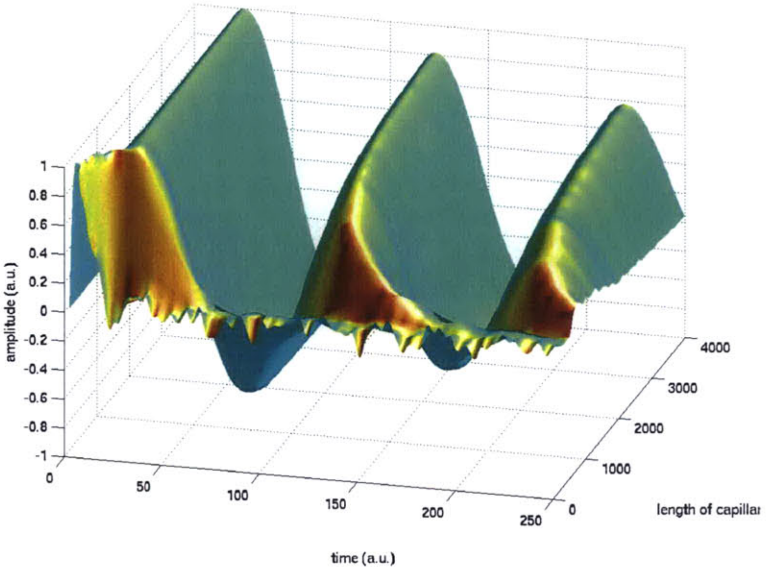

Figure 3-22: 1st view of the parameterization of the nutation plot as a function of length of a cylindrical sample above the 297 μm microslot. Sensitivity is compromised for RF homogeneity.

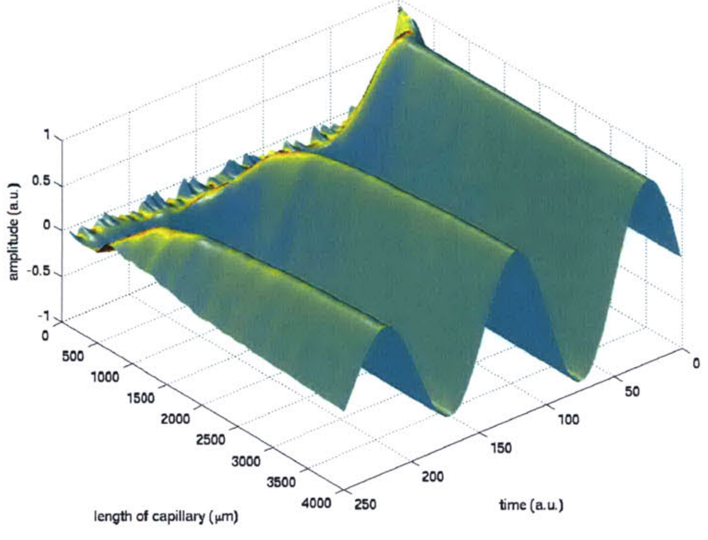

Figure 3-23: 2nd view of the parameterization of the nutation plot as a function of length of a cylindrical sample above the 297 μm microslot.

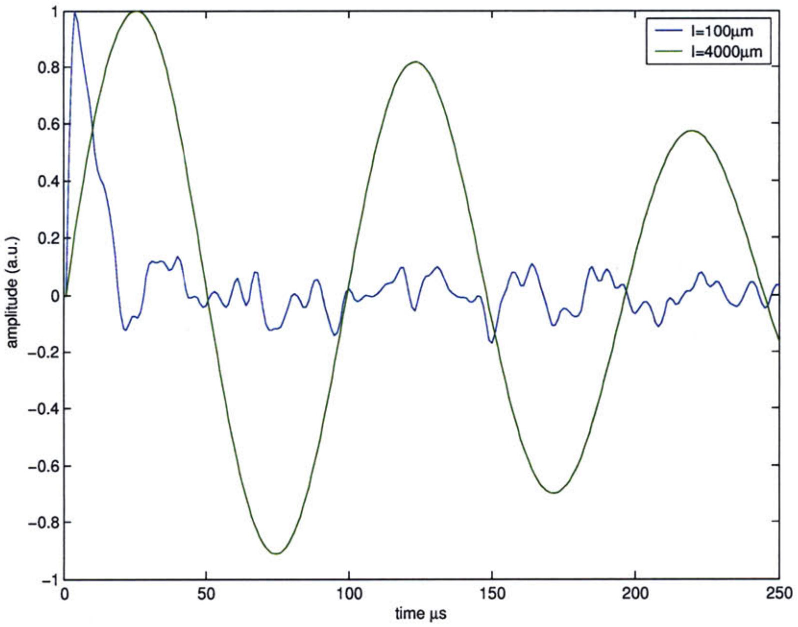

Figure 3-24: Nutation plots for the two extremes of the length of the cylinder. Note the large tradeoff in RF homogeneity for sensitivity for the type (b) slot (from figure 2-10).

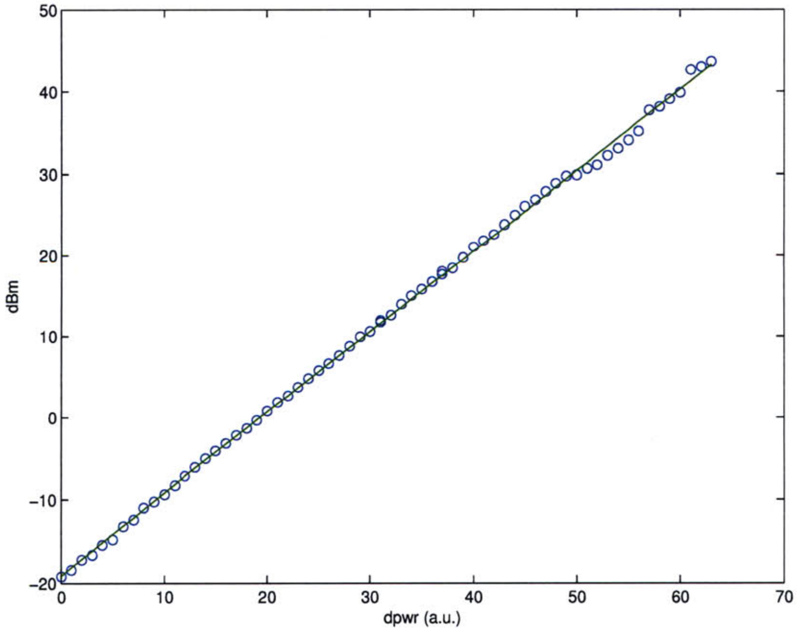

Figure 3-25: Power (dBm) versus tpwr setting for H^1 channel, slope=0.9913, offset=-19.15.

3.4 Modeling Observations

The most important observation about this modeling exercise above is that there are two effects to consider when scaling this geometry. The first is the skin effect, which restricts the current flow to a shell of the conductor. The second is the proximity effect, whereby current within a conductor will re-orient to minimize the loss of interacting with a field produced by the time-varying current itself. For this particular geometry, the proximity effect causes the current to bunch up at the edges of the conductor, though somewhat counter-intuitively improves the RF homogeneity.

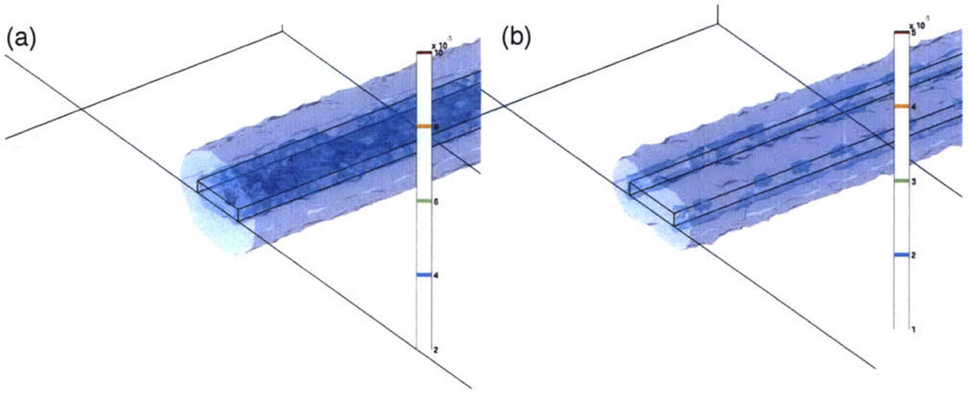

Figure 3-26: Comparison of the field produced as a function of frequency. With the skin effect aside, there are no wavelength-dependent effects for the microslot. However, there are frequency-dependent effects. (a) is a simulation of a microstrip at 60 Hz, while (b) is the same simulation at 500 MHz.

3.5 Geometry Scaling

As introduced in the last chapter, an analytical model cannot be obtained for the microslot, therefore scaling must be understood numerically. A plot of the scaling is shown in figure 3-27 from 60 μm to 1200 μm. This plot was made by parameterizing the microslot model and calculating the mean field of a volume above the microslot for the width range specified above (found in Appendix D).

It is also important to understand the physical properties that must be included in the model as a function of size. The possible phenomena to consider in scaling are skin depth, current distribution, spin noise, equipartition and shot noise, and ballistic transport. Skin depth, the current distribution and equipartition noise have already been discussed in the previous sections of this chapter. Spin noise is the effect seen when the transverse component of magnetization from N spins produces fluctuations proportional to $\sqrt{N}$. Stimulated emission in a resonant cavity enhances the normal spontaneous emission rate [78] by the factor

$$Qc^3/2\pi\nu^3 v_s, \tag{3.7}$$

where ν is the frequency of resonance, c is the speed of light, and v_s is the volume of the sample. However,

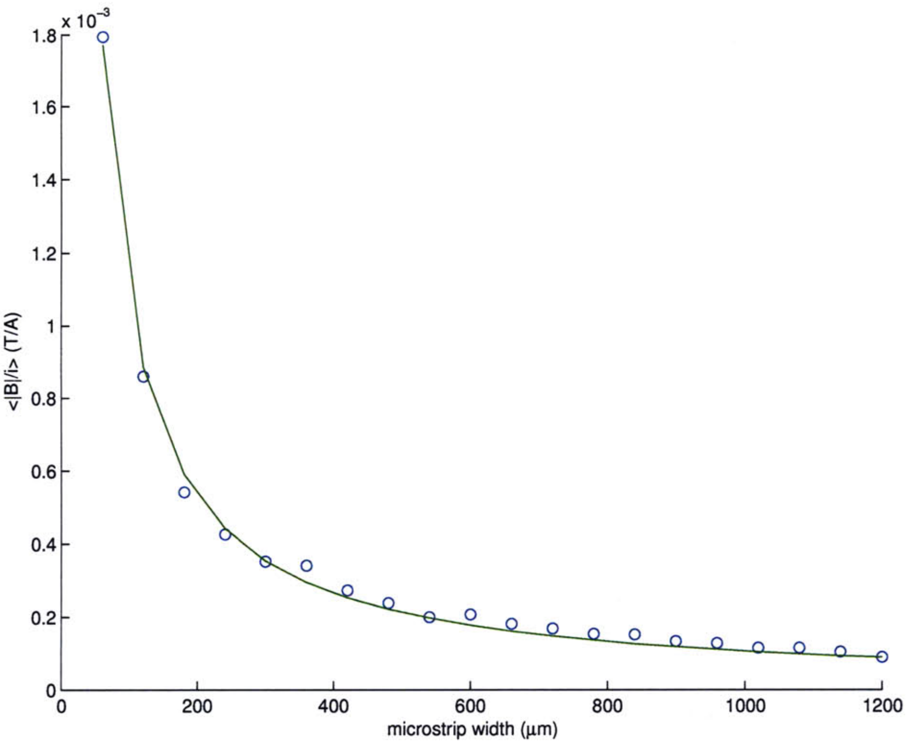

Figure 3-27: Plot showing 1/r dependence of $\langle|B|\rangle/i$ versus microslot width. Data is computed between 60μm and 1.2mm.

the total spontaneous emissive rate is [77]

$$2\pi NQ\hbar\gamma^2/v_s, \tag{3.8}$$

where γ is the gyromagnetic ratio. Given that the density N/v_s is constant, the spin noise in a mesoscopic sample is the same as in a macroscopic sample. As the sample continues to decrease, since the Q is decreasing, the spin noise contribution will become negligible.

Shot noise and ballistic transport are the dominant mechanisms that impact noise spectral density when shrinking a conductor. As conduction electrons develop a phase coherence, the noise characteristics of conductors are affected [1] [94]. Phase coherence happens when the conductor is smaller than the mean scattering length and electron transport can occur without collisions. The mean free path is

$$l_m = \frac{\sigma m \nu_F}{ne^2}, \tag{3.9}$$

where σ is the room temperature conductivity, m is the mass of the electron. ν_F is the Fermi velocity calculated as $\nu_F = \sqrt{\frac{2E_F}{m}}$, where E_F is the Fermi energy or the maximum energy occupied by an electron at 0K. $E_F = 0.7eV$ for copper, $n = 8.46 \times 10^{28}/m^3$ is the electron bulk density for copper, and e is the electric charge. Substituting into equation refmeanpath, we obtain a mean free path, $l_m \approx 40nm$. The behavior of electrons below this regime is active research [73] and is not considered in this thesis. Thus, shot noise need only be considered below the mean free path and therefore, at scales larger than 40nm at room temperature, the microslot can be understood using a completely classical model for bulk conductance. However, with feature sizes this small, Coulomb blockade effects (especially around microslot constrictions) could have adverse effects on this simplifying model [33]. It is also important to point out at this scale, the sensitivity of such small microslots (not sensitivity per unit volume) does not imply they will work properly for room temperature NMR.

Chapter 4

Physical Construction and Network Analysis

The next step in this thesis work was experimental verification. It was a design constraint (in the interest of time) to use an unmodified commercial NMR spectrometer to test the idea. Therefore, the two fabrication challenges required for the microslot were: 1) the fabrication of the microslot itself; 2) the probe housing for this custom probe (since empty probe housings are expensive and potentially difficult to modify for a microslot).

With the goal of rapid prototyping, rather than semiconductor processes and masks, traditional circuit board fabrication techniques and some new manufacturing techniques were employed. Empty probe housings are expensive and potentially difficult to modify for a microslot, so a custom one was designed and built.

4.1 Board fabrication

Given the difficulty of full three-dimensional mesoscale fabrication encountered in Chapter 2, the microslot poses fabrication advantages due to its planar structure. The essential design is no different than that of a traditional microwave circuit board. To maximize the quality factor of the microslot, the board substrate was made of Rogers 5880, a glass-reinforced Teflon substrate that has one of lowest tangent losses at RF frequencies (δ = 0.0004 at 1 GHz) [21]. The dielectric constant was 2.2 at 1 GHz and was approximated to be the same at 500 MHz. The substrate thickness was 3mm to minimize dielectric losses in the material. Two different copper thicknesses were tested, 1-ounce and 2-ounce roll laminates (30 and 60 μm respectively). Though it was more difficult to micromachine, the thicker copper was preferred because the larger conduction pathway for the current resulted in lower losses.

The main pattern for the circuit board was made with traditional fabrication tools, that is, conventional circuit design software (Orcad) and chemical etching by a board fabrication house (Cirexx). The PCB CAD drawing is shown in figure E-6, and a photograph of the board before component population is shown in figure 4-1. The layout is somewhat unconventional but was designed with the goals of 1) allowing all components on a single side of the circuit board, 2) making the path length to the variable capacitors as short as possible, and 3) keeping the capacitors away from the center, where magnetic field susceptibility is crucial.

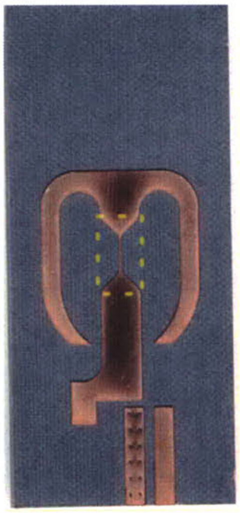

Figure 4-1: Final chemical etch of the probe circuit board showing the 300 μm wide macroscopic microslot (the microscopic microslot not yet fabricated). The back side of the board is full copper.

4.2 Micromachining

To fabricate the microscopic microslot, an excimer laser micromachining center from Resonetics was used. This machine uses mask projection of a 248 nm ultra-violet pulsed laser beam. Laser pulses on the order of 300 mJ per pulse can be projected down to a spot size of about 1-5 μm on a side. With a pulse firing rate of up to 200 pulses per second, this large energy per unit area, or fluence, is capable of creating a plasma out of many materials of interest, including metals. The profile of the beam generated by the KrF laser is a Gaussian box shape that is filtered by the mask and optical train to yield a uniform beam over the mask shape. One issue in creating a mask is that the plasma generation rate along a particular direction is influenced by the geometry itself. For example, since the structure was created along a thin piece of copper, the large thermal mass along the axial direction indicated the mask had to be slightly larger than calculated in that direction.

Through empirical experience, it was determined that the typical fluence required for metals is 10-40 J/cm^2. This means a high demagnification factor is required from the fluence (typically 100 mJ/cm^2) that comes directly from the laser. The common procedure for generating a mask is to chemically etch stainless steel shim stock at a size about 28× larger (demagnification factor) than the final structure.

With the machine running, there were three issues that made fabrication difficult. The first was the anisotropy of the mask relative to the final structure. A simple search process over masks yielded the optimal shape. The second issue, which was more difficult to work through, was that the plasma had a tendency to extend beyond the excited region and blow out the thin side. This phenomena is called plasma blowout. A great deal of time was spent optimizing fluence and pulse rate to minimize plasma blowout. The third issue was that the walls generated from the laser were not vertical, but sloped towards the center of the laser spot. This characteristic is a strong function of the thickness of the material and the material itself. Though it was not clear what impact it would have on the NMR data, the sloping was tolerated.

4.3 Polishing

After laser micromachining, there was a great deal of debris on the microslot probe boards that needed to be removed. Also, the original surface finish of the copper had surface features that could have caused problems to the B_0 homogeneity, especially considering the close proximity to the sample. An example of one of these surfaces is shown in figure 4-2. The process used for removing these extraneous features was mechanical abrasion. Stages of different micropolish solutions from Buehler were used. The surfaces were initially rinsed with distilled water and isopropanol. Then a Buehler 2 7/8" Texmet 1000 polishing disc was dabbed with Metadi 9 μm diamond paste and soaked with Metadi solution. To preserve the edges of the stripline, the wiping motion was confined to the axis of the microstrip. This motion was performed for about 2-5 minutes. The surface was washed in water and isopropanol and viewed under an optical microscope to observe the progress. This sequence was repeated several times until a consistent finish was seen. This overall process was then repeated with a 3 μm diamond paste followed by a 1 μm diamond paste. Since the grain size was now small compared to feature size, polishing was done in a circular manner to obtain an isotropic finish.

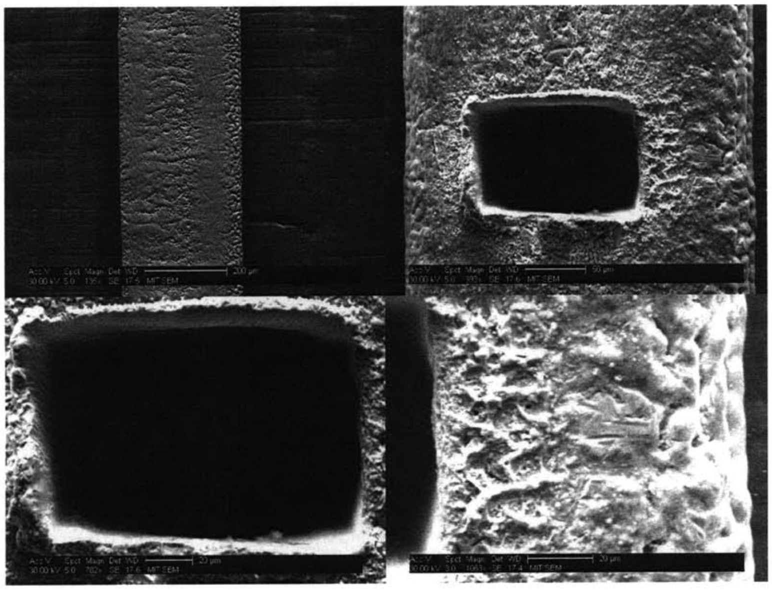

Figure 4-2: This is an example of microslot immediately after micromachining. One can see debris produced by the excimer laser and surface features from the original electroplating/rolling and chemical etching.

The final polish was a sub-micron colloidal silica (SiO_2) solution. A felt-based Microcloth polishing disc was used with distilled water as the solution, and this process was applied 2-3 times (with optical microscope viewing) for about 5-10 minutes each. A progression of the entire mechanical abrasion process is shown in figure 4-3.

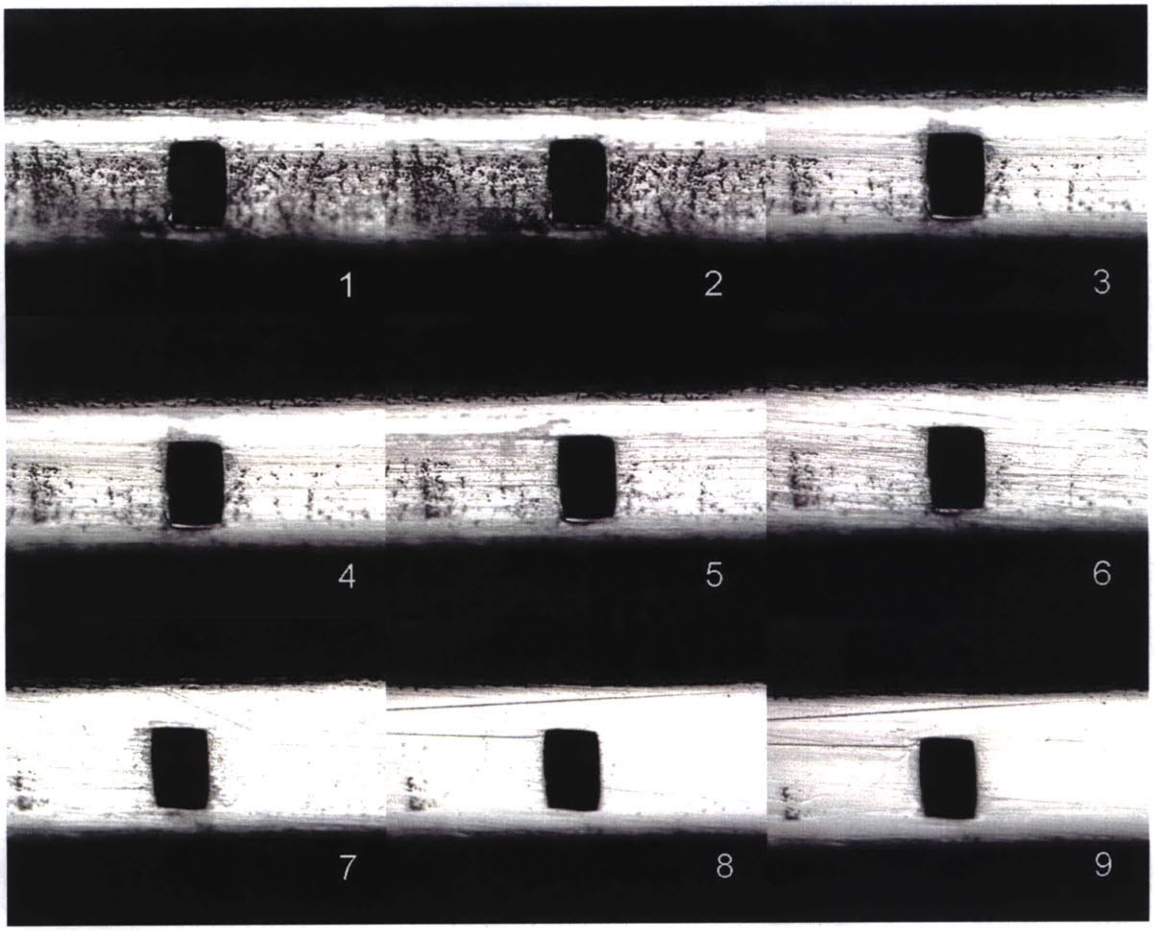

Figure 4-3: Example progression from an original unpolished microslot (1) to the final finished state (9).

4.4 Probe Construction

The probe is composed of three major parts in a single, rigid unit: 1) the base at the bottom of the superconducting magnet, which connects to the NMR spectrometer console; 2) the inductive resonator, which in this case is the microslot board that is situated in the middle of the magnet; and 3) the thin, metal tubing and inner mechanical/electrical connections that connect the base to the microslot board. The most important factor to consider in probe construction is mitigation of magnetic materials. Brass alloys, copper beryllium and certain aluminum alloys are all permissable. The tube and all major pieces were made of 6061-T6 aluminum (1% Mg, 0.6% Si, 0.3% Cu, 0.3% Cr, up to 0.7% Fe) as outlined in [26]. This is a common aluminum alloy that is suitable for thin cylinders and support structures because the iron is usually in a nonmagnetic phase ($FeAl_3$ or Fe_2Al_7). Standoffs (for mechanical fixturing) were made of an unknown alloy of aluminum from McMaster-Carr, but were kept at least 5cm from the sample. Nonmagnetic screws were made of a brass alloy, guaranteed to be nonmagnetic to 1 part in 400 million, made by Voltronics Corporation. The solder used for the 6.9mm board was 96% Sn, 4% Ag from Merway, Inc. For the 297 μm board, 96%Sn-3.5%Ag nonmagnetic solder (part no. 89875), from Doty Scientific was used. For the 6.9mm probe, the board inserts/guides were made of fluoropolymer FEP (Fluorinated Ethylene-Propylene). For the 297 μm microprobe, these were made of Virgin Electrical Grade Teflon, since with a Rockwell hardness of RR55-58 versus RR25 for FEP, it was much easier to machine without mechanical deformation and achieve high tolerances.

The following is a description of the construction process for the probe, inspired by the design of a traditional probe made by Nalorac. The base piece was made from a single piece of aluminum. A billet was cut using a gravity-fed saw and then trimmed down and polished on an Alpha 330S CNC lathe. The main cavity and trim cuts were cut on a Haas CNC mill, as were all the holes. The bottom holes (0.1" deep) were cut using a #40 drill deep and then threaded for a 2-56 screw. The base cover was cut on an Omax water jet cutter from 1/4" thick aluminum plate. The holes were marked using the water jet cutter and then cut using a drill press. Both faces were finished and trimmed down on the lathe. A picture of the final base pieces is shown in figure 4-4. The main tube was taken from 1.5" aluminum tubing and cut to the required length using the gravity-fed saw. The tube was mounted in the lathe and the ends were cut flat. While spinning the tube at a low speed, a scrubbing mat was used to polish the surface. Using a protractor made on a laser cutter, three holes near the bottom of the tube were marked and then drilled using a countersink for a 1/8" 2-56 screw. The cleaning procedure for all machined parts was a wash in soap water, rinse in deionized water and isopropanol, a spray clean with pressurized air, and an air dry. Mechanical drawings are in Appendix D for reference.

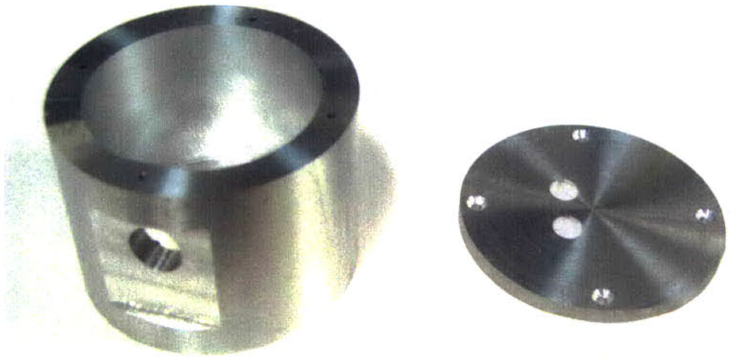

Figure 4-4: Photograph of the base of the probe. A CAD drawing of these pieces can be found in figure E-1. The width is 2.5" and the height is 1.74". The thickness of the base plate is 0.25".

4.5 Probe Assembly

A 20" piece of copper beryllium semi-rigid coaxial cable was cut (RG-58 coaxial from Haverhill Cable, P.O. Box 8222 Haverhill, MA). This cable was used for carrying the NMR signal to the base, as well as providing mechanical support. To produce a good, clean edge, the outer copper part was scored with a sharp hobby knife. Using needle nose pliers, this score was broken and the excess copper removed. Using the same knife, an edge was cut into the Teflon core until the knife just touched the inner conductor. The cable was rotated 90 degrees and a second edge was cut. This was repeated 2 more times and then the Teflon core was removed. This ensured that there were no scores on the copper conductor, which could have caused loss and reflections. The coaxial cable was mounted with a bulkhead jack from AMP (Part Number 1331693-1). This is a nonmagnetic, gold-plated copper beryllium center conductor BNC connector with a silver-plated brass shell. The cable was soldered to the connector as shown in figure 4-5. This cable assembly was then mounted inside the base with the cable extending through the top. Three 16.5" coaxial segments were cut without exposing any extra dielectric or center conductor. These pieces act as ground and mechanical support for the structure. 5 support circuit boards (see figure E-3) were constructed to support the coaxial structure and to make a horizontal structure on which to mount the probe circuit board. These were made from double-sided 1-ounce copper laminate FR4. Since the support circuit boards were only cutouts, requiring no patterning of the surface, they were made on a table-top milling machine. A Roland MDX-20 with a 30 mil tool was used. The boards were sanded with fine grit alumina paper to remove any residual tool chips and then cleaned using the process outlined above.

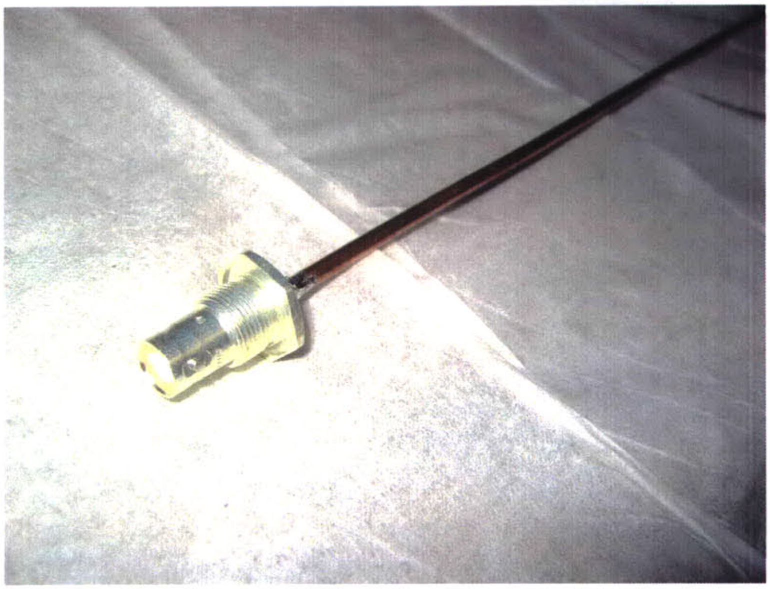

Figure 4-5: Photograph of the nonmagnetic bulkhead BNC jack soldered to nonmagnetic semirigid coaxial cable. This cable carries the signal from the spectrometer console to the probe in the center of the magnet and also carries the NMR signal from the sample back to the console. The end of the jack is 0.437" in diameter.

Using a #40 drill, a hole was cut 6.6 mm up on one side of a 4-40 round aluminum standoff. Then a 2-56 threading tool was used to thread the hole. Three standoffs of this kind were made and attached to the top of the base with nonmagnetic screws. A support board was placed on top of the standoffs and soldered to the 4 pieces of coaxial cable. Care was taken to make sure the bottom of each piece of coaxial cable was flush with the base, as shown in figure 4-6. Due to the large pieces of thermally conductive copper on the base, a clean, flat-tipped soldering iron was used to heat the cable first to obtain good solder joints. With all four cables soldered both on the top and the bottom of the support board to ensure proper ground conductivity, the board was screwed down on top of the base standoffs. Using a laser cutter, a 98.1 mm spacer was made to ensure each subsequently soldered board was horizontal. To ensure the overall structure was mechanically stable, tight tolerances were required on the support boards relative to the inner diameter of the aluminum tubing. (If the support boards had not been very close to horizontal, the resulting tilt would not have allowed the tube to slide over the assembly). The remaining 4 boards were soldered in this fashion, as shown in figure 4-7.

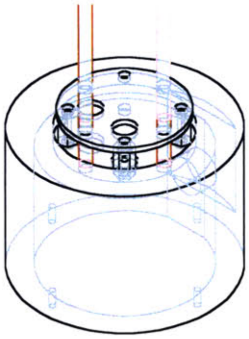

Figure 4-6: CAD drawing of the probe base assembly with the first PCB cutout and semi-rigid coaxial cables.

Since the probe circuit board was connected to the middle of the probe structure by a coaxial cable, this cable was bent into the middle and through the last cutout as seen in figure 4-8.

Nonmetallic support pieces were required to mount the microslot probe board. Two fluorinated polymer (FEP for the 6.9 mm probe and Teflon for the 297 μm probe) pieces were cut from a 1.5" diameter stock on a lathe. For each, the face was finished and then the center cavity was cut using a 1" end mill mounted on the lathe. (For the 6.9mm probe, one of the pieces was cut with a 7/32" drill bit to allow the 5mm tube to pass through). Using the same drill, a small indent was cut out of the second piece in order to center the sample tube. The diameter of the cylinder was trimmed down to 1.435" and then cut from the stock using a cutoff tool. The cut pieces were separately mounted in the Haas Mill and holes and slots were cut according to the CAD drawings in Appendix B. Excess material was trimmed using a hobby knife and then cleaned using the standard process. The bottom fluorinated polymer piece was mounted to the top support circuit board using three 2-56 aluminum round standoffs and nonmagnetic 2-56 1/4" screws. The microslot probe circuit board was placed in the FEP/Teflon insert and the coaxial cable was trimmed down and repositioned to be soldered to the board. The next step was to mount the microslot circuit board to the FEP/Teflon pieces. Since

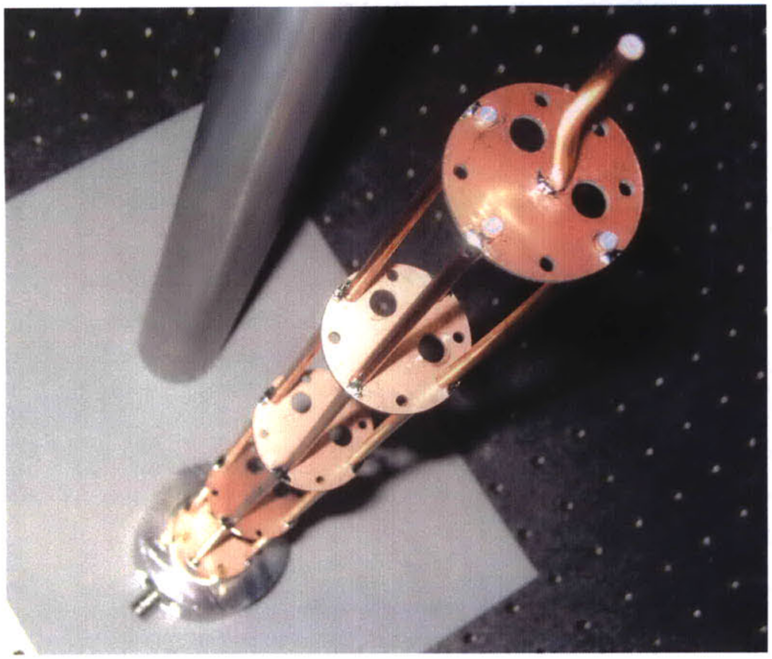

Figure 4-7: Photograph showing the assembled stacked cutout structure soldered to the semi-rigid coaxial cable and attached to the base. Each copper cutout is 1.435" in diameter.

the microslot circuit board substrate is itself made of Teflon, it was difficult to glue to the inserts. Therefore the surfaces were abraded using very fine sandpaper, sprayed clean with compressed air and then glued with Permabond 910 general purpose adhesive. The final result shown in figure 4-8. The last step in building the

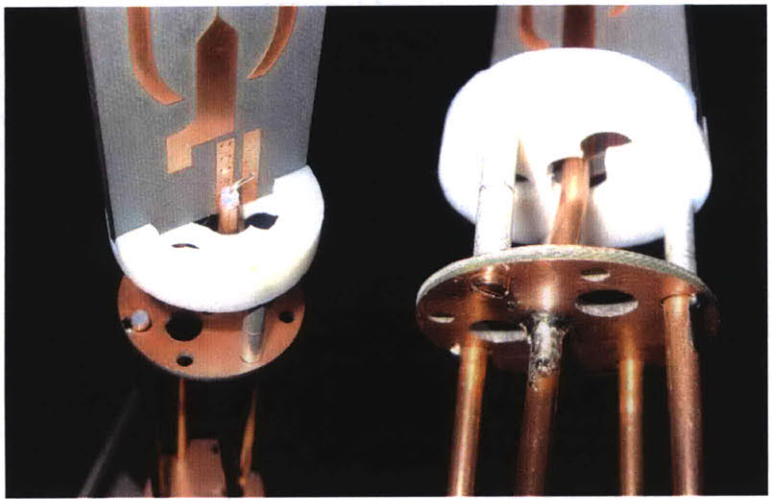

Figure 4-8: Two views of the unpopulated probe circuit board mounted in the 297 μm probe. The copper cutout is 1.435" in diameter.

probe was to make tuning rods to adjust the capacitors on the microslot board. Ceramic tuning sticks were extracted from a pair of screwdrivers from Voltronics. By using diagonal cutters, the plastic was stripped and the ceramic tuning tools removed and cleaned. 0.25" acrylic rods were scored with a hobby knife and cut to lengths of 20". The rods were drilled 0.2" deep with a #40 drill on one end and a 0.125" drill on the other end. They were cleaned and dried. Using Permabond 910 adhesive, a ceramic tuning stick was glued into one side of an acrylic rod and a brass knurled knob was glued into the other end of the acrylic rod. The same process was repeated with the second acrylic rod. To affix the rods within the probe, the holes in the support boards were designed so as to not perfectly align to allow friction to hold them in place. Also, snap-on pieces of acrylic were cut out of a 1/16" acrylic sheet on a laser cutter and press-fitted onto the acrylic tubes once they were mounted. The tuning sticks were passed through the base plate and up through the probe and positioned to allow adjustment of both tuning capacitors. The base plate was screwed to the base using nonmagnetic, 2-56 flat head screws. The tube housing was passed over the structure and screwed with 3 nonmagnetic 1/8" 2-56 screws at the bottom, thus completing the probe. A final shot of the probe, fully assembled, is shown in figure 4-9.

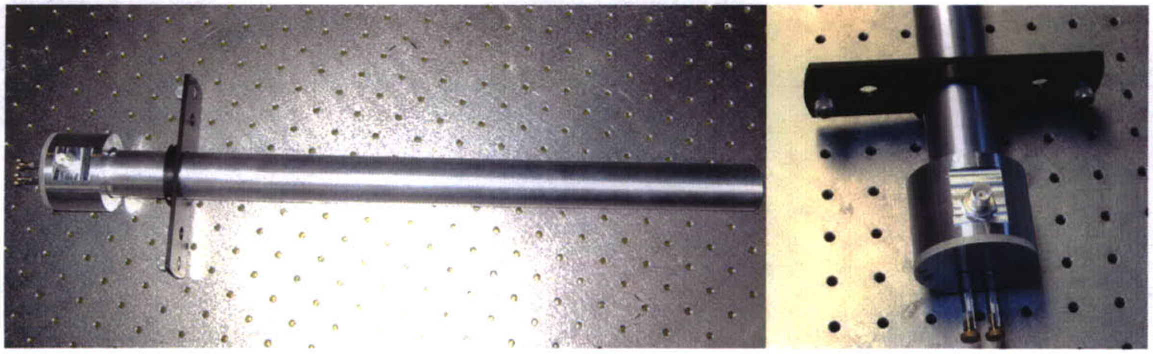

Figure 4-9: The final probe. The total length, not including acrylic rods is 22.5".

4.6 Sample Preparation

For the 5mm NMR sample tube experiment, a 10% H_2O in 90% D_2O solution was sealed with paraffin wax in a standard 5mm Wilmad tube. The sample was placed through the top FEP insert until it stopped at the second FEP insert.

For the 297 μm probe, 100% deionized H_2O was used in microcapillary tubing from PolyMicro. This 100 μm inner diameter (ID), 165 μm outer diameter (OD) tubing was coated with a thin layer of polyimide and arrived in a 1m long spool. It was then cut to a length of approximately 6mm by passing a hobby knife very lightly over the surface of the capillary. Then, both ends of the tube were held under tension and pulled apart. This achieved a very clean cut on both ends. The capillary was taped down with Kapton tape to a flat surface and run under a high pressure stream of tap water in order remove all debris from the inside. Using a spray bottle full of deionized water, the capillary was rinsed with high velocity water to force the tap water out. The capillary was then sprayed with compressed air and allowed to dry, while monitoring the drying process under a microscope. Once dry, a small drop of deionized water was placed on one end of the tube and immediately sucked in via capillary forces. With the sample inside the capillary, the ends were sealed with a tacky wax from McMaster-Carr (part number 1129K14) to prevent rapid evaporation. The wax preparation process was to dip the ends of the capillary in the wax and then wipe away any excess with isopropanol. See figure 4-10 for an image of a capillary with sample and wax plug.

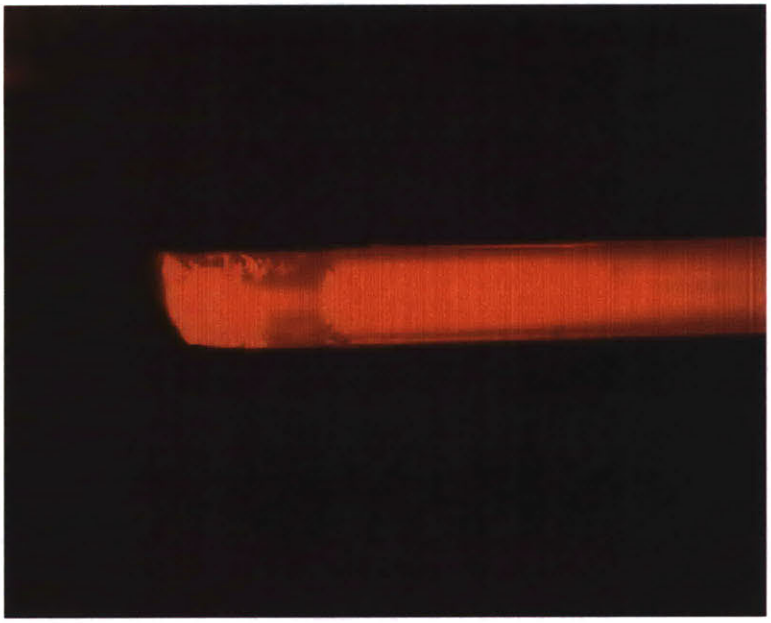

Figure 4-10: Microcapillary viewed under a microscope with a contrasting reflector. The outer diameter is 165 μm and in the inner diameter is 100μm. Note the meniscus of the deionized water. The end is sealed with a wax plug.

4.7 Network Analysis

As was discussed in Chapter 3, it was very important to understand the current gain in the microslot circuit to enable the modeling. A model and measurements of the network graph of the circuit were required. In general, the non-idealities of passive reactive components must be considered for an accurate model. A simple model for inductors and capacitors at high frequencies is shown in figure 4-11.

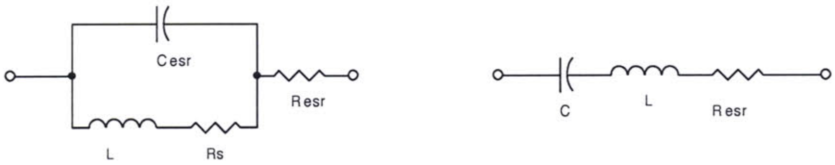

Figure 4-11: Models of inductor (a) and capacitor (b) at RF frequencies.

A microstripline can be modeled more as an inductor than a capacitor:

$$Z_0 = \sqrt{\frac{L}{C}}. \tag{4.1}$$

Since Z_0 is higher than 50Ω for a thin stripline, for $L \approx 10nH$, $C < 4pF$. For the inductor on the left in figure 4-11, the capacitor C_{esr} comes from inter-turn capacitance from coil windings, which results in self-resonance of the structure. While not measured, this self-resonance should be approximately 10 GHz, hence $C_{\text{esr}} \approx$ 10fF and can be ignored at 500 MHz. In this case, we can combine R_s, the resistance due to the finite conductivity of the inductor, and R_{esr}, the contact resistance of the inductor. The capacitor model on the right includes a self-resonant inductor and contact resistance that are generated from the leads of the package. The same argument of self-resonance at 500 MHz can be made for the capacitors, which typically are self-resonant at about 8 GHz, such that the inductor $L \approx$ 1nH can be removed from the model. The final model for the system is shown in figure 4-12.

The capacitors used for this system were air-core, variable NMAJ15HV from Voltronics and 100B series porcelain capacitors from American Technical Ceramics. The R_{esr} parameters were obtained from data sheets. To find the inductance and its series resistance, a fixed capacitor was used as the resonating impedance. Network plots, shown in figures 4-13 through 4-16, were generated from a Agilent 8753 Network Analyzer after the probe was matched to $Z = 50 + i0\ \Omega$. From the quality factor of the probe at the resonant frequency, three simultaneous nonlinear equations were solved to yield L, r_s and C_2. The first two are straightforward:

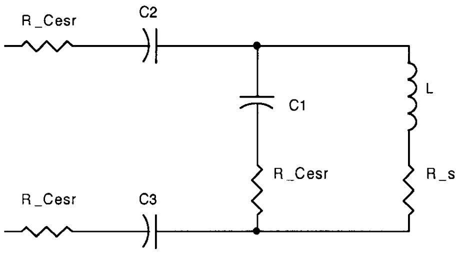

Figure 4-12: Reduced network model of the probe.

$$\begin{aligned}
\text{Re}(Z) = {} & \frac{(1-\omega_0^2 C_1 L)(r_s+\omega_0^2 C_1 R_{C1} L)+\omega_0^2 C_1 (R_{C1}+r_s)(C_1 R_{C1} r_s + L)}{(1-\omega_0^2 C_1 L)^2+\omega_0^2 C_1^2 (R_{C1}+r_s)^2} \\
& +R_{C3} + R_{C3} = 50\,\Omega, \\
\text{Im}(Z) = {} & \frac{\omega_0 (C_1 R_{C1} r_s + L)(1-\omega_0^2 C_1 L) - \omega_0 C1 (R_{C1}+r_s)(r_s+\omega_0^2 C_1 R_{C1} L)}{(1-\omega_0^2 C_1 L)^2+\omega_0^2 C_1^2 (R_{C1}+r_s)^2} \\
& -\frac{1}{\omega_0 C2} - \frac{1}{\omega_0 C3} = 0\,\Omega.
\end{aligned} \tag{4.2}$$

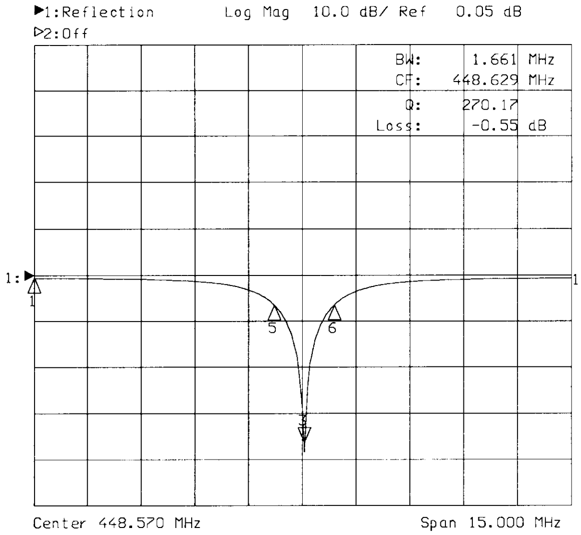

Figure 4-13: Log magnitude of S_{11} for the 6.9mm probe at 448 MHz, with a fixed capacitance for C_1 to find the inductance and resistance of the structure.

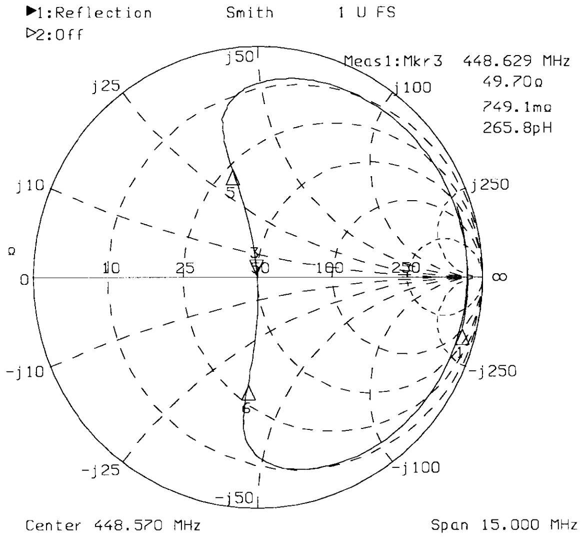

Figure 4-14: Smithchart for the 6.9mm probe at 448 MHz, showing the the network is matched to 50 Ω.

The last equation is more difficult:

$$\begin{aligned}
Q &= \frac{f_0}{\Delta f} \\
\Delta f &= f_2 - f_1 \text{ where } \exists\ (f_2, f_1) \text{ such that } L(f) = 1/2 \\
L(f) &= |R(f)|, \\
\text{where } R(f) &= \frac{Z(f) - R_{in}}{Z(f) + R_{in}} \text{ and } R_{in} = 50\ \Omega.
\end{aligned} \tag{4.3}$$

By measuring the quality factor Q, the parameters r_s and L could be solved at 500 MHz. From this, the

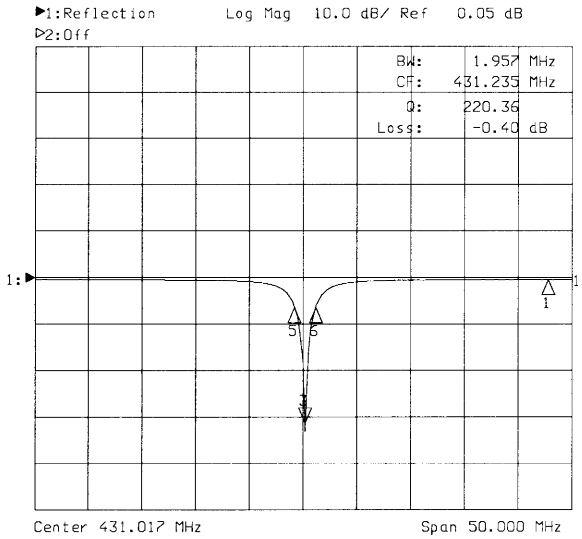

Figure 4-15: Log magnitude of S_{11} for the 297μm probe at 431 MHz, with a fixed capacitance for C_1 to find the inductance and resistance of the structure.

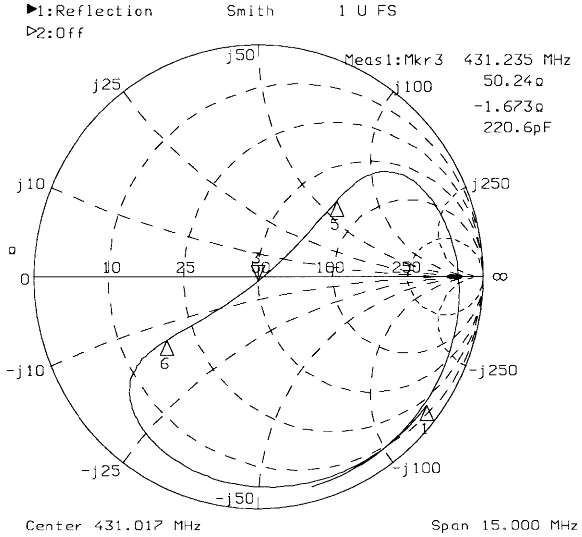

Figure 4-16: Smith chart for the 297μm probe at 431 MHz, showing that the network is matched to 50 Ω.

capacitors to match the probe at 500 MHz could also be calculated. The simulation of S_{11} and the corresponding Smith chart at 500 MHz is shown in figure 4-17 based on these results, and a table of values measured and calculated for the probe are found in table 4-1. With the estimated parameters, variable capacitors in the range of the calculated values were utilized and the probe was matched to 50 Ω. Figures 4-18 and 4-19 show S_{11} and the Smith chart respectively for the 6.9 mm probe, while figures 4-20 and 4-21 show the results for the 297μm probe. With the probes built and matched at 500 MHz, we were now able to use them for NMR measurements.

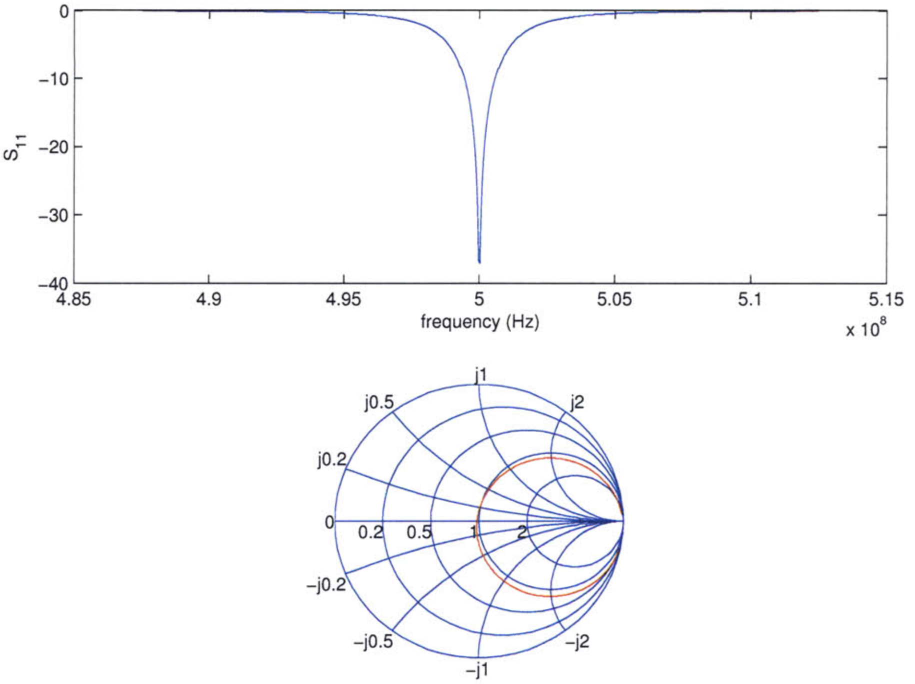

Figure 4-17: Simulation of the 297μm probe network using measured and derived values at 500 MHz.

Probe size	Fixed capacitance (pF)	L (μH)	r_s,Q at 500 MHz	r_s,Q at ν MHz
297 μm	4.7	26.5	0.24, 256	0.22, 220, 431
6.9 mm	3.9	29.5	0.26, 285	0.21, 270, 448

Table 4.1: Measured properties of the circuit in figure 4-12 for the 297μm and 6.9mm probe needed to calculate the capacitors required at 500 MHz.

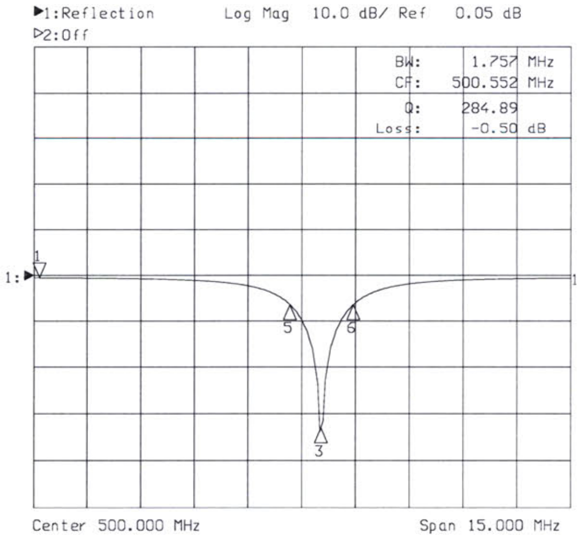

Figure 4-18: Log magnitude of S_{11} for the 6.9mm probe at 500 MHz (using the calculated impedances), showing strong absorption.

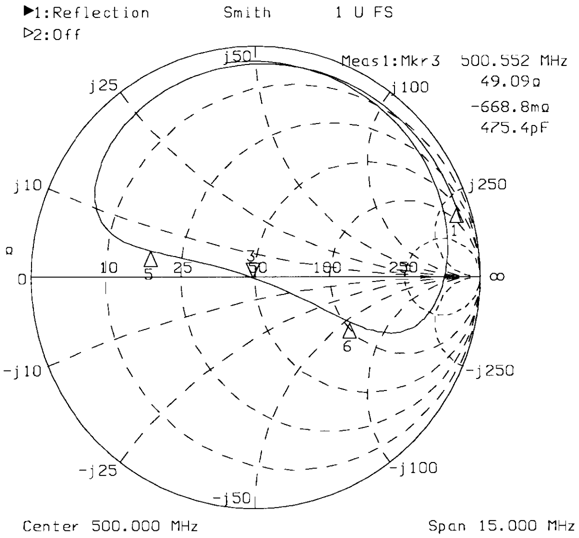

Figure 4-19: Smith chart for the 6.9mm probe at 500 MHz, showing the network is matched to 50 Ω.

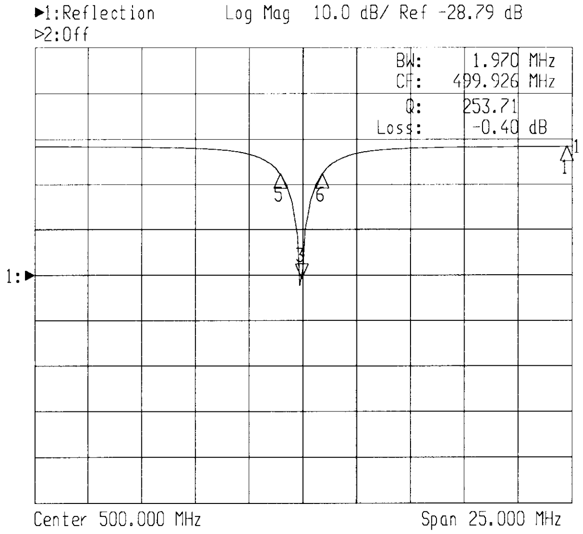

Figure 4-20: Log magnitudeof S_{11} for the 297μm probe at 500 MHz (using the calculated impedances), showing strong absorption.

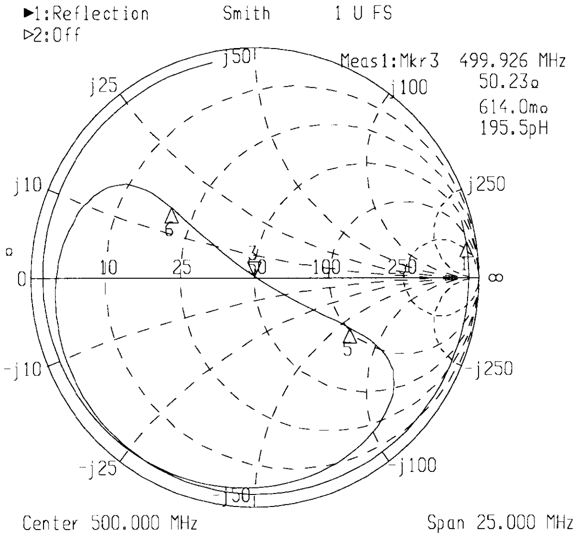

Figure 4-21: Smith chart for the 297μm probe at 500 MHz, showing the network is matched to 50 Ω.

Chapter 5

NMR Results

5.1 Experimental Setup

This chapter reviews all non-biological experiments done for this thesis work. The experimental work was important to: 1) demonstrate and test several theoretical predictions about the design introduced in Chapters 2 and 3; 2) begin to understand how to optimize the design; and 3) compare the performance of the microslot to other small detection schemes. The testable theoretical predictions were: 1) a microslot is feasible for NMR detection and can be built; 2) a microslot can obtain a high signal to noise ratio per unit volume with low inhomogeneous broadening; and 3) a microslot can achieve high RF homogeneity. To test the theoretical predictions and explore optimizations, a number of experiments and were collected for 100% deionized water. To compare the microslot to other detection schemes, a sensitivity analysis was done for sucrose, a standard sample.

These experiments were run on a Varian Inova 500 spectrometer with the 297 μm probe. A single nutation experiment was conducted for the 6.9 mm probe to make a scaling comparison. Since the probe was modeled after a conventional NMR probe, no modifications to the spectrometer were required to run experiments. The only software modification required was to increase the gain of the receiver for the 297 μm probe by 20 dB so as to avoid digitization noise.

5.1.1 Probe Centering

The first experiment that was conducted was designed to confirm that the 297 μm probe was centered in the magnet. This was important to maximize signal to noise ratio via minimizing inhomogeneity. The sample prepared was deionized water. A picture of the sample is shown in figure 5-1. Care was taken with a high pressure air supply to confine the sample length to about 4mm, to accommodate a sample of approximately 30 nL.

At the center of the magnet, one should find that changing the z_1 shim only broadens the spectrum of

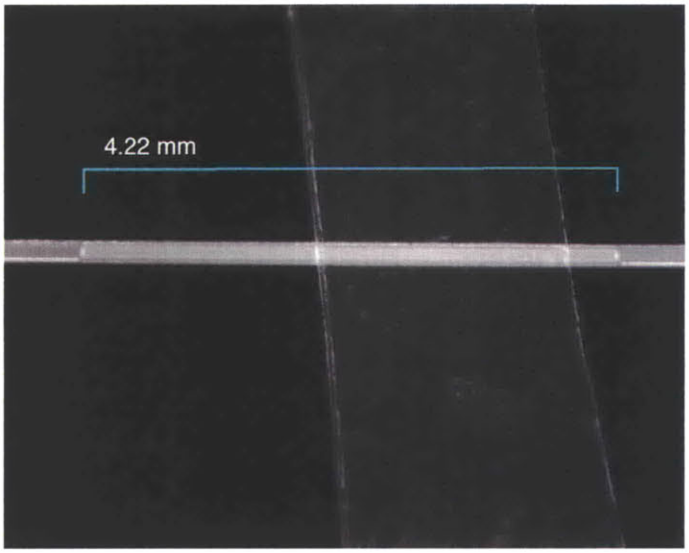

Figure 5-1: Photograph of the capillary tube showing the total length to be 4.22 mm. In the background, a vertical strip of polyimide tape can be seen.

the free induction decay (FID) of 100% deionized water. Changing this shim when the sample is below the center line should cause the mean of the spectrum to move in one direction, and when the sample is above the center line, the mean should move in the other direction. This dependence is shown in figures 5-2 through 5-4. The pulse sequence was a single $\pi/2)_x$ pulse with a 0.5s acquisition time.

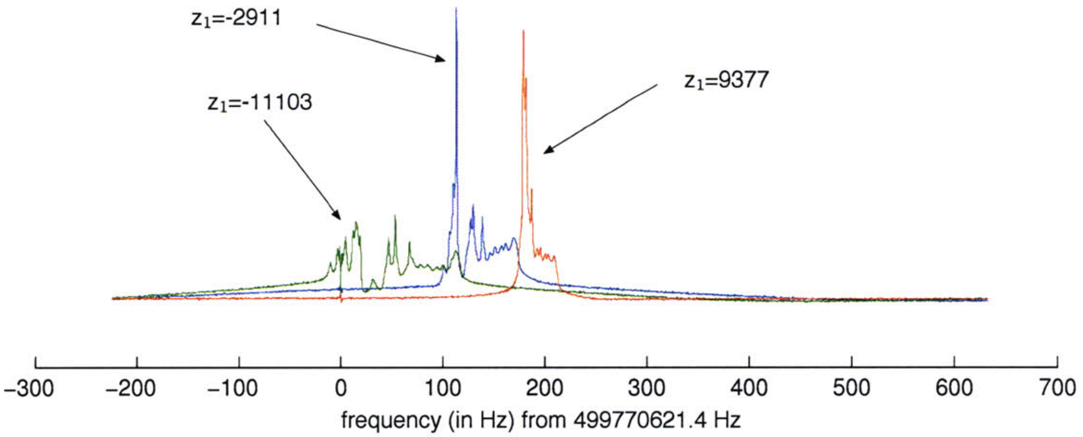

Figure 5-2: Varying z_1 4.0mm below the centerline of the probe. Various z_1 settings are marked.

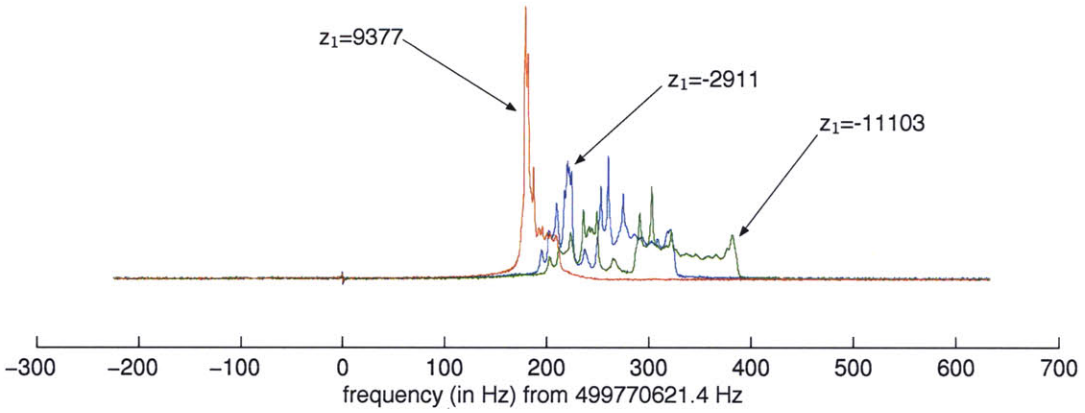

Figure 5-3: Varying z_1 2.7mm above the centerline of the probe. Various z_1 settings are marked. Notice the positions of the z_1=9377 and -11103 are swapped relative to figure 5-2.

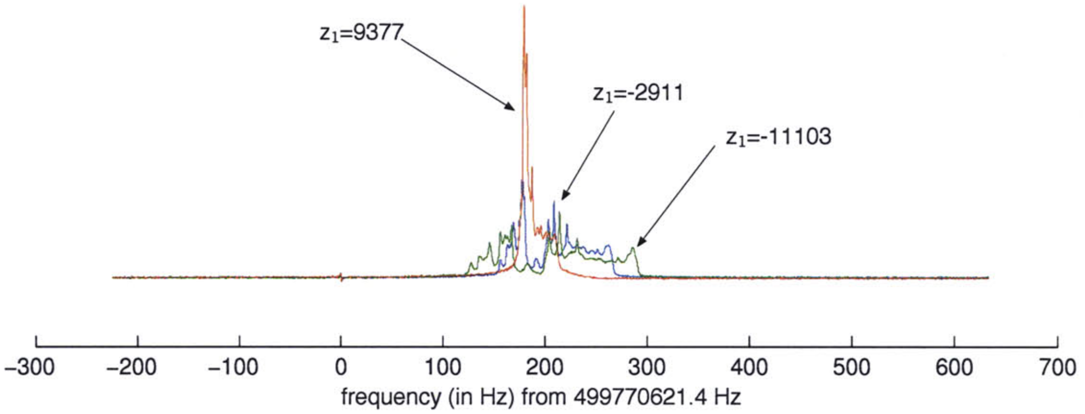

Figure 5-4: Varying $z_1 \approx 0.0$mm from the centerline of the probe. Various z_1 settings are marked. Each spectrum is now overlapping with the z_1 shim, changing the frequency variance of the spin distribution rather than the position.

5.2 Water Analysis

In this set of experiments, the signal from a high concentration of spins in a simple spectrum was measured to accomplish: 1) an estimate of sensitivity and linewidth for a single line; 2) understand how to optimize the system for capillary width and sample height from the surface; 3) measure RF inhomogeneity; 4) measure T_1 and T_2 to demonstrate estimating simple NMR parameters on mass-limited samples; 5) do a gradient imaging experiment to verify flux concentration in the microslot.

The first water experiment was performed using the 6.9mm microslot with a 10% H_2O sample. The sample volume estimated was about 220 μL. The shimmed spectrum is shown below in figure 5-5. The pulse sequence was a single $\pi/2)_x$ pulse with 1.0s acquisition time.

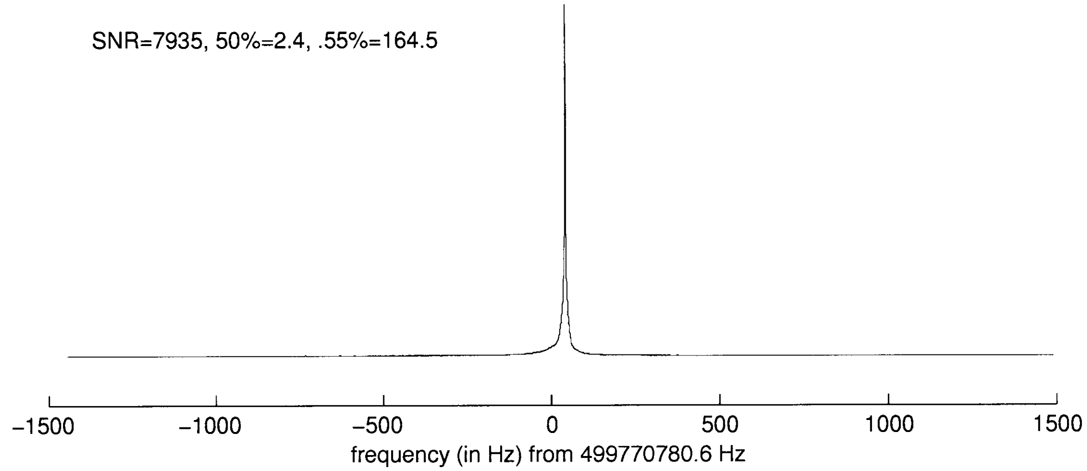

Figure 5-5: Water signal from 6.9mm probe for 10% H_2O in D_2O. The linewidths at various heights of the Lorentzian peak are given.

Next, we obtained the signals from the 297 μm probe with 100% deionized water (same sample as that from previous section), as shown in figure 5-6. With the smaller probe, we obtained an improved linewidth (1.1 versus 2.4 Hz) and improved signal to noise ratio per unit volume (1380 versus 6.5/umol/$\sqrt{Hz}$). As shown in figure 5-7, the line from the 297 μm water sample has a broad lineshape. Using the "integral lineshape" feature in the Varian VNMR software, it is clear that just over half of the signal is in the tails of the spectrum. There are two reasons why the shape is non-Lorentzian. As discussed in Appendix C, if the probe is not perfectly aligned, the entire surface of the probe can act as a surface of magnetic charge and hence produce inhomogeneity. The smaller microslot can also act as a source of inhomogeneity. This point will be discussed in Section 5.4.

5.2.1 Parametric Analysis

It was important to understand how the signal to noise ratio of the water data could be optimized. This was especially important since, with a two-dimensional microslot rather than a three-dimensional coil, there were more degrees of freedom for sample placement. The first parameterization was to determine how the sensitivity scales as a function of diameter of the capillary tube. A table of capillary tubes readily available from Polymicro are shown below in table 5.1, along with the mean field strengths across the volume of the sample and figures of merit relative to the 100 μm tube. It was assumed the sample was placed on a spacer 70 μm thick. From this table, if we were to increase the volume of the sample from 33 nL using the 100 μm tube to 193 nL, the signal to noise ratio should increase by a factor of approximately 4.3. Therefore, to increase sample volume, it is a better strategy to increase the length of the tube rather than the diameter of the tube, provided that the B_0 homogeneity allows this. To test this assertion, an experiment was performed with a

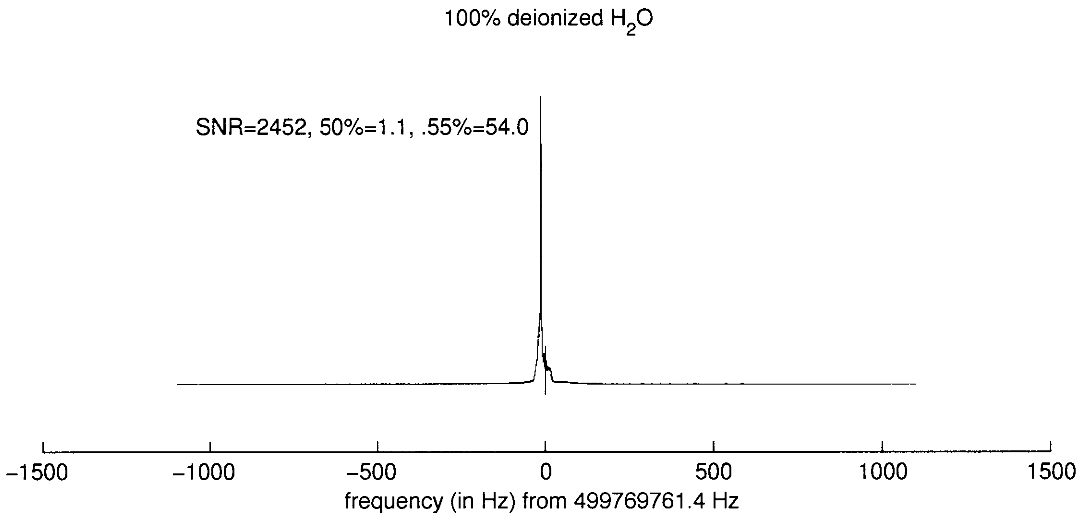

Figure 5-6: Water signal from the 297μm probe for 32 nL of 100% deionized H_2O. The linewidth is 1.1Hz 50%, 54Hz 0.55%.

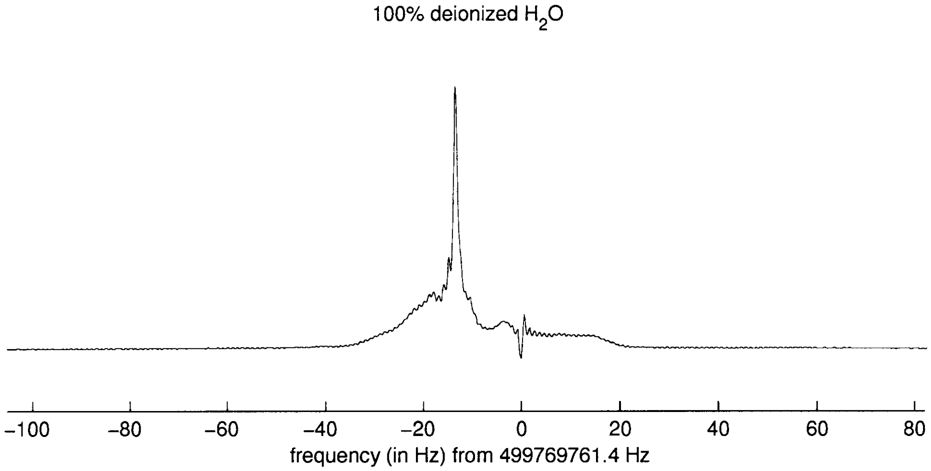

Figure 5-7: A closer inspection of the previous plot shows broad tails that could either be from the slot itself or a non-vertical alignment of the probe circuit board.

248 μm capillary. In this experiment, the linewidth increased to 3.7 Hz, from 1.15 Hz with careful matching of the pulse width. The signal to noise ratio increased by a factor of approximately 3.2, which is 74% of that predicted by the FEM calculation.

The second parameterization was to determine the sensitivity as a function of the sample's height off the surface of the probe. The sensitivity was measured with the sample on the surface of the conductor (0 μm) and at two tape thicknesses (140 μm) above. The tape used was 3M 5413 polyimide film wave solder tape, which was 70μm thick including 30μm of backing thickness. (The adhesive was slightly compressed under application, so the 140μm estimate may be a little high). In general we see reasonable agreement with the

i.d. (μm)	o.d. (μm)	$< \|(B_x, B_y)\|/i >$	figure of merit
75.0	152.0	9.65x10^{-}4	1.03
102.0	169.0	9.36x10^{-}4	1.00
248.0	354.0	6.81x10^{-}4	0.727

Table 5.1: Properties of various capillary tubes used.

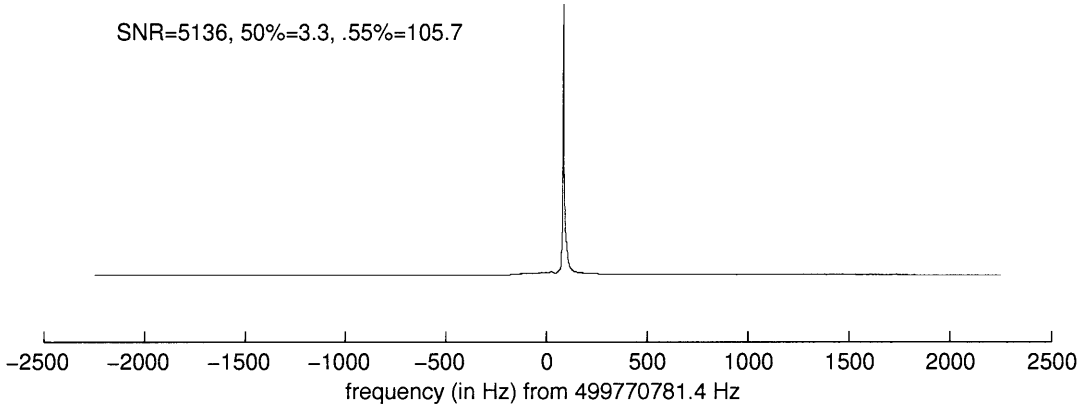

Figure 5-8: Water signal from the 297 μm probe with a 248 μm wide capillary tube. The linewidth was measured to be 3.4Hz wide, with an SNR of 5810.

FEM as shown in figures 5-9 and 5-10, but the greatest difference close to the surface. It should be noted the field strengths observed are all slightly higher than predicted by the model.

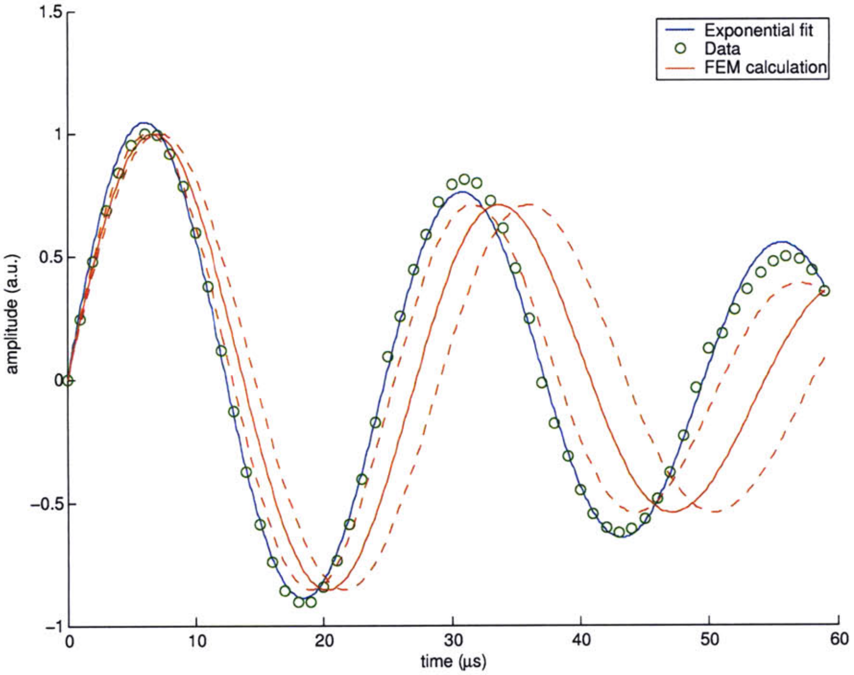

Figure 5-9: Nutation plot with y_0=140μm. The ratio of A_{270} to A_{90} is 0.91. (Dashed lines represent error limits from calculation.)

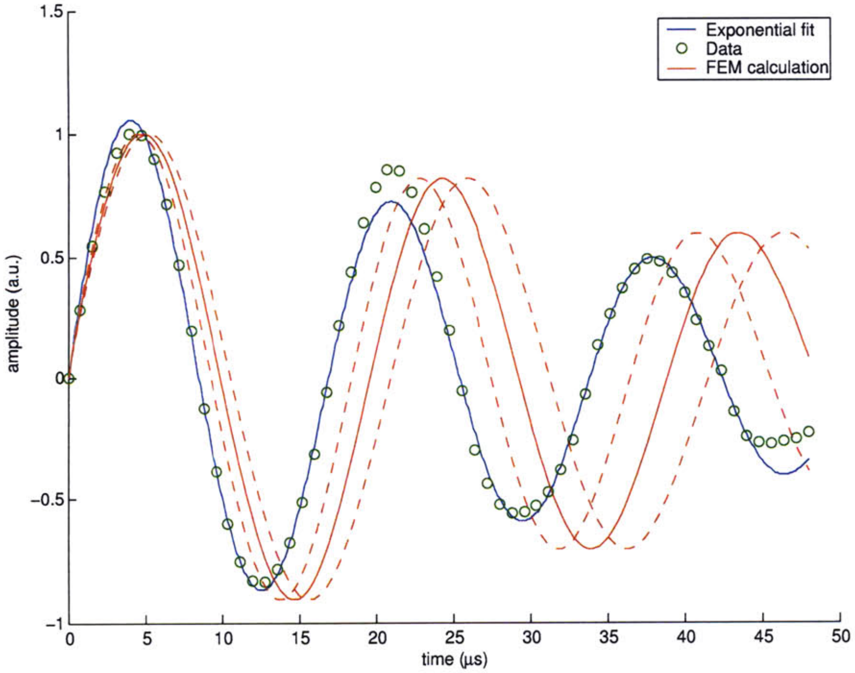

Figure 5-10: Nutation plot with y_0=0μm. The ratio of A_{270} to A_{90} is 0.84. (Dashed lines represent error limits from calculation.)

5.2.2 Nutation Plots For Model Verification

The next set of experiments were proper nutation experiments at different power settings. They were performed with a standard pulse sequence and a delay of 20s to allow proper T_1 equilibration. The first plot in figure 5-11 shows a concatenation of the spectra of each experiment showing that overall the baseline is relatively flat and each spectrum is free from artifacts. Figures 5-12 and 5-13 show the nutation data with FEM predictions for power settings of tpwr 45 and 51 (29.55 and 35.27 dBm respectively) for the 297 μm probe. Figure 5-14 shows the nutation data for the 6.9mm probe. It is important to note the effects of the detector scaling (smaller): the time to rotate the spins by $\pi/2$ has decreased substantially and the RF homogeneity has increased.

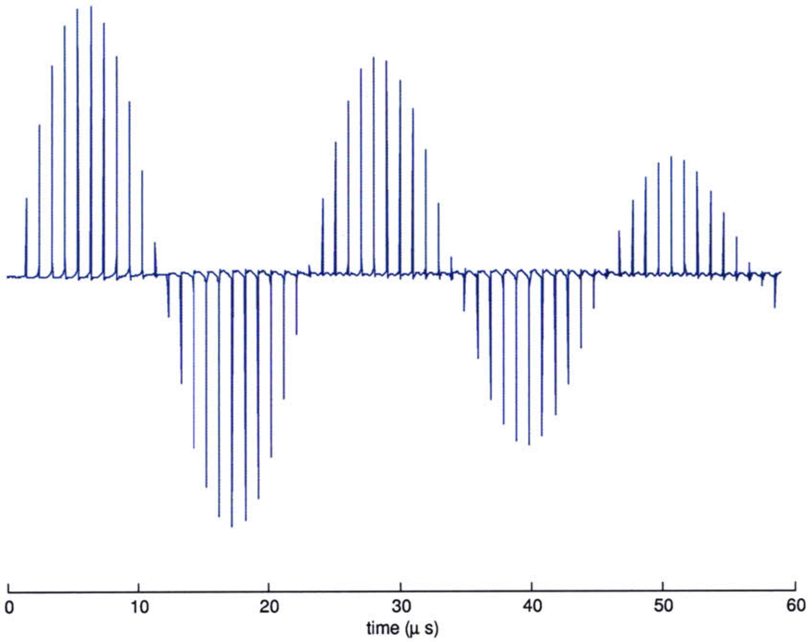

Figure 5-11: Concatenation of the spectra as a function of pulse width for tpwr=45 (29.55 dBm) for over 5π cycles. The ratio of A_{270} to A_{90} is 0.95. (Dashed lines represent error limits from calculation.)

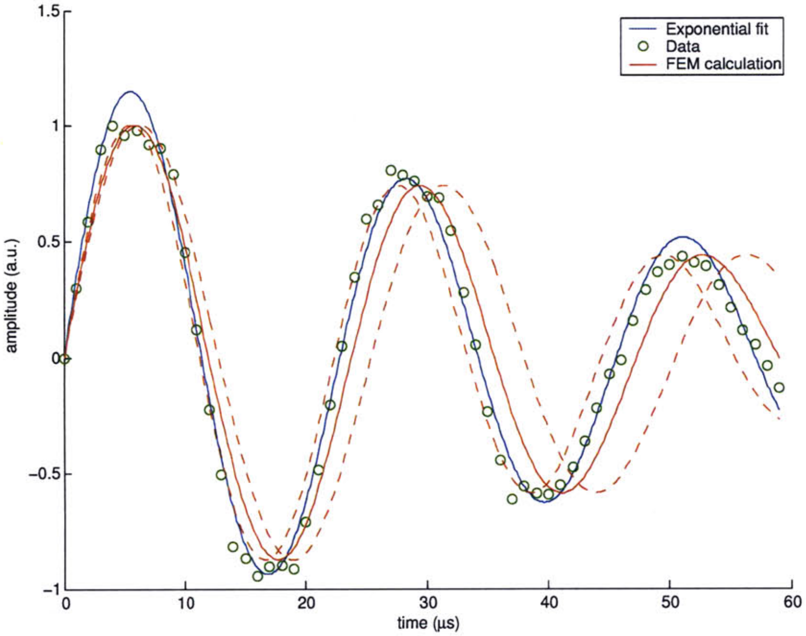

Figure 5-12: Nutation plot of experimental data from the 297μm probe, exponential line fit, and FEM prediction with error curves using tpwr=45 (29.55 dBm) data and experimentally measured current gain. The ratio of A_{270} to A_{90} is 0.97. (Dashed lines represent error limits from calculation.)

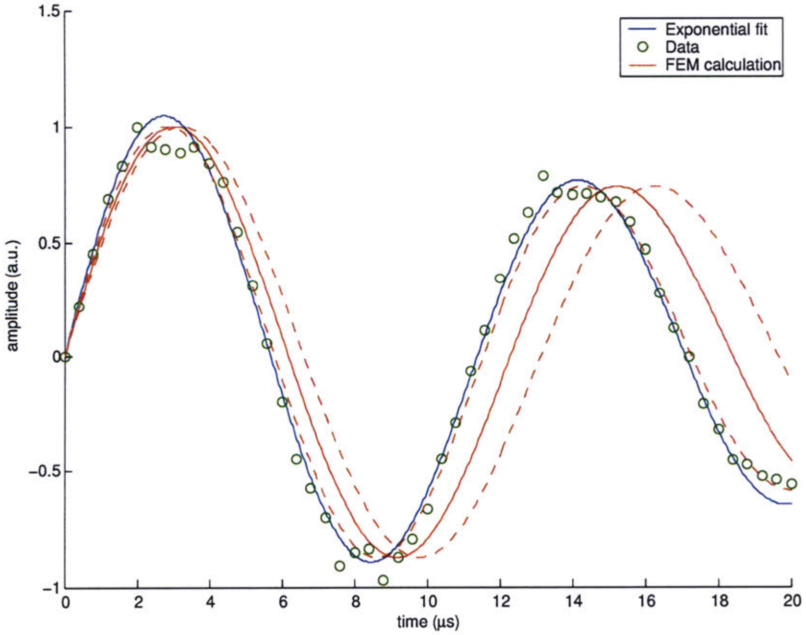

Figure 5-13: Nutation plot of experimental data from the 297μm probe, exponential line fit, and FEM prediction using tpwr=51 (35.27 dBm) data and experimentally measured current gain. The ratio of A_{270} to A_{90} is 0.97. (Dashed lines represent error limits from calculation.)

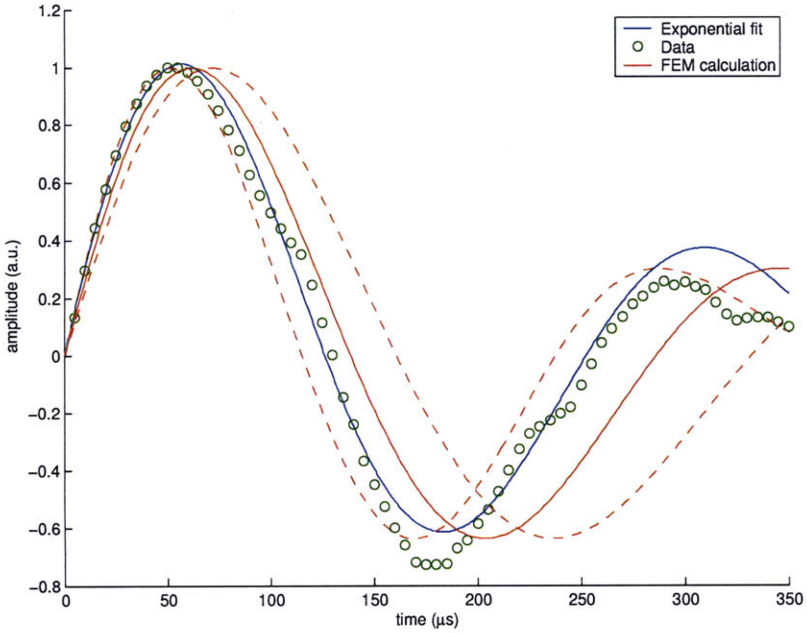

Figure 5-14: Nutation plot of experimental data from the 6.9mm probe, exponential line fit, and FEM prediction using tpwr=58 (38.25 dBm) data and experimentally measured current gain. The ratio of A_{270} to A_{90} is 0.71. (Dashed lines represent error limits from calculation.)

5.2.3 T$_1$ Measurement

The general pulse sequence for T$_1$ measurement is shown in figure 5-15. T$_1$ is calculated over a series of experiments in which τ is changed. The density operator evolution [27] [56] for the experiment is:

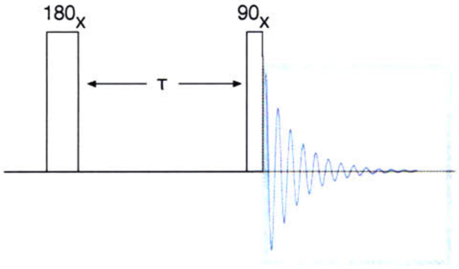

Figure 5-15: Pulse sequence for the T$_1$ measurement experiment.

$$\sigma_0 \xrightarrow{\pi I_x} \sigma_1 \xrightarrow{\mathcal{L}\tau} \sigma_2 \xrightarrow{\pi/2 I_x} \sigma_3 \xrightarrow{\mathcal{L}\sqcup} \xrightarrow{\omega t I_z} \sigma_4, \tag{5.1}$$

where the equilibrium state $\sigma_0 = I_z$ is transformed into $\sigma_1 = -I_z$. After relaxation, we have:

$$\sigma_2 = I_z(1 - 2\exp(-\tau/T_1)). \tag{5.2}$$

After the second pulse, we have (ignoring further relaxation):

$$\sigma_3 = (1 - 2\exp(-\tau/T_1))(-I_y \cos\omega t - I_x \sin\omega t). \tag{5.3}$$

By either taking the first point of the FID or the peak of the spectrum, we can plot σ_3 as a function of τ to obtain the T_1 decay. By undersampling this curve, it is easy to reconstruct the relaxation dynamics. The relaxation delay between experiments was taken to be 20 s. T$_1$ was determined to be 3.7 ± 0.1 s.

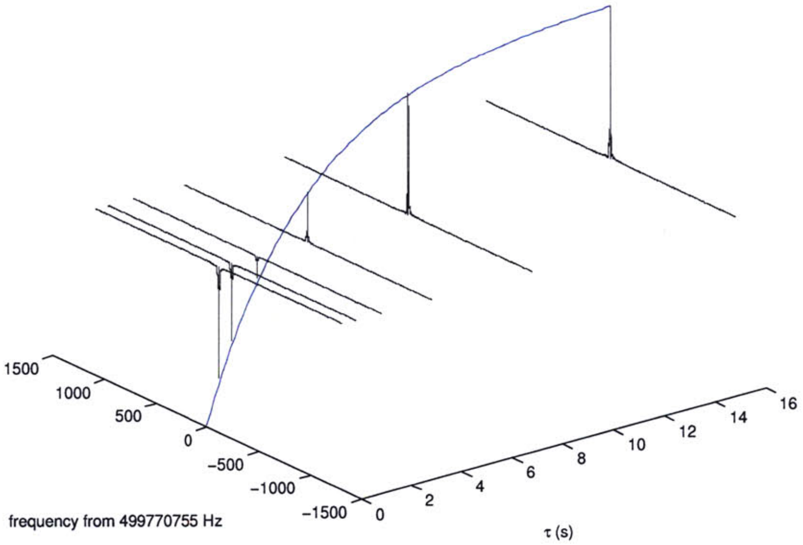

Figure 5-16: Stacked FID plot for the data collected for various settings for τ to recover T_1. Exponential fit of equation 5.2 for the data collected. T_1=3.7 ± 0.1 s.

5.2.4 T_2 Measurement

When one measures the relaxation dynamics of an FID, the relaxation is driven by T_1 and T_2^* dynamics, where

$$1/T_2^* = 1/T_2 + 1/T_{2\text{ inhom}}. \tag{5.4}$$

In order to measure the true T_2, a sequence was modeled after the spin echo sequence. The sequence is shown in figure 5-17 and is discussed in Appendix A. The product operator evolution is shown below in equation 5.5. The goal of the second refocusing step is to correct for imperfections in the pulses. T_2 was determined to be 1.8 ± 0.2 s.

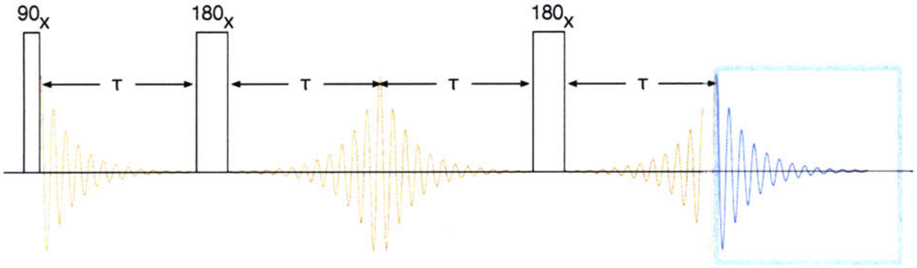

Figure 5-17: CPMG sequence used for determining T_2.

$$\sigma_0 \xrightarrow{\frac{\pi}{2}I_x} \sigma_1 \xrightarrow{\mathcal{L}\tau}\xrightarrow{\omega\tau I_z} \sigma_2 \xrightarrow{\pi I_x} \sigma_3 \xrightarrow{2\mathcal{L}\tau}\xrightarrow{2\omega\tau I_z} \sigma_4 \xrightarrow{\pi I_x} \sigma_5 \xrightarrow{\mathcal{L}\tau}\xrightarrow{\omega\tau I_z}\xrightarrow{\mathcal{L}t}\xrightarrow{\omega t I_z} \sigma_6 \tag{5.5}$$

With a measurement of the true T_2, we can estimate the smallest Full Width at Half Maximum (FWHM) peak as

$$\Delta f = \frac{1}{\pi T_2^*}. \tag{5.6}$$

The minimum Δf is thus 0.18 Hz. With the best observed linewidth of 1.15 Hz, $T_{2\text{ inhom}}$ is 0.33 s and T_2^* is 0.277 s.

5.2.5 RF Imaging

In order to prove the micromachined microslot works, it was important to understand the source of the signal relative to the sample spin distribution. Although the signal from the smaller microslot is predicted to be larger, without proper susceptibility matching, this signal could be inhomogeneously broadened more than the signal from the larger microslot, resulting in decreased gain. To explore this possibility, a variant of the experiment to do gradient shimming was performed using the homospoil gradient on the Inova 500 console, since the normal pulsed field gradients are ineffective at this scale. The experiment performed is illustrated in figure 5-19.

The first pulse, *pw*, is arrayed from 0 to 100μs in 1μs steps. The purpose of the refocusing step is to

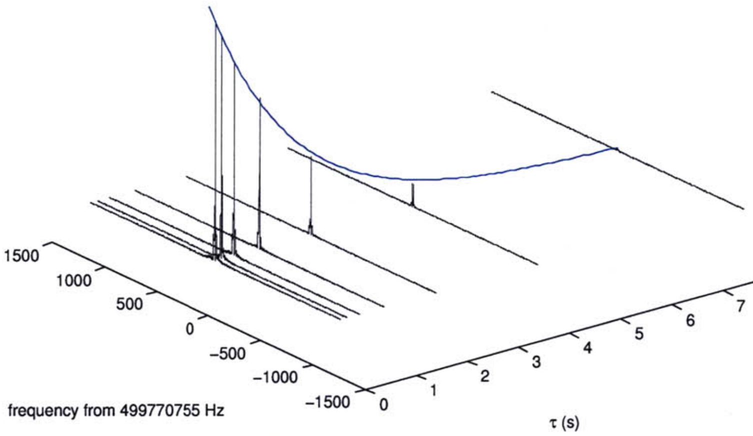

Figure 5-18: Exponential fit of the data collected for the T_2 experiment. T_2=1.8 ± 0.2 s.

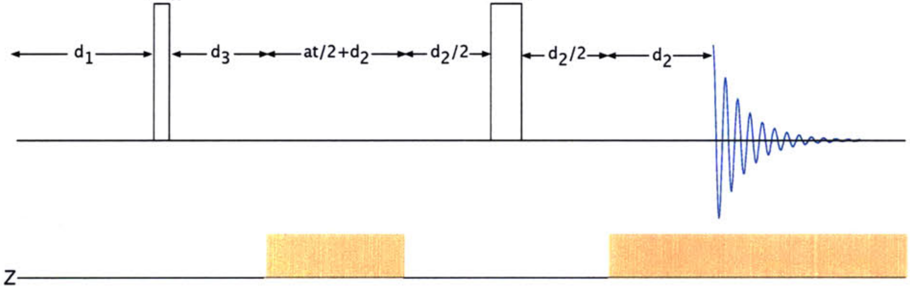

Figure 5-19: The homospoil spin echo experiment for mapping the RF field. The rectangles on the z-axis indicate the applications of the homospoil gradient.

remove the effects of RF inhomogeneity on the pulses. The first gradient phase encodes a spin isochromat with a phase $\phi = zG_z(at/2 + d_2)$. This phase is reversed by time $at/2$ of the acquisition phase and then the FID is phase-encoded with the final phase $\phi = zG_z at/2$. The data for $pw = [5, 10]$ is shown in figures 5-20 and 5-21. The strength of the homospoil gradient is 200Hz/mm. From the plot at 9μs shown in figure 5-21, the width of the spectrum is estimated to be 780Hz. This corresponds to a sample of approximately 3.90 mm in length, which is just short of the 4.22 mm determined optically, but confirms the whole sample is producing a measurable signal. It can also be seen that the capillary was not placed exactly symmetrically about the slot. From these plots, the peak signal from the microslot is approximately 3 times larger than the rest of the sample, confirming that there is flux gain around the micromachined slot. One might question the cause of the extra peak. The same experiments were repeated with the capillary sample rotated around the

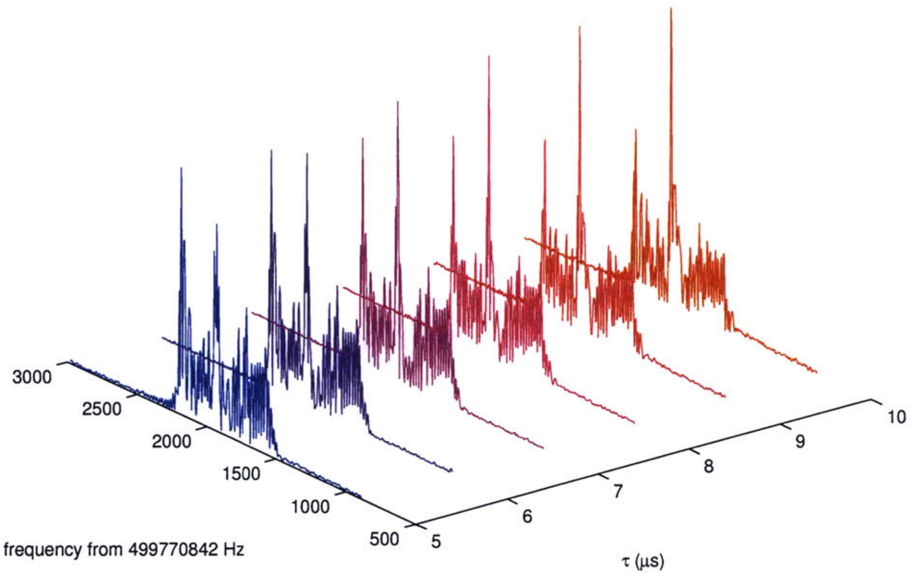

Figure 5-20: Subset of the gmapz experimental results for varying lengths of the pulse width pw. Note the peak heights are changing due to their relative B/i, but the largest signal is coming from the center. Note also a large peak at the part of the sample furthest downfield.

x-axis by 180° to confirm the peak was not generated by the sample in the capillary. Surprisingly, the signal was still present on the downfield side. Upon visual inspection, a likely culprit was found – there were large, irregular curved microslots (from the chemical etching) on the downfield side (shown in figure 5-22) that were likely acting as flux concentration zones.

5.3 Sucrose Analysis

After the water analysis, the experiments progressed to more interesting samples, such as sucrose, a benchmarking sample used in the literature [61]. A diagram of the sucrose molecule is shown in figure 5-23, with the anomeric proton highlighted. The sensitivity of this particular proton (scaled to 600 MHz), is a benchmark to compare different probe designs. Sucrose has a molecular weight of 342.30 g/mol. A spectrum of 361 μmol of sucrose dissolved in 600 μL of 100% D_2O is shown in figure 5-24. For the microslot probe, a sample was prepared that contained 15.6 nmol of material. This was done by creating a 0.59 M solution and then creating a 3.38 mm long sample (as shown in figure 5-25) through capillary action. An experiment was performed with 16 scans and an acquisition time of 1.25 s and line-broadening of 1.3 Hz, shown in figure 5-26. Given the measured SNR of 50.1 for the anomeric proton, the sensitivity is 984/μmol/$\sqrt{Hz}$, scaled to 600 MHz.

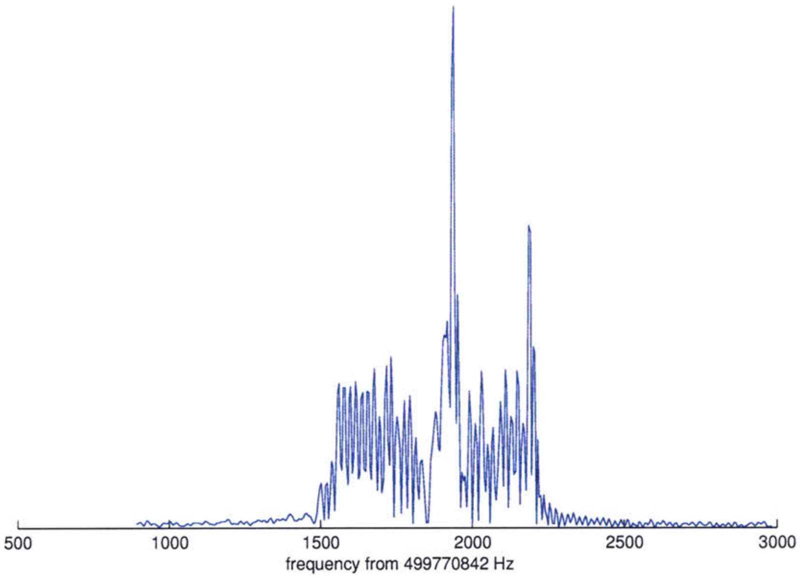

Figure 5-21: Plot of the spectrum at $9\mu s$ used to measure the effective sample volume.

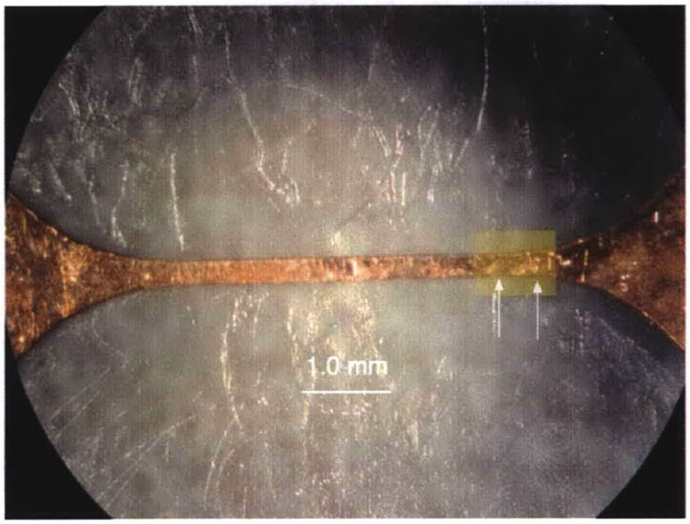

Figure 5-22: Photograph of the probe board showing imperfections in the larger microslot stripline on the downfield side. Arrows indicate imperfections.

Current results from a variety of systems are reported in table 5.2 There are not many published results on planar microcoils using sucrose, assumedly because their signal to noise ratio and linewidth is too low. In the work of Stocker et al. [81], using a 60 μm square, planar 3.5 turn microfabricated coil, 440 pmols of sucrose was analyzed for 2260 s at 250 MHz to obtain an estimated signal to noise ratio of about 2 (SNR not given in the paper), giving an upper bound of $442/\mu\text{mol}/\sqrt{Hz}$ at 600 MHz. They also measured water and

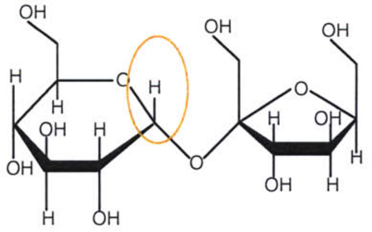

Figure 5-23: Sucrose molecule, with the anomeric proton highlighted.

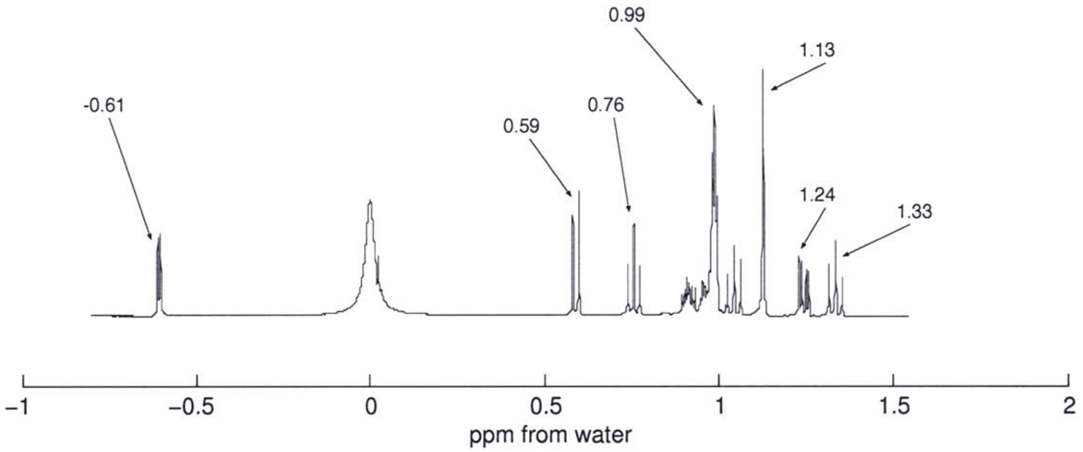

Figure 5-24: 361 μmol of sucrose dissolved in 600 μL of 100% D_2O. The observe volume is 220 μL. The anomeric proton is represented by the peak furthest to the left.

obtained a sensitivity of $324/\mu\text{mol}/\sqrt{Hz}$ (1090 scaled to 500 MHz) with a linewidth of 1.8 Hz. In this paper [81], a susceptibility matching fluid was used. In a paper by Rogers et al. [68], 8 nL of neat acetone and 8 nL neat ethylbenzene were analyzed at 300 MHz. For acetone (C_3H_6O), at 58.08 g/mol and a density of 789.9 kg/m^3 at 20^{o}C, a signal to noise ratio of 138 was obtained in 65.5 s, giving a sensitivity of $87.8/\mu\text{mol}/\sqrt{Hz}$ at 600 MHz for a single proton.

For all cases except for the wound microcoils, the microslot performs better without any susceptibility matching. With scaling and susceptibility matching, it is highly likely this geometry in an optimized form could do better than any published result. One important point to consider is that for wound coils, both

Probe type	SNR/μmol/$\sqrt{Hz}$ @ 600 MHz	Sample size V_{obs}	Frequency (MHz)
Nalorac 5mm	134	220 μL	600
Nalorac SMIDG 3mm	320	40 μL	600
microcoil A	5580	5 nL	300
microcoil B	1530	620 nL	500
planar microfluidic	124	470 nL	300
microslot	984	25 nL	500

Table 5.2: Performance of various probes for sucrose. Nalorac and microcoil data taken from [48] and planar microfluidic data taken from [55].

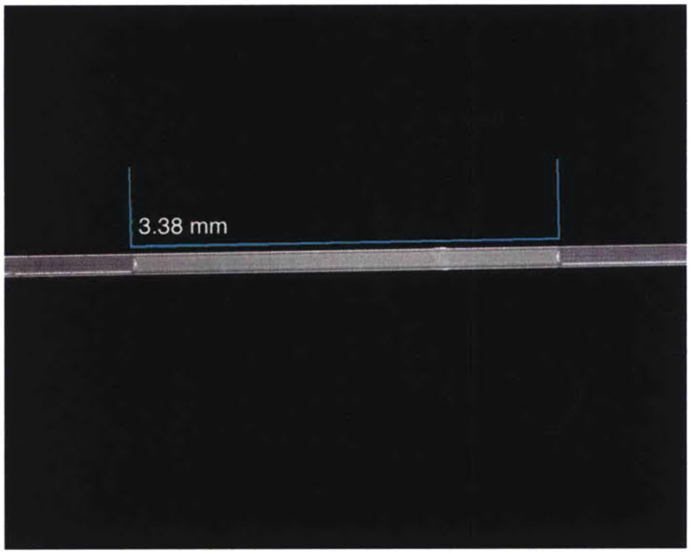

Figure 5-25: Photograph of the capillary tube containing sucrose solution, showing the total length to be 3.38 mm.

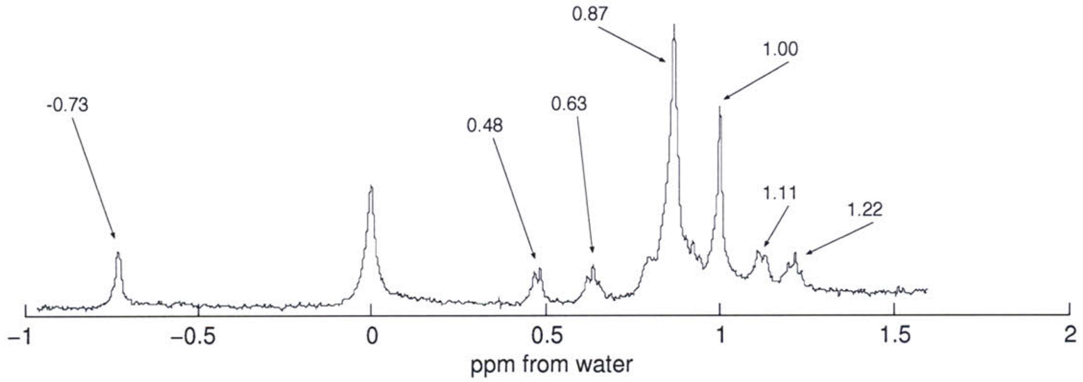

Figure 5-26: 15.6 nmol of sucrose in 100% D_20. The signal to noise ratio of the anomeric proton is 50.1. 1.3 Hz of line broadening was applied. The plot shows the sum of 16 scans (each with an acquisition time of 1.25s). Note the peak positions for the microslot probe, possible caused by temperature differences and/or absence of lock signal, are about 0.13 ppm from the Nalorac probe.

planar and solenoids, the non-idealities of these structures (distributed capacitance, proximity effect) at RF frequencies may preclude their scaling to higher frequencies, which may mean the $(B_{600}/B_{\text{expt}})^{7/4}$ scaling may not be correct.

5.4 Susceptibility Matching of the Slot

The non-Lorentzian shape of water from the microcoil is suspected to come from the susceptibility mismatch of the slot itself (as well as the entire copper surface). To test this hypothesis, four 20-30μm glass spheres were placed inside the slot, where they became electrostatically bound. No appreciable improvement in the lineshape of the signal was seen. This strongly suggests the inhomogeneous broadening is likely due to the lack of plating of copper, not the microslot itself. To correct this problem, a thin layer of palladium needs to be applied. Palladium cannot be sputtered on, like other metals, because there are too many impurities (especially argon) [9]. Thus, one must do electroplating and be very careful about the timing of this operation. A Vibrating Sample Magnetometer (VSM) or other device is needed to characterize this process to get a proper matching of the material. This process was outside the scope of this work and will be considered in the future. [9].

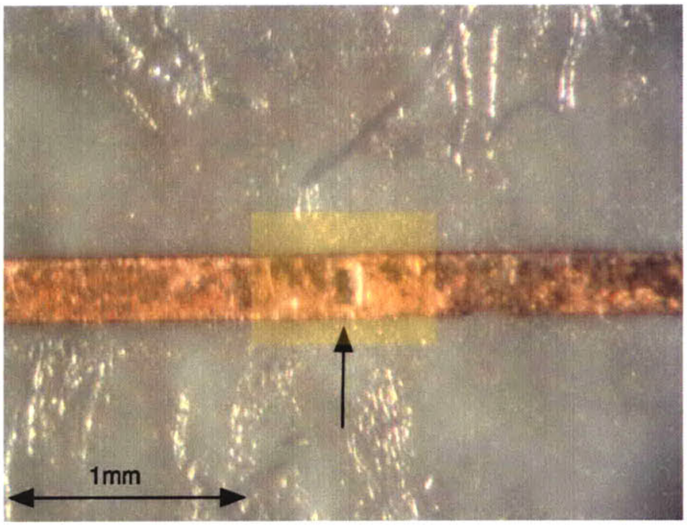

Figure 5-27: Image of 4 glass microspheres, 20-30μm in diameter to fill the slot for susceptibility matching. The spheres were electrostatically bound.

Chapter 6

Biology Experiments

6.1 DAR Peptide

To test the capability of the microslot probe to detect biomolecules, a simple biological molecule was analyzed. The molecule chosen was the Acetyl-DDDDAAARRRR-Amide molecule, with a molecular weight of 1356.6 g/mol, from Research Genomics. The structures shown in figures 6-1 and 6-2 were rendered by molecular dynamics simulations by Dr. Shuguang Zhang.

The experimental progression started with measurements of 1D spectra from a commercial NMR probe and a microslot probe to estimate linewidths and peak positions for less than three orders of magnitude less sample. Then, two-dimensional data was collected for both probes to show off-diagonal elements could be measured by the microslot probe. Finally, given tabulated statistical properties of amino acids, the molecule was labeled with results from the one- and two-dimensional experiments.

To prepare the sample, 3.3mg of the peptide was placed in a sealed 1 mL syringe (sealed using paraffin wax) and filled to the 0.5 mL mark with D_20 to give a 4.9 mM solution. The sample was shaken vigorously to make sure the peptide was fully dissolved. The peptide was very white and fluffy, suggesting that is was pure, but contained a lot of water. All of the solution was placed in a standard 5mm NMR tube from Wilmad, part number 535-PP-8. Using a pipette, a small amount of solution was transferred to a plastic petri dish containing a cleaned capillary tube. A small amount of solution (<0.5 mm long) was drawn into the capillary tube due to it having higher viscosity (than that of pure water). The remaining solution was forced in via high pressure bursts from the pipette. The sample was not centered, so careful bursts of compressed air were applied to center the sample within the capillary. A photo of the capillary with sample is shown in figure 6-3.

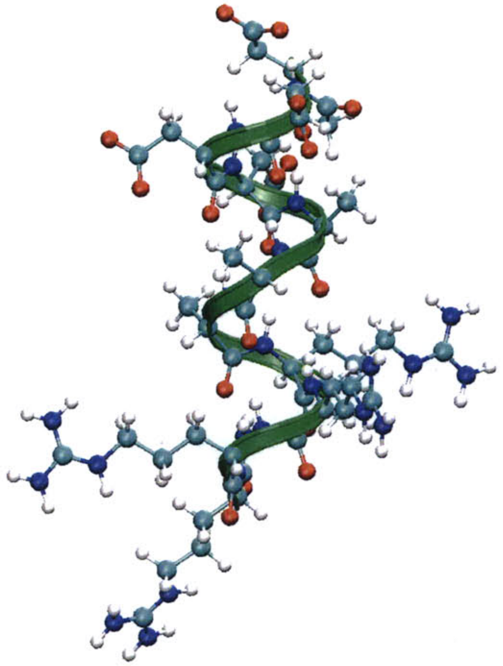

Figure 6-1: Tranverse view the DAR molecule. Arginine is at the bottom.

6.2 1D Experiments

For the 1D data, spectra were acquired from a standard Nalorac probe as well as from the microslot probe. For the 5mm Nalorac probe, data was acquired in 3.73 minutes. For the microslot probe, data from approximately 1100× less sample was acquired in 25 minutes. The capillary used was a 248/356 μm tube. The total volume of the sample was 190 nL, or about 940 pmols. Comparisons of the complete and partial spectra are shown in figures 6-4 through 6-6. We can see that all the major peaks are present except for peak 1, which has been overwhelmed by the water peak. Also important to note is that the peaks from the microslot probe are slightly shifted. This is because the sample is at a different temperature (no thermal stabilization was used in the microslot probe).

6.3 2D Experiments

The next set of experiments focused on two-dimensional data to examine structure. The canonical COSY sequence (see Appendix A for details) with absolute value spectra was used, as shown in figure 6-7. The first two-dimensional experiment was done on the Nalorac 5mm probe. The experiment was run for 2.5 hours, as shown in figure 6-8. We see the large water peak on the lower left and cross-peak data (upper left and lower right quadrants) suggesting structure. Some peaks are not as visible as others due to an incomplete sampling of J-space. Next, the same experiment was performed in 6 hours for the microslot probe. The

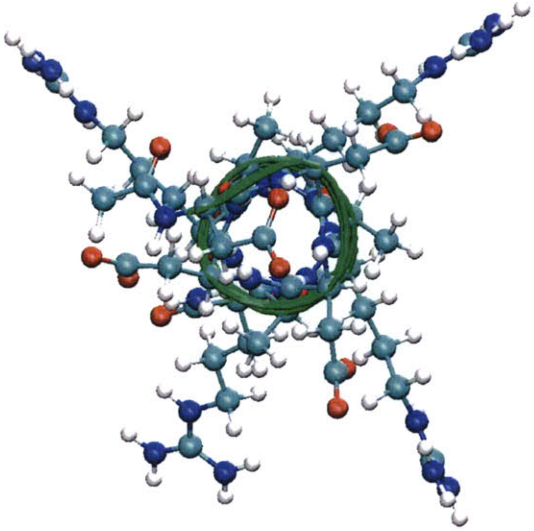

Figure 6-2: Axial view of the DAR molecule.

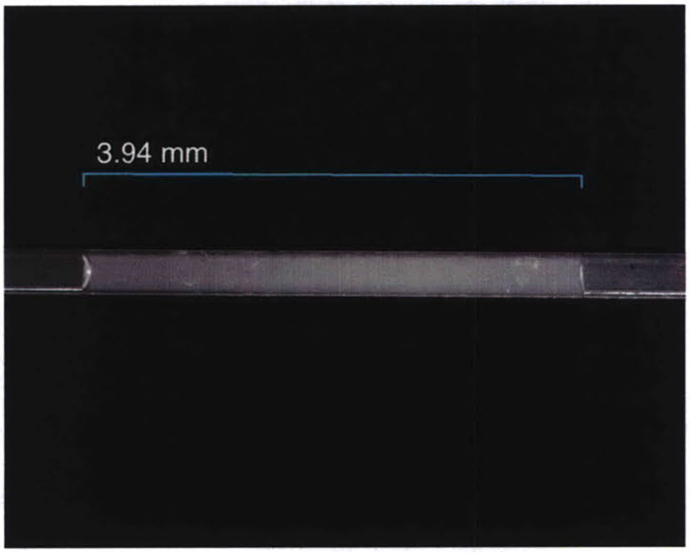

Figure 6-3: Photograph of the capillary tube showing the total length of the sample to be 3.94 mm.

spectra collected is shown in figure 6-9 and shows no cross-peak structure, only a smearing of peak data. Looking closely at the water peak in figure 6-10, we see a drift of approximately 30 Hz over 25 minutes. This is a symptom that all the peaks were slowly changing over time.

This drift behavior can be produced with the Nalorac probe as well. By keeping the lock on and the lock signal marginal, the frequency of the water peak can change quite substantially, as evidenced by the top graph in figure 6-11. When the lock is turned off, the peak is stabilized, as shown in the bottom graph of the same figure. In the COSY experiment for the microslot, plotting the water peak as a function of time for

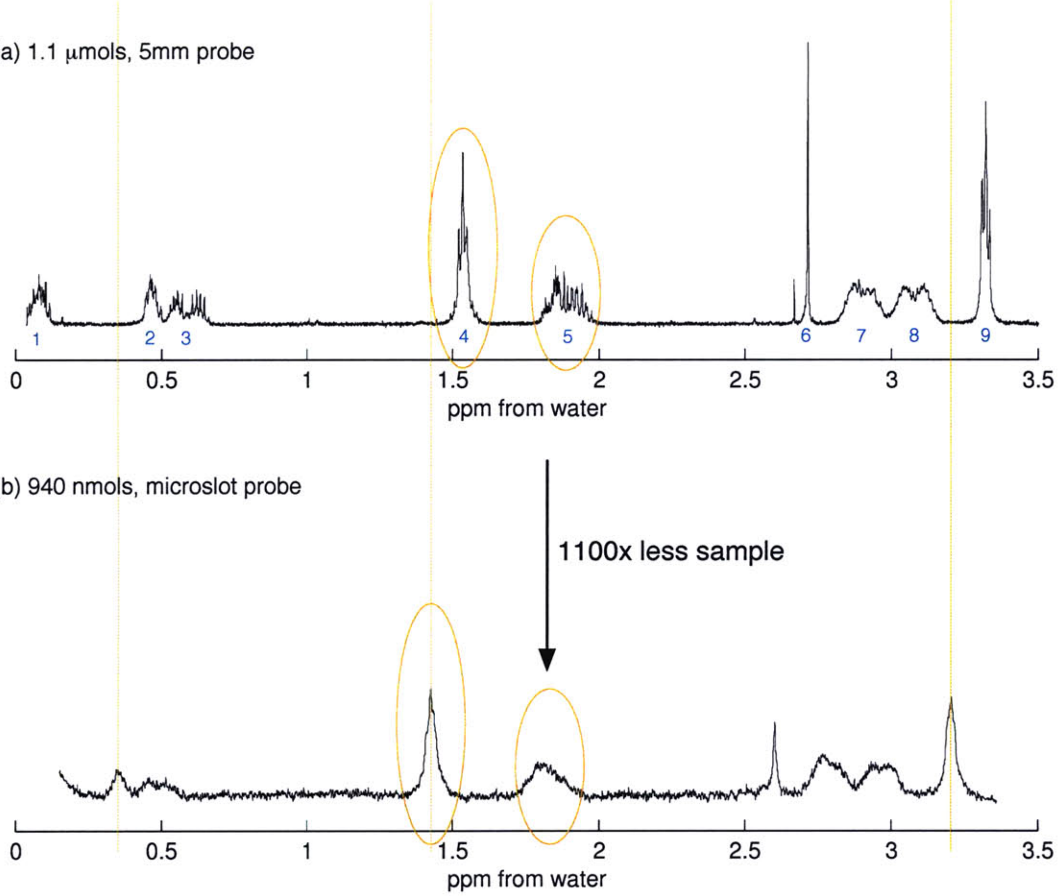

Figure 6-4: In (a), 1.1 μmols DAR 1D spectrum from Nalorac 5mm probe. The total acquisition time is approximately 3.7 minutes. In (b), 940 pmols of DAR 1D spectrum from microslot probe with a least squares baseline subtraction. The total acquisition time is approximately 25 minutes. The numbers represent the peaks of interest. The circled peaks are expanded in figures 6-5 and 6-6. The line broadening for (b) was 1.0 Hz, while 0.0 Hz was applied to (a).

the duration of the experiment and continuing for an additional three hours, the peak continues to change, as shown in figure 6-12. This shows that the effect, caused either by heating or by a control loop, is not caused by the microslot probe itself. To avoid the complication of creating a lock signal for the microslot, rather than averaging of the signal, each separate FID was saved to a file. A periodogram was calculated for each file and from the frequency of the largest peak, the whole spectrum was frequency-shifted by the difference of this frequency and the first FID. A final transform was a demodulation in the indirect dimension based on the frequency shift vector previously calculated. The final fixed spectrum is shown in figure 6-13. Here we see cross-peak structure, but not all peaks are present due to lower signal to noise ratio and water saturation. It is interesting to note that the peaks that were not resolved in 1D are now resolvable, due to the Gaussian and sine-bell weighting functions.

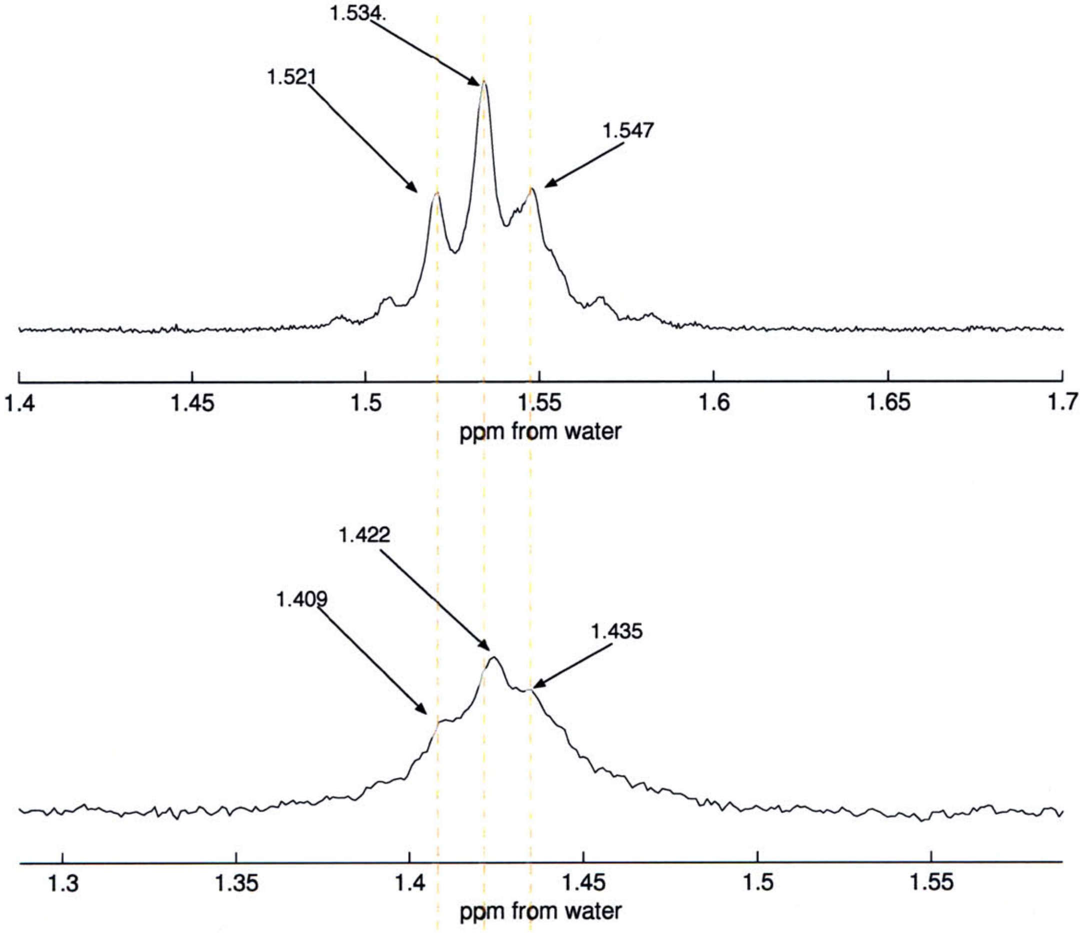

Figure 6-5: Closeups of the 1.5ppm peak given by the Nalorac probe (on top) and the microslot probe (on bottom). The numbers on the graph give more detailed information on peak locations. The microslot probe structure produced peaks 0.112 ppm from the Nalorac data.

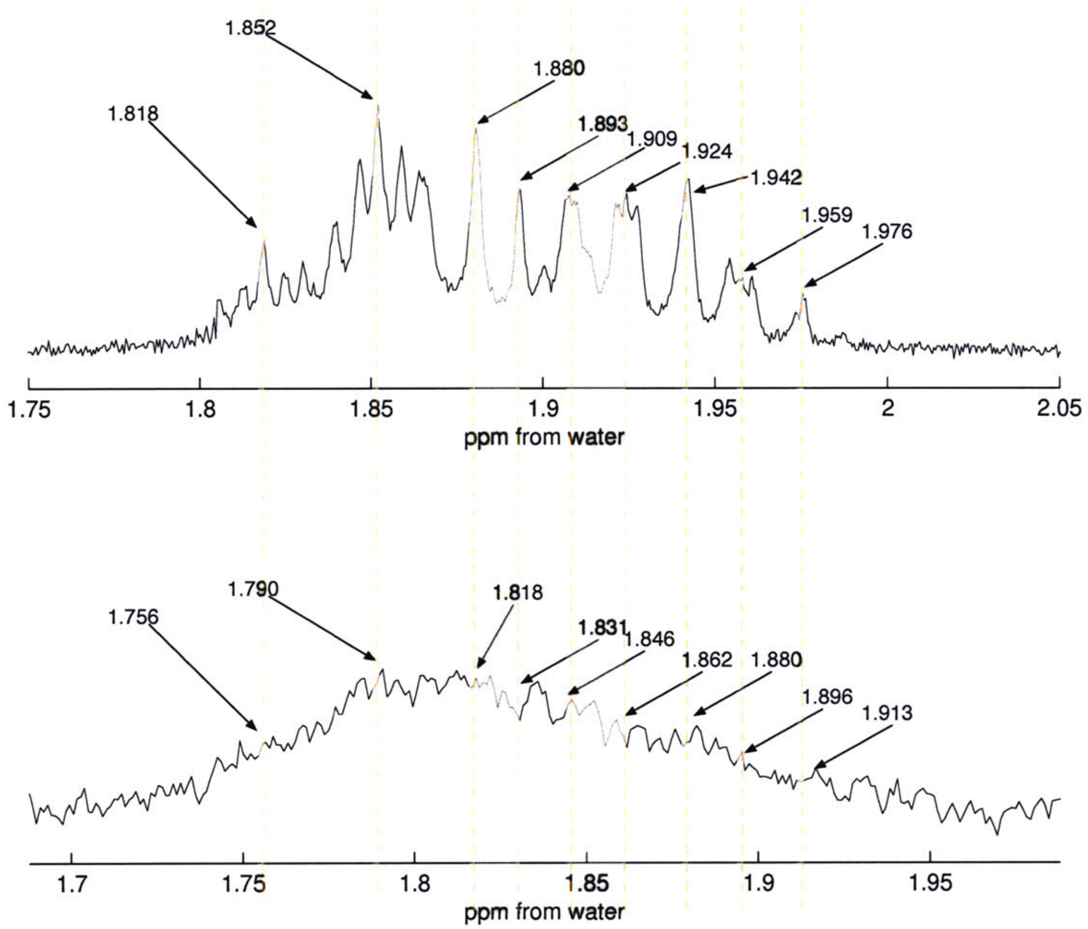

Figure 6-6: Closeups of the 1.9ppm peak given by the Nalorac probe (on top) and the microslot probe (on bottom). The numbers of the graph give more detailed information on peak locations.

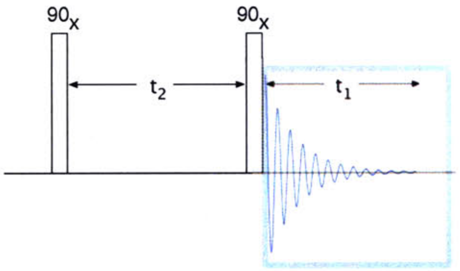

Figure 6-7: The canonical COSY sequence showing the two dimensions that are used to produce a two-dimensional spectrum.

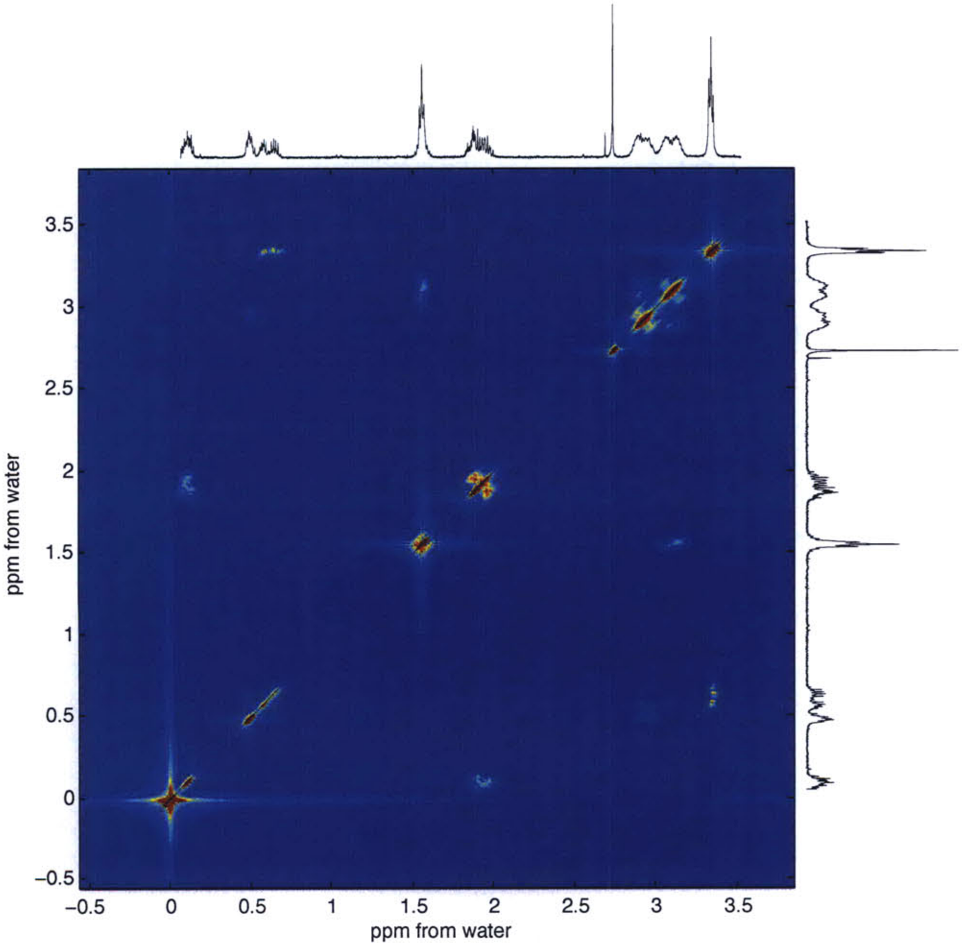

Figure 6-8: COSY spectrum from the Nalorac probe. lb=0.0, sb=0.116, lb1=0.32, sb1=0.058.

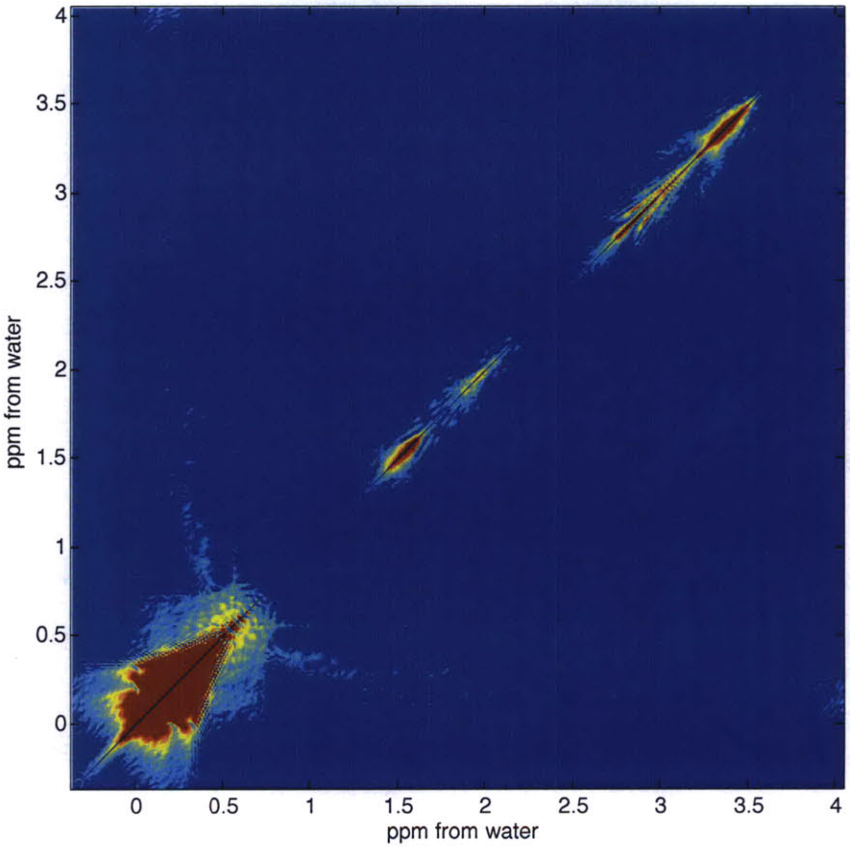

Figure 6-9: COSY spectrum from the microslot probe before drift correction was applied. There is no evidence of correlations. lb=0.6, gf=0.08, lb1=0.61, sb1=0.078, gf1=0.4.

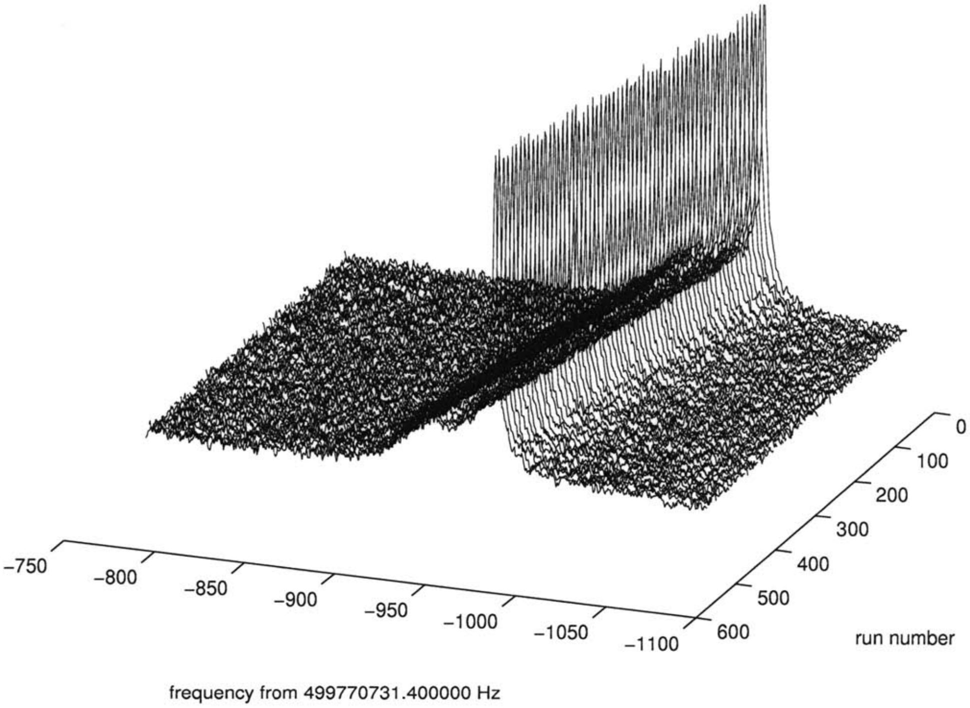

Figure 6-10: Plot of the residual H_2O peak showing the drift of approximately 30Hz over 25 minutes.

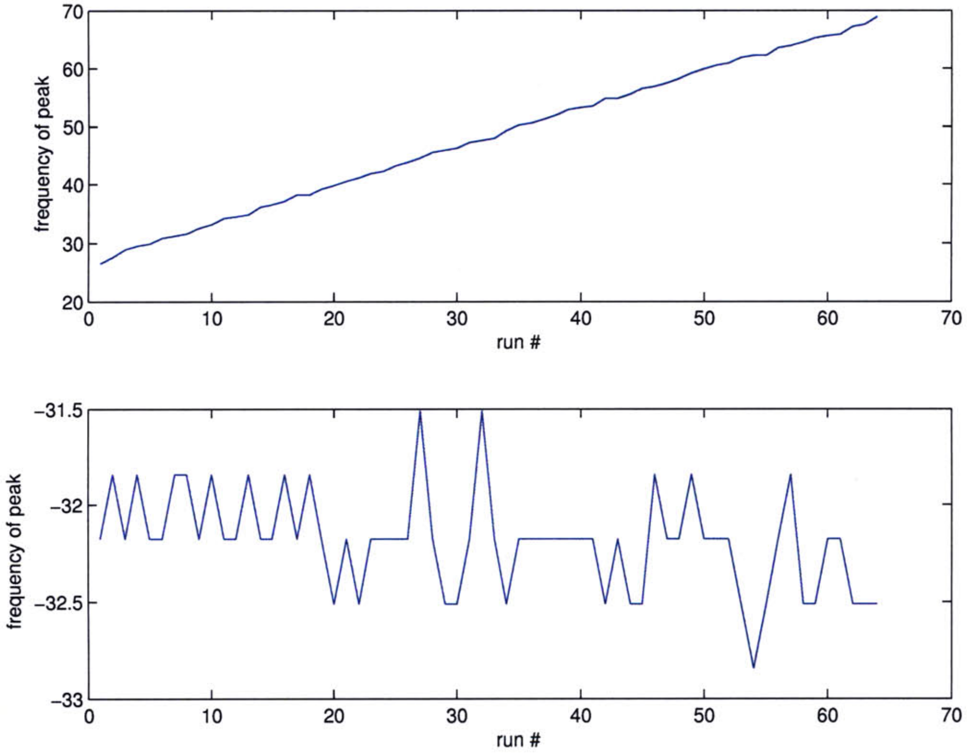

Figure 6-11: Top plot shows the drift from the Nalorac probe when the lock is on but the lock signal is marginal. Bottom is the drift for the same lock signal, but with the lock simply turned off.

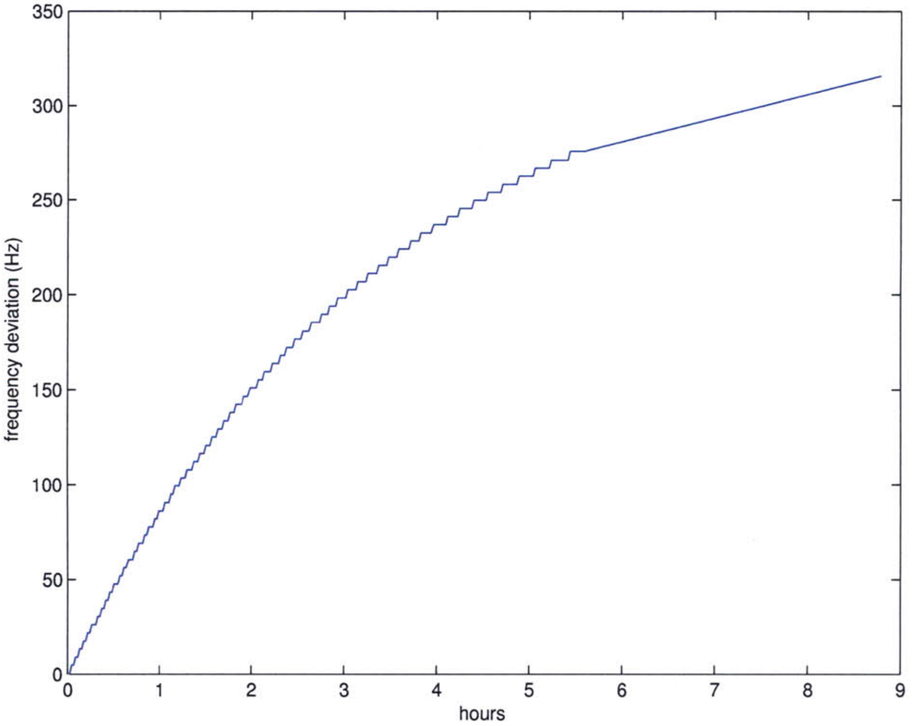

Figure 6-12: Plot of the drift of the water peak during a nearly 6-hour COSY experiment for the microslot probe. The linear part of the curve shows no data was gathered between 6 and 9 hours. At the 9th hour (3 hours after data collection stopped), a single acquisition was made, showing that the heating is not from the probe itself.

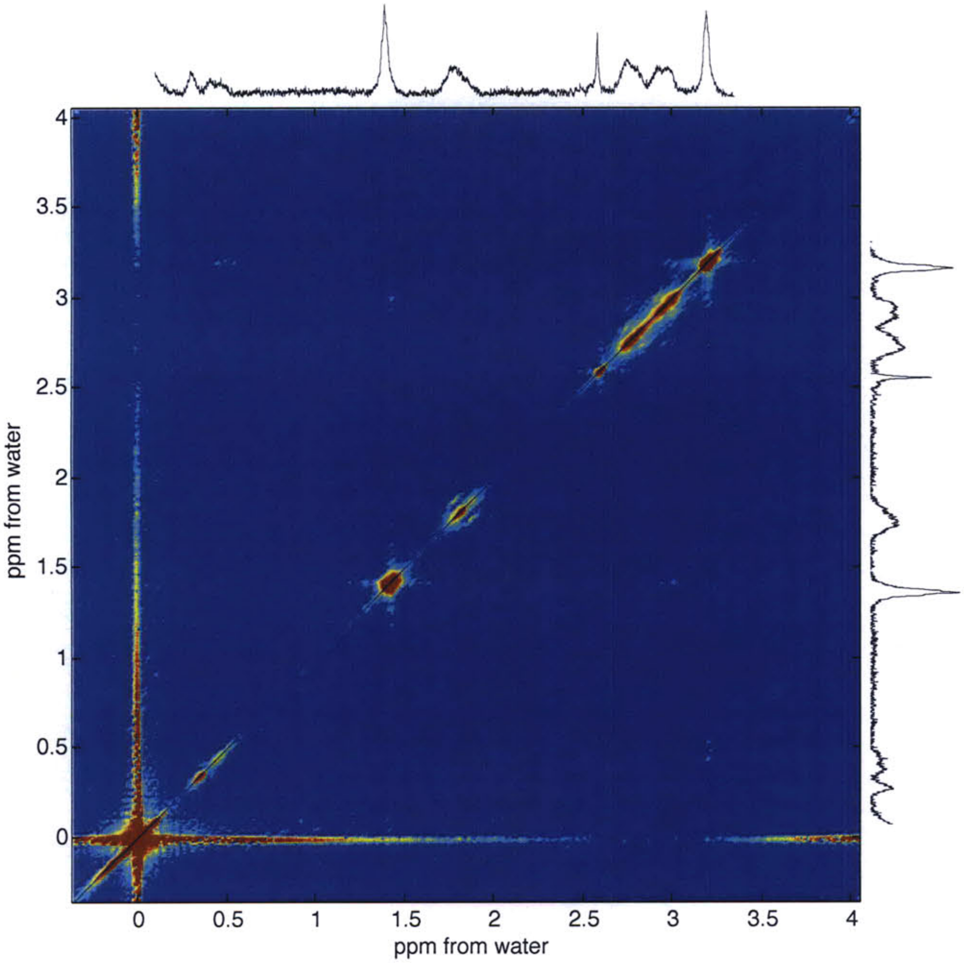

Figure 6-13: COSY spectrum from the microslot probe. lb=0.6, gf=0.08, lb1=0.61, sb1=0.078, gf1=0.4.

Amino Acid	Atom Name	# shifts	Avg shift	σ
alanine A	H	12280	8.19	0.63
	H^{α}	10494	4.26	0.45
	H^{β}	9658	1.37	0.28
arginine R	H	8011	8.23	0.61
	H^{α}	6882	4.29	0.48
	$H^{\beta 2}$	6001	1.80	0.30
	$H^{\beta 3}$	5522	1.78	0.29
	$H^{\gamma 2}$	5160	1.58	0.28
	$H^{\gamma 3}$	4629	1.56	0.29
	$H^{\delta 2}$	4985	3.12	0.30
	$H^{\delta 3}$	4390	3.11	0.28
	H^{ϵ}	2294	7.33	0.64
	$H^{\eta 11}$	281	6.83	0.50
	$H^{\eta 12}$	220	6.80	0.48
	$H^{\eta 21}$	245	6.77	0.46
	$H^{\eta 22}$	221	6.77	0.48
aspartic acid D	H	9737	8.34	0.60
	H^{α}	8272	4.61	0.34
	$H^{\beta 2}$	7474	2.77	1.08
	$H^{\beta 3}$	7080	2.72	1.10

Table 6.1: Amino acids in the DAR molecule.

6.4 Analysis

To analyze the 1D and 2D data for structural information, first consider the chemical shifts collected for the various amino acids in table 6.1 [11]. The most important rule in studying these systems is that amide protons will exchange with D_2O solvent, meaning the protons will be seen as water in the rapidly tumbling limit.

Looking at the simplest amino acid in the sequence, alanine (A), we expect the H proton with no signal, an H^{α} signal from 3 amino acids at 4.26 ppm, and an H^{β} signal at 1.37 ppm. Since we do not have a true reference signal like TetraMethySilane (TMS), the best we can do is calibrate the water signal. From Cavanaugh [18], we can expect the water signal to be at about 4.7 ppm. At approximately 3.25 ppm, we find the H^{β} signal. From the COSY plot in figure 6-13, we see a correlation with peak number 4 at about 0.5 ppm, very close to the 4.26 ppm predicted for the H^{α}. Even though the linewidth of the one-dimensional spectrum cannot distinguish between the 3 slightly different alanine sites on the molecule, the COSY spectrum clearly does.

In the case of aspartic acid (D), the H^{α} peak should be at 4.61 ppm, very close to the 4.70 ppm of the water. This peak is lost both due to the higher temperature in the microprobe and due to the water peak being too broad. We also lose the cross-peak to peak number 6, where we expect the H^{β} peaks (seen in the conventional probe, which has tighter water line width and lower sample temperature). The strong cross-peak correlation within peak 6 on the COSY plot is apparent, suggesting $H^{\beta 2}$ to $H^{\beta 2}$ coupling.

This feature is also seen in the Nalorac probe COSY plot. Finally, for arginine (R), we lose H, H^{ϵ} and $H^{\eta[11,12,21,22]}$ due to proton exchange. We expect the H^{α} proton to be coupled to the H^{β} protons, at about

2.9 ppm (peak 8), but we do not see this coupling on the microslot probe plot, and it is very faint in the commercial probe plot. It is assumed the experiment was not run long enough the extract this feature. The H^γ peaks are clearly at 3.0 ppm and are nicely cross-coupled to the H^β peaks from the microslot probe. It is clear also that within the H^γ and H^β peaks in the COSY, we can see coupling of one proton to the other over the carbon backbone. The last peak to identify on arginine is the H^δ region, at about 1.5 ppm from water. Looking closely at this peak, we see that there appears to be substructure, indicating the multiple arginines in the peptide, and although the resolution is limited, it is indeed present in the conventional probe spectrum. From the COSY plot, we see a nice two-peak correlation with the H^γ protons. There is not a strong coupling between H^δ peaks to indicate correlations in neither the Nalorac probe image nor in the microprobe data. The final peak assignment is shown in figure 6-14.

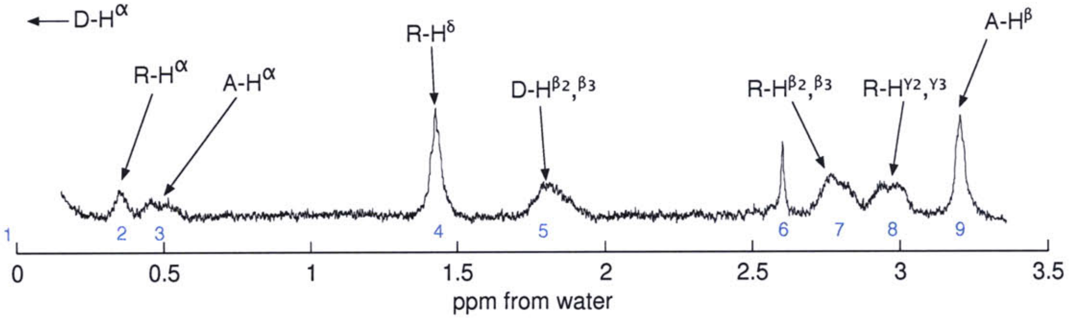

Figure 6-14: Final assignment of the DAR molecule to the 1D spectrum based on the spectrogram obtained from the microslot probe and the COSY plot. Note peak 6 represents an impurity present (also present in the Nalorac probe data).

Chapter 7

Results and Discussion

7.1 Contributions

The contributions of this thesis work can be summarized as follows:

1. The creation of a new type of magnetic probe for NMR that can scale from centimeters to micrometers (and potentially tens of nanometers) while still maintaining its electromagnetic properties. This microslot probe is based on planar waveguided circuits with specific boundary condition control to achieve flux concentration.

2. The microslot has been demonstrated to be the highest sensitivity planar detector to date. For sucrose, the sensitivity measured was $984/\mu\text{mol}/\sqrt{Hz}$, and approaches the best microcoil work [48].

3. The microslot has been demonstrated to have high RF homogeneity ($A_{270}/A_{90} > 0.97$) at RF frequencies due to current bunching on the sides of the conductor.

4. The microslot has been demonstrated to work at high NMR frequencies (500 MHz) with a circuit model that agrees strongly with network measurements.

5. The microslot has been fabricated with very simple manufacturing techniques. The general structure was made using chemical etching and the small slot in the microstrip was made using an excimer laser micromachining center. This rapid prototyping machine allowed a high iteration rate on designs, but conventional microfabrication techniques could be used to make microslots in the future. The microslot design should be easily fabricated even to scales less than 1 μm, in contrast to microcoils, which have only been made to an inner diameter of 75 μ via hand winding.

6. A microslot probe was made at widths 297 μm and 6.9 mm. Modeling was done between 60 μm and 6.9 mm, and a $1/r$ relationship was found. The field strengths from the two fabricated probes fit on

the curve. This result indicates that the same performance curves for microcoils can be obtained with microslots, while providing the added ability to scale to very small sizes.

7. The microslot probe was used to do two-dimensional spectroscopy on ≈ 1 nmol of a small peptide, or 10^{14} peptide molecules. Cross peaks were visible showing that at this small sample size, microslots can be used to elucidate protein and peptide structure. This is the first time that peptide measurement has been demonstrated on a planar probe with a volume of material this small.

7.2 Microslot Improvements

This research marks the beginning of a new inductive method for measuring spins using NMR. In its nascent stage, it has demonstrated the highest sensitivity of any planar probe and promises to improve sensitivity with decreasing scale. Still, there are many ways the microslot could be improved:

1. *Fabrication scaling.* This is the most important for sensitivity improvement. The current limit of detection for the 297 μm probe is approximately 2.1 nmol/$\sqrt{Hz}$ (SNR=3) for 100% H_2O. Based on the $1/r$ scaling curve shown in Chapter 3, the signal to noise ratio of a detector should scale as V/r, or r^2, for a spherical sample. We can then calculate the smallest microslot that should have a signal to noise ratio of 3 in 1s based on
$$\text{scale factor} = \sqrt{\frac{\text{SNR}}{\text{LOD}}}. \tag{7.1}$$
With the SNR for 100% water measured to be 2452 for 1.8 μmol of material, the scale factor is 28.6. The most sensitive LOD detector will be a 10.4 μm wide microslot, where the Limit Of Detection (LOD) is 76.1 pmol/$\sqrt{Hz}$. Based on the scaling of the sensitivity for water, this will correspond to about $3.9\times10^4/\mu\text{mol}/\sqrt{Hz}$, much higher than any published result. The fabrication of a 10μm wide microslot should be relatively easy using conventional microfabrication techniques.

2. *Spectral tails.* As was shown in Chapter 5 for water, the shape of the spectrum was non-Lorentzian and over 1/2 of the integrated signal was in the tails. Susceptibility matching of the probe could improve the sensitivity by close to a factor of 2. A preliminary attempt in which the microslot was filled with glass spheres did not improve the situation. A uniform coating of polyethylene on the surface of the probe is a more promising approach [9]. The best option is to match the susceptibility of copper with a metal such as palladium to the correct thickness. (The deposition of palladium must be electroplated rather than sputtered, due to argon contamination).

3. *Decreasing resistance.* The geometry of the microslot circuit board is the first of its kind and was not optimized for maximizing inductance and lowering resistance. These issues raise the general question of how to create boundary conditions given the constraints of a fixed surface area. There are techniques [10] that may allow for optimization given these constraints, but for geometric problems with expensive

function evaluation, they are nontrivial. Thickening the copper should provide improvements, as the conduction pathways for current will increase. Ideally, for structures above and below the skin depth regime, the cross-section of the conductor should be as tall as it is wide, which is more feasible as the structure size decreases.

4. *Microfluidics*. On the short term, integrating microfluidics is a key goal for the future of this project. The simple planar geometry of this structure makes it highly amenable to microfluidic integration. Namely, the slot itself could pose as an interesting outlet port for microfluidic integration. A sample cavity could be etched into the dielectric, or even better would be a cavity sandwiched on the top of the copper surface. One of the issues facing microslots and other microprobe technology is sample access for picoliter to nanoliter volumes. Capillary tubes do not scale much further than the 75-300 μm range currently being tested, because the capillary wall thickness versus sample volume ratio must increase in order to maintain mechanical strength. Ideally, if the homogeneity of the microslot could be improved by palladium plating, the sample could be placed directly on the surface of the probe, further improving both homogeneity and sensitivity. One tremendous contribution that could be offered by the integration of microslots and microfluidics is to CIDNP protein work, in which the protein and flavin sensitizer could be reflowed once the sensitizer is consumed.

7.3 Ultimate Microslot Scaling

Although scaling was covered in the previous section, questions remain about the ultimate scaling of the microslot. Based on the analysis above, we can plot the SNR/$\sqrt{Hz}$ and number of molecules detectable for the sensitivity from 40 nm to 297 μm. We see in figure 7-1 the 10 μm cutoff point where the sensitivity is approximately 3, and at length scales much smaller than 10 μm it becomes increasingly difficult to measure the spins in a reasonable amount of time. One contributing factor to this is that the scaling law changes from $1/r$ to $1/r^{1/2}$ below the skin depth of 2.64 μm at 600 MHz.

Detecting quantities of spins below a picomol is shown to be difficult at room temperature but is very feasible at low temperatures. Recall from equations 2.10 and 2.11, the SNR scales as $T^{3/2}$. If we consider a temperature of 100 mK, where the Boltzmann approximation is still valid and copper does not superconduct (it does not at any temperature), we can plot this as well in figure 7-1. Here we see we can detect 2.6×10^6 spins in about 1 s at 40nm. If we could collect data for 1×10^4 s (under 3 hours), we could detect about 2.6×10^4 spins, which is about a factor of 10 within the best work done for mechanical detection to date [69]. Thus, microslots could have a future in the most sensitive spin detection experiments, especially when combined with mechanical detection techniques.

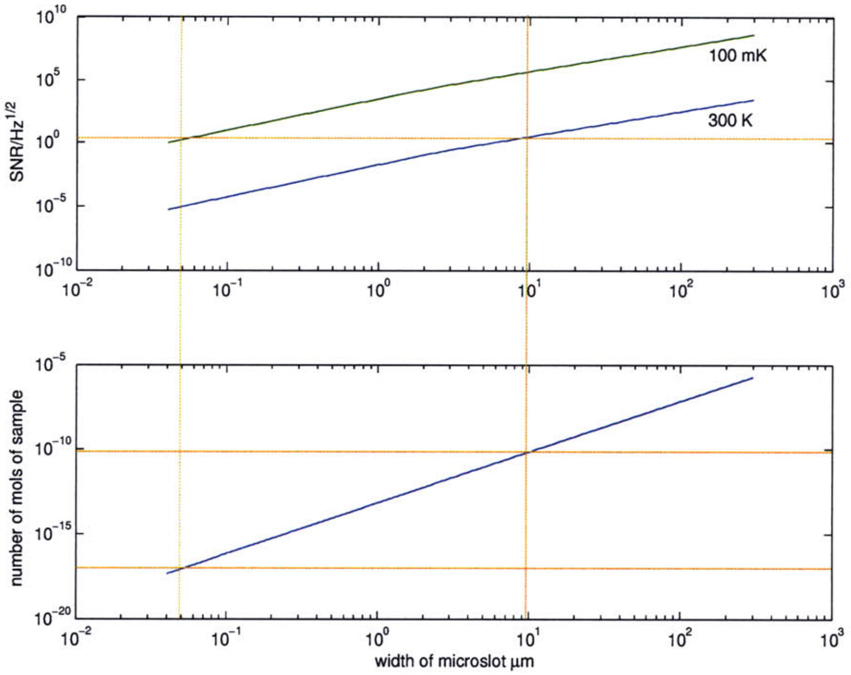

Figure 7-1: Sensitivity scaling of the microslot as a function of the microstrip width at room temperature (300 K) and at 100 mK. At room temperature, the limit of detection of nuclear spins is about 100 fmol-10 pmol and about 10×10^4 at 100 mK.

7.4 Future NMR Applications

There are a number of potentially interesting uses for microslots in the field of NMR:

1. *Cell/neuron spectroscopy.* Because the microslot probe is planar and has high sensitivity, it could be a platform for detecting molecular transport in cells/neurons. (With microcoils, sample access for these biological samples would be very difficult).

2. *Solid-state NMR.* Sample spin speed has a tremendous effect on solid linewidth [18]. With a small sample and a microslot, one may be able to spin samples at much higher frequencies. Such an innovation could lead to a new type of MEMS solid-state NMR.

3. *TOCSY and QI.* Both TOtal COrellation SpectroscopY (TOCSY) transfers [18] and Quantum Information (QI) gates [59] can be implemented with smaller error from shorter pulse widths for a $\pi/2$ pulse. Given that B/i is 10-30× higher for a microslot probe than for a conventional probe or cooled probe, enormous benefits could be gained.

4. *Microimaging.* For microimaging of cells and other microscopic objects, a microslot could pose an enormous benefit for an imaging setup as the field gradients and spin probe could be made on a single substrate with high sensitivity.

5. *HPLC-NMR.* High Performance Liquid Chromatography (HPLC) has had enormous impact in chemistry labs in which on-line spectroscopy during separations is used. Integrating a microfluidic system with a microslot for doing HPLC could be of great benefit for chip-scale chemical laboratories.

6. *Parallel acquisition.* Given the ease of fabrication of a microslot probe and its planar geometry, it has great potential for any problem that involves inspecting samples in parallel or HPLC separations. Microslot probes also have the ability to do continuous NMR acquisition, i.e. while spins are relaxing in one sample tube, useful data could be collected using additional probes.

7. *Small molecule combinatorial chemistry.* Combinatorial chemistry [60] relies on mass spectroscopy for creating a feedback process to select chemical pathways. With the much higher sensitivity and applicability to large-scale parallelism that microslots can provide, NMR, with its ability to do detection in the liquid phase, could have much greater impact.

8. *Table-Top NMR.* A holy grail for NMR is to do high resolution spectroscopy on a table-top system so that an entire room of expensive electronics and magnets could be replaced by a small and inexpensive table-top system. Since the sample volume required by microslots is much smaller than that required by conventional NMR, microslots could have high homogeneity from much more inhomogeneously broadened magnets than superconducting magnets. This may allow simple magnetic loop circuits that generally obtain part per thousand homogeneity over a 5mm tube to have part per million or billion homogeneity over a 10-100 μm sample diameter.

7.5 Other Applications

There are a range of non-NMR applications based on the simple design and ease of fabrication of microslots:

1. *Micromanipulation or heating of nanoparticles.* Work by Hamad et al. [34] has been useful for reversibly manipulating DNA and other biomolecules. Microslots could be used to make very local stimulators for precise drug delivery or on "lab on a chip" type scenarios, a sketch shown in figure 7-2. A rapidly varying and strong magnetic field could also be used to make ratchet motors using thermal motion of a magnetic particle.

2. *Electromagnetic imaging.* One immediate application of a microslot could be as a non-contact detector of the electromagnetic fields produced by powered integrated circuits. There is a burgeoning field of scanning microwave spectroscopy using the tip of a coaxial cable [91], a small hole in a waveguide, a microstrip resonator [84], or conventional SFM [89], to scan surfaces. It has been shown both for microwaves and optical wavelengths that by geometric boundary conditions, evanescent waves can obtain resolution much smaller than the diffraction limit [5] ($\lambda/10^6$ in demonstrated cases [46]). These techniques have been used to monitor individual digital lines using an EFM [38] and image passive

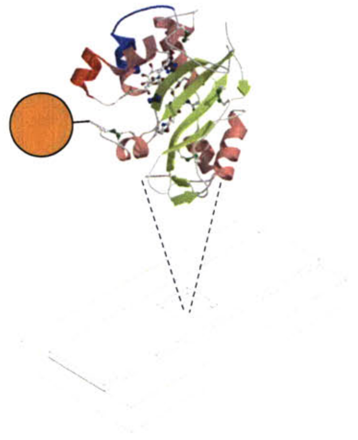

Figure 7-2: Sketch of a microslot could be used to control biomolecules attached to nanoparticles.

structures as small as 8μm using a dipole pattern on the tip of an STM [2]. A microstrip structure could be used to scan the electromagnetic signature of a running integrated circuit to learn about good and bad design, characterize faulty chips, and potentially replace expensive probe scanners.

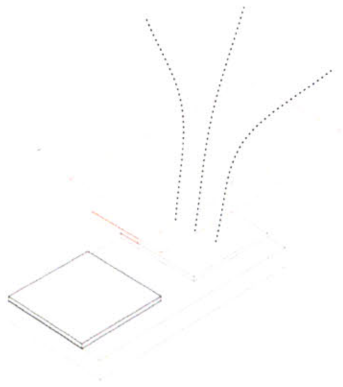

Figure 7-3: Sketch of pads on an integrated circuit with one pad being scanned by a microslot.

3. *Parasitic electronics*. Simple metal structures may be used as detectors of electric or magnetic fields within integrated circuits and circuit board designs. Conventional circuits generally operate in the basis of {V,I}, but could be extended to {E,B} in the RF regime, since any voltage or current in a circuit will produce a field that can be measured, and if the detector is small, then the impedance load of the detector can also be small (parasitic). As an example, parasitic electronics could potentially be useful for power amplifier designs that use feedback from the measured E field from a chip to confirm that the power output is stable. Calibration could then be based on geometry and laser-trimmed in the factory for proper power settings.

4. *High speed capacitive interconnect buses*. IBM has designs for the Blue Gene supercomputer that

used capacitive interconnects for high speed parallel data buses [28]. Figure 7-4 shows a slotline on a dielectric with symmetric protrusions creating a concentrated electric field at their interface with no magnetic component in the middle. This is a capacitive corollary to the inductive microslot and could also be arrayed and used as an element of a bus system.

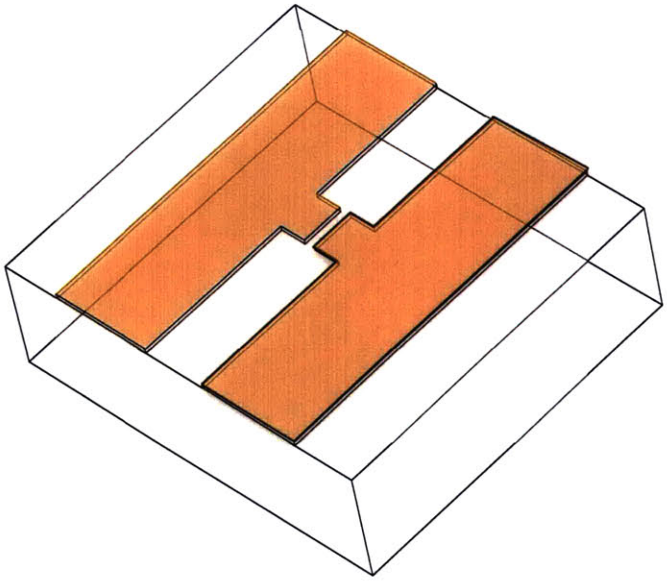

Figure 7-4: Slotline with a microdisturbance. This geometry creates a concentrated E-field, while the inductance in unaffected.

Appendix A

Introduction to NMR

For the sections that follow, basic knowledge of quantum statistics and quantum mechanics are assumed. For a good introduction to relevant aspects of quantum mechanics, consult [27] for a basic introduction related to NMR and [65] for a more detailed discussion. For quantum statistical mechanics, a number of good resources exist, most notably [40] [6].

A.1 Nuclear Paramagnetism for an Ensemble of Spin s Nuclei

Assuming the number of particles is fixed for a system of equilibrated, non-interacting nuclear spins at some finite temperature, we can derive the statistics of this system using a Gibbs canonical ensemble since magnetic work is being done. To begin, define T as

$$T = 1/k_B\beta. \tag{A.1}$$

For a quantum system, the Gibbs canonical thermal equilibrium density matrix is defined as

$$\rho(\beta) = \frac{e^{-\beta\mathcal{H}}}{\mathcal{Z}(\beta)}. \tag{A.2}$$

It is convenient to measure the density matrix in the eigenbasis of the Hamiltonian. We will only consider the reduced density matrix that acts exclusively on spin variables only. All other degrees of freedom will be termed "the lattice" [27]. Since $\mathrm{tr}(\rho) = 1$, $\mathcal{Z}(\beta) = \sum_m e^{-\beta\mathcal{E}_m}$. For N molecules of spin s with a Hamiltonian

$$\mathcal{H} = M \cdot B,$$

where

$$M = \sum_{i=1}^{N} \gamma\hbar I_i \tag{A.3}$$

is the total magnetization (the sum of the dimensionless angular momentum, I_i of all the spins). The measured value of I_i is an element of the set $m_i = -s, -s+1, \dots s$. $\gamma = e/2mc$ is the gyromagnetic ratio of the spins. If the magnetic flux density is in the z-direction,

$$\mathcal{E}_m = \gamma\hbar \sum_{i=1}^{N} m_i B_0. \tag{A.4}$$

Thus the partition function for the system is

$$\mathcal{Z} = \left[\sum_{m_i=-s}^{s} \exp(\beta B_0 \gamma\hbar \sum_{i=1}^{N} m_i) \right] = \left[\sum_{m_i=s}^{s} \exp(\beta B_0 \gamma\hbar m_i) \right]^N . \tag{A.5}$$

Solving the simple geometric series yields:

$$\mathcal{Z} = \left[\frac{\sinh\left(\beta\gamma\hbar B_0(s+1/2)\right)}{\sinh \beta\gamma\hbar B_0/2} \right]^N . \tag{A.6}$$

The Gibbs free energy is thus

$$\begin{aligned} G &= E - BM = -k_B T ln \mathcal{Z} \\ &= -N/\beta \ln[\sinh(\beta\gamma\hbar B_0(s+1/2))] + N/\beta \ln[\sin\left(\beta\gamma\hbar B_0/2\right)]. \end{aligned} \tag{A.7}$$

Using the small angle approximation where θ is small,

$$\sinh\theta \approx \frac{1}{2}(2\theta + 2\frac{\theta^3}{3!}) + \mathcal{O}(\theta^5) \tag{A.8}$$

and $\ln(1+x) = x - x^2/2 + x^3/3 - \dots$, we can solve for equation A.7:

$$G \approx G_0 - \frac{N\gamma^2\hbar^2 B_0^2 s(s+1)}{6k_B T} + \mathcal{O}(B_0^4). \tag{A.9}$$

Combining the magnetic susceptibility, $\chi = \partial\langle Mz \rangle \partial B_0|_{B=0}$, with $\langle M_z \rangle = \partial G/\partial B_0$ yields:

$$\chi = \frac{N\gamma^2\hbar^2 s(s+1)}{3k_B T}. \tag{A.10}$$

As a final note, computing the magnetization $\langle M_z \rangle$ from equation A.7 yields:

$$\begin{aligned} \langle M_z \rangle &= N\gamma\hbar[(s+1/2)\coth\left(\beta\gamma\hbar B_0(s+1/2)\right) - (1/2)\coth\left(\beta\gamma\hbar B_0/2\right)] \\ &= N\gamma\hbar B_s(\beta\gamma\hbar B_0 s), \end{aligned} \tag{A.11}$$

where B_s are the spin s Brillouin functions. For $s = \frac{1}{2}$, since $\coth(x) - (1/2)\coth(x/2) = (1/2)\tanh(x/2)$, the spin $\frac{1}{2}$ magnetization is

$$\langle M_z \rangle = (N\gamma\hbar/2)\tanh(\beta\gamma\hbar B_0/2). \tag{A.12}$$

A plot of this normalization as a function of temperature along with the Boltzmann approximation ($\tan\delta = \delta$) is shown below in figure A-1. The Boltzmann approximation is valid down to very low temperatures (< 0.1K).

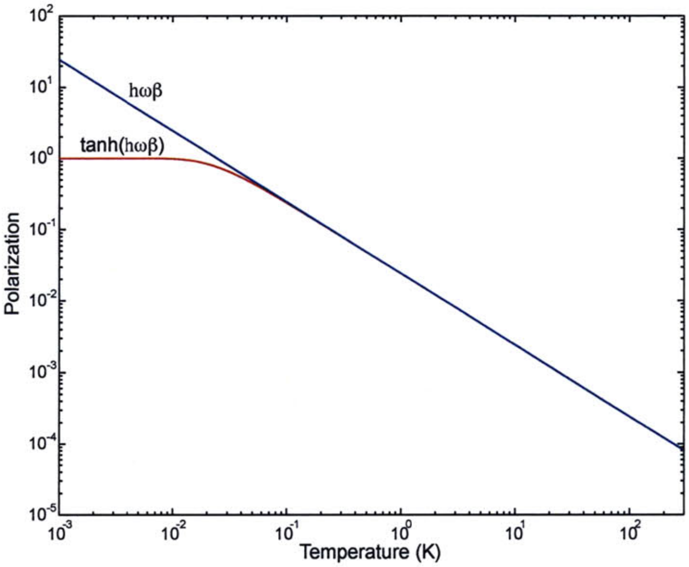

Figure A-1: Plots of the polarization versus temperature for an ensemble of spin particles and the Boltzmann approximation.

A.2 Nuclear Spin Dynamics of a Spin in a Static Field

We saw in the last section that a spin in a static, z-directed flux density, B_0, gave energies that were eigenvalues of spin I_z. From equation A.4, for a single spin, the time-dependent wave function is therefore

$$\Psi_{l,m}(t) = \Psi_{l,m} e^{-(i/\hbar)\mathcal{E}_m t}. \tag{A.13}$$

The most general solution is a linear superposition of the m states,

$$\Psi(t) = \sum_{m=-s}^{s} a_m \Psi_{l,m} e^{-(i/\hbar)\mathcal{E}_m t}. \tag{A.14}$$

The expectation value for the magnetization is thus

$$\begin{aligned}\langle\vec{\mu}(t)\rangle &= \int \Psi^*(t)\vec{\mu}\Psi(t)d\tau \\ &= \sum_{m,m'} \gamma\hbar a'^{*}_{m'} a_m \langle m'|\vec{I}|m\rangle e^{-(i/\hbar)(\mathcal{E}_{m'}-\mathcal{E}_m)t}. \end{aligned} \tag{A.15}$$

Starting with the μ_x term, it is useful to redefine I_x and I_y in terms of the raising and lowering operators I^+ and I^-:

$$I_x = \frac{1}{2}(I^+ + I^-),\ I_y = \frac{1}{2i}(I^+ - I^-), \tag{A.16}$$

where

$$\begin{aligned} I^+\Psi_{I,m} &= \sqrt{I(I+1) - m(m+1)}\Psi_{I,m+1}, \\ I^-\Psi_{I,m} &= \sqrt{I(I+1) - m(m-1)}\Psi_{I,m-1}. \end{aligned} \tag{A.17}$$

Therefore $\langle m'|I^{\pm}|m\rangle = 0$ unless $m' = m \pm 1$. Solving for μ_x for spin $\frac{1}{2}$,

$$\langle\mu_x(t)\rangle = \gamma\hbar[c^*_{1/2}c_{-1/2}\langle\frac{1}{2}|I_x| - \frac{1}{2}\rangle e^{-i\gamma B_0 t} + c^*_{-1/2}c_{1/2}\langle -\frac{1}{2}|I_x|\frac{1}{2}\rangle e^{i\gamma B_0 t}. \tag{A.18}$$

To simplify, express the normalization coefficients in terms of complex exponentials: $c_{1/2} = ae^{i\alpha}$ and $c_{-1/2} = be^{i\beta}$, where $a^2 + b^2 = 1$, giving:

$$\langle\mu_x(t)\rangle = \gamma\hbar ab\cos(\alpha - \beta + \omega_0 t),\ \text{where}\ \omega = \gamma B_0. \tag{A.19}$$

Similarly, $\langle\mu_y(t)\rangle = -\gamma\hbar ab\sin(\alpha - \beta + \omega_0 t)$ and $\langle\mu_z(t)\rangle = \gamma\hbar(a^2 - b^2)/2$. This motion yields a classical picture of a vector making a fixed angle to the z-axis processing in the x-y plane at the so-called Larmor frequency. Consult [79] for a more detailed discussion.

A.3 Spin Dynamics with a Rotating Magnetic Field

Consider a second magnetic field

$$\vec{B}(t) = \hat{z}B_0 + \hat{x}B_1\cos\omega_z t + \hat{y}B_1\sin\omega_z t. \tag{A.20}$$

From the Schrödinger equation,

$$-\frac{\hbar}{i}\frac{\partial\Psi}{\partial t} = -\vec{\mu}\cdot\vec{B}\Psi = \gamma\hbar[B_0 I_z + B_1(I_x\cos\omega_z t + I_y\sin\omega_z t)]\Psi. \tag{A.21}$$

Using the identity $e^{-iI_z\phi}I_x e^{iI_z\phi} = I_x\cos\phi + I_y\sin\phi$, we obtain:

$$-\frac{\hbar}{i}\frac{\partial\Psi}{\partial t} = -\vec{\mu}\cdot\vec{B}\Psi = \gamma\hbar[B_0 I_z + B_1 e^{-iI_z\omega_z t} I_x e^{iI_z\omega_z t}]\Psi. \tag{A.22}$$

It becomes easy to understand the evolution of Ψ by looking in the rotating frame:

$$\Psi' = e^{i\omega_z t I_z}\Psi,$$

or

$$\Psi = e^{-i\omega_z t I_z}\Psi'. \tag{A.23}$$

Therefore,

$$\frac{\partial\Psi}{\partial t} = -i\omega_z I_z e^{-iI_z\omega_z t}\Psi' + e^{-iI_z\omega_z t I_z}\frac{\partial - \Psi'}{\partial - t}. \tag{A.24}$$

Substituting this into equation A.22 and multiplying both sides by $e^{i\omega_z I_z t}$ gives

$$-\frac{\hbar}{i}\frac{\partial\Psi}{\partial t} = -\vec{\mu}\cdot\vec{B}\Psi = \gamma\hbar[B_0 I_z + B_1(I_x\cos\omega_z t + I_y\sin\omega_z t)]\Psi. \tag{A.25}$$

The effects of the rotating field have now been removed. On resonance, $\omega_z = -\gamma B_0$ yields:

$$-\frac{hbar}{i}\frac{\partial\Psi'}{\partial t} = -\gamma\hbar B_1 I_x\Psi'. \tag{A.26}$$

The dynamics are very similar to that of a static field rotation about the x-axis. The final dynamics for the single spin magnetization expectation values are for $\gamma B_1 = \omega_1$:

$$\begin{aligned}
\langle\mu_z(t)\rangle &= \langle\mu_z(0)\rangle - \cos\omega_1 t + \langle\mu_y(0)\rangle\sin\omega_l t \\
\langle\mu_y(t)\rangle &= \langle\mu_y(0)\rangle - \cos\omega_1 t + \langle\mu_z(0)\rangle\sin\omega_l t \\
\langle\mu_x(t)\rangle &= \langle\mu_x(0)\rangle.
\end{aligned} \tag{A.27}$$

A.4 The NMR Hamiltonian

The complete Hamiltonian for a nuclear spin is enormously complex, but one of the beautiful aspects of nuclear magnetic resonance is that the Hamiltonian can be reduced to a very simple expression with a few phenomenological constants. The Hamiltonian is broken up into three parts, as

$$\mathcal{H} = \mathcal{H}_{\mathcal{Z}} + \mathcal{H}_{\text{R.F.}} + \mathcal{H}_J. \tag{A.28}$$

The first term $\mathcal{H}_{\mathcal{Z}}$ is the Zeeman interaction, which for N spins on a molecule is of the form

$$\mathcal{H}_{\mathcal{Z}} = \sum_{k=1}^{N} \gamma I_{kz} B_0 = \sum_{k=1}^{N} \omega_k I_{kz} \text{ for a z-directed static field.} \tag{A.29}$$

The second term $\mathcal{H}_{\text{R.F.}}$ is the radio frequency field interaction. In the rotating frame of each spin on resonance,

$$\mathcal{H}_{\text{R.F.}} = -B_1 \sum_{k=1}^{N} \gamma_k (I_{kx} \cos\phi + I_{ky} \sin\phi). \tag{A.30}$$

The last term $\mathcal{H}_J$ is due to the electron-mediated nuclear spin-spin interaction, and is of the form

$$\mathcal{H}_{\mathcal{J}} = 2\pi \sum_{k<l} \vec{I_k} \vec{I_l} \vec{J_{kl}}. \tag{A.31}$$

In the weak coupling limit, $2\pi |J_{kl}| \ll \omega_{k,l}$, we can keep only one term of the scalar coupling:

$$\mathcal{H}_{\mathcal{J}} = 2\pi \sum_{k<l} J_{kl} I_{kz} I_{lz}. \tag{A.32}$$

The full dipolar term and quadrupolar terms rarely show up in solution NMR since these interactions are averaged away by rapid tumbling of the molecules.

A.5 Spin Echos and CPMG

Refocusing affects time-reversal of the Hamiltonian [56] only in the absence of irreversible spin-spin relaxation. However, the relaxation time T_2^* is reversible while T_2 relaxation persists. Through refocusing it seems possible to reverse the effects of T_2^* spectral broadening. This was Erwin Hahn's discovery, which essentially started the field of pulse NMR [79]. Consider the spin echo pulse sequence in figure A-2. If there is no relaxation, the density operator at time 2τ using product operators is $-I_y$, the same as it was after the I_{x90} pulse. Considering the effects of T_2^*, let us presume the signal is a superposition of signals from small volumes of spins resonating at slightly different frequencies. For simplicity we assume that each microscopic volume contains a large number of spins resonating at the same frequency, creating isochromats. Up until the so-called π pulse is applied, the spins precess out of phase with each other, such that the free induction decay

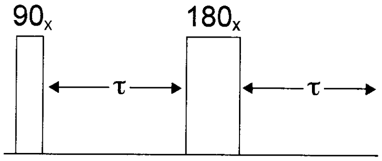

Figure A-2: Basic spin echo sequence that demonstrates the difference between reversible and irreversible coherence times.

of nuclear spin magnetization detected by the coil decays with a time constant T_2^*. However, the spins are out of phase in a geometric way, resulting in no loss of information other than through irreversible T_2 relaxation. Figure A-3 shows two graphical illustrations of the spin echo. The first plot shows the phase versus time of the spin echo, the second shows isochromatic spin vectors on the Bloch sphere. The isochromats begin to diverge causing T_2^* relaxation. After the π pulse, the isochromats begin to converge again and finally meet at the -y–axis at a time 2τ later.

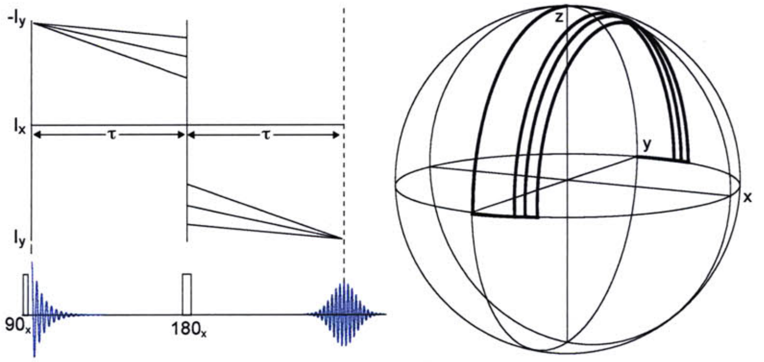

Figure A-3: Two different graphical ways to understand the spin echo. On the left is the angle versus time of isochromats in the transverse plane. On the right is the motion of the spin vectors on the Bloch sphere.

This is an interesting experiment because it shows how to measure information about the spin system for longer time scales than the inhomogeneity would allow. The Carr-Purcell sequence is essentially a spin echo followed by a train of π pulses spaced 2τ apart. This experiment allows one to measure the irreversible spin-spin coherence time, since the only term that does not refocus is the relaxation time T_2. One simply measures the echo envelope at $2n\tau$ where $n = 1, 2, \ldots$.

It is difficult to create a perfect π pulse and hence perform a Carr-Purcell sequence without accumulating large errors. Meiboom and Gill created a pulse sequence (CPMG) very similar to that of Carr and Purcell, but with a few key changes [57] [30]. The first change was to alternate the phase of the π pulses between the +x and -x–axes. The second change was to introduce a $\pi/2$ phase shift for the first pulse. Meiboom and Gill were the first to show that these two changes would not accumulate errors–one could remove the systematic experimental error. A consequence of this modified pulse sequence is that all echos have the same phase rather than alternating by 180°.

A.6 2D Fourier Spectroscopy (COSY)

Two-dimensional techniques were an extremely powerful development in the history of NMR. Jeener first explored two-dimensional Fourier transformation for NMR but it was Ernst who fully appreciated the power of this method [79]. The power of 2D COrrelation SpectroscopY (COSY) is that it allows separation of terms in the Hamiltonian to determine properties of molecular systems. Chemical shifts can be fully distinguished from scalar coupling, and the locations of peaks on a 2D plot show all the coupling relationships in a molecule. These observations allow one to work backwards towards constructing a model of a particular molecule. COSY gives NMR unprecedented power to elucidate molecular structure in biology, chemistry and medicine, supporting techniques such as x-ray crystallography and FTIR spectroscopy.

The basic 2D experiment is shown in figure A-4. This pulse sequence collects an FID that is a function of the two times t_1 and t_2. Then one takes a 2D Fourier transform of the result. Using the product operator formalism for a 2-spin J-coupled system, the density operator evolution for the experiment is:

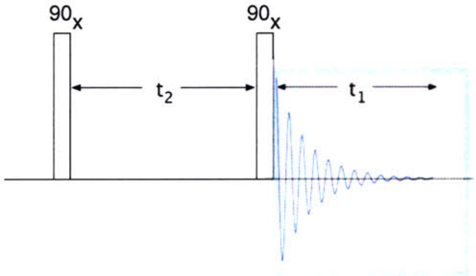

Figure A-4: Basic COrrelation SpectroscopY (COSY) experiment.

$$\sigma_0 \xrightarrow{(\pi/2)(I_{kx}+I_{ix})} \sigma_1 \xrightarrow{\omega_k t_2 I_{kz}} \xrightarrow{\omega_t t_1 I_{lz}} \xrightarrow{\pi J t_1 2 I_{kz} I_{lz}} \sigma_2 \xrightarrow{(\pi/2)(I_{kx}+I_{lx}} \sigma_3 \xrightarrow{\omega_k t_1 I_{kz}} \xrightarrow{\omega_l t_1 I_{lz}} \xrightarrow{\pi J t_1 2 I_{kz} I_{lz}} \sigma_4. \tag{A.33}$$

The equilibrium state $\sigma_0 = I_{kz} + I_{lz}$ is transformed into $\sigma_1 = -I_{ky} - I_{ly}$. After precession and J-coupling, we generate

$$\begin{aligned} \sigma_2 = &- \left[I_{ky} \cos\omega_k t_2 - I_{kx} \sin\omega_k t_2\right] \cos\pi J t_2 \\ &- \left[I_{ly} \cos\omega_l t_2 - I_{lx} \sin\omega_l t_2\right] \cos\pi J t_2 \\ &+ \left[2I_{kx} I_{lz} \cos\omega_k t_2 + 2I_{ky} I_{lz} \sin\omega_k t_2\right] \sin\pi J t_2 \\ &+ \left[2I_{kz} I_{lx} \cos\omega_l t_2 + 2I_{kz} I_{ly} \sin\omega_l t_2\right] \sin\pi J t_2. \end{aligned} \tag{A.34}$$

Next, we apply a pulse, yielding

$$\begin{aligned} \sigma_3 = &- \left[I_{kz} \cos\omega_k t_2 - I_{kx} \sin\omega_k t_2\right] \cos\pi J t_2 \\ &- \left[I_{lz} \cos\omega_l t_2 - I_{lx} \sin\omega_l t_2\right] \cos\pi J t_2 \\ &- \left[2I_{kx} I_{ly} \cos\omega_k t_2 + 2I_{kz} I_{ly} \sin\omega_k t_2\right] \sin\pi J t_2 \\ &- \left[2I_{kz} I_{ly} \cos\omega_l t_2 + 2I_{ky} I_{lz} \sin\omega_l t_2\right] \sin\pi J t_2. \end{aligned} \tag{A.35}$$

Pausing for a moment to look at the observable signal

$$s(t_1, t_2) = s(0,0)\mathrm{tr}\{\sigma(t_1, t_2)\sum I_k^+\}, \tag{A.36}$$

where $I_k^+ = I_{kx} + iI_{ky}$. Only terms with $p = -1$ are observable due to the single polarization of the detector. Hence the observable terms are

$$\begin{aligned}\sigma_3^{obs} &= I_{kx}\sin\omega_k t_2 \cos\pi J t_2 \\ &+ I_{lx}\sin\omega_l t_2 \cos\pi J t_2 \\ &- 2I_{kz}I_{ly}\sin\omega_k t_2 \sin\pi J t_2 \\ &- 2I_{ky}I_{lz}\sin\omega_l t_2 \sin\pi J t_2.\end{aligned} \tag{A.37}$$

Again, after chemical shift and J-coupling evolution, we are left with the final state:

$$\begin{aligned}\sigma_4^{obs} &= [I_{kx}\cos\omega_k t_1 + I_{ky}\sin\omega_k t_1]\sin\omega_k t_2 \cos\pi J t_2 \cos\pi J t_1 \\ &+ [I_{kx}\cos\omega_k t_1 + I_{ky}\sin\omega_k t_1]\sin\omega_k t_2 \sin\pi J t_2 \sin\pi J t_1 \\ &+ [I_{lx}\cos\omega_l t_1 + I_{ly}\sin\omega_l t_1]\sin\omega_k t_2 \cos\pi J t_2 \cos\pi J t_1 \\ &+ [I_{lx}\cos\omega_k t_1 + I_{ly}\sin\omega_l t_1]\sin\omega_k t_2 \sin\pi J t_2 \sin\pi J t_1.\end{aligned} \tag{A.38}$$

The observable signal (with relaxation) is therefore

$$\begin{aligned}s(t_1, t_2) &= e^{i\omega_k t_1}e^{-(t_1+t_2)\lambda}[\sin\omega_k t_2 \cos\pi J t_2 \cos\pi J t_1 + \sin\omega_l t_2 \sin\pi J t_2 \sin\pi J t_1] \\ &+ e^{i\omega_l t_1}e^{-(t_1+t_2)\lambda}[\sin\omega_l t_2 \cos\pi J t_2 \cos\pi J t_1 + \sin\omega_k t_2 \sin\pi J t_2 \sin\pi J t_1].\end{aligned} \tag{A.39}$$

Taking the Fourier transform for the function $e^{i\omega_A t}e^{-t\lambda}$ yields the complex Lorentzian peak:

$$Z_A(\omega) = \frac{\lambda}{\lambda^2 + (\omega - \omega_A)} + \frac{i(\omega - \omega_A)}{\lambda^2 + (\omega - \omega_A)} = a_A(\omega) + id_A(\omega),$$

where $A = \{k, l\}$. Since $\sin\omega t_1 = (e^{i\omega t_1} - e^{-i\omega t_1})/2i$ and $\cos\omega t_1 = (e^{i\omega t_1} + e^{-i\omega t_1})/2i$, there will be peaks at $\omega_A \pm J$ along the ω_2–axis. Similarly, along the ω_1–axis there will be peaks at $\pm\omega_A \pm J$. To place the entire signal on positive axes for both ω_1 and ω_2, take the cosine transform along the ω_1–axis:

$$\mathcal{F}^C(s(t)) = \int_{-\infty}^{\infty} s(t)\cos\omega t dt = \frac{\mathsf{S}(\omega) + \mathsf{S}(-\omega)}{2}, \tag{A.40}$$

where $\mathsf{S}(\omega)$ is the Fourier transform of $s(t)$. For a cosine transform, signals that are antisymmetric about the origin of ω_1 yield pure dispersive Lorentzians. Thus, terms with $\sin\omega_A t_2 \cos\pi J t_2 \cos\pi J t_1$ add modulations that yield in-phase dispersive signals:

$$s_A^{id}(\omega_1, \omega_2) = [d_A(\omega_1 - J) + d_A(\omega_1 + J)][d_A(\omega_2 - J) + d_A(\omega_2 + J)]. \tag{A.41}$$

Terms symmetric about the origin yield pure absorptive Lorentzian. Terms with $\sin\omega_A t_2 \sin\pi J t_2 \sin\pi J t_1$ add modulations that yield antiphase absorptive signals:

$$s_A^{aa}(\omega_1, \omega_2) = [a_A(\omega_1 - J) - a_A(\omega_1 + J)][a_A(\omega_2 - J) - a_A(\omega_2 + J)]. \tag{A.42}$$

The final results are summarized graphically in figure A-5. Along the line $\omega_1 = \omega_2$ is a normal dispersive 1D spectrum composed of chemical shifts and J-couplings together. In 2D, the J-coupling terms cause off-diagonal peaks to appear, separating terms in the Hamiltonian. Peaks on the off-diagonal axis, $(\omega_1, \omega_2) = (\omega_k, \omega_l), (\omega_l, \omega_k)$, represent correlations between spins that lead to inference about molecular structure. For large molecules with complex conformations, 2D methods are extremely useful.

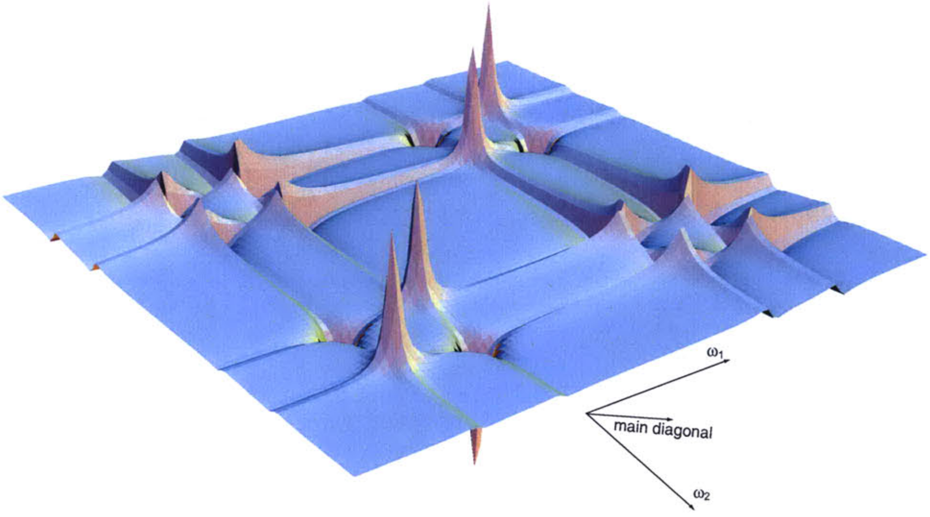

Figure A-5: COSY plot for two coupled heteronuclear spins showing chemical shift evolution separated from J-coupling.

Appendix B

Introduction to Proteins and Structure Determination

The genetic codons in DNA encode 20 standard amino acids shown in B-1. In proteins, the α-carboxyl group of one amino acid joins to the α-amino group of another to form a peptide bond with the production of water, as shown in figure B-2. The hydrolysis reaction is thermodynamically downhill over the synthesis step, thus the formation of peptide bonds requires a free energy input. The peptide bond forms a rigid planar unit, as shown in figure B-3, because the carbon-nitrogen bond has partial double-bond character. On either side, the peptide bond has a large degree of rotational freedom. It is the rigidity of the peptide backbone that enables proteins to have a well-defined form, and the freedom of rotation allows proteins to fold in many ways. The combination of these effects, in addition to steric hindrances, gives us the Ramachandran plot that dictates the two major and one minor regions of secondary structure: β, α, and L (left-handed α-helical) [22].

B.1 Alpha- and Beta-Helices

This structure has a ϕ, ψ pair of angles of approximately -60° and -50°, respectively. The α-helix has 3.6 residues per turn at 1.5 $\AA$ per residue, hydrogen bonds between C'=O of residue n, and NH of residues $n + 4$. The dipole moments of the peptide units align to create a large dipole moment, crucial to stabilizing this structure. The right-handed turn is the only permissible configuration due to steric collisions, an example shown in B-4. For stability, a pair will often form a coiled-coil, the basis for fibrous proteins. These structures are so stable that they can form strands up to 100nm in length. Some common motifs are 2, 3, and 4 helix bundles in which 2-4 helices are arranged in parallel or antiparallel. Another common motif is the helix-turn-helix, or EF-hand motif. The most common α structure is the globin fold, comprised of 8 helices that form a pocket in which the heme group is bound.

The β-helix, discovered in 1993, is a wide coiled helix formed by parallel β strands separated by flexible

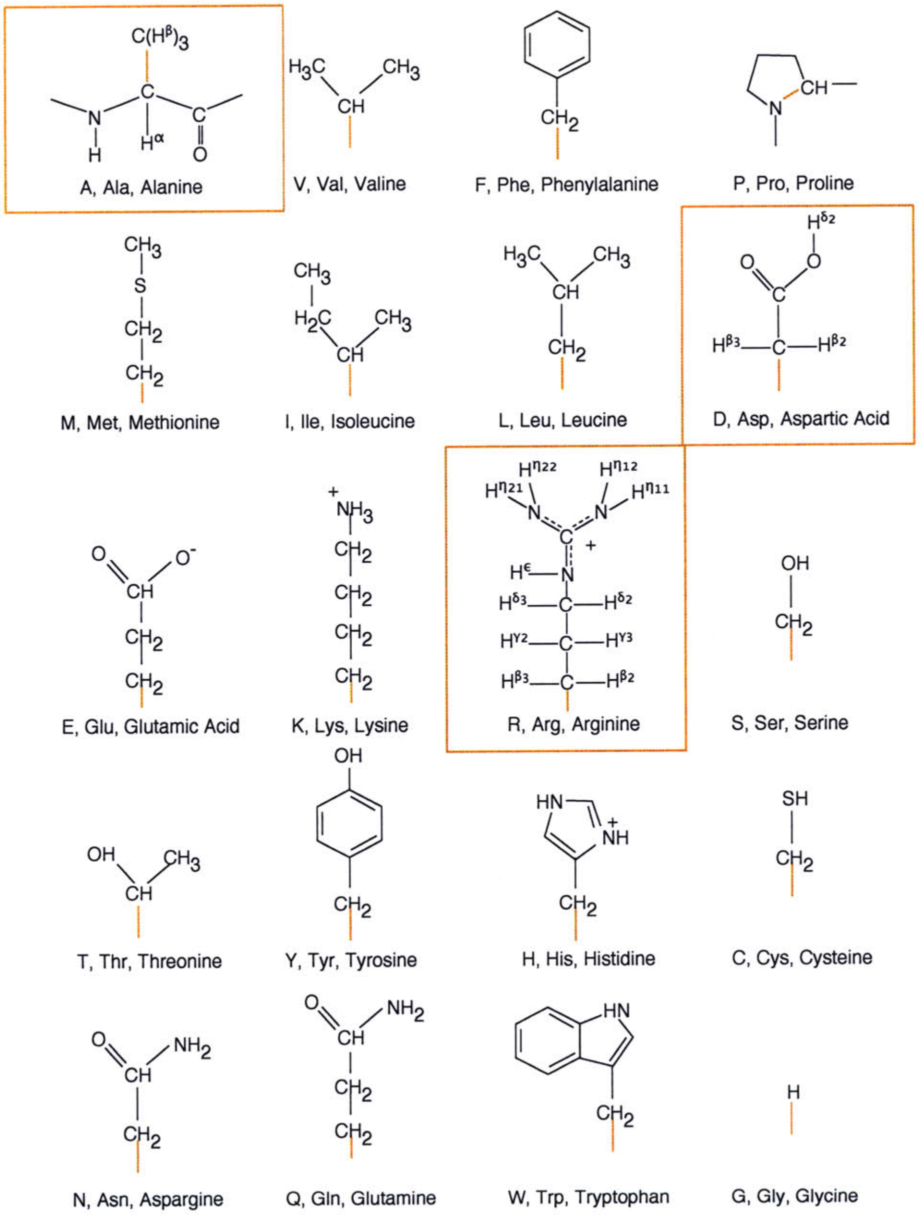
A, Ala, Alanine
V, Val, Valine
F, Phe, Phenylalanine
P, Pro, Proline
M, Met, Methionine
I, Ile, Isoleucine
L, Leu, Leucine
D, Asp, Aspartic Acid
E, Glu, Glutamic Acid
K, Lys, Lysine
R, Arg, Arginine
S, Ser, Serine
T, Thr, Threonine
Y, Tyr, Tyrosine
H, His, Histidine
C, Cys, Cysteine
N, Asn, Aspargine
Q, Gln, Glutamine
W, Trp, Tryptophan
G, Gly, Glycine

Figure B-1: The 20 L-amino acids. Only the side chains are shown except for alanine, which is shown with its backbone. The boxed amino acids are the components of the peptide analyzed in Chapter 6.

loop regions. There are two types: The two-stranded and three-stranded β-helix. The former has a helix that has two β strands per turn of the helix and two loop regions. This structure is repeated 3 times in extracellular bacterial proteinases to form a right-handed coil with a hydrophobic core. The basic form contains 18 amino acids, 3 in each β strand and 6 in each loop. A specific amino acid pattern is Gly-Gly-X-Gly-X-Asp-X-U-X (where X is any amino acid, and U is a large hydrophobic one like leucine). The loops are stabilized by calcium ions binding to the aspartic acid (Asp) residue. The three-stranded helix has two strands arranged adjacent to each other and a third almost perpendicular to the other two. One loop is formed from two

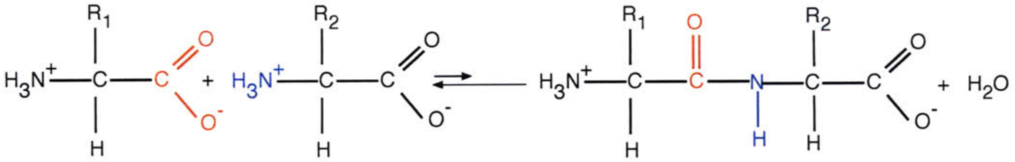

Figure B-2: Formation of a peptide bond.

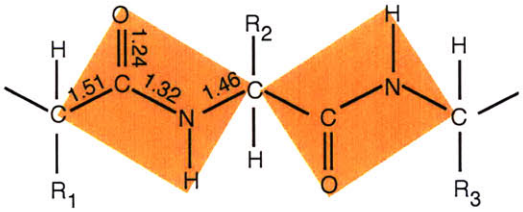

Figure B-3: Peptide bond with bond lengths shown in Å.

invariant residues, while the other two loops are long and form the active site. The interior is packed with hydrophobic groups, both polar and charged, with their side chains linearly arranged along the helical axis. The three-stranded helix is more prevalent and is found in pectate lyase and the bacteriophage P22 tailspike protein.

B.2 Beta Sheets

β-sheets, built from discontinuous regions of the polypeptide chain, are the second major structural element in proteins. β strands are aligned adjacent to each other so that hydrogen bonds can form between the C'=O and NH groups between strands. The sheet that is formed is pleated. The strands can act in a parallel, antiparallel, or mixed fashion, a simple example shown in figure B-5. Almost all β sheets have right-handed twisted strands. The β domain structure is the most diverse. Some common motifs are the $\beta - \alpha - \beta$ motif (forming a parallel configuration), the Greek-key motif, the up-down motif, and the jelly-roll motif. β-sheets tend to self-assemble into fibrous structures. These fibers can be used as nanofibers for many protein-material applications [90].

B.3 Water

The structure of water can be described in two parts. The first is the structure of the molecule itself and the second is the network of bonds between them. The molecule itself is a polar molecule, in which the oxygen nucleus draws electrons away from the hydrogen nuclei. The result is a triangular shape shown in figure B-6. At liquid temperatures, water forms an extensive network of hydrogen bonds. A positively charged region in one water molecule tends to orient itself towards a negatively charged region of a neighbor. In ice, a regular

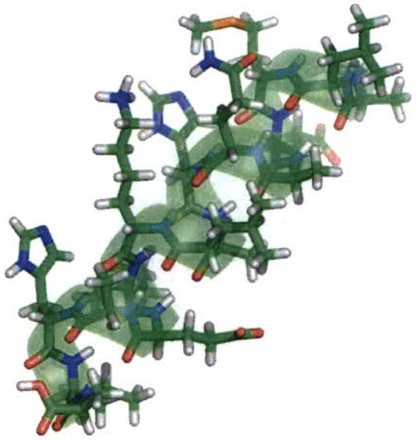

Figure B-4: Picture of a 16 residue α-helix, showing the stick-model amino acids. Rendered using PyMOL [25].

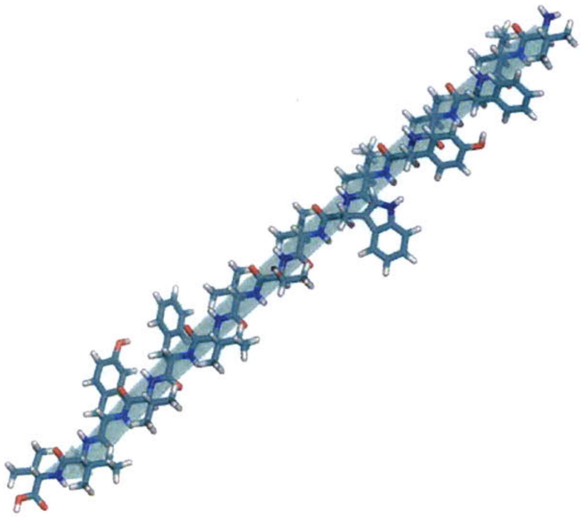

Figure B-5: Picture of a 16 residue β-sheet, showing the stick-model amino acids. Rendered using PyMOL [25].

crystalline structure of hydrogen bonds exists with hexagonal symmetry. The coordination of an individual molecule is tetragonal, as each molecule is bonded to 4 neighbors. Liquid water undergoes constant breaking and reorganization of hydrogen bonds on a picosecond timescale, but on average the molecules form a random network with an average of 3.4 neighbors. From the ice to liquid state, the regular hexagonal packing of water gives way to a disordered network. As the temperature increases in the liquid state, water molecules gain enough energy to bend and break their hydrogen bonds. The size of ordered clusters begins to decrease, but the hydrogen bonding is still considerable (i.e. at least one hydrogen bond). In the gaseous state, water molecules are no longer hydrogen-bonded to each other [7].

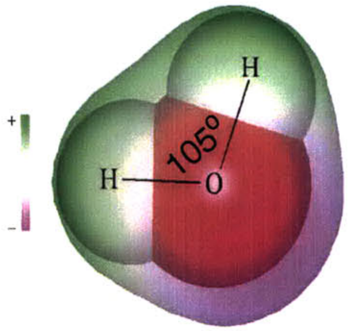

Figure B-6: The schematic and orbital versions of water.

Water has a dielectric constant of about 80, due to its polarity and ability to shield ions by forming solvent shells around them. As a result, water is an excellent solvent for polar molecules and is effective at grouping together nonpolar molecules to minimize their solvent surface area. The latter capability is the basis for the *hydrophobic interaction.* This hydrophobic interaction is one of the most important principles in protein structure - proteins pack hydrophobic side chains into the interior of the molecule. The problem is that the protein backbone is highly polar. The solution is the formation of regular secondary structure. The hydrogen bond donor NH and acceptor C'=O form a hydrogen bond, as part of either an α-helix or a β sheet. The final tertiary structure of a protein is fundamental to the function of the protein. This three-dimensional shape results by forming a hydrophobic core surrounded by a hydrophilic shell to favorably interact with water's polar structure.

Furthermore, one of the important pieces of protein-protein function is *specificity.* Specificity is the formation of a weak set of noncovalent bonds: hydrogen bonds, ionic bonds and van der Walls attractions. Hydrogen and ionic bonds are stronger if water is present. By having a few isolated bonds, water will tend not to compete for hydrogen bonds because it is energetically more favorable for the water molecules to remain part of the large hydrogen-bonded network. Thus a ligand binding site can remain completely dry and form a strong protein-protein interface.

Due to water's extensive hydrogen bonding network, when a protein is placed in water, the *bound* form of water is integrated, or immobilized from complete freedom of rotation. When a protein is crystallized, this bound water crystallizes as part of the structure of the protein and typically accounts for nearly half of the mass of the crystal. These bound water molecules are important for connecting a protein to the rest of the hydrogen bonding network and maintaining protein solubility.

B.4 Structure Determination

B.4.1 X-ray Crystallography

X-ray crystallography is a tool that enables high resolution ($\approx 1\mathring{A}$) three-dimensional models of crystallized proteins to be obtained by diffracting short wavelength electromagnetic radiation off the crystal planes of a protein. Bragg's Law governs the angle of diffraction for a given crystallographic plane separation d and a wavelength λ, as $2d \cdot \sin\theta = \lambda$. A major problem in x-ray diffraction is that it is not holographic, that is, the phase of the wave is not directly obtainable. Without the phase, the full three-dimensional structure cannot be determined. By using doped heavy metals in a technique called *multiple isomorphous replacement*, phase can be determined. (Jerome Karle was awarded the Nobel Prize in chemistry for his contribution for his work [22]).

Another technique called *multiwavelength anomalous diffraction* can also be used. From the amplitude and phase information, one can calculate an electron density map. The resolution of such a map varies from about $5\mathring{A}$ for coarse molecular shape, to about $1\mathring{A}$ for individual atoms. From an amino acid sequence and judicious placement of water molecules, a model that fits the electron density map is made. The whole process is reasonably automated and can be done in a few days. Two problems with x-ray crystallography are that not all proteins can be crystallized and protein dynamics can only rarely be measured.

B.4.2 NMR

NMR is an indirect tool for obtaining protein structure. Many nuclei such as ^{1}H, ^{13}C, ^{15}N and ^{31}P have a magnetic moment, or *spin*. When placed in a large static magnetic field, some spins (approximately 1 in 10^4) will align with this field. Radio frequency fields can excite transitions of the nuclear states to produce a signal that probes the local chemical environment of each atom in a molecule (see Appendix A for more details). The chemical environment is represented as a shift in the frequency of the spin as it experiences a slightly different local field environment. This effect is called a *chemical shift*. This can be degenerate for chemically equivalent species, such as protons in methane. To disambiguate a crowded spectrum, NMR spectroscopists have come up with ingenious techniques for drawing correlations between atoms to reveal which atoms are connected to each other. COrrelation SpectroscopY or COSY, is an experiment that reveals covalent bonding relationships between atoms in residues (e.g. an amino proton connected via 3 bonds to the C_α atom). From this map, one can use a fingerprint for each type of amino acid to label each residue along the chain and calculate the peptide backbone rotation angles.

Another technique, known as Nuclear Overhauser Effect SpectroscopY, or NOESY, develops proximity (less than $5\mathring{A}$) by means of relaxation via dipolar coupling. This technique yields through-space distance information between two spins, and thus 3-dimensional information about the protein structure. From these distance and angle constraints, one can construct a model of the protein structure. This assignment process can take many weeks because of combinatorial complexity and degeneracy. Isotope labeling is used with ^{13}C

and ^{15}N for large proteins to simplify the spectrum and assignment.

NMR is a much slower, lower resolution (on the order of 3-4 $\AA$) technique than x-ray crystallography, and is limited to about 60kDa structures. However, it works for proteins in solution and can monitor dynamical properties and kinetics. As a result, there are many structures that can only be determined by NMR.

Appendix C

Relevant Instrumentation and Electromagnetics

C.1 Class E Amplifiers

For NMR spectrometers, large amounts of agile RF power at the Larmor frequency are required to control nuclear spins. The pulse length for a $\frac{\pi}{2}$ pulse is

$$\tau \approx \frac{P^{\frac{1}{2}}}{Q}. \tag{C.1}$$

As pulses grow in length, problems of RF inhomogeneity and the frequency representation of the pulse itself cause distortions in the spectra. It is therefore important to have power pulses as high as possible.

In RF power amplifier design, there are several basic classes of amplifiers defined by their linearity and power efficiency. The basic distinguishing factor for linear amplifiers is the bias point of the transistor about which the input voltage oscillates. Class A amplifiers operate in the linear regime of a transistor I-V curve. They allow the wide frequency agility, linear phase, and amplitude response required for NMR. However, current flows during the entire time the amplifier is on. It would be advantageous to transmit power only when power is needed, but still give frequency and phase control. A class E amplifier achieves close to 100% efficiency by minimizing the overlap integral of voltage and current within the transistor. while delivering all the input power to the load [80]. Class E amplifier performance is explained in the next section.

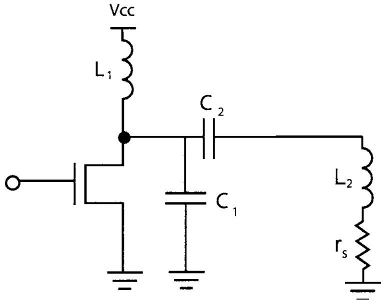

Figure C-1: General schematic for a class E amplifier

C.1.1 System of Equations for Class E Amplifiers

From [51],

$$\begin{aligned} i_0 &= I_0 \sin(\omega t + \phi), \\ v_s(t) &= V \sin(\omega t + \phi_1), \\ V &= I_o R_L \sqrt{1 + \frac{X^2}{R_L^2}}. \end{aligned} \tag{C.2}$$

The current equation at node 1 is

$$\begin{aligned} i_L(t) &= i_c(t) + I_0 \sin(\omega t + \phi), \\ V_{cc} - v_c(t) &= L_1 \frac{di_L(t)}{dt}, \\ C_1 \frac{v_{\mathrm{coff}}(t)}{dt} &= i_{\mathrm{coff}}(t). \end{aligned} \tag{C.3}$$

Solving for the boundary condition of the ON state gives:

$$i_{L\mathrm{on}}(t) = \frac{V_{cc}}{L_1}(t - \pi/\omega) + i_c. \tag{C.4}$$

Solving for the boundary condition of the OFF state gives:

$$\begin{aligned} i_{L\mathrm{off}}(t) &= A \sin(\omega_0 t) + B \cos(\omega_0 t) + \dots \\ &\quad \frac{I_0}{1-\beta^2} \sin(\omega t + \phi), \\ \omega_0 &= \frac{1}{\sqrt{L_1 C_1}}, \\ \beta &= \omega/\omega_0. \end{aligned} \tag{C.5}$$

By L_1 continuity of $i_L(t)$,

$$\begin{aligned} i_{L\text{off}}(\frac{\pi}{\omega}) &= i_{L\text{off}}(\frac{\pi}{\omega}), \\ i_{L\text{off}}(0) &= i_{L\text{off}}(\frac{2\pi}{\omega}). \end{aligned} \tag{C.6}$$

By C_1 continuity of $v_c(t)$,

$$v_c(0) = i_{L\text{off}}(\frac{\pi}{\omega}) = 0. \tag{C.7}$$

Adding three more constraints for class E:

$$\begin{aligned} \frac{dv_c(\frac{\pi}{\omega})}{dt} &= 0, \\ P_{in} = V_{cc}I_{dc} = P_{out} &= \frac{I_o^2}{2}R_L. \end{aligned} \tag{C.8}$$

Finally, solve for β by root-finding given P, L_1, R_L, ω, V_{cc}, then solve for ϕ, I_0, A, B, and C.

C.1.2 Class E Experiment

To test the theory of class E operation, a circuit board was designed and built to operate at 34 MHz (resonance frequency for ^{35}Cl in mothballs) and 4 watts for a Pure Quadrupolar Resonance (PQR) experiment. See [24] for a detailed description of PQR. The amplifier was designed to receive a pulsed, sinusoidal signal at 34 MHz that was amplified and directly connected to the probe. A schematic for this is shown in figure C-2 and a photograph of the final assembled board used is in figure C-3. Since this is a digital amplifier, i.e. the amplifier is completely off when the input is low voltage, noise from the source is suppressed by the MOSFET. On the other hand, for a linear amplifier, this noise is amplified. When not transmitting, this noise suppression from the class E amplifier allows the weak PQR signal to go through the receiver chain with less noise. An FID from the PQR class E experiment is shown in figure C-4. It was estimated that the signal to noise ratio improved by a factor of 8 over a linear, Amplifier Research 75AP250 linear amplifier.

With this experiment completed, it was important to reflect on the circuit for the class E amplifier. The reactive circuit highlighted in figure C-5 has a network model very similar to a probe, so a design study was conducted to merge the phase shift network for class E operation with the probe itself to make an integrated amplifier-probe. A schematic for this design is shown in figure C-6, but was not built. With microfabrication and miniaturization, integrated probes and electronics could be an important piece of future NMR/PQR on-a-chip designs.

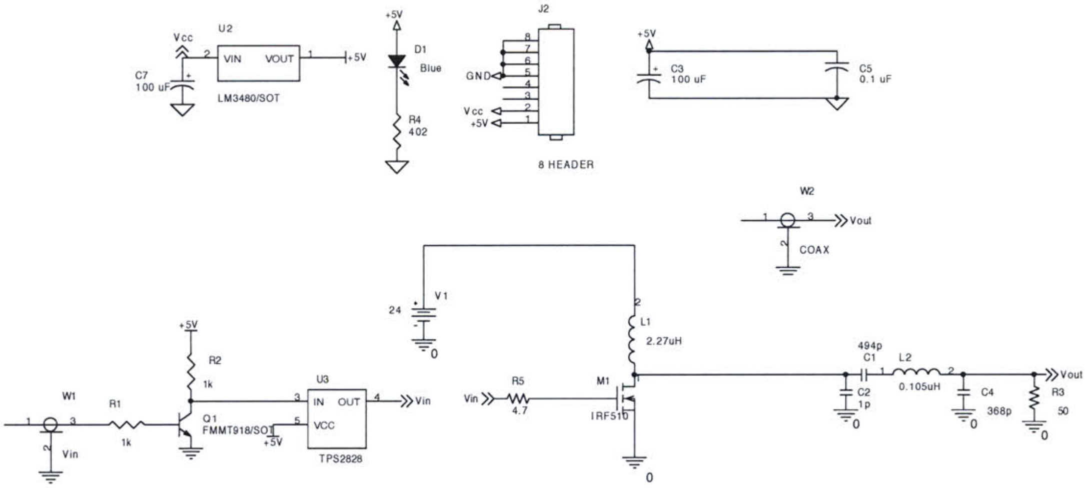
U2
Vcc
VIN
VOUT
C7
100 uF
LM3480/SOT
+5V
D1
Blue
R4
402
J2
GND
Vcc
+5V
8 HEADER
C3
100 uF
C5
0.1 uF
W2
COAX
Vout
V1
24
0
L1
2.27uH
494p
C1
L2
0.105uH
C2
1p
C4
368p
R3
50
M1
IRF510
R5
4.7
Vin
U3
IN
OUT
VCC
TPS2828
R2
1k
Q1
FMMT918/SOT
W1
R1
1k

Figure C-2: Schematic for the class E amplifier to operate at 34 MHz.

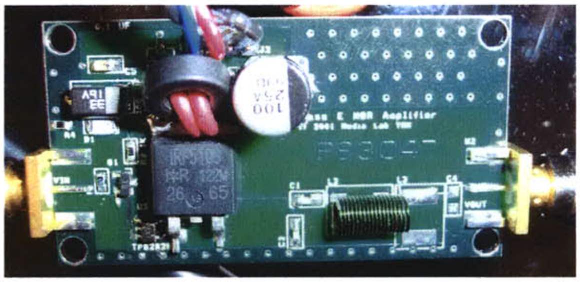

Figure C-3: Fabricated class E amplifier operating at 34 MHz for ^{35}Cl. This amplifier was capable of about 4W of output power. The dimensions are 3cm × 5.5cm.

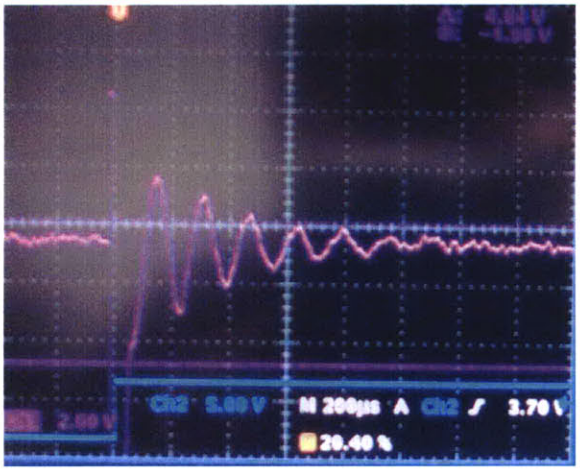

Figure C-4: FID from the PQR apparatus showing good signal to noise ratio.

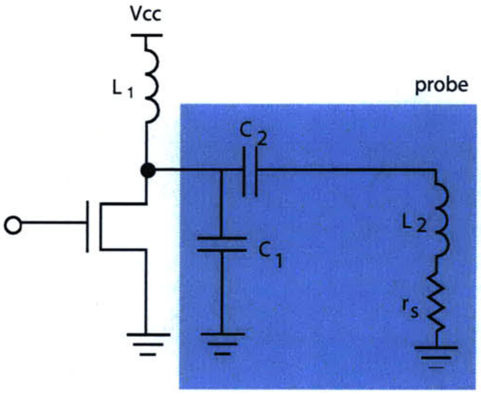
Vcc
L 1
probe
C 2
C 1
L 2
r s

Figure C-5: Class E amplifier with an integrated probe.

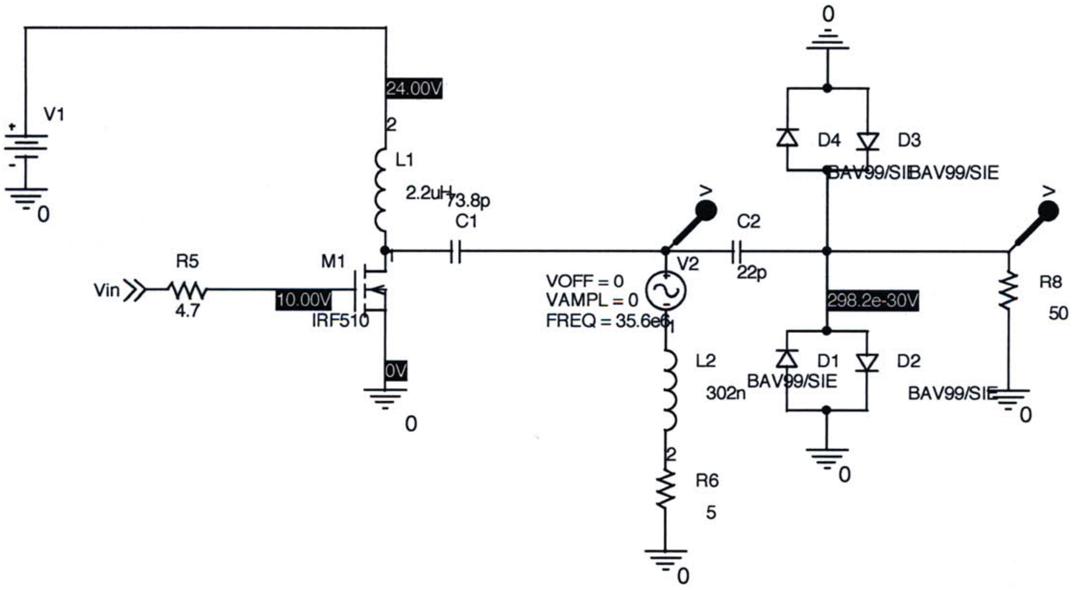
0
V1
+
-
0
24.00V
2
L1
2.2uH
73.8p
C1
D4
D3
BAV99/SIE
BAV99/SIE
V
V
C2
22p
Vin
R5
4.7
M1
10.00V
IRF510
0V
0
V2
VOFF = 0
VAMPL = 0
FREQ = 35.6e6
1
298.2e-30V
R8
50
L2
302n
D1
D2
BAV99/SIE
BAV99/SIE
0
2
R6
5
0
0

Figure C-6: A proposed design for an integrated class E amplifier and probe.

C.2 Susceptibility Mismatch and Magnetic Boundary Conditions

First, let us consider the boundary conditions on the magnetic field H and the magnetic flux density B. From Maxwell's equation,

$$\begin{aligned} \nabla \times \vec{H} &= \vec{J}, \\ \nabla \cdot \vec{B} &= 0. \end{aligned} \tag{C.9}$$

Using Stokes' theorem for the first equation and the divergence theorem for the second equation, we are left with:

$$\begin{aligned} \int_S (\nabla \times \vec{H}) \cdot \vec{n}\, da &= \oint_C \vec{H} \cdot d\vec{l}, \\ \int_V \nabla \cdot \vec{B}\, d^3x &= \int_S \vec{B} \cdot \vec{n}\, da. \end{aligned} \tag{C.10}$$

Taking these integrals over an infinitesimal volume at the boundary of two surfaces in the absence of any current $\vec{J}$ yields:

$$\begin{aligned} \oint_C \vec{H} \cdot d\vec{l} &= (\vec{H}_2 - \vec{H}_1) \times \vec{n} = 0, \\ \int_S \vec{B} \cdot \vec{n}\, da &= (\vec{B}_2 - \vec{B}_1) \cdot \vec{n} = 0. \end{aligned} \tag{C.11}$$

For a cylinder or rectangular object with $\vec{B}$ normal to the ends of the object, $\vec{B}_1 = \vec{B}_2$. However, the normal component of the field changes discontinuously across the surface and so a *surface charge density* must be introduced. (This situation is similar to that in electrostatics [43]). To calculate what this charge density is when the current density, $\vec{J}$ vanishes, it is possible to write a scalar potential for the magnetic field such that

$$\vec{H} = -\nabla \Phi_M. \tag{C.12}$$

Since $\vec{B} = \mu_0(\vec{H} + \vec{M})$, from the divergence theorem we can write:

$$\nabla \cdot \vec{B} = \mu_0 \nabla \cdot (\vec{H} + \vec{M}) = 0. \tag{C.13}$$

Therefore, substituting equation C.12 into C.13 yields:

$$\nabla^2 \Phi_M = -\rho_M = \nabla \cdot \vec{M}. \tag{C.14}$$

Again applying the divergence theorem yields the effective surface-charge density,

$$\sigma_M = \vec{n} \cdot \vec{M}. \tag{C.15}$$

The solution to this magnetostatic Poisson equation in the case of a uniform magnetization within a solid is

$$\Phi_M(\vec{x}) = \frac{1}{4\pi} \oint_S \frac{\sigma'_M \, da'}{|\vec{x} - \vec{x}'|}. \tag{C.16}$$

From equation C.16 we can see that any surface perpendicular to the main static field will produce susceptibility variations, while any surface parallel to the field will not. Therefore, even though a material such as a copper has a susceptibility mismatch with air, as long as the perpendicular surface is far away from the sample, this should not matter. On the other hand, the sample-air boundary itself will cause a susceptibility mismatch that will be difficult to shim away.

Appendix D

Simulation Code

D.1 6.9mm simulation

Below is the code to do the finite element and nutation plot analyses from section 3.2.1. The model is shown here in figure D-1.

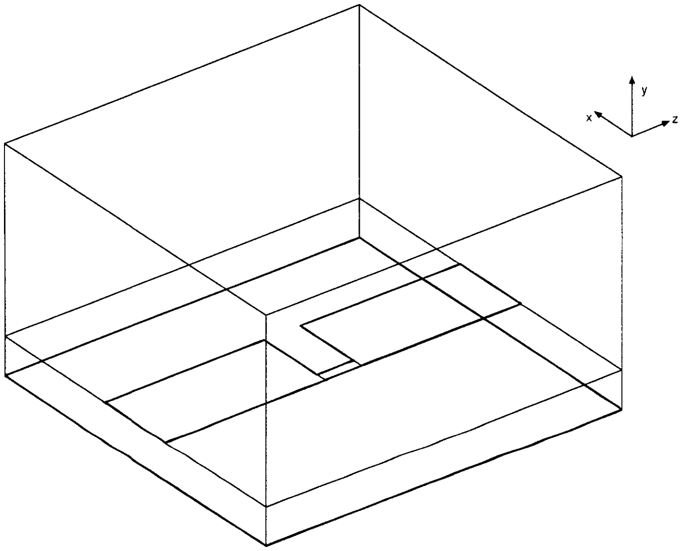

Figure D-1: Microslot geometry used for the 6.9mm simulation.

```
% FEMLAB Model M-file
%
% (c) 2003,2004 MIT
% author: Yael Maguire <yael at media.mit.edu>

% Recorded command sequence

% Geometry
% units in um
% length of conductor - taken from actual board
l=30400;
```

```
% length of slit
% gl=3200; (pre 121503)
gl=3100;
% width of microstrip
w=6900;
% thickness of copper
t=300;
% width of slit
gw=900;
dh=3000;
% taken from actual board
dw=29200;
%ah=10000; (pre 121503)
ah=15000;

fprintf(1,'Starting geometry construction....');

% metal
g3=block3(l/2-gl/2,w,t,'corner',[-l/2 -w/2 0],[0 0 1],0);
g5=block3(l/2-gl/2,w,t,'corner',[gl/2 -w/2 0],[0 0 1],0);
g6=block3(gl,gw,t,'corner',[-gl/2 -w/2 0],[0 0 1],0);
g7=geomcomp({g3,g5,g6},'ns',{'BLK2','BLK3','BLK4'},'sf','BLK2+BLK3+BLK4', ...
'face','all','edge','all','out',{'ftx','ctx','ptx'});

% dielectric
g8=block3(l,dw,dh,'corner',[-l/2 -dw/2 -dh],[0 0 1],0);
% bottom conductor
g9=block3(l,dw,t,'corner',[-l/2, -dw/2,-(dh+t)],[0,0,1],0);

% air
g10=block3(l,dw,ah,'corner',[-l/2, -dw/2, 0],[0 0 1],0);

g11=geomcomp({g7,g8,g9,g10},'ns',{'CO1','BLK1','BLK2','BLK3'},'sf','CO1+BLK1+BLK2+BLK3', ...
'face','none','edge','all','out',{'ftx','ctx','ptx'});

fem.geom = scale(g11,1e-6,1e-6,1e-6);

fprintf(1,'done\n');

fprintf(1,'Setting up problem and mesh...');

clear appl

appl.mode=flcemqav3d;
appl.var.omega=500e6*2*pi;
appl.elemdefault='Lag1';

% epsilon,sigma,init must equal the number of subdomains
% 2.20 is the dielectric constant for rogers 5880
appl.equ.epsilonr={{{'1'}},{{'2.2'}},{{'1'}},{{'1'}}};
% conductivity for copper
appl.equ.sigma={'1/1.664e-8','1','1','1/1.664e-8'};
appl.equ.init={{{'V'};{'0'};{'0'};{'0'}},...
               {{'V'};{'0'};{'0'};{'0'}},...
               {{'V'};{'0'};{'0'};{'0'}},...
               {{'V'};{'0'};{'0'};{'0'}}};

% for a current of 0.5101 A (4 domains)
appl.bnd.V={'0','0','0','0.0001','-0.0001'};

% boundary conditions
appl.bnd.type={'nA','A0','tH0','nV','nV'};
% 1 = electric current, magnetic potential
% 2 = ground/magnetic insulation
% 3 = solve for it
% 4 = electric potential
%
% all borders should be 3
% indices       1 2 3 4 5 6 7 8 9 0 1 2 3 4 5 6 7 8 9 0 1 2 3 4 5 6 7 8 9 0 1
appl.bnd.ind=[2 2 2 1 1 3 1 1 3 1 4 3 3 3 3 3 2 3 1 3 3 3 3 3 3 3 3 2 1 1 5];

fem.appl=appl;
fem=multiphysics(fem);

fem.mesh=meshinit(fem,...
                'Hauto',4);

fem.xmesh=meshextend(fem);

fprintf(1,'done\n');

% You can now solve the electrostatic equation, to compute the
% currents.
fprintf(1,'Solving electrostatic problem...');
fem.sol=femlin(fem,'Solcomp',{'V'});
fprintf(1,'done\n');

% Follow this by solving the magnetostatic equations to get the
% magnetic flux density around the coils.
fprintf(1,'Solving magnetic problem...');
fem.sol=femiter(fem,...
               'init',fem.sol.u,...
               'Solcomp',{'Ax','Ay','Az'},...
               'prefun', 'luinc',...
               'prepar', {'droptol',{0.0001}});

% Visualize the result of the simulation, with the following
% properties to the plot function.
fprintf(1,'done\n');

% second vector are elements to exclude
nBdl = setdiff(1:31,[1:10 16:19 28:30]);

fprintf(1,'Plotting...');
postplot(fem,...
        'bdl',nBdl,...
        'cont', 'internal',...
        'tridata','V',...
        'tribar', 'on',...
        'flowtubescale',0.05,...
        'flowtype','tube',...
        'flowcolor','cycle',...
        'flowdata',{'Bx','By','Bz'},...
        'flowlines',15,...
        'flowback','on',...
        'flowsteps',150,...
        'scenelight','on',...
        'scenelightpos',[-1 1 1],...
        'Lightreflection','metal',...
        'axisequal','on',...
        'axisvisible','off',...
        'renderer','opengl',...
        'transparency',0.6)

fprintf(1,'done...\n');

fprintf(1,'Calculating curent...');
fem.cur=postint(fem,'nJ','dl',11,'edim',2)
fprintf(1,'done\n');
```

```
% (c) 2003,2004 MIT
% author: Yael Maguire <yael at media.mit.edu>

r=4240e-6/2;
z0=(5436+60)*1e-6;
```

```
h=30000e-6;
x0=h/2;
y0=0;

orientation = 'axial';
fems.geom = c;
fems.mesh=meshinit(fems);
fems.xmesh=meshextend(fems);

N=250;
By=postinterp(fem,'By',fems.mesh.p);
Bx=postinterp(fem,'Bz',fems.mesh.p);

% 1/2 at the end comes from the fact that we can only use the
% component rotating with the field
% the first 2 constants are the correction for the current in the model
% the 3rd constant is the current gain of the circuit

fems.sol.u=c1*2/fem.cur*c2*(By'+i*Bx')/2; %tpwr=58
T=linspace(0,350e-6,N);
f0=499.95e6;
B0=11.7;
s=[];

for j=1:N
  fems.variables= {'T',T(j),'f0',f0};
  s(j) = postint(fems,'exp(-i*atan(real(u)/imag(u)))*sin(-2*pi*f0/B0*abs(u)*T)');
  fprintf(1,'.');
  if (mod(j, N/5)==0)
     fprintf(1,'\n');
  end
end

hom=real(s)/max(abs(real(s)));

if (max(real(s))<0)
plot(T,hom)
m=min(hom)
else
plot(T,-hom)
m=min(-hom)
end

titl=sprintf('RF homogeneity for %d\\mum wide, %d\\mum long sample, z_0=%d\\mum, %s oriented, ...
FOM = %f ',2*r*1e6,2*x0*1e6,z0*1e6,orientation, m);
title(titl);
```

D.2 297μm simulation

Below is the code to do the finite element and nutation plot analyses from section 3.2.2. The model is shown here in figure D-2.

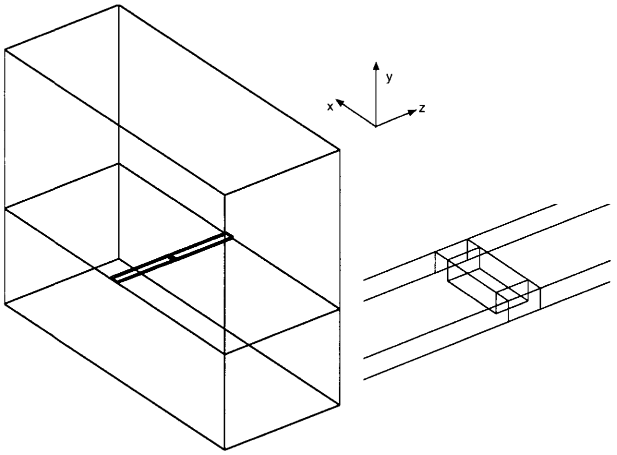

Figure D-2: Geometry for the 297 μm microslot simulation.

```
% FEMLAB Model M-file
%
% (c) 2003,2004 MIT
% author: Yael Maguire <yael at media.mit.edu>

% Recorded command sequence

% Geometry

fprintf(1,'Starting geometry construction....');

%units in um
l=4000;
gl=100;
w=297;
t=60;
%gw=w/10;
%gw=36;
gw=50;
dh=3000;
dw=10000;
ah=5000;

%metal
g3=block3(l/2-gl/2,w,t,'corner',[-l/2 -w/2 0],[0 0 1],0);
g5=block3(l/2-gl/2,w,t,'corner',[gl/2 -w/2 0],[0 0 1],0);
g6=block3(gl,gw,t,'corner',[-gl/2 w/2-gw 0],[0 0 1],0);
g7=block3(gl,gw,t,'corner',[-gl/2 -w/2 0],[0 0 1],0);
g8=geomcomp({g3,g5,g6,g7},'ns',{'BLK2','BLK3','BLK4','BLK5'},'sf','BLK2+BLK3+BLK4+BLK5', ...
'face','all','edge','all','out',{'ftx','ctx','ptx'});

% dielectric
g9=block3(l,dw,dh,'corner',[-l/2 -dw/2 -dh],[0 0 1],0);
% bottom conductor
g10=block3(l,dw,t,'corner',[-l/2, -dw/2,-(dh+t)],[0,0,1],0);

% air
```

```
g11=block3(l,dw,ah,'corner',[-l/2 -dw/2 0],[0 0 1],0);
g12=geomcomp({g8,g9,g10,g11},'ns',{'CO1','BLK1','BLK2','BLK3'},'sf',...
  'CO1+BLK1+BLK2+BLK3','face','none','edge','all','out',{'ftx','ctx','ptx'});

fem.geom = scale(g12,1e-6,1e-6,1e-6);

fprintf(1,'done\n');

fprintf(1,'Setting up problem and mesh...');
clear appl

appl.mode=flcemqav3d;
appl.var.omega=500e6*2*pi;
appl.elemdefault='Lag1';

% these must equal the number of subdomains
appl.equ.epsilonr={{{'1'}},{{'2.2'}},{{'1'}},{{'1'}}};
% conductivity for copper
appl.equ.sigma={'1/1.664e-8','1','1','1/1.664e-8'};
appl.equ.init={{{'V'};{'0'};{'0'};{'0'}},...
               {{'V'};{'0'};{'0'};{'0'}},...
               {{'V'};{'0'};{'0'};{'0'}},...
               {{'V'};{'0'};{'0'};{'0'}}};
% to get 1 A of current
appl.bnd.V={'0','0','0','0.0001','-0.0001'};

% boundary conditions
appl.bnd.type={'nA','A0','tH0','nV','nV'};
% 1 = electric current, magnetic potential
% 2 = ground/magnetic insulation
% 3 = solve for it
% 4 = electric potential
%              1 2 3 4 5 6 7 8 9 0 1 2 3 4 5 6 7 8 9 0 1 2 3 4 5 6 7 8 9 0 1 2 3 4 5
appl.bnd.ind=[2 2 2 1 1 2 1 1 3 1 4 3 3 3 3 3 2 1 3 1 3 3 3 3 3 3 3 3 3 1 1 1 1 5 ];

fem.appl=appl;
fem=multiphysics(fem);

fem.mesh=meshinit(fem,'Hauto',2); % above is equivalent to Hauto=5

fem.xmesh=meshextend(fem);

fprintf(1,'done\n');

% You can now solve the electrostatic equation, to compute the
% currents.

fprintf(1,'Solving electrostatic problem...');
fem.sol=femlin(fem,'Solcomp',{'V'});
fprintf(1,'done\n');

% Follow this by solving the magnetostatic equations to get the
% magnetic flux density around the coils.
fprintf(1,'Solving magnetic problem...');
fem.sol=femiter(fem,...
              'init',fem.sol.u,...
              'Solcomp',{'Ax','Ay','Az'},...
              'prefun', 'luinc',...
              'prepar', {'droptol',{0.0001}});

% Visualize the result of the simulation, with the following
% properties to the plot function.
fprintf(1,'done\n');

%nBdl = setdiff(1:26,[1:7 13:15 24:25]);
nBdl = setdiff(1:30,[1:7 13:15 28:30]);

fprintf(1,'Plotting...');
```

```
postplot(fem,...
        'bdl',nBdl,...
        'cont', 'internal',...
        'tridata','normJs',...
        'tribar', 'on',...
        'flowtubescale',0.05,...
        'flowtype','tube',...
        'flowcolor','cycle',...
        'flowdata',{'Bx','By','Bz'},...
        'flowlines',15,...
        'flowback','on',...
        'flowsteps',150,...
        'scenelight','on',...
        'scenelightpos',[-1 1 1],...
        'Lightreflection','metal',...
        'axisequal','on',...
        'axisvisible','off',...
        'renderer','opengl',...
        'transparency',0.6)

fprintf(1,'done...');

fprintf(1,'Calculating curent...');
cur=postint(fem,'nJ','dl',8,'edim',2)
fprintf(1,'done\n');
```

```
% (c) 2003,2004 MIT
% author: Yael Maguire <yael at media.mit.edu>

r=100e-6/2;
% the last 30 um is from the thickness of the copper
% the first 70 um is the tape, the 35 is the fact that the capillary is 169/163 um wide
z0=(70+35+30)*1e-6+r;
x0=h/2;
y0=0;

vol=pi*r^2*h

% create a volume to do integration over
c=cylinder3(r,h,[-x0,y0,z0],[1,0,0],0); % axial
orientation = 'axial';
fems.geom = c;
fems.mesh=meshinit(fems,'Hauto',3);
fems.xmesh=meshextend(fems);

N=250;
By=postinterp(fem,'By',fems.mesh.p);
Bz=postinterp(fem,'Bz',fems.mesh.p);

% 1/2 at the end comes from the fact that we can only use the
% component rotating with the field
% the first 2 constants are the correction for the current in the model
% the 3rd constant is the current gain of the circuit

fems.sol.u=0.1899/fem.cur*12.1471*(By'+i*Bz')/2; %tpwr=45 (mid)
T=linspace(0,59e-6,N);
f0=500e6;
B0=11.7;
s=[];

for j=1:N
  fems.variables= {'T',T(j),'f0',f0};
  s(j) = postint(fems,'exp(-i*atan(real(u)/imag(u)))*sin(-2*pi*f0/B0*abs(u)*T)');
  fprintf(1,'.');
  if (mod(j, 50)==0)
     fprintf(1,'\n');
  end
```

```
end

hom=real(s)/max(abs(real(s)));

if (max(real(s))<0)
plot(T,real(s)/max(abs(real(s))))
m=min(real(s)/max(abs((real(s)))))
else
plot(T,-real(s)/max(abs(real(s))))
m=min(-real(s)/max(abs((real(s)))))
end

titl=sprintf('RF homogeneity for %d\\mum wide, %d\\mum long sample, z_0=%d\\mum, %s oriented, ...
FOM = %f ',2*r*1e6,2*x0*1e6,z0*1e6,orientation, m);
title(titl);
```

D.3 Scaling simulation

```
% FEMLAB Model M-file
%
% (c) 2003,2004 MIT
% author: Yael Maguire <yael at media.mit.edu>

% Recorded command sequence

% Geometry

fprintf(1,'Starting geometry construction....');

%metal
g3=block3(l/2-gl/2,w,t,'corner',[-l/2 -w/2 0],[0 0 1],0);
g5=block3(l/2-gl/2,w,t,'corner',[gl/2 -w/2 0],[0 0 1],0);
g6=block3(gl,gw,t,'corner',[-gl/2 w/2-gw 0],[0 0 1],0);
g7=block3(gl,gw,t,'corner',[-gl/2 -w/2 0],[0 0 1],0);

g8=geomcomp({g3,g5,g6,g7},'ns',{'BLK2','BLK3','BLK4','BLK5'},'sf',...
        'BLK2+BLK3+BLK4+BLK5', 'face','all','edge','all','out',...
        {'ftx','ctx','ptx'});

% dielectric
g9=block3(l,dw,dh,'corner',[-l/2 -dw/2 -dh],[0 0 1],0);

% air
g10=block3(l,dw,ah,'corner',[-l/2 -dw/2 0],[0 0 1],0);
g11=geomcomp({g8,g9,g10},'ns',{'CO1','BLK1','BLK2'},'sf','CO1+BLK1+BLK2', ...
'face','none','edge','all','out',{'ftx','ctx','ptx'});

fem.geom = scale(g11,1e-6,1e-6,1e-6);

fprintf(1,'done\n');

fprintf(1,'Setting up problem and mesh...');
clear appl

appl.mode=flcemqav3d;
appl.var.omega=500e6*2*pi;
appl.elemdefault='Lag1';

% these must equal the number of subdomains
appl.equ.epsilonr={{{'10'}},{{'1'}},{{'1'}}};
% conductivity for copper
appl.equ.sigma={'1','1','1/1.664e-8'};
appl.equ.init={{{'V'};{'0'};{'0'};{'0'}},...
          {{'V'};{'0'};{'0'};{'0'}},...
          {{'V'};{'0'};{'0'};{'0'}}};
```

```
% to get 1 A of current
appl.bnd.V={'0','0','0','0.0001'};

% boundary conditions
appl.bnd.type={'nA','A0','tH0','nV'};
% 1 = electric current, magnetic potential
% 2 = ground/magnetic insulation
% 3 = solve for it
% 4 = electric potential
%appl.bnd.ind=[1 1 2 1 1 3 3 4 3 3 3 3 3 1 1 3 3 3 3 3 3 3 3 1 1 2];
%             1 2 3 4 5 6 7 8 9 0 1 2 3 4 5 6 7 8 9 0 1 2 3 4 5 6 7 8 9 0
appl.bnd.ind=[1 1 2 1 1 3 1 4 3 3 3 3 3 1 1 3 3 3 3 3 3 3 3 3 3 3 3 1 1 2];

fem.appl=appl;
fem=multiphysics(fem);

fem.mesh=meshinit(fem,'Hauto',meshlevel); % above is equivalent to Hauto=5

fem.xmesh=meshextend(fem);

fprintf(1,'done\n');

% You can now solve the electrostatic equation, to compute the
% currents.

fprintf(1,'Solving electrostatic problem...');
fem.sol=femlin(fem,'Solcomp',{'V'});
fprintf(1,'done\n');

% Follow this by solving the magnetostatic equations to get the
% magnetic flux density around the coils.
fprintf(1,'Solving magnetic problem...');
fem.sol=femiter(fem,...
                'init',fem.sol.u,...
                'Solcomp',{'Ax','Ay','Az'},...
                'prefun', 'luinc',...
                'prepar', {'droptol',{0.0001}});

% Visualize the result of the simulation, with the following
% properties to the plot function.
fprintf(1,'done\n');

fprintf(1,'Calculating curent...');
cur=postint(fem,'nJ','dl',8,'edim',2)
fem.cur=abs(cur);
fprintf(1,'done\n');
```

```
% (c) 2003,2004 MIT
% author: Yael Maguire <yael at media.mit.edu>

% generate the geometry:
% units in um

k=1;

for w=2000:250:6000
l=40/3*w;
gl=w/3;
gw=w/6;

% these are fixed
t=60;
dh=3000;
dw=20000;
ah=15000;

r=w/3*1e-6;
```

```
id=2*r;
od=2*id;
z0=(t)*1e-6+od/2;
h=l*1e-6;
x0=h/2;
y0=0;

% do the FE simulation
meshlevel=4;
fem=[];
microsag;

[s,m]=unix('date +"%m%d%y-%H%M"');
% remove the \n
m(end)='';
fname=sprintf('scaling/micros%d-%s.mat',w,m);

% now, save the results
flsave(fname,fem);

rffomas;
vfom(k)=fom;
k=k+1;
end
```

Appendix E

CAD drawings

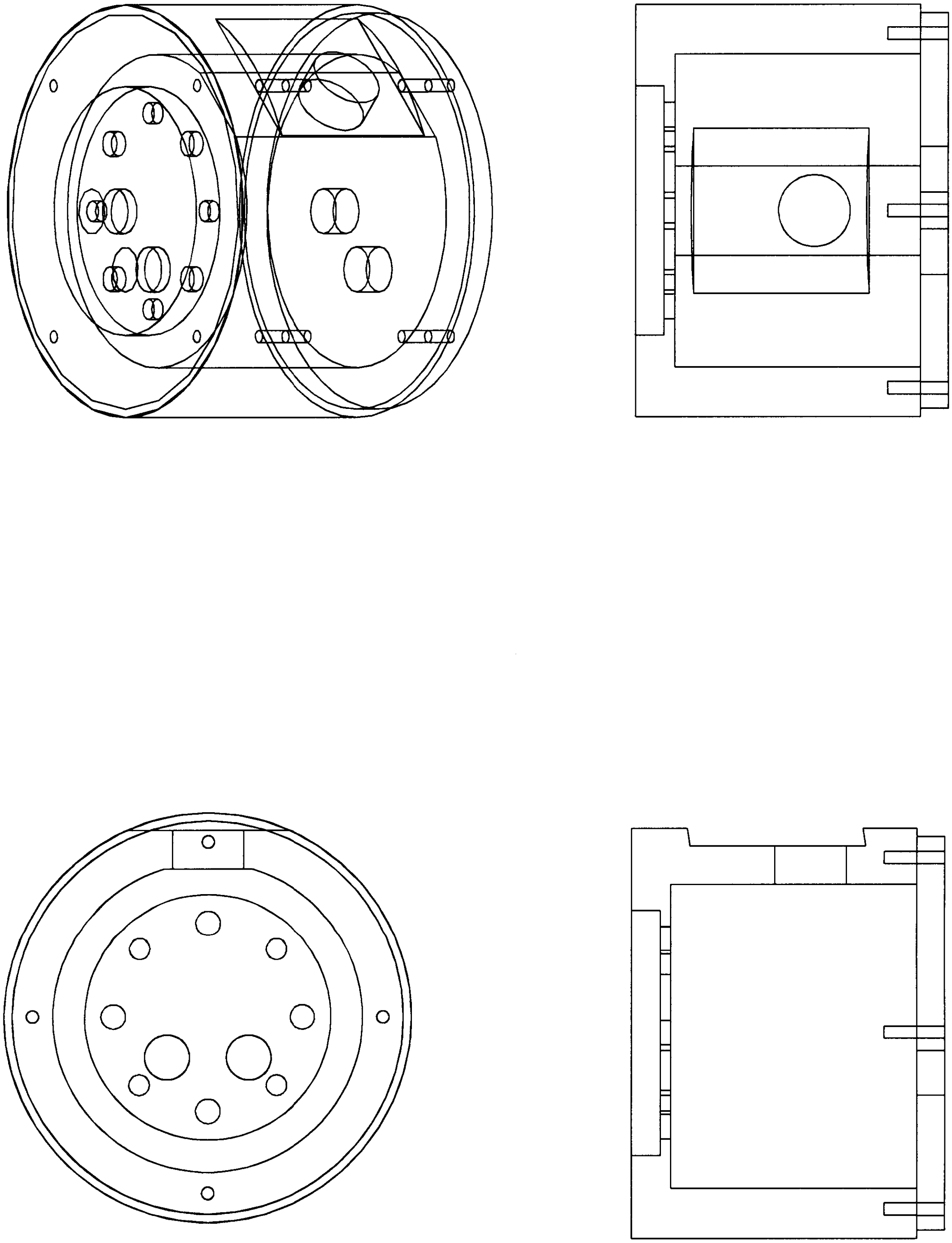

Figure E-1: Probe base. Scale is 1:1.

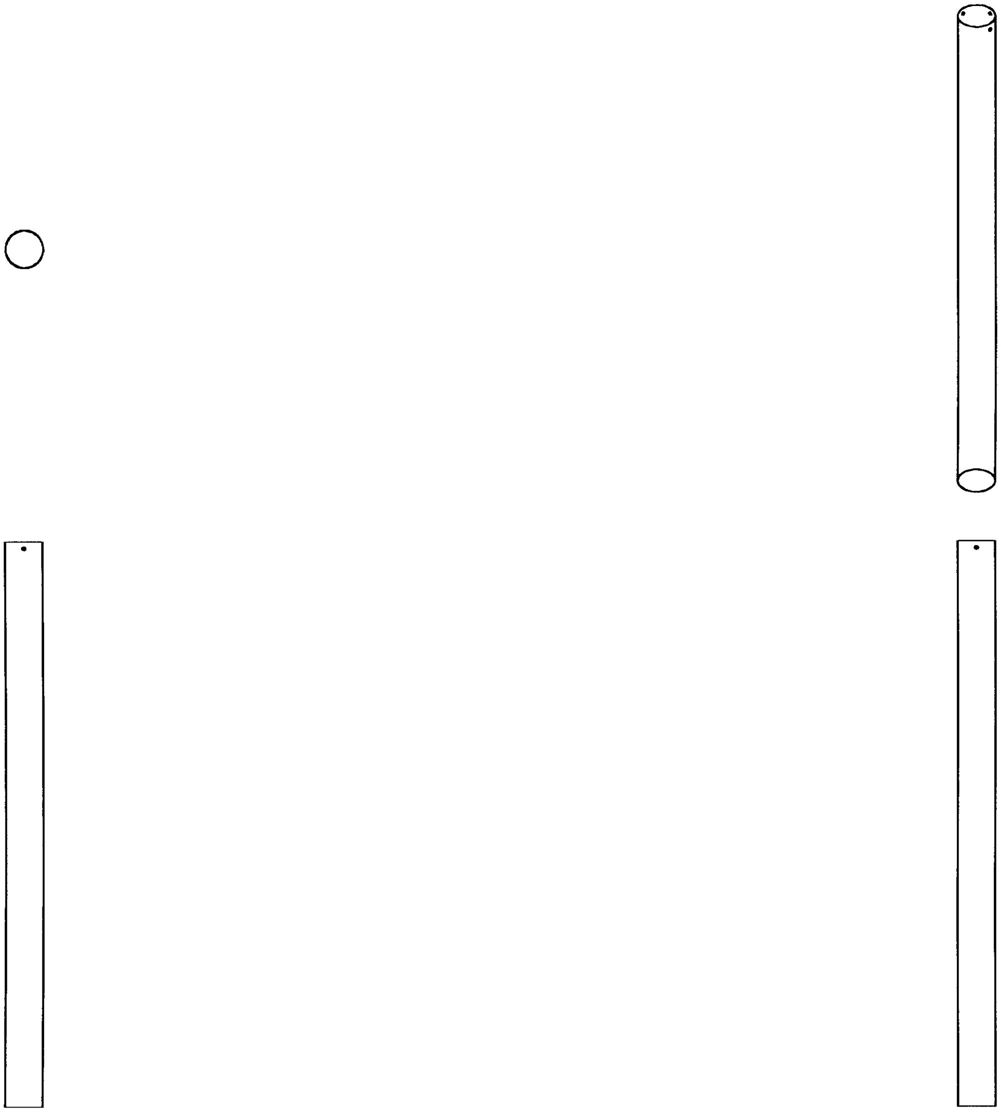

Figure E-2: Probe tube. Scale is 1:7.41.

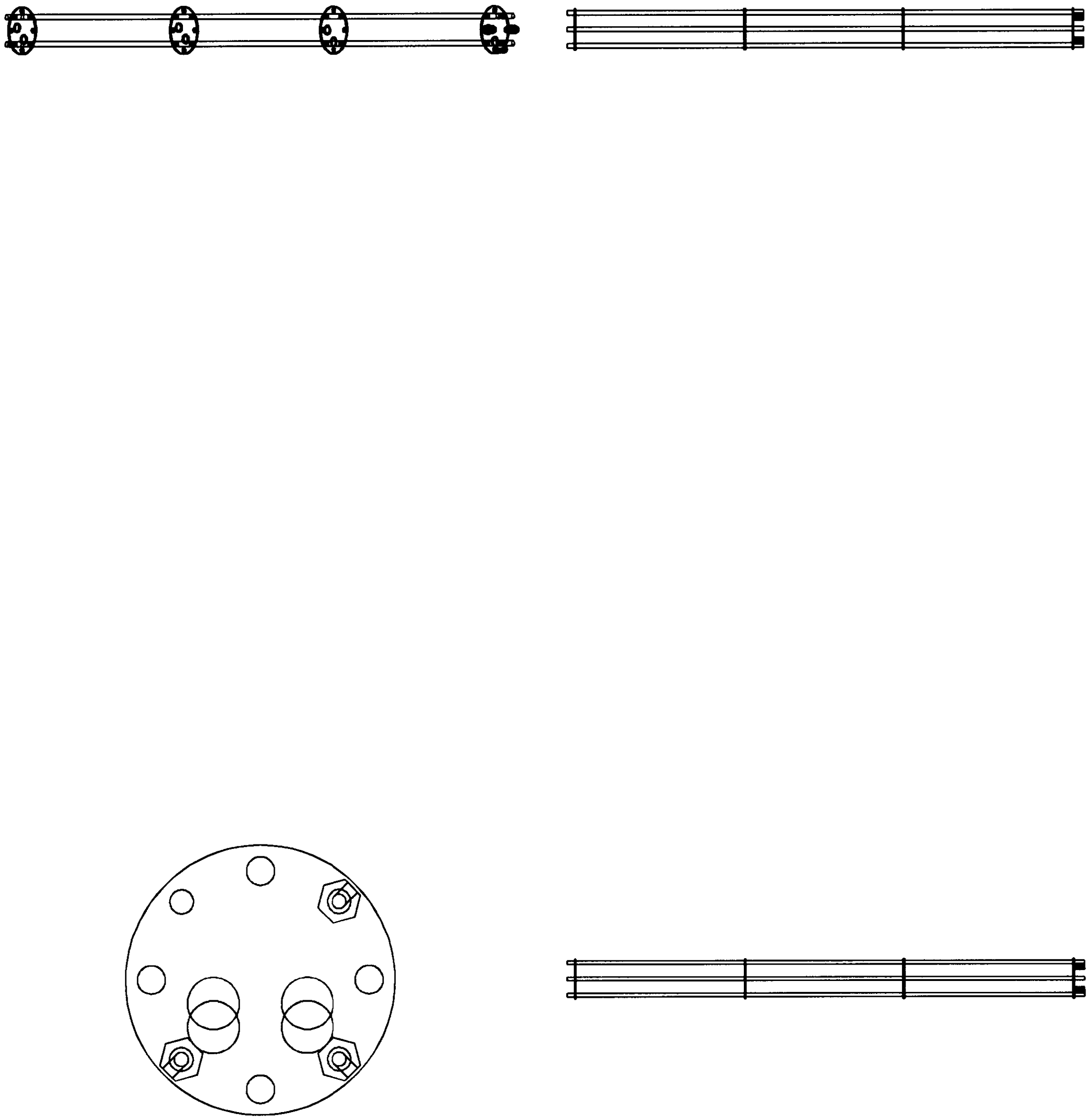

Figure E-3: Tube assembly. Scale is 1:1 and 1:6.67.

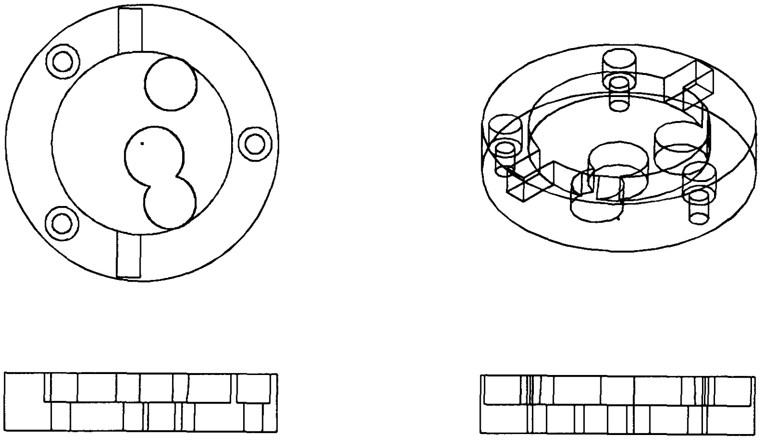

Figure E-4: FEP/Teflon base. Scale is 1:1.

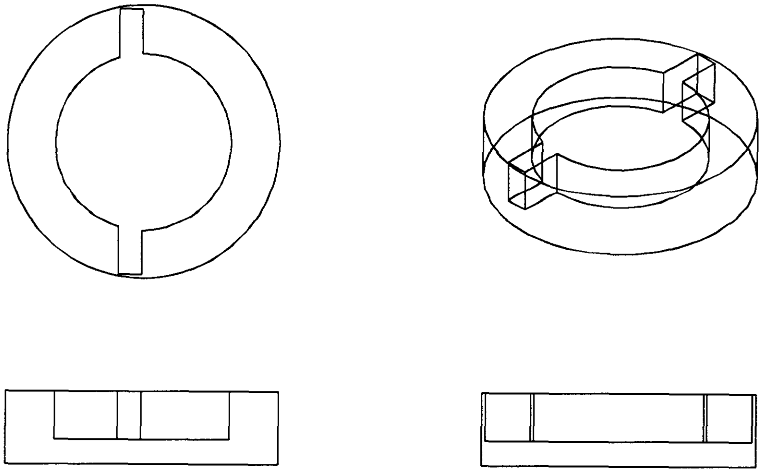

Figure E-5: FEP/Teflon base top. Scale is 1:1.

Bibliography

[1] Elihu Abrahams. Electron-Electron Scattering in Alkali Metals. *Physical Review*, 95:839–840, 1954.

[2] V. Agrawal, P. Neuzil, and D.W. van der Weide. A microfabricated tip for simultaneous acquisition of sample topography and high-frequency magnetic field. *Applied Physics Letters*, 71(16):2343–2345, 1997.

[3] Bruce Alberts, Alexander Johnson, Julian Lewis, Martin Raff, Keith Roberts, and Peter Walter. *Molecular Biology of The Cell*. Garland Science, New York, 2002.

[4] Alan Allan, Don Edenfeld, William H. Joyner Jr., Andre B Kahng, Mike Rodgers, and Yervant Zorian. 2001 Technology Roadmap for Semiconductors. *IEEE Computer*, 35(1):42–53, 2002.

[5] E.A. Ash and G. Nicholls. Super-resolution aperture scanning microscope. *Nature*, 237:510, 1972.

[6] Roger Balian and D. Ter Haar. *From Microphysics to Macrophysics : Methods and Applications of Statistical Physics*. Springer Verlag, New York, 1992.

[7] Philip Ball. *Life's Matrix*. Farrar Straus Giroux, New York, 2000.

[8] Protein Data Bank. `http://www.rcsb.org/pdb/`.

[9] Tom Barbara. *Personal communication*. Varian Inc.

[10] Dimitri P. Bertsekas. *Dynamic Programming and Optimal Control*. Athena Scientific, Nashua, NH, 2003.

[11] BioMagResBank. `http://www.bmrb.wisc.edu/ref_info/statful.htm`.

[12] R.D. Black, T.A. Early, P.B. Roemer, O.M. Mueller, A. Mogro-Campero, L.G. Turner, and G.A. Johnson. A High-Temperature Superconducting Receiver for Nuclear Magnetic Resonance Microscopy. *Science*, 259:793–795, 1993.

[13] Carl-Ivar Branden and John Tooze. *Introduction to Protein Structure.* Garland Publishing, New York, 1999.

[14] A.C.J. Brouwer, J. Köhler, E.J.J. Groenen, and J. Schmidt. ^{13}C isotope effects for pentacene in *p*-terphenyl: High-resolution spectroscopy and single spin detection. *Journal of Chemical Physics*, 105(6):2212–2222, 1996.

[15] A.C.J. Brouwer, J. Köhler, A.M. van Oijen, E.J.J. Groenen, and J. Schmidt. Single-molecule fluorescence autocorrelation experiments on pentacene: The dependence of intersystem crossing on isotopic composition. *Journal of Chemical Physics*, 110(18):9151–9159, 1999.

[16] S. Butterworth. Eddy-Current Losses in Cylindrical Conductors, with Special Applications to the Alternating Current Resistances of Short Coils. *Philosophical Transactions of the Royal Society of London, Series A, Containing Papers of a Mathematical or Physical Character*, 222:57–100, 1922.

[17] S. Butterworth. On the Alternating Current Resistance of Solenoidal Coils. *Proceedings of the Royal Society of London, Series A*, 107:693–715, 1925.

[18] John Cavanaugh, G. Arthur Palmer III, Wayne Fairbrother, and Nick Skelton. *Protein NMR Spectroscopy: Principles and Practice.* Academic Press, New York, 1996.

[19] W. Chiu. What Does Electron Cryomicroscopy Provide that X-Ray Crystallography and NMR Spectroscopy Cannot? *Annual Review of Biophysics and Biomolecular Structure*, 22:233–255, 1993.

[20] Christopher L. Chua, David K. Fork, Koenraad Van Schuylenbergh, and Jeng-Ping Lu. Out-of-Plane High-Q Inductors on Low-Resistance Silicon. *Journal of Microelectromechanical Systems*, 12:989–995, 2003.

[21] Rogers Corp. `http://www.rogers-corp.com/mwu/pdf/5000data.pdf`.

[22] Thomas E. Creighton. *Proteins: Structure and Molecular Properties.* W. H. Freeman and Company, New York, 1997.

[23] F. H. C. Crick and J. D. Watson. Molecular Structure of Nucleic Acids. *Nature*, 171(4356):737–738, 1953.

[24] T.P. Das and E.L. Hahn. *Nuclear Quadrupole Resonance Spectroscopy.* Academic Press, London, 1958.

[25] W.L. DeLano. The PyMOL Molecular Graphics System. `http://www.pymol.com`, 2002.

[26] F. David Doty. Probe Design and Construction. *NMR Encyclopedia*, pages 3753–3762, 1994.

[27] Richard E. Ernst, G. Bodenhausen, and A. Wokaun. *Principles of Nuclear Magnetic Resonance in One and Two Dimensions.* Clarendon Press, Oxford, 1987.

[28] F. Allen et al. Blue Gene: A vision for protein science using a petaflop computer. *IBM Systems Journal*, 40(2):310–327, 2001.

[29] R.J. Fitzgerald, K.L Sauer, and W. Happer. Cross-relaxation in laser-polarized liquid xenon. *Chem. Phys. Lett.*, 284:87–92, 1998.

[30] Ray Freeman. *Spin Choreography: Basic Steps in High Resolution NMR.* University Science Books, Sausalito, CA, 1997.

[31] Murat Gel, Shoji Takeuchi, and Isao Shimoyama. Fabrication method for out-of-plane, micro-coil by surface micromachining. *Sensors and Actuators A*, 97–98:702–708, 2002.

[32] Neil A. Gershenfeld and Isaac L. Chuang. Bulk spin resonance quantum computation. *Science*, 275:350–356, 1997.

[33] Hermann Grabert and Michel H. Devoret. *Single Charge Tunelling: Coulomb Blockade Phenomena in Nanostructures.* Plenum Publishing Corporation, New York, 1992.

[34] Kimberly Hamad-Schifferli, John J. Schwartz, Aaron T. Santos, Shuguang Zhang, and Joseph M. Jacobson. Remote electronic control of DNA hybridization through inductive coupling to an attached metal nanocrystal antenna. *Nature*, 415:152–155, 2002.

[35] A. Henstra, T.-S. Lin, J. Schmidt, and W. Th. Wenckebach. High dynamic nuclear polarization at room temperature. *Chemical Physics Letters*, 165:6, 1990.

[36] Wolfgang J. R. Hoefer. Equivalent Series Inductivity of a Narrow Transverse Slit in Microstrip. *IEEE Transactions on Microwave Theory and Techniques*, MTT-25(10):822–824, 1977.

[37] Michael J. Hollas. *Modern Spectroscopy.* John Wiley and Sons, New York, 1996.

[38] J.W. Hong, Z.G. Khim, A.S. Hou, and Sang il Park. Noninvasive probing of high frequency signal in integrated circuits using electrostatic force microscope. *Review of Scientific Instruments*, 68:4506–4510, 1997.

[39] D. I. Hoult and R.E. Richards. The Signal-To-Noise Ratio of the Nuclear Magnetic Resonance Experiment. *Journal of Magnetic Resonance*, 24:71–85, 1976.

[40] Kerson Huang. *Statistical Mechanics*. John Wiley and Sons, New York, 1987.

[41] H.W. Weijers et al. Development of a 5 T HTS Insert Magnet as Part of 25 T Class Magnets. *IEEE Transactions of Applied Superconductivity*, 13(2):1396–1399, 2003.

[42] M. Iinuma, Y. Takahashi, I. Shaké, M. Oda, A. Masaike, and T. Yabuzaki. High Proton Polarization by Microwave-Induced Optical Nuclear Polarization at 77 K. *Physical Review Letters*, 84:171–174, 2000.

[43] John David Jackson. *Classical Electrodynamics*. John Wiley & Sons, Inc., New York, 1999.

[44] Tom F. Knight Jr. and Gerald Jay Sussman. Cellular Gate Technology. `http://www.ai.mit.edu/people/tk/ce/cellgates.ps`, 1997.

[45] Satoshi Kawata and Tomokazu Tanaka. Finer features for functional microdevices. *Nature*, 412:697–698, 2001.

[46] F. Keilmann, D.W. van der Weide, T. Eickelkamp, R. Merz, and D. Stöckle. Extreme subwavelength resolution with a scanning radio-frequency transmission microscope. *Optics Communications*, 129:15–18, 1996.

[47] N. Kernevez and H. Glénat. Description of a high sensitivity CW scalar DNP-NMR Magnetometer. *IEEE Transactions on Magnetics*, 27(6):5402–5404, 1991.

[48] Michael E. Lacey, Raju Subramanian, Dean L. Olsen, Andrew G. Webb, and Jonathan V. Sweedler. High-Resolution NMR Spectroscopy of Sample Volumes from 1 nL to 10 μL. *Chemical Reviews*, 99:3133–3152, 1999.

[49] Thomas Laurell and György Marko-Varga. Miniaturisation is mandatory unravelling the human proteome. *Proteomics*, 2(4):345–351, 2002.

[50] Garett M. Leskowitz, Louis A. Madsen, and Daniel P. Weitekamp. Force-detected magnetic resonance without field gradients. *Solid State Nuclear Magnetic Resonance*, 11:73–86, 1998.

[51] C.H. Li and Y.O. Yam. Maximum frequency and optimum performance of class E power amplifiers. *IEE Proceedings Circuits Devices and Systems*, 141(3):174–184, 1994.

[52] H.W. Long, H.C. Gaede, J. Shore, L. Raven, C.R. Bowers, J. Kitzenberger, T. Pietrass, and A.J. Pines. High-field cross polarization NMR from laser-polarized xenon to a polymer surface. *J. American Chem. Soc.*, 115:8491–8492, 1993.

[53] John D. Madden and Ian W. Hunter. Three-Dimensional Microfabrication by Localized Electrochemical Deposition. *Journal of Micoelectromechanical Systems*, 5:24–32, 1996.

[54] D. Marek, M. Haeberli, R. Triebe, M. Warden, L. Baselgia, T. Gerfin, O. Schett, and F. Laukien. Ultra Sensitive High-Resolution NMR Probes. *Experimental NMR Conference, Orlando, FL, Poster No. 122*, 1997.

[55] C. Massin, F. Vincent, A. Homsy, K. Ehrmann, G. Boero, P.A. Besse, A. Daridon, E. Verpoorte, N.F. de Rooij, and R.S. Popovic. Planar microcoil-based microfluidic NMR probes. *Journal of MAgnetic Resonance*, 164:242–255, 2003.

[56] Gheorghe D. Mateescu and Adrian Veleriu. *2D NMR Density Matrix and Product Operator Treatment*. Prentice Hall, New Jersey, 1993.

[57] S. Meiboom and D. Gill. Modified Spin-Echo Method for Measuring Nuclear Relaxation Times. *The Review of Scientific Instruments*, 29(8):688–691, 1958.

[58] Kevin R. Minard and Robert A. Wind. Picoliter ^{1}H NMR Spectroscopy. *Journal of Magnetic Resonance*, 154:336–343, 2002.

[59] Michael A. Neilsen and Isaac L. Chuang. *Quantum Computation and Quantum Information*. Cambridge University Press, Cambridge, UK, 2000.

[60] K.C. Nicolaou, Rudolf Hanko, and Wolfgang Hartwig. *Handbook of Combinatorial Chemistry: Drugs, Catalysts, Materials*. Wiley-VCH, New York, 2002.

[61] Dean L. Olson, Timothy L. Peck, Andrew G. Webb, Richard L. Magin, and Jonathan V. Sweedler. High-Resolution Microcoil ^{1}H-NMR for Mass-limited, Nanoliter-Volume Samples. *Science*, 270:1967–1970, 1995.

[62] Timothy L. Peck, Richard L. Magin, and Paul C. Lauterbur. Design and Analysis of Microcoils for NMR Microscopy. *Journal of Magnetic Resonance, Series B*, 108:114–124, 1995.

[63] T.L. Peck, R.L. Magin, J. Kruse, and M. Feng. NMR Microscopy Using 100 μm Planar RF Coils Fabricated on Gallium Arsenide Substrates. *IEEE Transactions on Biomedical Engineering*, 41(7):706–709, 1994.

[64] T.L. Peck, J.E. Stocker, Z. Chen, L. LaValle, and R.L. Magin. Application of Planar Microcoils Fabricated on Glass Substrates to NMR Microscopy. *IEEE-Engineering in Medicine and Biology Society*, 1:843–844, 1995.

[65] Asher Peres. *Quantum Theory: Concepts and Methods*. Kluwer Academic Publisher, 1993.

[66] David M. Pozar. *Microwave Engineering*. Addison-Wesley Publishing Company, Reading, MA, 1990.

[67] I.I. Rabi, J.R. Zacharias, S. Millman, and P. Kusch. A new method of measuring nuclear magnetic moment. *Physical Review*, 53:318, 1938.

[68] John A. Rogers, Rebecca J. Jackman, George M. Whitesides, Dean L. Olson, and Jonathan V. Sweedler. Using microcontact printing to fabricate microcoils on capillaries for high resolution proton nuclear magnetic resonance on nanoliter volumes. *Applied Physics Letters*, 70:2464–24, 1997.

[69] D. Rugar, R. Budakian, H.J. Mamin, and B.W. Chui. Single spin detection by magnetic resonance force microscopy. *Nature*, 430:329–332, 2004.

[70] D. Rugar, C.S. Yannoni, and J.A. Sidles. Mechanical detection of magnetic resonance. *Nature*, 360:563, 1992.

[71] D. Rugar, O. Zuger, S. Hoen, C.S. Yannoni, and H.M. Vieth and. Force Detection of Nuclear Magnetic Resonance. *Science*, 264:1560, 1994.

[72] G. Salis, D.T. Fuchs, J.M. Kikkawa, D.D. Awschalom, Y. Ohno, and H. Ohno. Optical Manipulation of Nuclear Spin by a Two-Dimensional Electron Gas. *Physical Review Letters*, 86(12):2677–2680, 2001.

[73] R.J. Schoenkopf, P.J. Burke, A.A. Kozhevnikov, D.E. Prober, and M.J. Rooks. Frequency Dependence of Shot Noise in a Diffusive Mesoscopic Conductor. *Physical Review Letters*, 78:3370–3373, 1997.

[74] R. Schueerlein, W. Gallagher, S. Parkin, A. Lee, S. Ray, R. Robertazzi, and W. Reohr. A 10 ns read and write non-volatile memory array using a magnetic tunnel junction and FET switch in each cell. In *Solid-State Circuits Conference, 2000. Digest of Technical Papers. ISSCC. 2000 IEEE International, 7-9 Feb. 2000*, pages 128–129, 2000.

[75] J.A. Sidles. Noninductive detection of single-proton magnetic resonance. *Applied Physics Letters*, 58:2854, 1991.

[76] J.A. Sidles, J.L. Garbini, K.J. Bruland, D. Rugar, O. Zuger, S. Hoen, and C.S. Yannoni. Magnetic resonance force microsopy. *Rev. Mod. Phys*, 67:249, 1995.

[77] Tycho Sleator, Erwin L. Hahn, Claude Hilbert, and John Clarke. Nuclear-Spin Noise. *Physical Review Letters*, 55(17):1742–1745, 1985.

[78] Tycho Sleator, Erwin L. Hahn, Claude Hilbert, and John Clarke. Nuclear-spin noise and spontaneous emission. *Physical Review B*, 36:1969–1980, 1987.

[79] C. P. Slichter. *Principle of Magnetic Resonance*. Springer-Verlag, New York, 1996.

[80] Nathan O. Sokal. Class E High-Efficiency Power Amplifiers, From HF to Microwave. In *Microwave Symposium Digest, 1998 IEEE MTT-S International*, volume 2, pages 1109–1112, Baltimore, MD, USA, 1998.

[81] J.E. Stocker, T.L. Peck, A.G. Webb, and R.L. Magin. Nanoliter Volume, High-Resolution NMR Microspectroscopy Using a 60-μm Planar Microcoil. *IEEE Transactions on Biomedical Engineering*, 44(11):1122–1126, 1997.

[82] Raju Subramanian, Wayne P. Kelley, Philip D. Floyd, Zhixin J. Tan, Andrew G. Webb, and Jonathan V. Sweedler. Microcoil NMR Probe for Coupling Microscale HPLC with On-Line NMR Spectroscopy. *Analytical Chemistry*, 71:5335–5339, 1999.

[83] Raju Subramanian, Jonathan V. Sweedler, and Andrew G. Webb. Rapid Two-Dimension Inverse Detected Heteronuclear Correlation Experiments with $<$100 nmol Samples with Solenoidal Microcoil NMR Probes. *Journal of the American Chemical Society*, 121:2333–2334, 1999.

[84] Massood Tabib-Azar, Neil S. Shoemaker, and Stephen Harris. Non-destructive characterization of materials by evanescent microwaves. *Measurement Science Technology*, 4:583–590, 1993.

[85] Ikuya Tagawa, Takao Koshikawa, and Yuji Sasaki. High Performance Write Head for 10 krpm HDD with High Data Rate Recording up to 45 MB/s. *IEEE Transactions on Magnetics*, 36(1):177–182, 2000.

[86] William R. Taylor. A 'periodic table' for protein structures. *Nature*, 416:657–660, 2002.

[87] Yu. P. Tsentalovich, J.J. Lopez, P.J. Hore, and R.Z. Sagdeev. Mechanisms of reactions of flavin mononucleotide triplet with aromatic amino acids. *Spectrchimica Acta Part A*, 58:2043–2050, 2002.

[88] D.J. van den Heuvel, A. Henstra, T.S.Lin, J. Schmidt, and W.Th. Wenckebach. Transient oscillations in pulsed dynamic nuclear polarization. *Chemical Physics Letters*, 188:194–200, 1992.

[89] D.W. van der Weide. Localized picosecond resolution with a near-field microwave/scanning-force microscope. *Applied Physics Letters*, 70(6):677–679, 1997.

[90] Sylvain Vauthey, Steve Santoso, Haiyan Gong, Nicki Watson, and Shuguang Zhang. Molecular self-assembly of surfactant-like peptides to form nanotube and nanovesicles. *to be published*, 2002.

[91] C.P. Vlahacos, R.C. Black, S.M. Anlage, A. Amar, and F.C. Wellstood. Near-field scanning microwave microscope with 100 μm resolution. *Applied Physics Letters*, 69:3272–3274, 1996.

[92] K. Wago, O. Zuger, R. Kendrick, C.S. Yannoni, and D.Rugar. Low-temperature magnetic resonance force detection. *Vac. Sci. Tecnol. B*, 14:1197, 1996.

[93] J.H Walton, J.S. de Ropp, M.V. Shutov, A.G. Goloshevsky, M.J. McCarthy, R.L. Smith, and S.D. Collins. A Micromachined Double-Tuned NMR Microprobe. *Analytical Chemistry*, pages A–G, 2003.

[94] S. Wind, M.J. Rooks, V. Chandrasekhar, and D.E. Prober. One-dimensional electron-electron scattering with small energy transfers. *Physical Review Letters*, 57:633–636, 1986.

[95] S.L. Winder, R.W. Boardhurst, and P.J. Hore. Photo CIDNP of amino acids and proteins: effects of competition for flavin triplets. *Spectrochimica Acta Part A*, 51:1753–1761, 1995.

[96] Andrew M. Wolters, Dimuthu A Jayawickrama, and Johnathan V Sweedler. Microscale NMR. *Analytical Techniques*, pages 711–716, 2002.

[97] San Ming Yang, Igor Sokolov, Neil Coombs, Charles T. Kresge, and Geoffrey A. Ozin. Formation of Hollow Helicoids in Mesoporous Silica: Supramolecular Origami. *Advanced Materials*, 11:1427–1431, 1999.

[98] Shuguang Zhang and Michael Altman. Peptide Self-Assembly in functional polymer science and engineering. *Reactive and Functional Polymers*, 41:91–102, 1999.

[99] Shuguang Zhang and Sabina Janciauskiene. Multitask ability of Proteins: α1-antichymotrypsin and the correlation with Alzheimer's disease. *To be published*, 2001.

[100] Shuguang Zhang and Alexander Rich. Direct conversion of an oligopeptide from a β-sheet to an α-helix: A model for amyloid formation. *Proceedings of the National Academy of Sciences of the United States of America*, 94(1):23–28, 1997.